MODELING STUDY ON REVERSE COMBUSTION PROMOTED BY *m*-$BiVO_4$

by

Camilo Javier Viasus Pérez

Thesis submitted to the University of Ottawa
in partial Fulfillment of the requirements for the
Doctorate in Philosophy degree in Chemistry

Department of Chemistry and Biomolecular Science
Faculty of Science
University of Ottawa

Abstract

Reverse combustion is a process converting CO_2 into its different reduced/hydrogenated forms while, ideally, oxygen is being released. Understanding how CO_2 is interacting/reacting with vanadium (main component in the CB of m-$BiVO_4$) in different oxidation states was our main goal. In this thesis we have attempted to contribute to the ongoing efforts for overcoming the formidable challenges posed by H_2 production and CO_2 activation.

In the process to prove the role of each metal during a reverse combustion process mediated by *m*-$BiVO_4$, several strategies were followed to prepare pure monoclinic $BiVO_4$ using different starting materials (Chapter 2). Hydrothermal processes in an autoclave were determined as the most efficient way to obtain *m*-$BiVO_4$. Photoirradiation experiments were performed in-situ and analyzed by EPR, demonstrating that a photoexcited species was generated. EPR spectra were compared with VO_2, which suggested that one electron is being transferred from the VB to the CB in the photoexcitation process, in this case forming a vanadium(IV). This experiment suggested that the reduction process of CO_2 is possibly occurring through a one-electron transfer process. Several attempts were made unsuccessfully to prepare a bismuth vanadate-like compound containing only vanadium(IV) in its structure. $Bi_4V_2O_{10}$ was obtained where the vanadium atom was present in a lower oxidation state but with different Bi/V ratio than in $BiVO_4$. This species does not present any photo-catalytic activity. Instead, it presented mild reactivity in hydrogen formation from formaldehyde in basic media. Photocatalytic experiments on pure *m*-$BiVO_4$ in the presence of water and CO_2 were performed and methanol was obtained as a product. In this process, vanadium leached out from the structure affording a mixture of V(IV) and V(V). On the surface of the remaining *m*-$BiVO_4$, Bi_2O_{4-x} was deposited as a result of the loss of vanadium.

The initial idea behind the preparation of a compound different to $BiVO_4$ was to produce a new photocatalyst that preserves the electronic characteristics of vanadium(V) as well as being a semiconductor (Chapter 3). In addition, a higher oxidation state than the vanadium +5 could provide longer electron-hole recombination times and increase lifetime of the photogenerated electrons. By having a +6-oxidation state, such as provided by a Cr atom, it could give a better chance to improve the reduction of CO_2 by facilitating oxygen release. Unfortunately, photochemical activity was not observed under any conditions. On the other hand, both monoclinic and orthorhombic $BiOHCrO_4$ were tested for formic acid thermal decomposition. These two unique crystal structures were analyzed by single crystal XRD. The monoclinic isomer displays a much higher thermal resilience and was chosen for the degradation of formic acid studies. During the process, an active species of $BiCrO_4$ was formed and identified.

When using vanadium aryloxide compounds in an oxidation state lower than +5 as possible reagents to reduce CO_2, interesting results were obtained (Chapter 4). These compounds were prepared aiming at mimicking the reduction of CO_2 as performed by hypothetically formed lower valent vanadium.

As presented in chapter 2, during the photoirradiation of $BiVO_4$ a new vanadium species is formed. EPR experiments indicated that it could be V(IV). As a result, while vanadium(IV) showed negligible reduction/interaction with CO_2, vanadium(III) aryloxide was a powerful reductant. Experiments attempting to control the electron transfer to CO_2 resulted in two different outcomes. Firstly, a two-electron transfer from the metal center to CO_2 was obtained affording CO and vanadyl(V) tris-aryloxide. Secondly the introduction of a halogen in the metal coordination sphere of a vanadium(III) compound triggered a radical behavior.

The use of a compound of vanadium(II) with polydentate oxygen-donor based ligand still yielded CO. However, an intermediate V-O-V moiety was formed in turn performing radical H atom extraction from the solvent through an unprecedented pattern of reactivity. DFT calculations confirmed the nature of the electronic transfer and the formation of V-O-V that acted as an intermediate for the second CO_2 interaction.

We successfully arrested the reaction to isolate an intermediate and an unprecedented (ONNO)V(OH)-OCO compound was isolated and fully characterized. This CO_2 complex provide the second example of a linearly end on bonded CO_2 and the first case of such a bonding mode to a transition element.

A further study of the reactivity of the vanadium trivalent state was carried out by modifying the ligand to H_2ONOO and secondly, by introducing a Cl atom as in LV-Cl (L = ONNO or ONOO) to enable the formation of derivative such as *p*-methoxy-phenoxide and methoxide ligands via simple ligand substitution.

Unfortunately, the $(ONOO)^{2-}$ ligand quenched the reducing power such that no reaction was observed with CO_2. Halogen replacement afforded (ONNO)V(*p*-methoxy-phenoxide)(THF) which displayed no reactivity with CO_2, but once the *p*-methoxy-phenoxide ligand was replaced by a methoxide group, formaldehyde and formate were formed. The DFT proposed mechanism presented an interesting interaction wherein the *cis*- position in $[V(ONNO)]^+$ is responsible for the H transfer to occur

Finally, we have prepared a heterobimetallic system containing Bi-V atoms (Chapter 6). The oxidation states of Bi and V were +3 and +5 respectively. One pot reaction was the most adequate procedure to obtain the heterobimetallic structure. Trasmetallation on Bi compounds by V atoms was

observed when attempting to build the heterobimetallic structure using more rational reaction pathways. Attempts to obtain a heterobimetallic structure in oxidation states different than that presented in m-$BiVO_4$ were unsuccessful. When oxidation states lower than +5 for vanadium (vanadium(III-II)) and +3 in bismuth were used, metallic bismuth and untreatable materials with a mixed-valence vanadium were formed.

Table of Contents

Acknowledgements

All results presented in this document and all 'invisible work' that was necessary to completed this thesis would not have been possible without the continuous effort of my supervisor and mentor professor Dr. Sandro Gambarotta. I am thankfully for his guidance, for showed me the way to improve my skills and knowledge, and his constant curiosity about chemistry allowed me to keep being surprised even by simple facts, and for paying my salary all these years.

Great thanks to everyone in Gambarotta group, in my beginnings until to the end, everyone was an important part during my progress in my academic and personal life experience (Dr. Sebastiano, Dr. Bala, Dr. Ahmed, Dr. Virginie, Dr. Nicholas, Johanna, Jake, Ms. Laura and Salimah), many thanks to all Thanks to Dr. Ilia and Dr. Bulat for the help in the X-ray structure determination and training. Sharon from Mass spec lab for all help received. Undergraduate lab for showed me how to improve my teaching skills. Glenn and Eric for the NMR and EPR help. To all professors in the Chemistry department that in one way or another contributed during my research formation. Thanks to Mike and Ian at the electronic shop.

To my Mom and Dad, my brothers Raul and Diego and sister Silvia in Colombia, for the constant support from far away, the family was always here.

A mi esposa bella Paola por la tenacidad de resistir estos años con amor infinito en constante apoyo y motivación para poder crecer juntos. Agradecido de que sigas creyendo en mí, lo que he cultivado en los últimos 8 años es gracias a ti. A mis pequeñas Victoria y Valentina, espero sigan siendo terriblositas para que puedan continuar en una constante búsqueda de felicidad y conocimiento.

Finally, to the University of Ottawa for giving me the opportunity to study and develop my personal and academic skills.

List of Charts

List of Figures

List of Schemes

List of Tables

List of Abbreviations

$(OONO)H_2$	2-methoxyethyl- amino-N,N-bis(2-methylene-4,6-dimethylphenol)
$(ONNO)H_2$	2,2'-[[[2-(dimethylamino)ethyl]imino]bis(methylene)]bis[4,6-dimethylphenol]
AcA	Acrylic acid
BM	Bohr magnetons
$BiOHCrO_4$	bismuth chromate oxide hydroxide, monoclinic and orthorhombic
$BiVO_4$	bismuth vanadate, monoclinic, tetragonal and tetragonal zircon type
Calix[4]	Calix[4]arene-*p*-tert-butylphenol
CB	Conduction band
CFI	Condensed Fukui Indexes
DFT	Density Functional Theory
DMMDO	4,4-dimethyl-5-methylene-1,3-dioxolan-2-one
EDS	Energy-dispersive X-ray spectroscopy
EPR	Electronic Paramagnetic Resonance
pFA	para-formaldehyde
GC-FID	Gas Chromatograph with Flame Ionization detector.
GC-TCD	Gas Chromatograph with Thermal-conductivity detector.
HC	Hydrocarbons
HOMO	Highest occupied molecular orbital
JCPDS	Joint Committee on Powder Diffraction Standards
LUMO	Lowest unoccupied molecular orbital
MesOH	2,4,6-trimethylphenol

MS-EI	Mass spectrometry with electronic impact
MOF's	Metal-organic framework
NMR	Nuclear Magnetic Resonance
p-GaP	p-type gallium phosphide
PVOH	polyvinyl alcohols
RhB	Rhodamine B
r-ROP	radical ring opening polymerization
SEM	Scanning electron microscopy
SEM-EDS	Scanning electron microscopy with Energy Dispersive X-Ray Spectroscopy
TMEDA	N,N,N',N'-Tetramethylethylenediamine
TOF-MS-ESI	Time of Flight - Mass spectrometry – electrospray ionization
TGA	Thermo-gravimetric analysis
UV	Ultraviolet
VAc	Vinyl acetate
VB	Valence band
XRD	X-ray diffraction
SC-XRD	Single crystal X-ray diffraction
XRF	X-ray fluorescence

Chapter 1. From Waste to Energy: Carbon dioxide activation and hydrogen production

CJV. I am the sole author with the guidance of my supervisor.

1.1. Introduction

For the past four decades, considerable research effort has been aimed at discovering new technologies for the production of clean and renewable energy.[1] One of the most promising avenues is the extraction of hydrogen from water (water splitting) due to large water availability, absence of waste products and perfect recyclability.[2] Today, water splitting is a widely studied process which can be carried out in a variety of ways: by electrolysis (ambient pressure and temperature, high pressure or thermal high pressure), photo-electrochemically, photochemically, by radiolysis or solar/thermal decomposition among others.[3,4] However, water splitting, albeit doable in the lab, is a yet-to-come process in terms of large-scale production.

The second possibility is to recycle and reconvert CO_2 into useful chemicals and possibly fuels. It should be noted that power plants release enormous amounts of CO_2 into the atmosphere at a surprising level of purity (>99%). Therefore, CO_2 is a completely inexpensive raw material and does not require initial treatment.

1.2. Hydrogen Production

The separation of water into the two gaseous components is a thermodynamically uphill process with a considerable ΔG (+228.71 kJ/mol). Therefore, the true challenge is about finding efficient techniques for providing the energy to overcome unfavorable thermodynamics. The utilization of photo-semiconductors is particularly appealing. These materials harvest energy from sunlight and convert it into electrochemical energy sufficient to trigger redox transformations (Scheme 1.1).

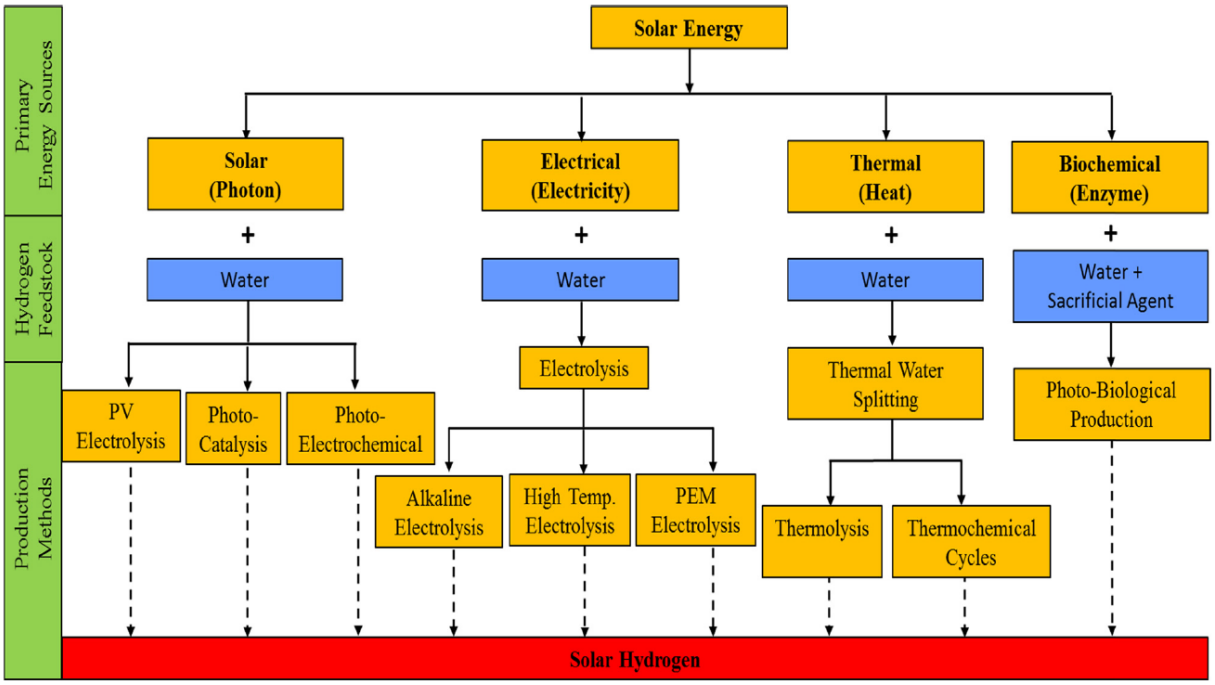

Scheme 1.1. Classification of solar hydrogen production methods. Reproduced from ref #[5] with permission by Elsevier.

The principle behind photo-semiconductors (using photonic energy) is quite simple. When the applied energy (incident light) is greater than the HOMO-LUMO (commonly named Valence and Conduction Bands) band gap, electrons are promoted from the valence to conduction band, forming positively charged holes in the valence band. Since the two bands also correspond to two defined structural sites, the acquired electrical charges turn those sites into ions where either oxidation or reduction can be performed when appropriate substrates are in their proximities. In the specific case of water splitting, protons from water molecules are reduced by the electrons to form H_2 while the oxygen is oxidized to O_2 by the positively charged holes.[4,6]

Some very important aspects of photo-semiconducting materials are the width of the band gap and the band edge of the solid, which must be larger than +1.23 V (1100 nm) and located between 0 and +1.23V

to allow the reduction and oxidation of water (Scheme 1.2). With that in mind, a large variety of heterogeneous materials have been prepared in the literature.[4,7–9]

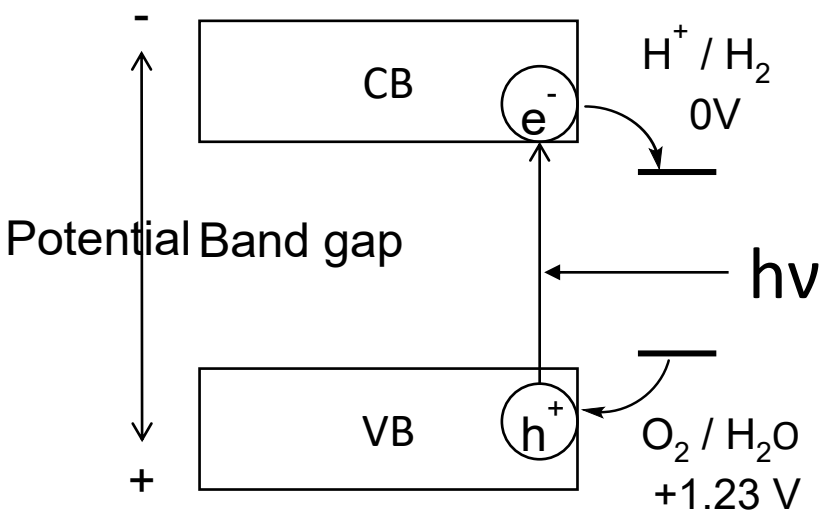

Scheme 1.2. Principle of water splitting using semiconductor photocatalysts. Reproduced from ref #[4] with permission by The American Chemical Society.

One of the best catalysts for pure water splitting is based on $NaTaO_3$:La in combination with NiO as a cocatalyst.[10,11] This system has an apparent 56% quantum yield conversion which can generate 19,800 and 9,700 µmol/h of H_2 and O_2, respectively. The band gap of $NaTaO_3$:La is 4.0 eV and has the correct band edge to generate both H_2 and O_2. NiO must be used as a co-catalyst to increase the hydrogen production and avoid the deactivation of the non-doped photo-semiconductor.[11]

In 2013 Peilin *et. al*.[12] showed how a good band edge alignment is important to achieve a high reaction rate in water splitting. The alignment was achieved by placing the conduction band in a potential more negative than that of a standard hydrogen reduction and the valence band in a potential more positive than required for water oxidation. In their work, the effects of proper band gaps and band edges of photo-semiconductors were computationally related to experimental data. These results enabled the authors to rationalize the behavior of the most extensively studied photo-semiconductor,

TiO_2, and understand the reasons for lower production of hydrogen (106 µmol/h) and oxygen (53 µmol/h) obtained when using Pt as co-catalyst.[13–15] The limiting aspect of those catalysts is the high band gap energy required. For example, with the bandgap of 3.2 eV (388 nm) for TiO_2, UV irradiation is necessary.

Recent studies in water splitting have developed composites that can be active at 600 nm and still provide adequate yield.[16,17] With the same aim, oxynitride photocatalysts have been prepared which can absorb visible light when used as a catalyst.[16,18] Oxynitride photocatalysts present a great improvement in activity due to the possibility of optimising the position of the valence band edge by simply varying the oxygen-nitrogen ratio. Also, by changing the size of the cation in the structure of $MTaO_2N$ (M = Ca, Sr and Ba) the position of the conduction band edge may be altered. In this particular case, smaller cations cause a shift toward higher energy.[19]

A few examples of pure water splitting using a single semiconductor are illustrated in Figure 1.1. The figure visualizes how the position and width of the band gap play an important role in hydrogen and oxygen evolution. In the family of $NaTaO_4$:La compounds, indium derivatives did not present such high activity due to the inert lone pair effect which generates high electron-hole recombination rates. In general, a single photo-semiconductor is unable to generate hydrogen and oxygen in large yields. This is the case in the series of $InVO_4$, $InNbO_4$, $InTaO_4$, where the bandgap between holes and photo-excited electrons is of sufficient energy to oxidize and reduce water. However, the current productivities remain too low for industrial applications.[20,21] Therefore it remains vital to prepare composite materials with improved activity.[22–24]

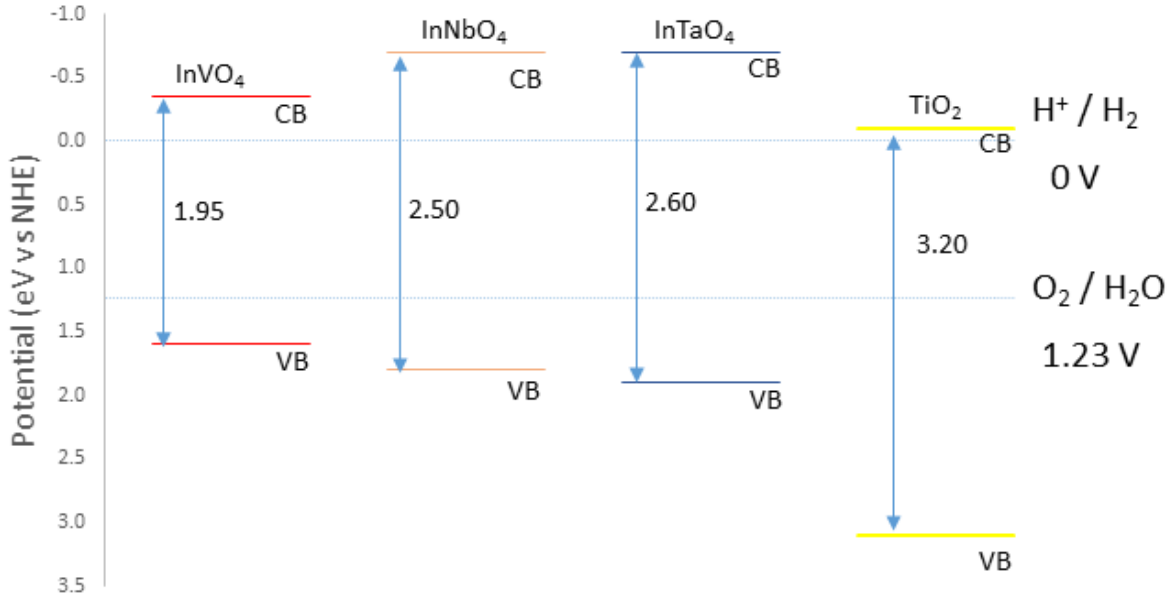

Figure 1.1. Band gaps of various semiconductors able to perform pure water splitting.[3,21,193,472]

Onishi and coworkers found that Sr^{2+} doped semiconductors made of alkali metals give higher resistance to etching compared to non-doped materials.[25,26] In this work, it was shown that the concentration of Sr can affect the electron hole recombination in the photocatalyst over time.

The second stage of water oxidation (oxygen release) is currently the rate determining step in the quest for new photo-semiconductors for water splitting. An effective strategy to bypass the difficulties arising from finding efficient oxygen evolution sites consists of the use of sacrificial agents, with alcohols being particularly popular. Many catalysts have been prepared while looking for pure hydrogen evolution with and without sacrificial agents.[27,28] Table 1.1 lists several semiconductor photocatalysts used in recent years in water splitting for hydrogen production.[5] Hydrogen production rates from zero to 500000 μmol/h/$g_{catalyst}$ with a variety of light sources, band gaps and co-catalysts have been obtained.

Table 1.1. Several semiconductor photocatalysts used in water splitting for hydrogen production. Reproduced from ref #[5] with permission by Elsevier.

Photo-catalyst	Co-catalysts (Element)	Light source (Power, type)	Band gap (eV)	Hydrogen production rate ($\mu mol/h/g_{catalyst}$)
γ-Al_2O_3 /O-g-C_3N_4	Pt	300 W, Xe	2.7	1288.0
N-doped Ta_2O_5	Au, Pt, Rh	Visible light ($\lambda \geq 420$ nm)	2.4	637.5
CdS NRs	CoP_x	300 W, Xe	–	500000.0
$LaMg_{1/3}Ta_{2/3}O_2N$	–	300 W, Xe	2	–
$Sm_2Ti_2S_2O_5$	Pt/IrO_2	300 W, Xe	2	40.6
$CuLi_{1/3}Ti_{2/3}O_2$	Ru, Pt	300 W, Xe	2.1	143.0
ZnS- Graphene	–	300 W, Xe	3.27–3.40	7.42
Ag-Au/TiO_2	–	300 W, Hg	2.3–2.4	718.0
Cu/ZnS	–	350 W, Xe	2.36–3.43	973.1
Cu_2ZnSnS_4/Cu_2NiSnS_4/ Cu_2CoSnS_4	–	Solar Light – XPS 300TM	1.18–1.59	670.0–1200.0
Black-colored ZnO NW/Carbon	–	300 W, Xe	3.37	1847.9
MoS_2/CdS	–	300 W, Xe	1.68–2.4	49800.0
Au/TiO_2	–	300 W, Xe	–	1019.0
Sn_3O_4	Pt	300 W, Xe	2.4–3.5	40.0
$BaZrO_3$–$BaTaO_2N$	Pt/Ir	300 W, Xe	1.8	14.2
g-C_3N_4/$BiVO_4$	–	300 W, Hg (Xe)	2.4–2.85	–
g-C_3N_4	Fe/Cu	Visible light ($\lambda \geq 420$ nm)	2.93–3.0	0.2
WO_3/Sb_2S_3	–	100 mW/cm^2, Xe	2.28–2.75	–
Cu_2O/$BiVO_4$	RuO_x	100 mW/cm^2	2.4–2.5	–
$Cd_{1-x}Zn_xS$ (ZB/WZ)	–	300 W, Xe	2.32–3.58	3130.0
g-C_3N_4	Au	300 W, Xe	2.65–2.72	223.0
CdS Np- Cd NS	Pt	Sunlight ($\lambda > 420$ nm)	2.42	820.0
$AgGaS_2$-Ni	Ru	300 W, Xe	1.9–2.6	243.0
NU1000 (MOF)	Ni-S	AM 1.5 Solar filter	–	4800.0
TiO_2/Al_2O_3/Cu_2O	Au	AM 1.5G	2.0–2.1 (Cu_2O)	–
Cu_2O/(ZnO,Al_2O_3)/TiO_2	MoS_{2+x}	AM 1.5G	3.2 (ZnO)	2700.0
CdS-Ti-MCM-48	RuO_2	Visible light ($\lambda > 420$ nm)		2730.0
Sr–$NaTaO_3$	–	350 W, Hg		275000.0
$LaTiO_2N$	CoO_x	300 W, Xe	2.1	–
Ti-MPF-NH_2	Pt	500 W, Xe		367.0
$C_3N_{4-x}S_x$	–	300 W, Xe	2.61–2.69	136.0
g-C_3N_4		Visible light ($\lambda > 420$ nm)	2.67	–
CeO_2	Pt	200 W, W	2.53–2.82	203.0
Fe-doped silicate Clay	–	300 W, Xe	3.75	210.0
$(CuGa)_{1-x}Zn_{2x}S_2$	Ru, $BiVO_4$, Co	300 W, Xe	2.2–2.3	120.0

Knowing that the overall water splitting mechanism consists of two separate stages of hydrogen and oxygen evolution (Eq. 1), researchers have been focussing on each half-reaction separately.[27,29–33] A recent publication by Kalisman *et. al.*[27] stated how the problem of hydrogen production can be apparently solved, with a maximum efficiency achieved when isopropanol was used as sacrificial agent.

$$
\begin{array}{lll}
H_2O \longrightarrow 2H^+ + 2e^- + 0.5O_2 & E_{anodic} = +1.23\ V & \\
2H^+ + 2e^- \longrightarrow H_{2(g)} & E_{cathodic} = 0\ V & \text{(Eq. 1)} \\
\hline
H_2O \longrightarrow H_{2(g)} + 0.5O_2 & E_{rxn} = +1.23\ V &
\end{array}
$$

A feasible strategy to improve yields is to decrease the trajectory that electrons must travel to the surface. This was cleverly accomplished by using nano-structured materials.[12] For example, the function of Pt particles has been shown to facilitate hydrogen evolution. Similar behavior was proposed when NiO is used as co-catalyst in $NaTaO_4$:La doped material.[11] The photocatalytic activity of Ga_2O_3 doped with Zn and $Rh_{2-y}CrYO_3$ as a co-catalyst has been reported.[34] Increasing the amount of Zn from 1 to 3% in the composite affords a record oxygen and hydrogen evolution from pure water (13.7 and 6.9 mmol for 1% and 21.0 and 10.5 mmol, for 3%). In line with the behaviour of the composite materials[35], an increase in activity when photo-catalysts are supported on conductive materials such as graphite[36] and graphene oxide[23,37–41] is commonly observed. The fact that the layered structure works as a support facilitates small particle size formation and deposition, and, as a result, the electron transfer to the surface of the catalyst becomes easier.

The fact that water splitting is a non-spontaneous thermodynamic process requiring a large energy input, it makes semiconductors the most economical and convenient catalysts.[42,43] A major challenge with these systems is how to generate a sufficient overpotential to facilitate the complete redox reaction. Currently, the majority of recent literature reports describe attempts to prepare efficient systems for either hydrogen or oxygen formation. It is conceivable that once they are combined together in a Z-scheme cycle, a water splitting system of very high efficiency might be achieved (Figure 1.2).[44,45]

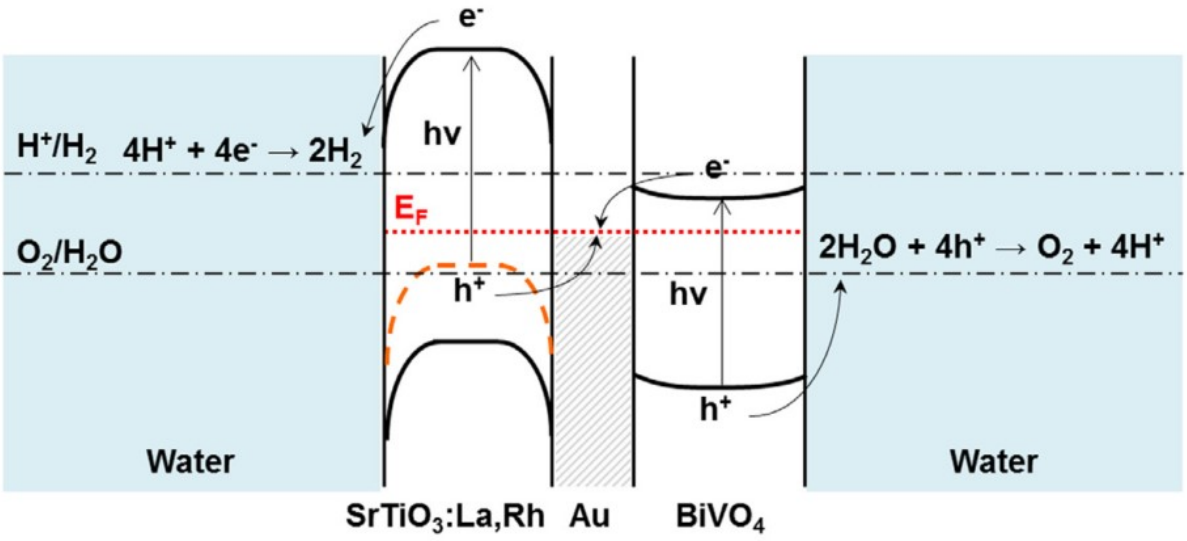

Figure 1.2. Schematic energy diagrams in a Z-scheme representation under illumination for water splitting process. Reproduced from ref #45 with permission by Elsevier.

The electron hole recombination remains a major challenge to be faced while using semiconductors. A major advance with this respect was recently achieved with the discovery that surface passivation (i.e. by acids) may generate higher efficiency in charge separation. In spite of rising expectations, it should be realistically noticed that this remains so far limited to photo-electrochemical systems.[46]

Finally, Prezhdo and coworkers have recently published a comprehensive theoretical study where electron transfer properties using different dyes were systematically analyzed (e.g.: sensitizers and dopants in perovskite and composite materials[47–55] for CO_2 transformation applications using Ru complexes attached to the surface[56,57]). The utilization of a co-catalyst or dye sensitization to improve light absorption or electron transfer during the redox process on the surface of the catalyst is a widespread technology. In all cases, harvesting more light into the system improves the formation of electron-hole pairs[47,58,59], but it does not modify the electron-hole recombination time. Instead, controlling this specific characteristic in a photochemical system provides the photo-excited electrons and holes with more time to perform a chemical reaction. In other words, if the time that the photo

excited electrons are available for is longer than the recombination lifetime, there will be an increased probability for performing chemical transformations.

Several composite materials have been reported using a mixture of *m*-$BiVO_4$ and V_2O_5 or Bi_2O_3.[60–65] The products were obtained with an additional amount of either Bi or V and dispersed onto the surface of the $BiVO_4$. Although the true nature of these materials remains unclear, the heterojunctions present an important improvement in their photocatalytic properties compared to pure *m*-$BiVO_4$ or each metal oxide used during their formation.

As highlighted above and although entirely possible, water splitting promoted by light is not currently feasible from the industrial point of view due to low productivity, slow processes and prohibitive costs. The most common and convenient method to obtain hydrogen remains steam reforming of methane in a reaction also producing CO (Eq. 2). Subsequently carbon monoxide and steam may be reacted in a slightly exothermic process (ΔH_r = -41 kJ/mol and ΔG_{293K} = -20.1 kJ/mol) called the 'water-gas shift' to produce, in presence of a catalyst, CO_2 and more hydrogen (Eq. 3).

$$CH_4 + H_2O \xrightarrow[3\text{-}25\ PSI]{700\text{-}1000^oC} CO + 3H_2 \quad \text{(Eq. 2)}$$

$$CO + H_2O \xrightarrow{cat.} CO_2 + H_2 \quad \text{(Eq. 3)}$$

The main disadvantage of this procedure is: 1) carbon dioxide formation and 2) the high endothermicity of the first step (ΔG_{293K} = +150.8 kJ/mol). This process is economically balanced by the fact that the raw materials such as water and methane are low cost. This procedure affords hydrogen in a price range of few dollars per kilogram, thus making this technology so far unbeatable.

Thermal processes and solar thermal water splitting can be used to generate hydrogen and oxygen from water. While harvesting and converting light to heat can be easily achieved with parabolic

mirrors, an array of catalysts has been developed for this purpose. For example CeO_2 can afford thermal water splitting through oxygen vacancies induced upon heating at 1090°C.[66] At this temperature, 5.5% of its mass is expelled as O_2. The vacancies can be regenerated using water, with parallel release of hydrogen. Solar thermochemical water splitting using doped ceria with Zr, Hf, Mg, Sc, Cu, Ni, Mn, Fe and Pr is presented in Table 1.2. The best dopant appears to be zirconium, producing hydrogen up to 6.67 mL/g in one cycle at 1400°C.

Table 1.2. Solar hydrogen production using doped ceria. Reproduced from *ref* #[66] with permission by The American Chemical Society

dopant-percentage	reduction temperature, °C	hydrogen production mL/g per cycle (μmol/g)
Zr-10%	1400	5.76 (257)
Zr-25%	1400	6.67 (298)
Zr-50%	1400	5.95 (266)
Hf-10%	1500	4.50 (201)
Sc-10%	1500	4.06 (181)
Mg-10%	1500	3.89 (174)
Ni-10%	1500	2.73 (122)
Fe-10%	1500	1.94 (87)
Mn-10%	1500	3.77 (168)
Cu-10%	1500	0.97 (43)
Pr-10%	1500	3.96 (177)

In a similar thermal process, Eq. 4 and 5 present the generation of oxygen vacancies in cobalt-ferrite and alumina upon heating. This process releases molecular oxygen, whilst the reduced metal can react with water, re-oxidizing the metal back while releasing hydrogen.[67]

$$CoFe_2O_4 + 3Al_2O_3 + \text{heat} \longrightarrow CoAl_2O_4 + 2FeAl_2O_4 + 0.5O_2 \quad \text{(Eq. 4)}$$

$$CoAl_2O_4 + 2FeAl_2O_4 + H_2O \longrightarrow CoFe_2O_4 + 3Al_2O_3 + H_2 \quad \text{(Eq. 5)}$$

While the reduction process with release of oxygen occurs at 1350°C, the hydrogen forms at only 1000°C. Even though the temperatures for water splitting seems to be relatively high, they are low when compared with the temperatures required for the direct thermolysis of water (2700°C). Figure 1.3 presents the consecutive redox cycles where the hydrogen and oxygen are obtained separately.[67]

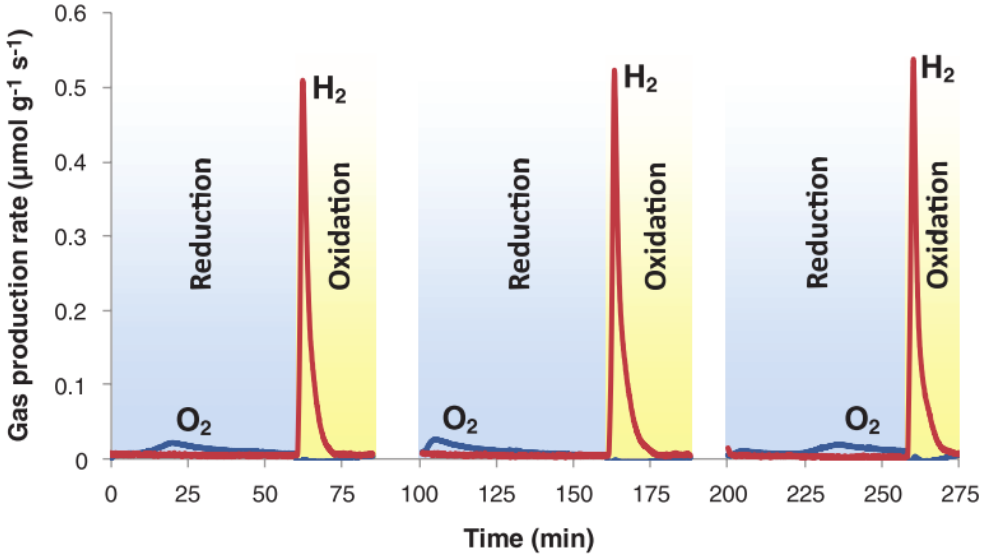

Figure 1.3. Isothermal water splitting at 1000/1350°C cycles. Reproduced from ref #[67] with permission by The American Association for the Advancement of Science.

More recently, photochemical-thermal water splitting was achieved by Docao *et al*. using Cu-loaded TiO_2. The Cu/TiO_2 material can release O_2 easily upon irradiation to form oxygen vacancies that consequently oxidize water to release hydrogen under thermal conditions (Figure 1.4).[68]

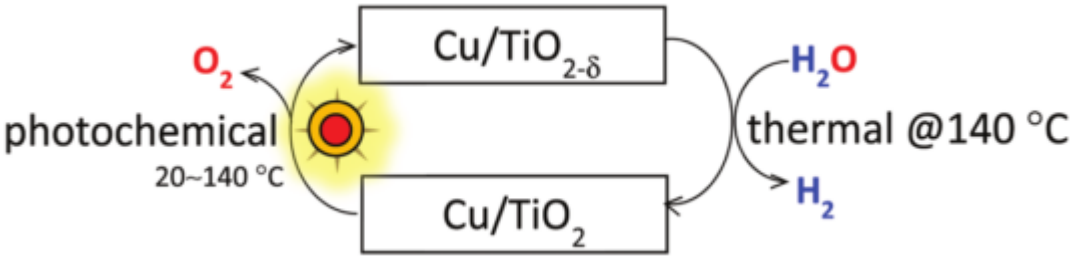

Figure 1.4. Solar photochemical-thermal water splitting using Cu/TiO_2. Reproduced from ref #[68] with permission by RSC Publishing.

Although ingenious, the conversion is too low for industrial scales. This achievement opens the view to new research areas where a simple metal oxide could be the answer to develop new systems for pure thermal or photochemical thermal water splitting.[69,70]

1.3. CO_2 recycling

Although the possibility of producing energy from water under the form of H_2 is exciting and promising, the reality is that so far, the release of carbon dioxide is still required during hydrogen production. The main production of carbon dioxide is by direct combustion of charcoal (42%).[71] The possibility of capturing and storing CO_2 produced by fossil fuel power plants by injecting it underground for long-term storage is not sufficient to avoid release into the atmosphere. Recycling is therefore the only feasible alternative.

The high thermodynamic stability of CO_2 makes its transformations particularly challenging (Scheme 1.3). Carbon dioxide is a three-atom linear molecule composed by a carbon in its maximum oxidation state (+4) located at the center of the molecule. The two oxygen atoms are bonded via σ- and π-bonds to the carbon, giving CO_2 a large amount of bond energy. Albeit an apolar molecule, the high electronegativity of oxygen atoms introduces polarity in each C-O bond causing its acid-base amphoteric behaviour.

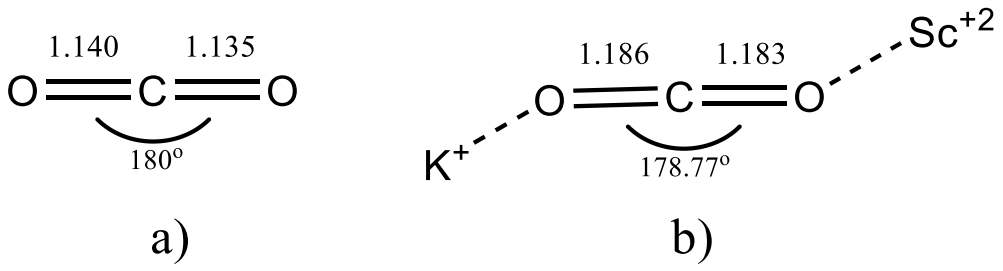

Scheme 1.3. a) free carbon dioxide captured in a pillared metal-organic framework.[72] b) coordinated carbon dioxide between two cations.[73]

The stability and low reactivity of carbon dioxide can be explained by the molecular orbital diagram shown in Scheme 1.4. The HOMO and the LUMO are located at lower energy when compared to similar molecules such as COS and CS_2. Reducing CO_2 implies adding electron(s) to the LUMO ($2\pi_u$) which becomes energetically more favored than HOMO ($1\pi_g$) if a bent molecular geometry is adopted. Disrupting the linearity is in fact the key to activation and explains why it is easier to reduce CO_2 when coordinated to metals.[74]

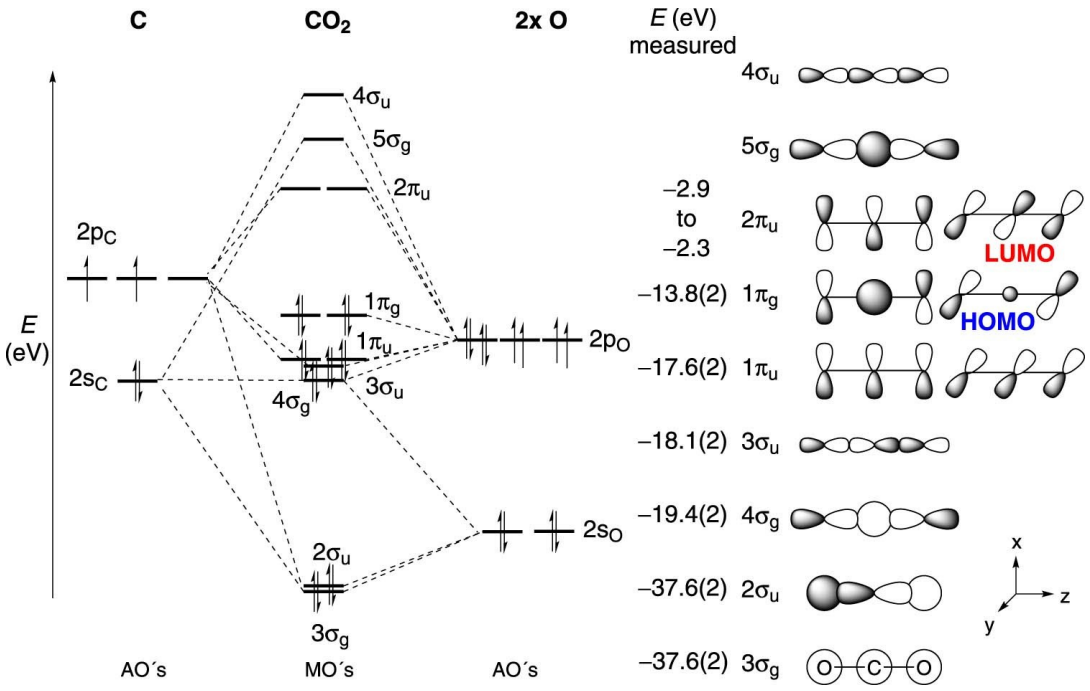

Scheme 1.4. Molecular orbitals for CO_2. Reproduced from ref #[74] with permission by Elsevier.

The number of CO_2-complexes reported in the literature is vast. Surprisingly, the general procedure to obtain CO_2-metal complexes is not through the direct interaction of metal compounds with CO_2 in different environments/metal oxidation states. Instead, reactions of metal oxides (M^{n+2}=O) with CO, metal carbonyl compounds (M^n←CO) with an oxidizing/oxygen atom transfer agent, e.g., O_2, or of M^n←CO with M^{n+2}=O are more frequently used (Scheme 1.5). The preparations may be organized in

the following categories: reaction with liquid or gaseous CO_2, photochemical, thermal reactions with additional triggering, direct addition of CO_2 or in situ generation of a CO_2 ligand, addition of CO_2 with or without replacement of any L-type ligands, formation of the ligand by insertion or addition and consecutive deprotonation or condensation, one- or two-electron reduction of CO_2 or no electron transfer and finally reduction by one or two metal centers by external reductants or by reductive elimination of ligands.[74] In general terms, electron-rich metal compounds are desirable to obtain CO_2 complexes. This characteristic must be properly tuned due to the possibility to obtain undesired products like CO or carbonates among others.[75,76]

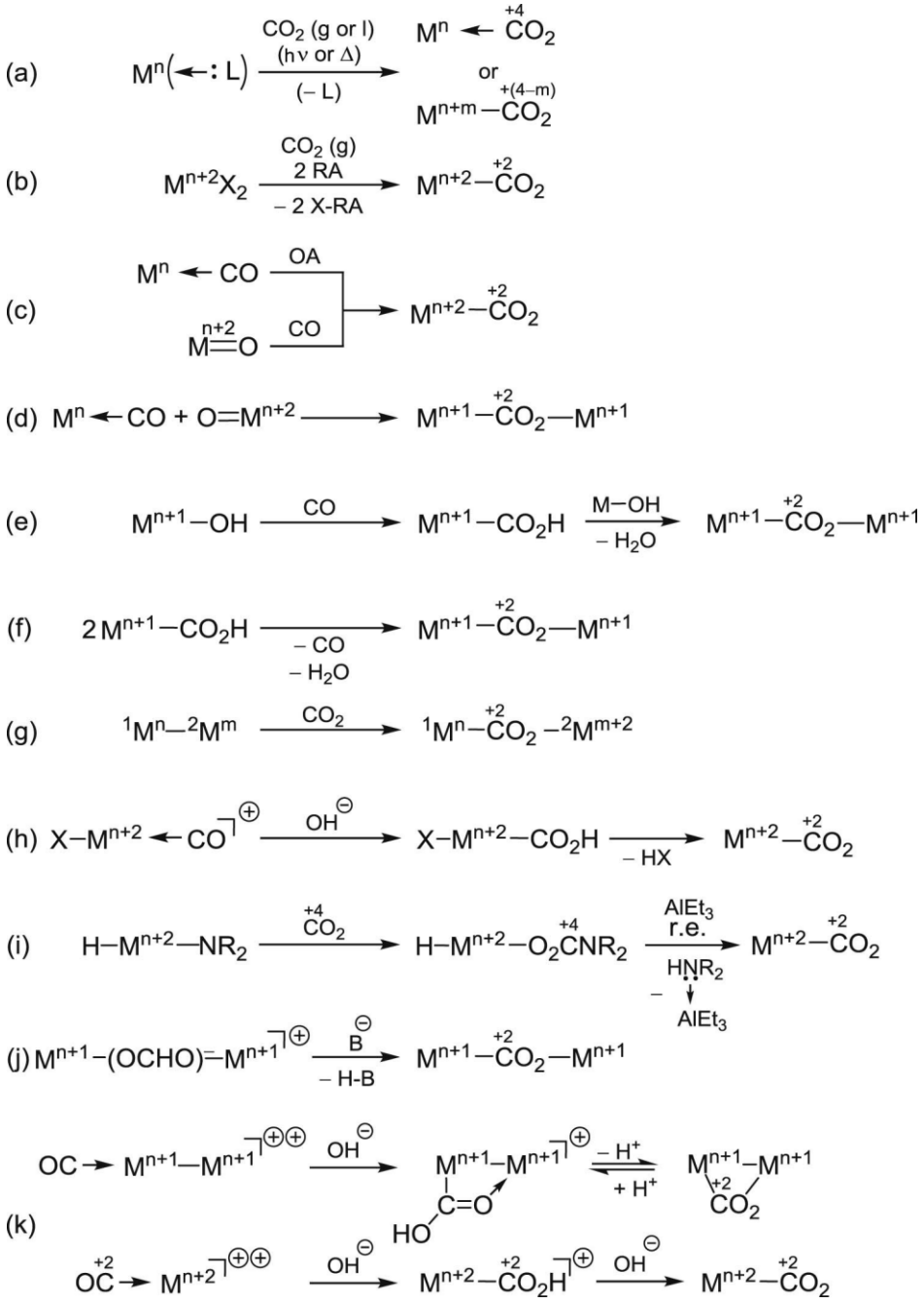

Scheme 1.5. Generalized synthetic methods for CO_2 complexes. Datively bonded metals are not displayed. X= halide; L = two-electron donor ligand, e.g., CO, PR_3, N_2, alkene, alkyne; m=1, 2; n = oxidation state of the center; RA= reducing agent, e.g., alkali metals; OA= oxidizing/oxygen atom transfer agent, e.g., O_2, organic and inorganic peroxides; r.e. = reductive elimination; R= organic groups; B = Brønsted base. Reproduced from ref #[74] with permission by Elsevier.

Considering the variety of possibilities to prepare carbon dioxide metal complexes, it comes as no surprise that different coordination modes have been identified using various oxidation states and metal centers (Scheme 1.6).

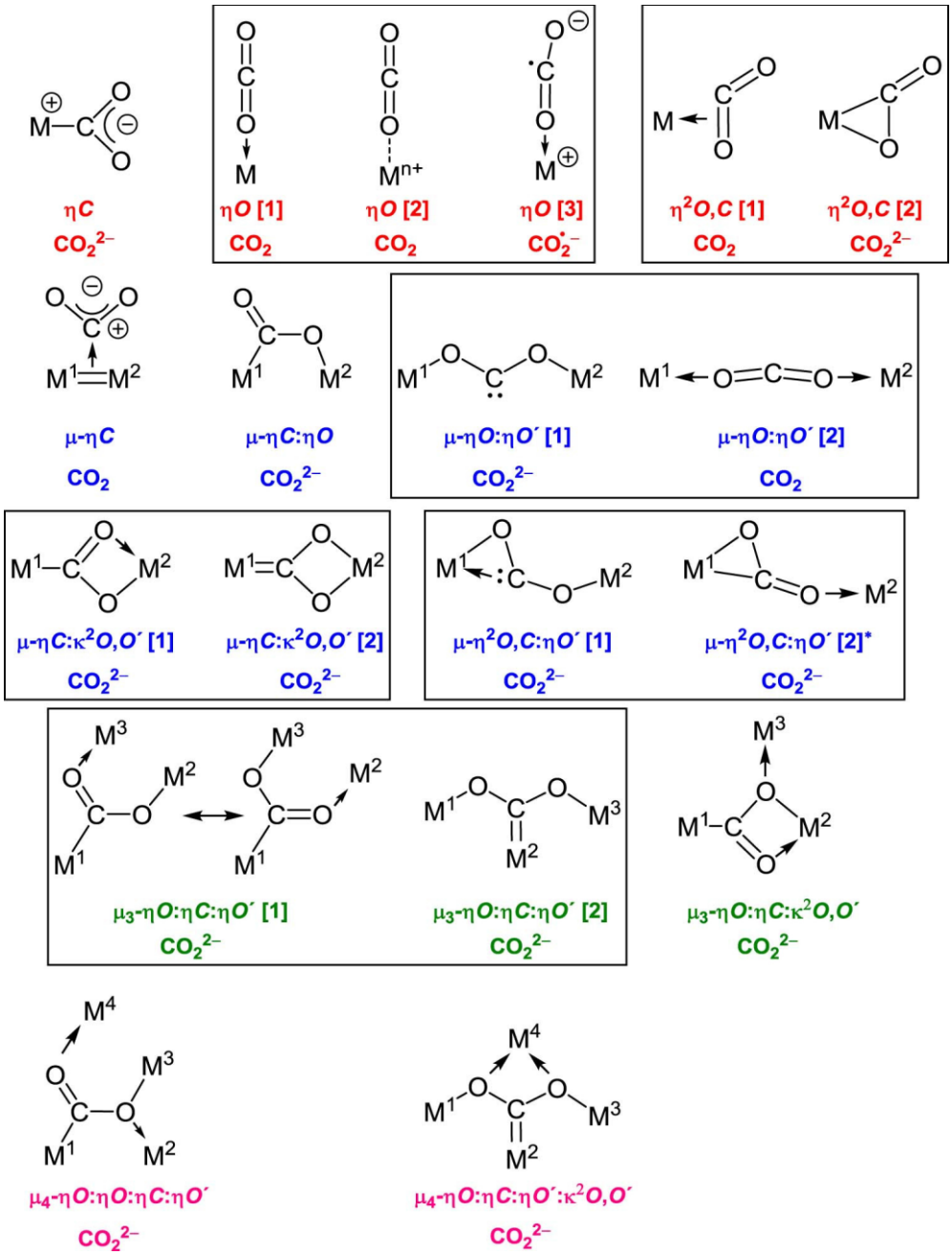

Scheme 1.6. Carbon dioxide bonding modes. Reproduced from ref #[74] with permission by Elsevier.

Activation of carbon dioxide implies moving from a linear to a bent geometry. Reduction of carbon dioxide instead, can be achieved by simply adding a low valent metal center. This is normally carried out in stoichiometric transformations rather that in the much more desirable catalytic fashion.

Due to the fact that a large amount of energy is released during formation of CO_2, the reverse reaction is extremely difficult without using sacrificial agents. This is one of the reasons why stoichiometric reductions require almost invariably high energy content compounds. The selectivity of the reduction process plays a determining role depending upon the hydrogen source and the catalyst used. Scheme 1.7 shows the entire redox series of C1 compounds.

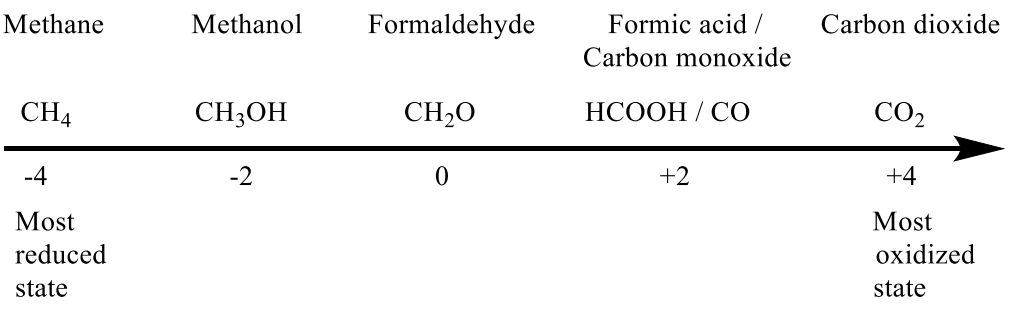

Scheme 1.7. Different small C1 molecules and their oxidation states for carbon.

Stoichiometric reactions of CO_2 are attractive when the final product is a high value-added product or a more reactive intermediate.[77–79] Reduced products as CH_4, CO and MeOH are less important since they can be directly obtained from *syngas* or from oil extraction.

1.4. CO_2 as raw material

Although not necessarily viable from a commercial point of view, there are efficient and scalable processes where carbon dioxide can be used as a raw material to obtain methanol, formic acid,

formaldehyde, carbon monoxide or methane.[80–83] Instead employment of CO_2 to form polycarbonates, in polymerization, as CO_2 building block materials, urea derivatives[84], carboxylic acid from styrene,[85] reductive functionalization with amines[86] and $C_{\geq 2}$ compounds[87] are a few examples of possible applications in this area. Reversible binding by MOF's (and especially insertion reaction of CO_2 into M-C bond to generate carboxylate ligands) are the quickest way to produce value-added derivatives using CO_2.[88] These last two topics will be further discussed in Chapter 3.

Radical polymerization using CO_2-containing building block materials have been widely studied in recent years.[89–93] A radical ring-opening (r-ROP) polymerization and a vinyl-type polymerization (VT) resulted in polymers bearing pendants carbonates (Figure 1.5).

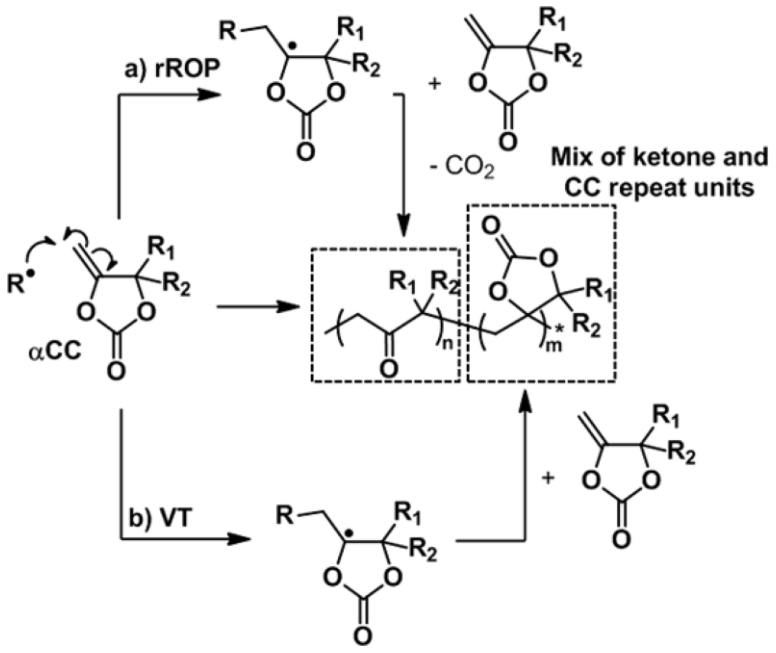

Figure 1.5. Radical polymerization of DMMDO and the reported occurrence of two polymerization mechanism. Reproduced from ref #[89] with permission by RSC Publishing.

The special characteristic of these cyclic carbonate groups is that they do not have hydrolyzed functions, thus making them attractive for future modification via post-polymerization reactions. The

formation of DMMDO using CO_2 and subsequent addition of VAc can afford very useful and functional PVOH after hydrolysis and post-modification procedures. The resulting copolymerization of DMMDO with VAc at low temperatures could be achieved using alkyl-Cobalt(III) acetylacetonate (R-Co(acac)$_2$) complex. The use of an alkyl chain as an initiator and Co(acac)$_2$ as a controlling agent makes the molar mass of the monomer increase linearly with the monomer conversion (Figure 1.6).

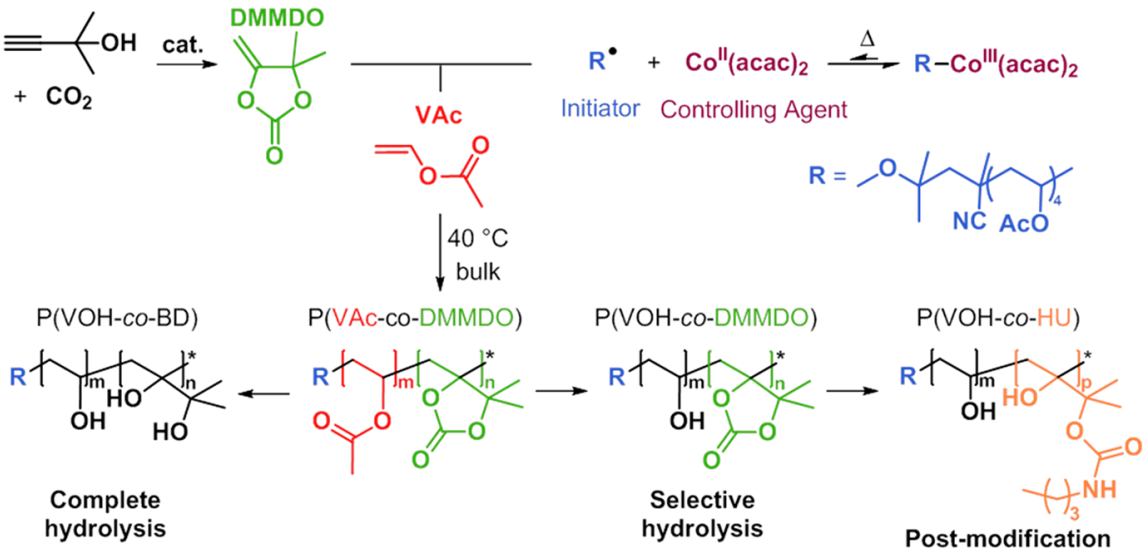

Figure 1.6. Cobalt mediated radical polymerization VAc and DMMDO and subsequence hydrolysis and post modification to yield functional PVOH. Reproduced from ref #[89] with permission by The American Chemical Society.

The utilization of CO_2 as a precursor for C1 building blocks and feedstock has been of great interest to the academic community over the past decade. Several metals such as Ag, Cu, Pd, etc., afford carboxylative cyclization for propargylamine.[94] The three component synthesis of propargylamine and its derivatives has been greatly improved in recent years.[95] In fact, applications in therapeutic drugs and polyfunctional heterocycles confer this reaction with an important role as an entry to many bio-active components such as conformationally restricted peptides, iso-esters, natural products, etc.

Figure 1.7 shows a three-component coupling of aldehydes, amines and alkyne into propargylamine where nano-crystalline copper(II) oxide is used as catalyst. Short reaction times (6h) and a high yield make the process feasible for commercial use.

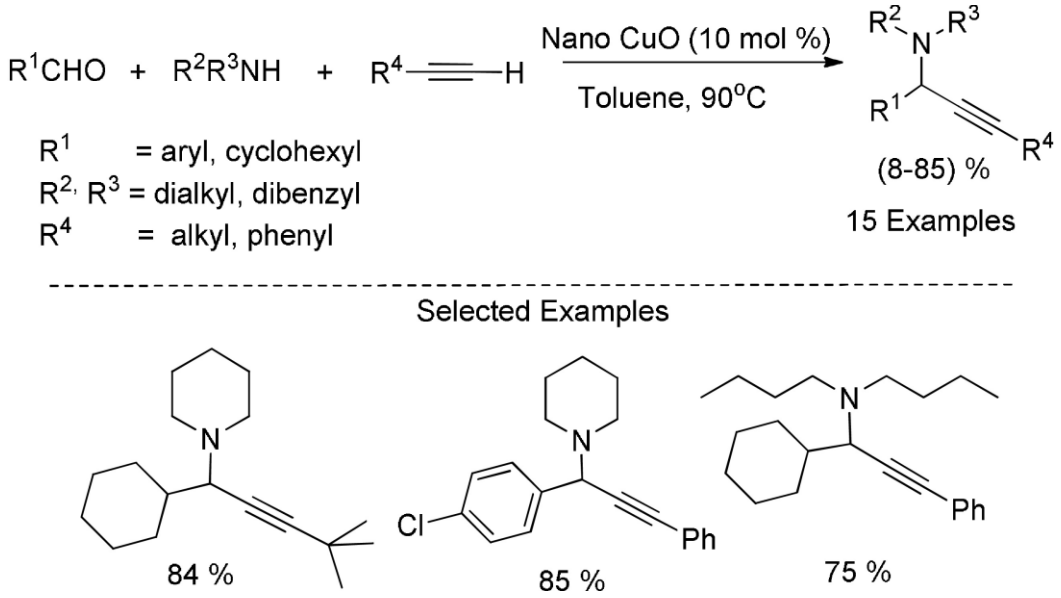

Figure 1.7. Synthesis of a few propargylamine derivatives by nano CuO. Reproduced from ref #[96] with permission by Elsevier.

Once the propargylamine precursors are obtained, the carboxylative cyclization reaction can occur using carbon dioxide as a C1 synthon (Figure 1.8). Yields up to 70% conversion to the cyclic carboxylate product were obtained when catalysts contained silver benzoate.

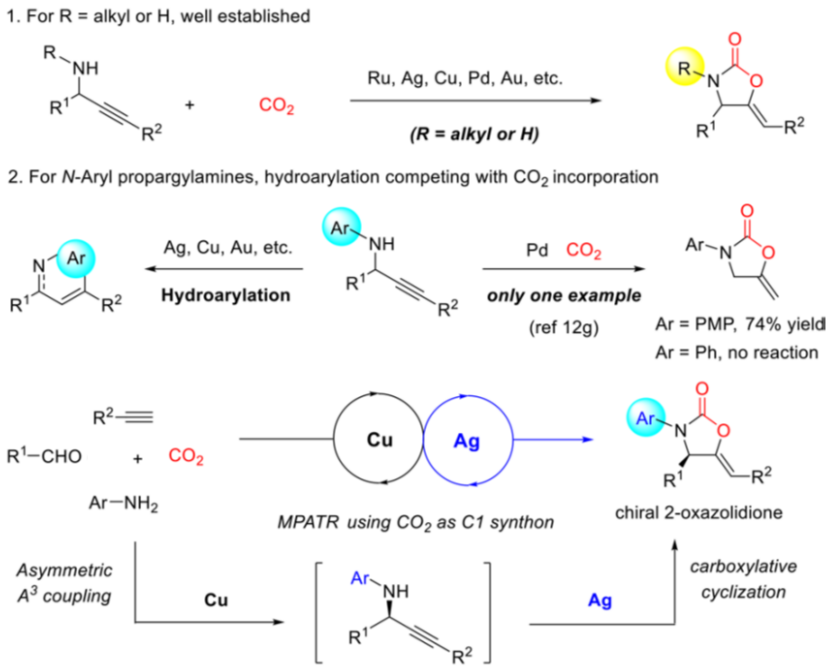

Figure 1.8. Carboxylic cyclization of propargylamines. Reproduced from ref #[94] with permission by The American Chemical Society.

Additives such as aniline improve the yield of the cyclization due to its ability to increase the effective concentration of CO_2 via carbamic acid formation. When $Cu(OTf)_2$ is used as additive, the observed yield dramatically increased up to 97%. The rationalization for this tandem-catalytic reaction is still not available in the literature.[94]

The use of CO_2 as a raw material for an alternative preparation of AcA has recently gained significant attention.[97–99] The relatively low energy barrier for the formation of AcA from carbon dioxide and ethylene instead of the usual selective oxidation of propane, makes the process important for CO_2-using transformations. Even though obtaining acrylic acid from CO_2 is a thermodynamically uphill process, theoretical studies have revealed several possibilities where the use of a catalyst might reduce the requirement of super critical CO_2 (Scheme 1.8).[100]

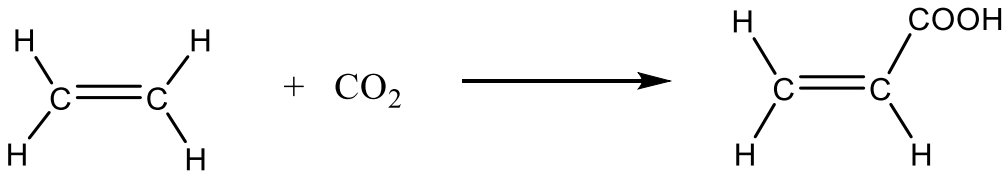

Scheme 1.8. C-C coupling using ethylene and CO_2 as raw material.

Among these possibilities, the most practical idea is to decrease the temperature of formation as well as the time/energy consumed in its purification process. Experimentally, Ni(II) and Pd(II)-phosphine complexes have been successfully used for acrylic acid sodium salt formation. However, sodium phenoxide was used as a sacrificial agent, making the process impractical.[101] Complexes containing molybdenum(0), molybdenum(I-IV) hydrides and cobalt(II) phosphine were used in preliminary screening for coupling carbon dioxide and ethylene.[97,98] The initial screening of cobalt compounds for ethylene-CO_2 coupling presented yields up to 30% in the production of acrylic acid in its optimized base/temperature conditions.[97] Still, a few issues in this transformation need to be addressed towards optimizing reaction conditions and ligand frameworks that might promotes this difficult coupling.[97] A more economically attractive process where C-C coupling involves CO_2 is when styrene can be used. Cinnamic acid is a useful product for manufacture of pharmaceutical, flavors and dyes; its major use is for the production of its methyl, ethyl and benzyl esters which are important components in the perfume industry. In addition, cinnamic acid is also a precursor of polyurethanes, polycaprolactam and aspartame among others.[102]

1.5. Hydrogenation of CO_2 by water: "reverse combustion"

The idea of using water as a hydrogenating agent for organic products, and for CO_2 in particular, is fascinating and potentially ground breaking. In 1978 Halmann was the first to report the

photoelectrochemical reduction of CO_2 in water using p-GaP[103], and ever since, a wide spectrum of semiconductors capable of both oxidizing water and reducing CO_2 has been actively pursued.[104–107] The work of Bocarsly in particular marked a milestone in the production of light organic fuels from CO_2/H_2O mixtures, a process now referred to as "reverse combustion". To overcome the unfavourable thermodynamics of this highly desirable transformation, energy has been provided with electrochemical,[108,109] photochemical[110,111] or photo-electrochemical devices.[112,113] However, the possibility of using purely photochemical devices remains the ultimate requisite for a completely sustainable and scalable reverse combustion.

Currently, titanium dioxide and $BiVO_4$ are the most popular photo-catalysts for this purpose. These materials have been modified to control size, conductivity and sensitivity to visible light[105,114–118]. A plethora of other photo-semiconductors that can efficiently absorb visible light and convert CO_2 to light organic fuels, especially methanol and methane, have also been discovered[119–125]. The unique popularity of $BiVO_4$ is justified by its demonstrated versatility as a water oxidation catalyst for selective alcohol production from CO_2 and also photodegradation of organic waste.[126–129] Monoclinic $BiVO_4$ has conduction and valence bands which are well suited for water oxidation coupled with CO_2 reduction and hydrogen evolution based upon its pH (Figure 1.9). Its use is, in principle, advantageous over other common water oxidation catalysts, including TiO_2, due to its narrow band gap of ~2.4 eV, which allows ready absorption of visible light. Its high selectivity towards oxygen evolution rather than hydrogen production make *m*-$BiVO_4$ a great candidate for reductive CO_2 reactions in the presence of water.

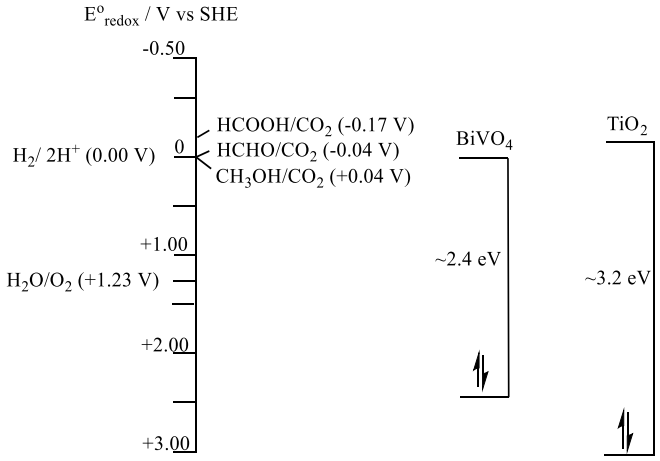

Figure 1.9. Band structure of monoclinic $BiVO_4$ and anatase TiO_2 demonstrating filled valence bands on the bottom (more positive) and empty conduction bands at the top (more negative). Reproduced in part from ref #[473] and #[474] with permission by The American Chemical Society and Elsevier respectively.

Furthermore, $BiVO_4$ has also been proven versatile as a photo-semiconductor for the reduction of CO_2 into methanol and ethanol[124,125]. The authors of these remarkable findings have reported promising hydrocarbon yields along with the possibility of regenerating $BiVO_4$ upon heating. The ability to regenerate $BiVO_4$ is a critical point for the performance of this photo-semiconductor which remains otherwise regrettably limited. In addition, $BiVO_4$ has been deposited over anodes to prepare photo-electroanodes with improved catalytic behaviour.[130] A recent study, however, has clearly demonstrated corrosion of the $BiVO_4$ film of the photo-anode in alkali media, thus reiterating the previously suspected ability of this binary oxide to irreversibly leach vanadium in alkali solution[131].

1.6. Thesis highlights

The appealing possibility of preforming reverse combustion and the issues described above for the usage of *m*-$BiVO_4$, have led us to reconsider the activation/deactivation pathways of *m*-$BiVO_4$ in a purely photochemical process without electrochemical input.[131] Our data are presented and discussed in Chapter 2.

In Chapter 2, we present how *m*-$BiVO_4$ could be initially activated by light, generating photoexcited species in the process. The decomposition of *m*-$BiVO_4$ after the first cycle in the reverse combustion process has been examined. Possible interferences by formate anions, formaldehyde and methanol formation in basic media using NaOH were evaluated and analyzed in an attempt to clarify the reaction pathway for the reverse combustion process.

Other photo-semiconductors were studied, evaluated and presented in Chapter 3. *o*-$BiOHCrO_4$ and *m*-$BiOHCrO_4$ were obtained aiming at replacing V^{5+} with isoelectronic but more oxidizing Cr^{6+}. The idea behind this study was to facilitate the oxygen releasing step of the reverse combustion process. Instead, bismuth chromate hydroxide oxides presented good activity for thermal disproportionation of formic acid into formaldehyde, CO_2 and water. A new and efficient photocatalytic system for the production of H_2 from formaldehyde is presented at the end of the same chapter which also covers a new concept for using tandem catalysis in water splitting based on a C1 shuttle.

Given the success of vanadium and its role played in reverse combustion promoted by *m*-$BiVO_4$, modeling studies aiming at clarifying the reactivity of low and mid-valent vanadium with CO_2 were performed. Several vanadium(II-III-IV) compounds were prepared using oxygen donor based ligand systems to better simulate the oxo environment of the above mentioned photo-semiconductors. Then reactions with carbon dioxide were examined. The variety of observed transformations (some highly unusual) span from a simple deoxygenation, radical behavior, incorporation into the formation of

organic esters, formation of formate anion via H-extraction from solvent to the most impressive isolation of a rare case of a vanadium-OCO linear adduct formation. DFT calculations were performed, when necessary, to support our findings and to explain their interesting activity. These data are highlighted and discussed in Chapters 4 and 5. Coordination of linear CO_2 using a rigid ligand is presented in Chapter 5. Its reactivity was evaluated experimentally and by DFT calculations.

Since the simultaneous presence of Bi and V is central to the photocatalytic performances of *m*-$BiVO_4$, we have also attempted the rational construction of molecular species containing both metals in the appropriate oxidation state to model reactivity with CO_2. These findings are presented in Chapter 6.

Finally in Chapter 7, conclusions and future work are discussed.

This work was published in part in: Sommers, Jacob M., Alderman, Nicholas P., **Viasus, Camilo J.** and Gambarotta, Sandro. *Dalton Trans.* **2017**, 46, 6404-6408

Chapter 2. Reverse Combustion promoted by monoclinic Bismuth Vanadate

CJV: The work was initiated by me and continued by Mr. Sommers in collaboration. I have tuned up all the synthesis and optimized the methodologies for data collection. I have actively participated in work of Mr. Sommers and contributed to the paper equally. Dr. Alderman was checking up all work done by myself and Mr. Sommers and helping the edition of the paper.

2.1. Introduction

The exponential increase of CO_2 production by human activities makes its recycling not only imperative but also potentially lucrative. The large thermodynamic stability of this pollutant, however, severely limits the choice of products that can be formed with catalytic processes.[132] The hydrogenation reaction leading to methanol, via transient formation of formaldehyde and formic acid, is the most obvious and desirable way to recycle CO_2 (Scheme 2.1).[133] This sequence of reactions can be successfully performed, in stoichiometric or even catalytic fashion, by taking advantage of the high energy content of hydrogen, hydrides or silanes.[134–137] The drawback is the high cost associated with these reducing agents, which makes these processes not viable for industrial scale endeavors. Therefore, different low-cost sources of hydrogen and reducing agents need to be identified.

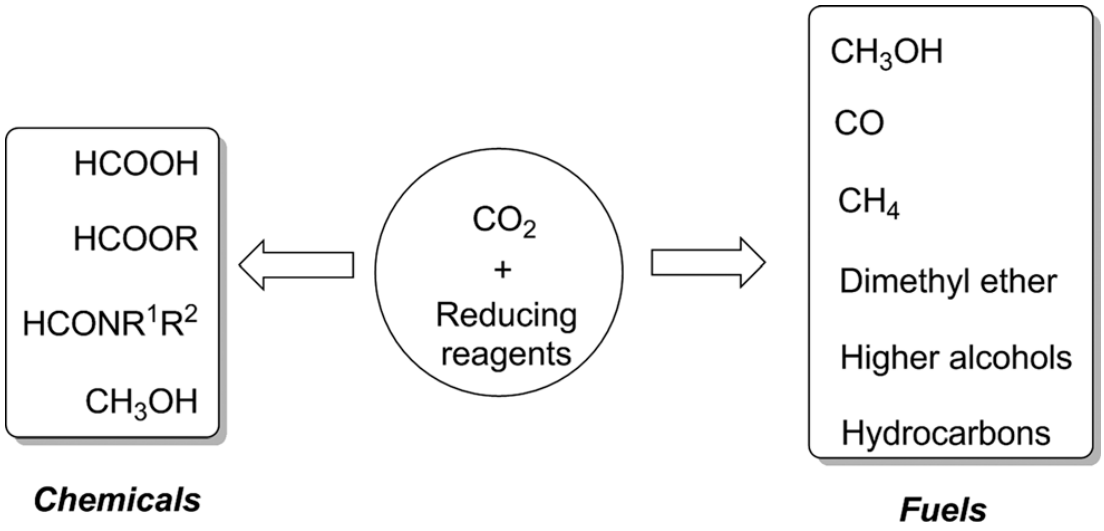

Scheme 2.1. Some carbon dioxide reduction possibilities. Reproduced from ref #[133] with permission by The Royal Society of Chemistry.

An interesting alternative to recycle CO_2 is its utilization as a raw material for preparing valuable polymers such as polycarbonates and polyesters. While this certainly would not solve the issue of CO_2 recyclability from the energy production standpoint, it can certainly be a contributing factor to its abatement. Epoxide-CO_2 copolymerization for polycarbonate production is probably the most successful example of this strategy (Scheme 2.2). It is also an alternative to the usage of toxic chemicals such as phosgene. The reaction proceeds by use of a Lewis acidic catalyst through a migratory-insertion mechanism.[138,139]

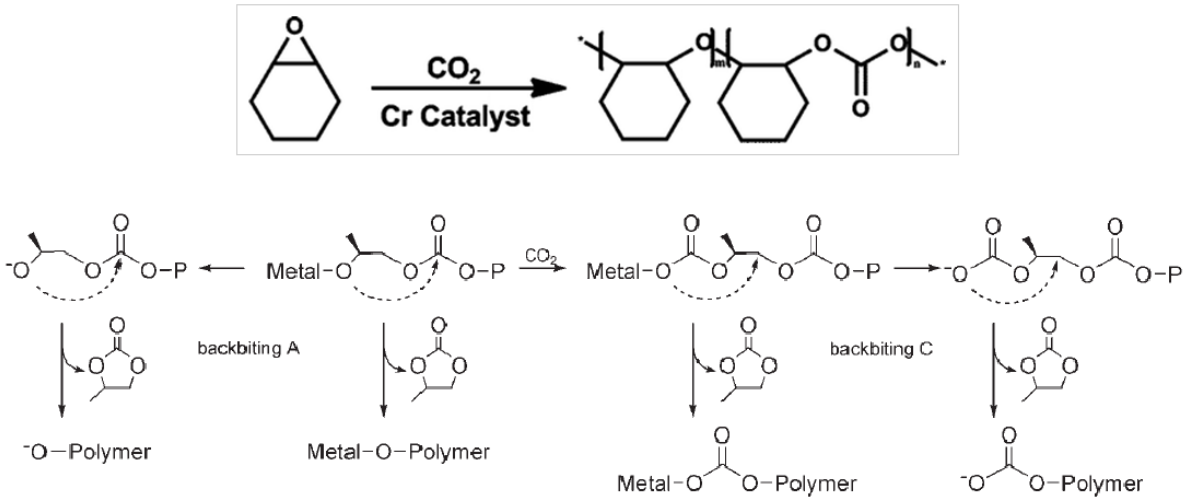

Scheme 2.2. Polycarbonate production using Cr(III) catalyst. Reproduced from ref #[138] and #[139] with permission by The American Chemical Society and John Wiley and Sons respectively.

Copolymerization of CO_2 with olefins to polyesters would be an even more attractive alternative. However, this reaction is substantially hampered by unfavorable thermodynamics necessarily requiring one to perform the copolymerization cycle in a step-by-step fashion.[140–142]

Another interesting possibility to recycle CO_2 is its transformation into oxalic acid. When the electron transfer during the reduction can be limited to only one electron, the initially formed $CO_2^{(\bullet-)}$ radical anion, by mainly being carbon centered, eventually may dimerize to form the oxalate dianion.[143,144] There are a few examples in the literature showing that this transformation is indeed possible while using low-valent lanthanides and transition metals.[73,143–151] This is not only an irreversible transformation but it also implies C-C bond formation starting from CO_2, a process which mirrors a fundamental step of the naturally occurring photosynthesis.[152–154] In this respect, the most spectacular advance probably remains the closure of a step-by-step catalytic cycle using a Cu(I) complex (Scheme 2.3).[148]

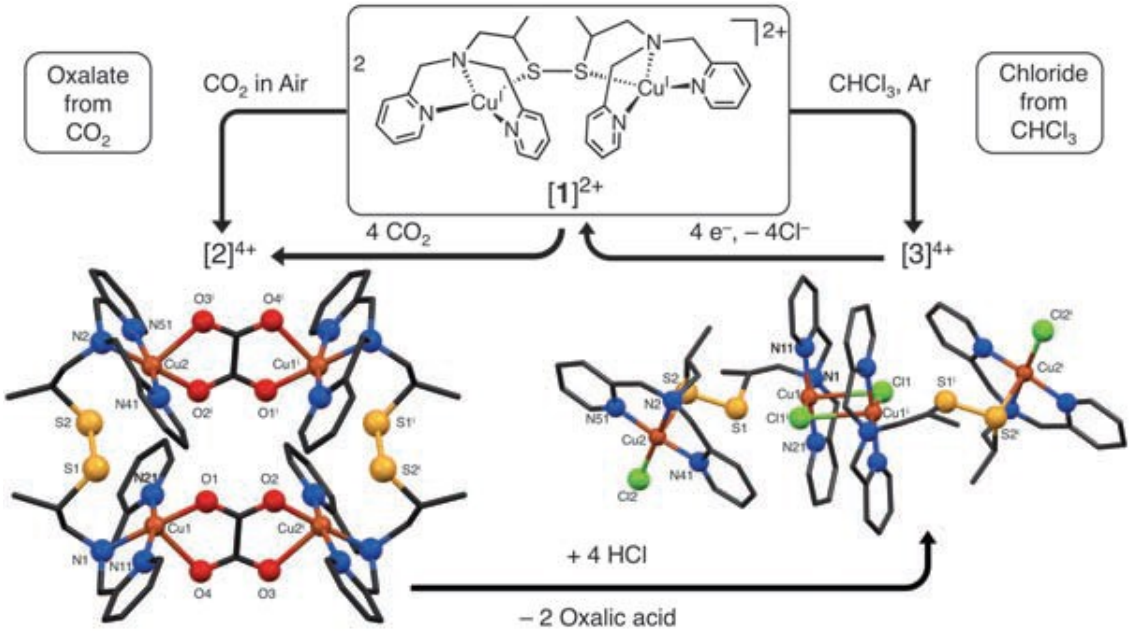

Scheme 2.3. Step by step oxalic acid formation with Cu(I). Reproduced from ref #[148] with permission by The American Association for the Advancement of Science.

Among the above processes employing CO_2 as a raw material, the hydrogenation remains the most straightforward and appealing for recycling, the source of hydrogen being the critical factor.[103,155] The most abundant and inexpensive source of hydrogen is of course water. If a way could be found of using H_2O as the ultimate source of hydrogen for hydrogenation, it would give accessibility to an inexhaustible source of fuels (Scheme 2.4). The hydrogenation of CO_2 with H_2O forming organics is appropriately called *"reverse combustion"* since the typical combustion products of any organic fuel are now being used as reagents.[117,156–159] Naturally, the fact that both CO_2 and H_2O are at the bottom of the thermodynamic well makes reverse combustion requiring a very significant input of energy. Therefore, this attractive transformation can only be realized thermally, electrochemically, photo-chemically or with a combination of these techniques.[111,160,161]

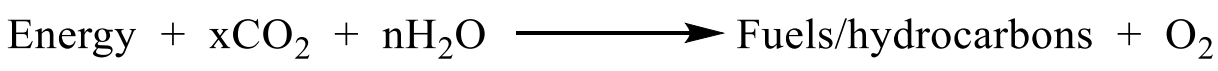

Scheme 2.4. General reverse combustion process.

Thermal reverse combustion has been observed at relatively moderate temperatures using Fe_3O_4. Products such as ethanol, acetaldehyde, acetic acid have been obtained at temperatures lower than 300°C. At higher temperatures, phenol and diphenyl ether are instead formed as main products.[162] Also attractive, thermal reduction of carbon dioxide into carbon monoxide and oxygen with 100% selectivity was obtained using CeO_2. In the absence of catalysts, prohibitively high temperatures (1450-1500°C) are required for the deoxygenation with no apparent carbon deposition.[163] This leaves the utilization of catalysts as the only possibility to allow the necessary energy input (283 kJ/mol).[163]

Electrochemical reduction of carbon dioxide was achieved in aqueous media from large (<1.0V) to medium (<0.5V) over potential with high selectivity to generate alcohols.[164] High surface electrode areas are always needed to make possible the stabilization of the initially formed radical $CO_2^{(\bullet -)}$ intermediates. The production of carbon monoxide, also occasionally observed,[164] is another attractive possibility from this point of view since it can be used as low cost reagent for reforming methane.[165,166] In the sequence of reduction intermediates, reduction can be selectively stopped at the level of formic acid by using copper foam electrodes at lower over potential (-0.45V).[167] Therefore, it is obvious that a wide amount of diversified products (formic acid, formaldehyde, methanol, methane and CO) can be realistically obtained via reduction of carbon dioxide using water as a reducing agent if the appropriate potential is applied and different reaction pathways judiciously selected.[156]

The photo-thermochemical reduction promoted by visible light is by far the most attractive option but it poses a major challenge, due to the high energy required for the process of splitting water to oxygen, protons and electrons.[4,117,158,159,168] On the other hand, reduction of carbon dioxide in the

presence of protons and electrons is something that can be achieved by using photo-semiconductors.[103,105] Therefore, if protons and electrons are generated with an efficient oxygen-evolving water-splitting process (either electro-[169,170] or photo-catalytic[171]), different ways to avoid their recombination to hydrogen can be turned instead into a convenient *in situ* hydrogenation reduction process.[111,172]

2.2. Photo-semiconductors.

A photo-semiconductor is a solid-state material whose atoms are organized in extended structures thus allowing electrons to move from the VB (HOMO) to the CB (LUMO) due to the presence of a small band gap. After a specific amount of energy is supplied by an external source, and based on the material characteristics, electrons may absorb energy and move to the CB. The appealing feature is that the required energy may be supplied under the form of photons. Under irradiation this material populates both its conduction (negatively charged) and valence band (positively charged "holes") and may thus perform both a reduction and an oxidation (Scheme 2.5).[107]

There are photo-semiconductors designed to achieve either only one process or both at the same time.[27,43,173] The possibility to perform different chemical processes is mainly based on the position where the CB and VB bands are located: the so-called band edge. The reduction potential of the target substrate must be consistent with the band positions of the photo-semiconductor.[107]

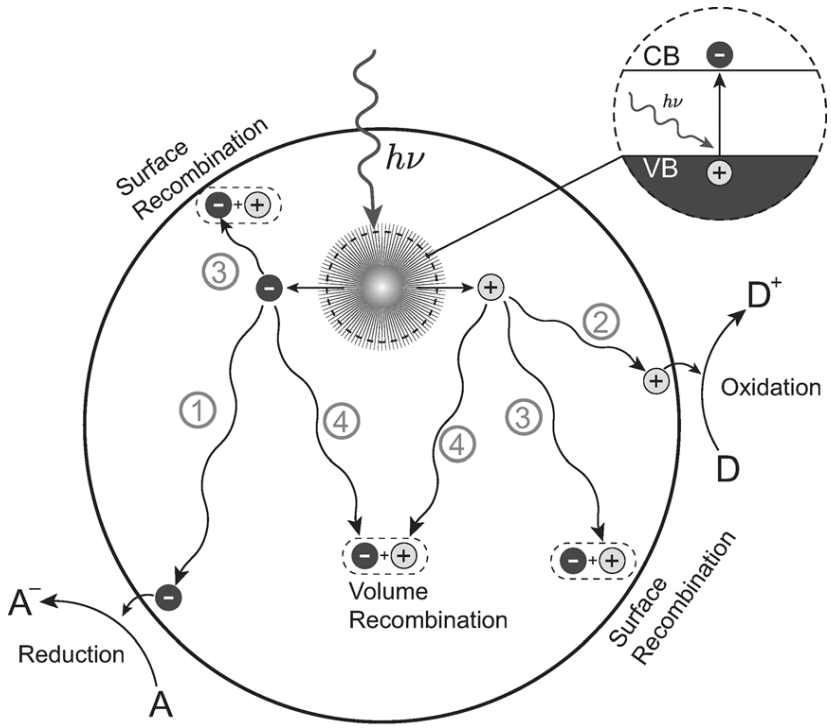

Scheme 2.5. Pictorial representation of a redox process at a photo-exited semiconductor surface. Reproduced from ref #[107] with permission by John Wiley and Sons.

For a photo-semiconductor to be useful in the general water splitting process, the valence band must have the necessary potential to perform an efficient oxygen evolution when protons and electrons are also being produced (+1.23 V, 1100 nm). On the other hand, the conduction band must be located at an energy level appropriate for the produced electrons and protons to be usable for generating molecular hydrogen. If instead the electrons and protons have to be used to target carbon dioxide to produce organic materials/fuels, a negative potential would be necessary (*reverse combustion)*.[107,108,166,174]

Therefore, reverse combustion, under illumination as an energy input, is indeed challenging and yet realistic. In fact, photochemical reverse combustion isn't a new topic.[103] It became popular a few decades ago with the discovery of light/temperature dependent CO_2 reduction processes.[8,111,175]

Although greatly appealing from green-chemistry standpoint, the products are systematically obtained in marginal yield. The poor activity and low selectivity is mainly due to material characteristics such as light absorption problems, kinetic barriers and electron-hole recombination phenomena among others.[46,58,107,176,177] Nonetheless, photo-semiconductors remain the most promising catalytic systems.[107,178,179] They are easy to prepare and to isolate/regenerate after each cycle and very stable under most conditions. A limiting requisite of reverse combustion is that the reduction of CO_2 may be accompanied by oxygen evolution, notoriously a highly reactive molecule. Nonetheless, there are several semiconductors capable of doing it.[33,180–182]

Photo-semiconductors with a band gap/band edge that produce molecular hydrogen are non-attractive for reverse combustion because of the competition of the electron reduction process mentioned above. Instead, they are usable in pure water splitting process.[183] A successful reverse-combustion semiconductor must have a proper combination of band edge position/selectivity parameters. The oxygen evolution (an oxidative process) must be accomplished beside the reduction process with protons and electrons selectively targeting carbon dioxide. A clear sense of the caliber of this challenge is visible while analyzing reverse combustion promoted by the so-called “artificial leaf”, a three-component photo-catalyst capable of efficiently splitting water (Scheme 2.6).[8,158] During the oxygen evolution, the catalyst either decomposes to metal oxides or leaches Ni out of the system. If reverse combustion is attempted, molecular hydrogen is produced instead of CO_2 reduction by protons and electrons. To improve that, Nocera *et. al*. have employed the bacterium *Ralstonia eutropha* to consume the produced hydrogen and to synthetize biomass and fuels from low CO_2 concentrations and in the presence of O_2.[184] This hybrid device, coupled with an actual photovoltaic system, can exceeded the activity of a natural photosynthetic systems. Regrettably, the yield remains too low for industrial applications.

Even when the hydrogen production is apparently a positive result, the necessity for purification from the carbon monoxide, methane or other byproducts as deriving from the concomitant CO_2 reverse combustion, impedes the economic viability of the entire process.[156,185] A *reverse combustion* is therefore industrially viable if it is hydrogen-free.

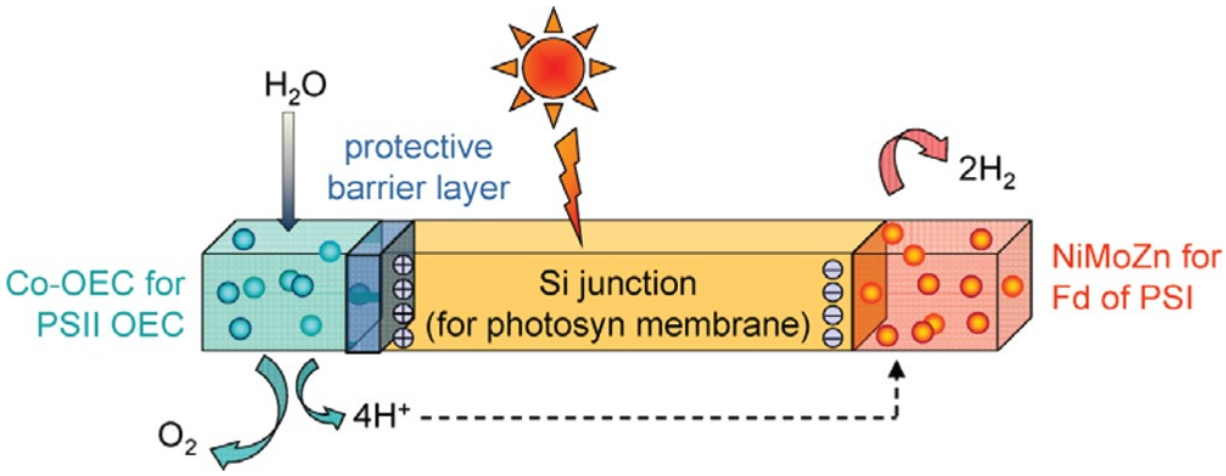

Scheme 2.6. Artificial leaf. Reproduced from ref #[8] with permission by copyright of The American Chemical Society.

2.3. $BiVO_4$ photo-semiconductor

As shown above, a photochemically-driven reverse combustion is possible, provided that an appropriate photo-semiconductor is identified. Several photo-semiconductors with similar electronic characteristics are shown in Scheme 2.7. Among them, only $BiVO_4$ was proven as an efficient and selective system to reduce carbon dioxide into methanol, ethanol, or methane without affording molecular hydrogen as byproduct. Solids like MVO_4 (M = In, Nb and Ta) and TiO_2 have been widely studied and it has been reported that they can also reduce carbon dioxide, but only aside the dominant production of molecular hydrogen.[186,187] On the other hand, the formation of molecular hydrogen, especially in small amount, can be potentially misleading since it is also formed by standard alcohols

during decomposition processes promoted by light in glass or quartz reactors.[188] It should be reminded that, alcohols are commonly used as sacrificial agents for hydrogen production.[27,189,190]

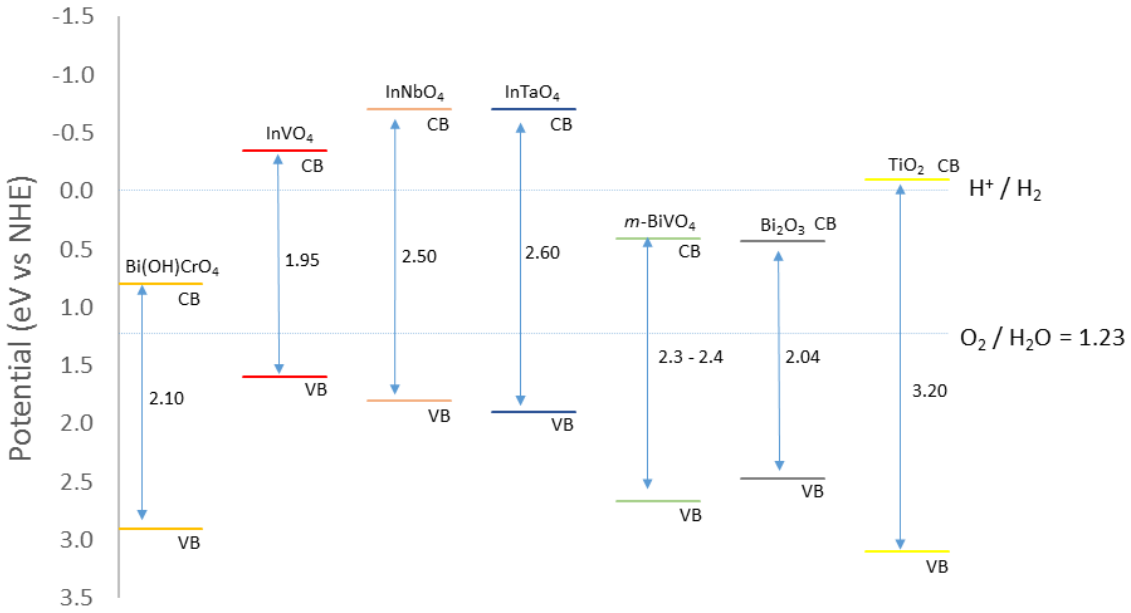

Scheme 2.7. Band gap and bad edges of several semiconductors that can be use in reverse combustion.[3,12,21,191–195]

In the large family of the established photo-semiconductors, monoclinic bismuth vanadate (*m*-$BiVO_4$) is particularly popular. It presents an interesting photo-electronic behavior which makes promising its usage for the reverse combustion process.[191,196] A band gap of ≈2.4 eV and a proper band edge position where oxygen can be evolved (0.40 – 2.70 eV), makes *m*-$BiVO_4$ indeed a very versatile material (Scheme 2.7). In addition, its conduction band is far away from the potential for molecular hydrogen production at pH=0. This the reason why *m*-$BiVO_4$ presents very low selectivity towards molecular hydrogen even at pH higher than 12.[197] In contrast, it can reduce carbon dioxide to different products. In theory, +1.23 eV is the minimum energy required to do water splitting, but the thermodynamic losses, estimated in the range of 0.4 eV, must be also considered. These are in addition to kinetic barriers to be overcome for the surface reactions in the system, and which may add another 0.3-0.4 eV, altogether ending in an

more realistic band gap of at least ≈2 eV.[4,12,104,125,198,199] Having this in mind, the actual *m*-$BiVO_4$ band gap of ≈2.4 eV exceeds the ideal band gap mentioned above for water splitting, thus making this material potentially even more versatile.

Variations in the preparation of *m*-$BiVO_4$, such as pH modifications, directly determine the morphology of the photo-semiconductor. In turn, the shape of the material affects oxygen evolution as a result of the shifting of the over-potential. By using a pH of 12, an over potential of -0.7 V is generated and which is just correct to obtain the reduction of carbon dioxide.[197] When comparing the shifted $BiVO_4$ over potential with that presented in Scheme 2.8 for carbon dioxide, it is clear that a pH increase improves the ability of $BiVO_4$ to reduce carbon dioxide[200] without producing hydrogen.[201] Only when using sacrificial agents and an appropriate potential, formation of molecular hydrogen may occur.[202] Incidentally, *m*-$BiVO_4$ can be used as photo-anode in a photo-electrochemical system producing hydrogen.[203] However, a reducing metal such Pt needs to be employed.

	E^o
$CO_2 + 2H^+ + 2e^- \longrightarrow CO + H_2O$	-0.53
$CO_2 + 2H^+ + 2e^- \longrightarrow HCOOH$	-0.61
$CO_2 + 4H^+ + 4e^- \longrightarrow HCHO + H_2O$	-0.48
$CO_2 + 6H^+ + 6e^- \longrightarrow CH_3OH + H_2O$	-0.38
$CO_2 + 8H^+ + 8e^- \longrightarrow CH_4 + H_2O$	-0.24
$CO_2 + e^- \longrightarrow CO_2^{\bullet -}$	-1.90

Scheme 2.8. Carbon dioxide reduction potentials at pH 7, 1 atm and 25°C.[204]

$BiVO_4$ can be prepared in two main crystalline forms, monoclinic and tetragonal (Scheme 2.9).[194] The two phases are interconvertible in the sense that the tetragonal is the less temperature stable and spontaneously transforms into the monoclinic upon heating. The monoclinic form is the most active

towards carbon dioxide reduction and thus was selected for this work. A third crystalline structure as tetragonal zircon on $BiVO_4$ has been identified but only as precursor/intermediate during the formation of the other two forms (Scheme 2.9c). It is also established how the size of the material particles, the pH employed for the synthesis and the use of morphological controlling agents might influence the formation of the three main structures (tetragonal zircon, tetragonal scheelite, and monoclinic scheelite structure) and consequently the photo-catalytic properties.

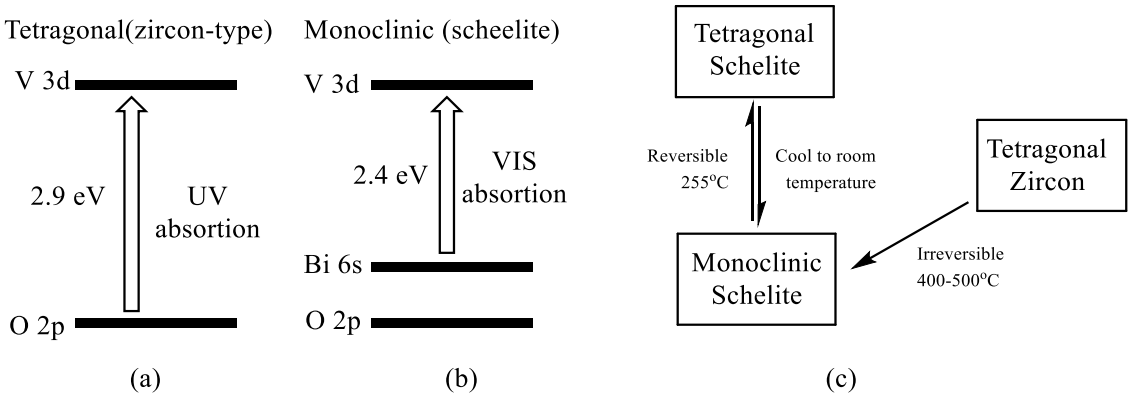

Scheme 2.9. Band gap of $BiVO_4$ tetragonal zircon type (a), Monoclinic scheelite (b) tetragonal scheelite compounds and their main atom composition at the conduction (top) and valence (bottom) bands; (c) diagram of preparation for the three $BiVO_4$ forms. Reproduced from ref #[194] and #[205] with permission by The American Chemical Society and Elsevier.

Scheme 2.10 shows the crystal structure of *m*-$BiVO_4$.[206] The geometry of bismuth is a BiO_8 distorted trigonal dodecahedron while vanadium is almost perfectly tetrahedral VO_4. Similar environment is present in the tetragonal structure with just a few differences in the M-O [M = V, Bi] bond distances. While the monoclinic structure contains the same Bi-O distance for each pair of oxygen atoms (Bi-O in Å = 2.354 x2, 2.372 x2, 2.516 x2 and 2.628 x2; V-O in Å = 1.69 x2 and 1.77 x2) in the tetragonal structure the differences are observed for every group of four atoms (Bi-O in Å = 2.453 x4 and 2.499 x4).[207]

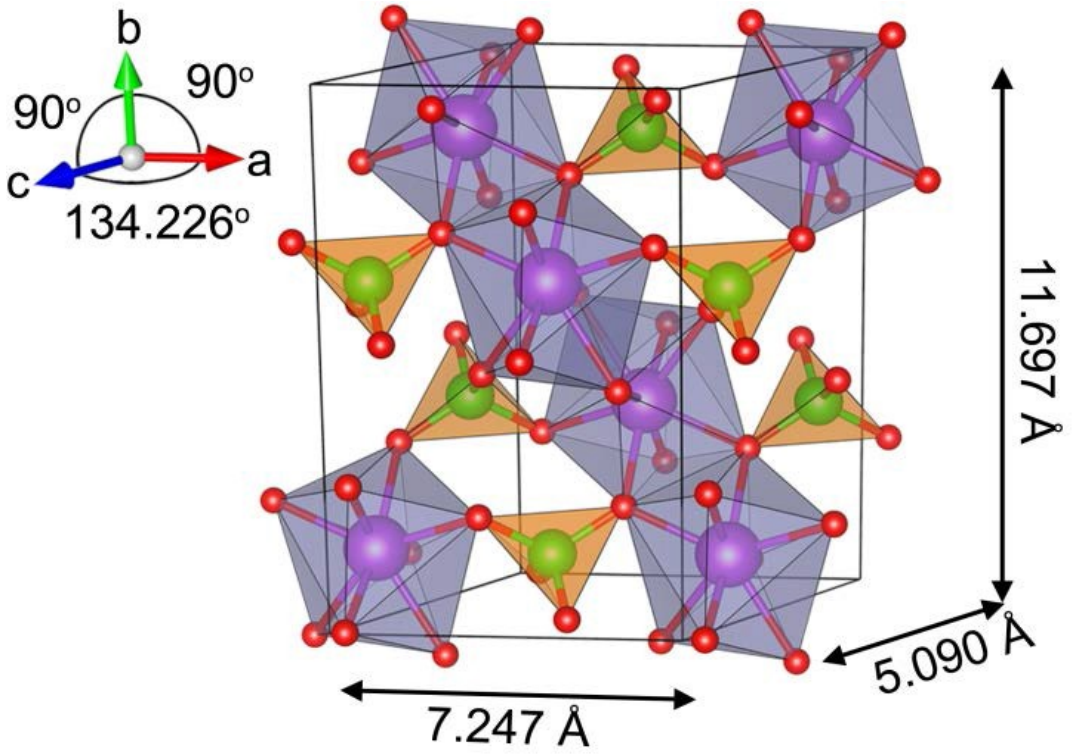

Scheme 2.10. Crystal structure of monoclinic scheelite $BiVO_4$ determine by power diffraction reported by Sleigh et. al., 2014. Reproduced from ref #[208] with permission by The American Chemical Society.

In a series of comprehensive studies[191,209–211] aiming at understanding the functioning of $BiVO_4$, it was pointed out that the presence in the valence band of an antibonding lone pair, described as Bi*6s* O*2p* hybrid, might be linked to the photo-catalytic characteristics. As a result of the irradiation, *m*-$BiVO_4$ migrates this hybrid electron density to the conduction band and, in doing so, it increases the mobility of the positive holes by decreasing their effective mass. In turn, this triggers the reactivity. Saison *et. al.* highlighted the behavioral differences between the two common structures, tetragonal scheelite and monoclinic scheelite, under visible light irradiation by comparing the activity for the degradation of the dye rhodamine B (RhB). The observed experimental differences between the two forms are directly related to the differences in metal-atom contributions to the valence band (Scheme 2.9). In previous analysis about the role of the metals involved in the photochemical process, it was

demonstrated that the conduction band is mainly contributed by vanadium 3d orbitals. By the same token, the valence band has a considerable Bi 6s character and it can be considered as mainly a Bi6s/O2p hybrid.[191,210] It is the Bi6s lone pair and the strong acidity of the surface sites that are responsible for the degradation of rhodamine (cycloreversion, N-deethylation and mineralization).[212] The monoclinic form, which has the highest Bi contribution to the valence band, is the most reactive. The particle size, morphology and surface dopants play a pivotal role in determining the level of activity.[210,213] In their seminal work, Saison *et. al.*, also described how $BiVO_4$ can generate different intermediates during the photo-irradiation with $OH^{(\bullet)}$ or $O_2^{(\bullet-)}$ radicals normally expected for a water-based photosystem being in fact conspicuously absent.

In spite of the above advances in the understanding of the functioning of $BiVO_4$, how carbon dioxide interacts and gets reduced in the *reverse combustion* process is still unclear. It seems conceivable though that the conduction band may be responsible for CO_2 reduction while the valence band affords oxygen evolution.

More than a thousand of scientific papers have been published in the last 60 years reporting photochemical applications of $BiVO_4$, thus reiterating the versatility of this photo-semiconductor.[214–218] Among the many transformations promoted by this material, reverse combustion to ethanol[124], methanol[125] or methane,[207] furthermore with high selectivity, are probably the most spectacular achievements. The reactions which at first glance looks the same, are in fact sensitive to minuscule procedural details responsible for the different outcomes. To obtain ethanol, carbon dioxide was bubbled through an aqueous solution at 0°C, whereas to obtain methanol, carbon dioxide needs to be solubilized in 1.0M NaOH aqueous solution at 20°C in a closed glass vessel. Finally, to obtain methane, carbon dioxide apparently needs to be bubbled in 0.1M Na_2SO_3 solution (additional reducing sacrificial agent) and in 0.1M NaOH solution.

In the three cases presented above, irradiation with visible light affords less activity than UV. This has to be expected due to the fact that more energetic photons will produce more photo-generated electrons and protons in turn leading to a large number of C1 intermediate species anchored at the surface of $BiVO_4$. This should facilitate methanol formation or ethanol (through subsequent dimerization).[124] Fascinating questions arise from the reaction mechanism but which has so far been neglected by this literature. It is only agreed that the oxidation of water produces molecular oxygen.

Another attractive feature of $BiVO_4$ is the apparent resiliency to decomposition since no mention was ever made about deactivation processes during a photochemical reaction. Yet, the reported activity diagrams for the product formation are never continuous but show interruptions and restarts of the catalytic activity with new fresh solutions thus leading the reader to believe that these catalysts are everlasting.

In summary, the different reductions of CO_2 under reverse combustion conditions involve different energies and therefore different reduction potentials (Scheme 2.8). The versatility of *m*-$BiVO_4$ relies on the fact that none of the above transformations occurs at a potential sufficient to generate hydrogen at pH = 0. Even in case that a negative over potential is required for a process, molecular hydrogen remains absent thus making *m*-$BiVO_4$ even more valuable.[197]

2.4. Work Hypothesis

Our interest for these systems was mainly stimulated by mechanistic curiosity. The claim for the formation of EtOH[124] was particularly puzzling to us given that the process implies not only CO_2 reduction but also a C-C bond formation, in an overall process closely reminiscent of the naturally occurring photosynthesis. Therefore, we have decided to revisit the reported reactions vis-à-vis of rationalizing the dependence of the reaction outcomes on relatively minor experimental details and aiming at proposing a sensible reaction mechanism encompassing and elucidating the three different

reductions. We were particularly focused on the oxidation states of the two metals, Bi and V, as generated during the light-induced electron displacement, responsible for both oxygen evolution and CO_2 reduction. We were also prepared to embark on separate modeling studies (See chapter 4, 5 and 6) where molecular complexes of each metal (or even both) could be prepared in a ligand environment as close as possible to that of $BiVO_4$.

As explained above, electrons and positively-charged sites (holes) are generated in the extended structure during a photo-excitation process. These electron-rich sites and holes can reduce and oxidize atoms involved in the conduction and valence bands respectively. The reduced species in the conduction band might now transfer the electrons earned during the photo-excitation process and reduce carbon dioxide. On the other hand, the generated holes can oxidize water producing protons and electrons while evolving oxygen (Figure 2.1). Figure 2.1 shows our representation of how methanol could be formed from carbon dioxide reduction by using *m*-$BiVO_4$ and water as only source of protons. The overall reduction process of CO_2 to MeOH requires 6 electrons and 4 protons, but we propose that electrons are delivered singularly step by step and possibly accompanied by simultaneous proton intake until the final product, MeOH, is generated.

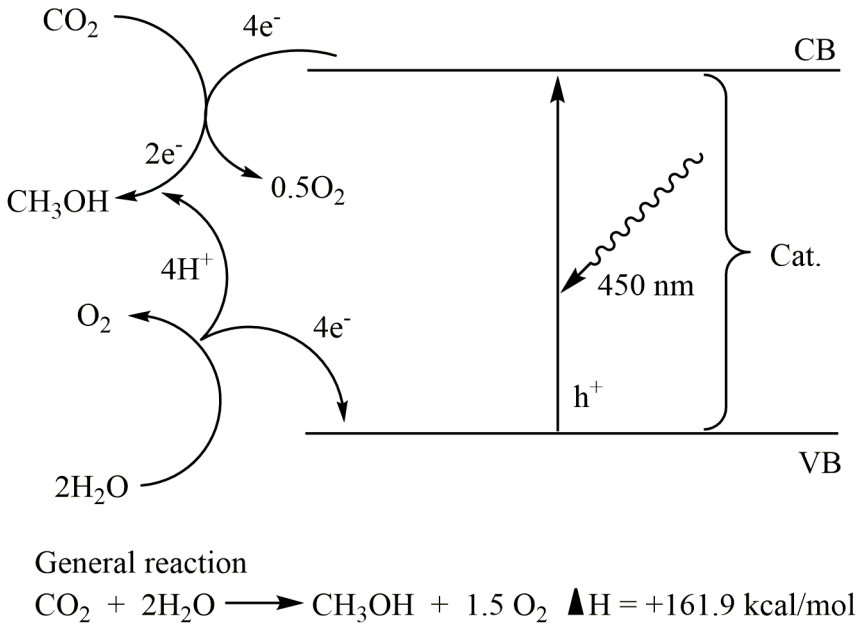

Figure 2.1. Proposed electrons pathway in methanol formation using carbon dioxide, water, light and a catalyst.

The efficiency of a chemical process promoted by a photo-semiconductor is determined by the intensity of the incident light, the energy carried by the photon (UV *versus* visible) on the surface of the solid and how efficient the excitation in the semiconductor is. Intrinsic characteristics such as the electron hole recombination process must be kept into consideration in order to analyze the formation of all the possible products (Scheme 2.1).[48] Finally, even the possible bonding mode in the coordination of the incoming CO_2 must be kept into account, since different bonding mode may prelude to different transformations (Figure 2.2).

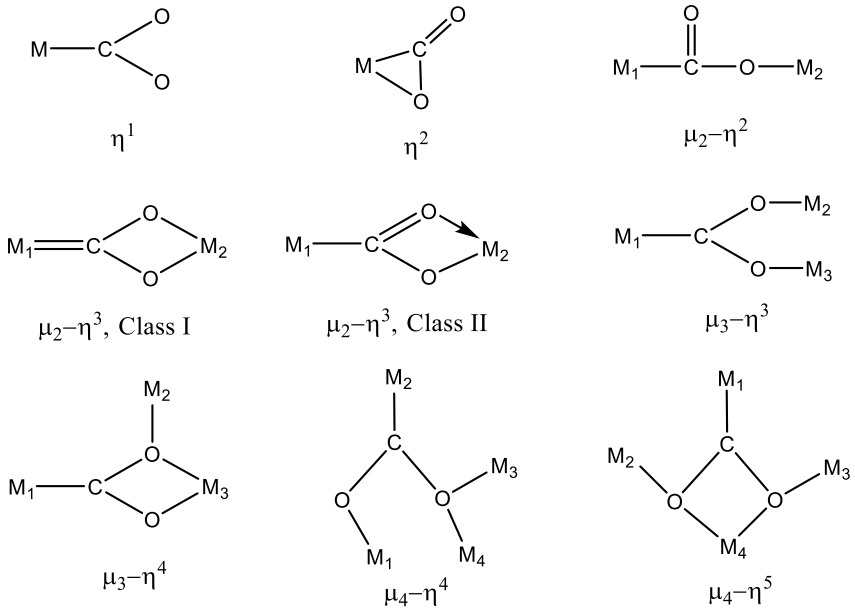

Figure 2.2. Several documented carbon dioxide bonding modes in metal complexes.

Under the safe assumption that the Bi-V couple in the solid structure acts as a redox pair during irradiation, the lone pairs of the Bi-6s/O-2p hybrids[208] are mostly present in the valence band. The electrons travel to the conduction band during the excitation to generate two main species: highly oxidized bismuth and low/mid-valent vanadium centers. As a result, one, two or up to three electrons (less probable) can then be transferred from the valence band to the conduction band. Based upon the light intensity, reduced species like V^{4+}, V^{3+} or even V^{2+} may be generated. Should the process be a one by one single electron shuttle, the oxidation state of vanadium would never go lower than 4+. In any event, the reduced vanadium(IV), (III) or (II) species can now interact with carbon dioxide by delivering the electrons and returning to a 5+ oxidation state to restart the cycle (Figure 2.1). Important questions remain about the number of electrons transferred by a vanadium center and how they are being delivered to carbon dioxide.

In the first step of Figure 2.3, we are assuming that a reduced specie of vanadium(IV) is formed in the conduction band and its partner bismuth(IV) in the valence band after the photo-

irradiation. If the photo-excitation is sufficiently strong, an additional electron may be transferred to form bismuth(V) and vanadium(III). This assumption can be also extended to the not unrealistic formation of vanadium(II), with the assumption that intermediate species are stables.

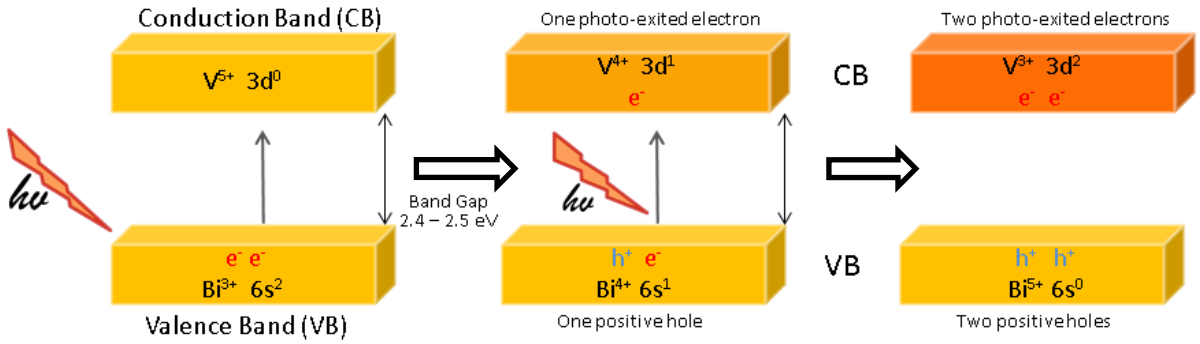

Figure 2.3. Proposed intermediates formation on m-$BiVO_4$ after photo-irradiation and until vanadium(III) specie formation.[208]

Bismuth in high oxidation state as in some metal oxides is regarded as a strong oxidizing agent.[219–221] During water oxidation, the high valent Bi reduces to the trivalent state where the lone pair, by being locked in the 6s orbital, is responsible for the special stability in turn requiring light for re-oxidation and catalytic cycle restart. Accordingly, $MBiO_3$ (M=Ag and Na) and Bi_2O_5 photo-semiconductors are examples of photo-semiconductors used for oxidation reactions. The oxidative ability of high-valent bismuth is also reiterated by the chemistry of organobismuth(V) compounds (Scheme 2.11) mainly known because of their ability to oxidize organic species.[220,222]

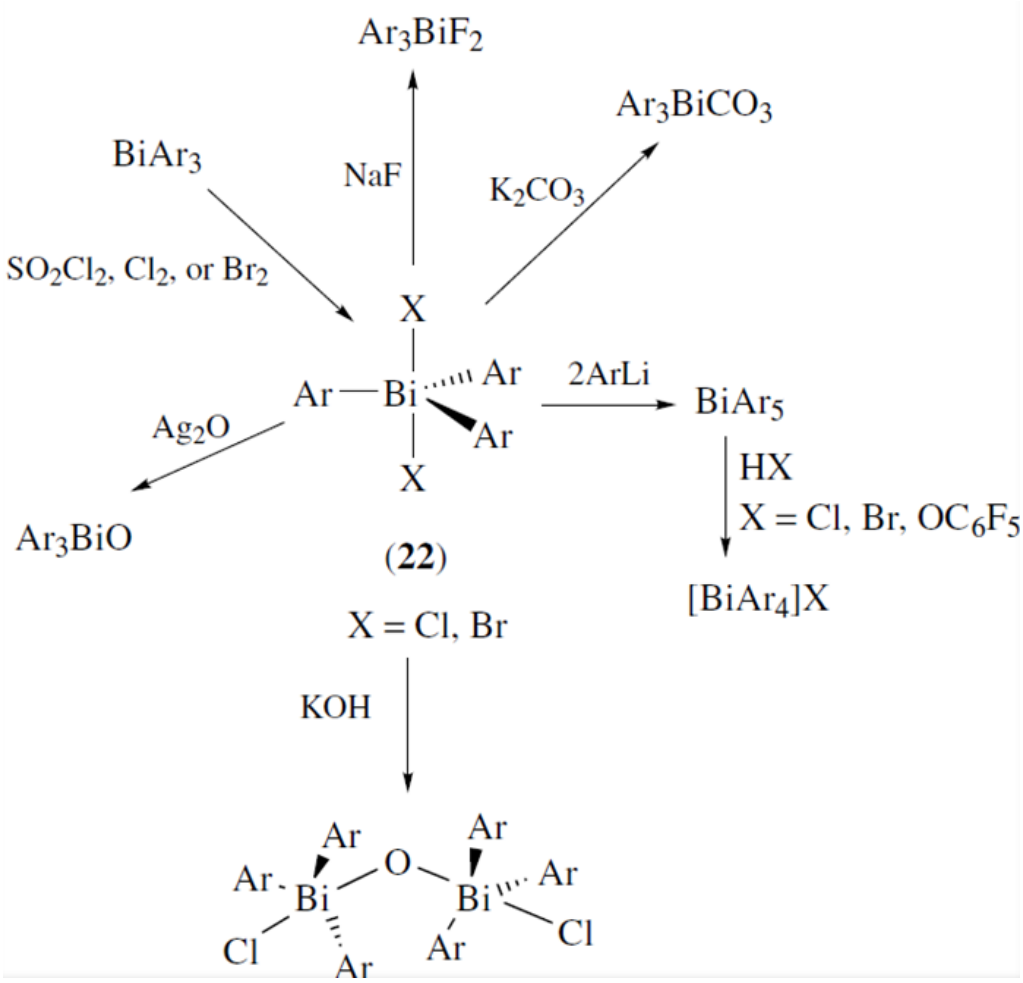

Scheme 2.11. Bismuth(III)Ar_3 as precursor for different bismuth(V) species. Reproduced in part from ref #[220] with permission by Elsevier Science.

On the other hand, low valent vanadium compounds, especially the di- and trivalent states display the characteristics of powerful reductants, having been prepared and used as binding models for dinitrogen, carbon dioxide, carbon monoxide and isocyanide.[223–229] Therefore, the combination of low-valent vanadium with high-valent Bi, as allegedly generated by the irradiation of $BiVO_4$, can indeed provide a reducing site for CO_2 and oxidizing site for water during the reverse combustion process.

2.5. Results and Discussion

At the beginning of this work, we were somewhat doubtful of the fact that such relatively minor changes in the experimental protocol of the $BiVO_4$-promoted reverse combustion may lead *selectively* to such a different array of products.[124,125,207] Last but not least, we wished to better understand the "reactivation" process of $BiVO_4$ and why such a "reactivation" was necessary if the catalyst was reported not to decompose. For our photochemical experiments, we have used monoclinic *m*-$BiVO_4$. Several procedures were analyzed for its preparation by changing the morphology controlling agents and synthesis temperatures. We have thus identified and selected the best way to obtain pure *m*-$BiVO_4$ that is presented at the end of this chapter.[124,125,207,230]

Characterization of *m*-$BiVO_4$. The solid was characterized by powder X-ray crystallography, XRF, SEM analysis and UV-vis diffuse reflectance. The XRD powder spectra (Figure 2.4 - black line) were always in good agreement with the JCPDS No. 14-0688. XRF analysis was performed on the *m*-$BiVO_4$ sample, obtaining a determined elemental composition (calculated) as Bi 64.11 (64.51%) and V 15.98 (15.73%). These results agreed with the 1:1 Bi/V molar ratio. SEM analysis showed the presence of two crystal shapes of *m*-$BiVO_4$. The first is plate-like while the second is sort of truncated hexagonal bipyramid. However, given that their diffraction patterns are indistinguishable, we assume that the two different shapes might be coincidental. The fact that the two samples never show cross-contamination of the two forms but always are homogeneous also reiterates that we are in the presence of pure samples. Also, from the SEM-COMPO analysis of the sample, it is clear that only one component is in the solid. Occasionally, the particle *size* is not homogeneous, but the shape is always the same.

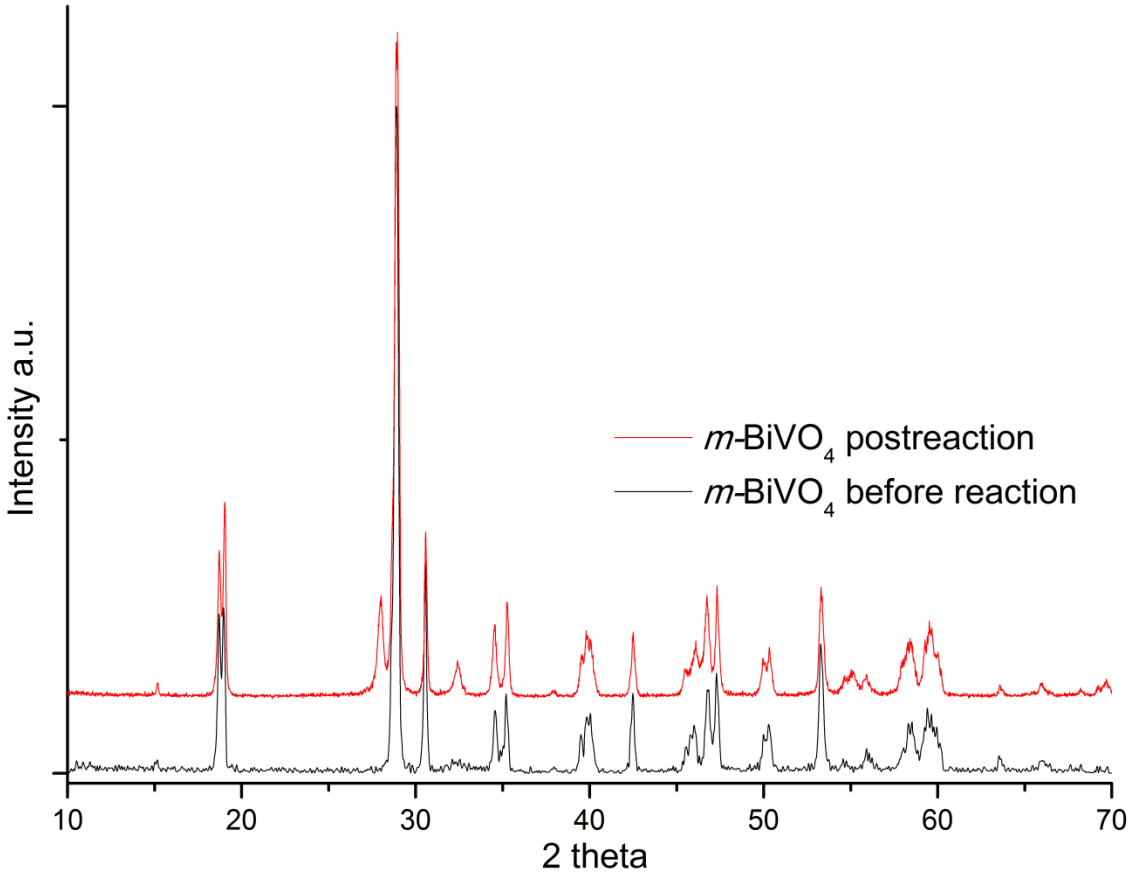

Figure 2.4. - Experimental XRD pattern of plates monoclinic $BiVO_4$, before (-) and after (-) reaction.

The resultant $BiVO_4$ yellow solid is expected to be diamagnetic because of its $Bi^{3+}/6s^0$ and $V^{5+}/3d^0$ electronic configuration of the precursors. In addition, no redox reaction was performed during the synthesis. However, a small amount of para-magnetism was occasionally observed in *m*-$BiVO_4$ if the stoichiometry of the preparation differed from the required one or the synthetic protocols were not rigorously followed. The appearance of residual paramagnetism was attributed to oxygen vacancies generated during the process with vanadium(IV) species resulting from that.[231] Accordingly, an eight lines EPR spectrum characteristic of a I=7/2 nuclear spin for a ^{51}V ($2I+1 = 8$) may be observed.[232–235]

The presence of any small amount of vanadium(IV) in the structure *prior* to the photo-excitation, led us to think about the tantalizing possibility that it might be this vanadium(IV) species

that performs reverse combustion. Another intriguing possibility is that once *m*-$BiVO_4$ is irradiated, the paramagnetic vanadium(IV) centers turn into vanadium(III)**.**

Following the methodology described in our work, we have obtained no dielectric or paramagnetic behavior in the samples of *m*-$BiVO_4$. Only in the case of a hydrothermal synthesis at low temperature (<120°C), where mostly tetragonal bismuth vanadate is produced, a tiny magnetic susceptibility signal was observed and an EPR spectrum could be recorded (Figure 2.5). By taking this solid and heating up to 450°C in air, the magnetism disappeared according to the oxidation of vanadium(IV) into diamagnetic vanadium(V) in the monoclinic phase. Is well known that the tetragonal structure in $BiVO_4$ is undesirable because of its lower activity towards carbon dioxide reduction.[124]

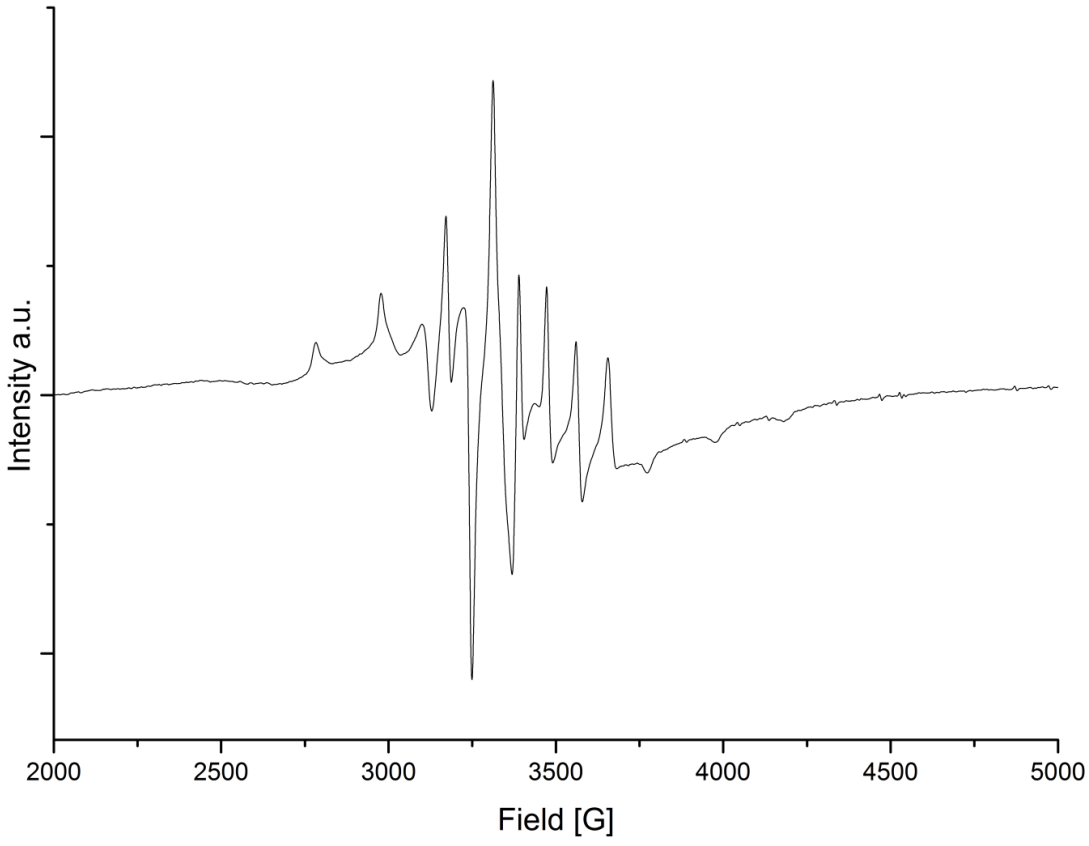

Figure 2.5. EPR spectra of m-$BiVO_4$ with residual V(IV) as a result of oxygen vacancies in the structure.

To further clarify this point, an EPR experiment was performed by irradiating diamagnetic *m*-$BiVO_4$. Figure 2.6 shows the EPR spectra of three systems: VO_2 purchased from Strem used as a reference, *m*-$BiVO_4$ diamagnetic prepared with our methodology and *m*-$BiVO_4$ obtained upon irradiation inside the cavity of the EPR spectrometer.

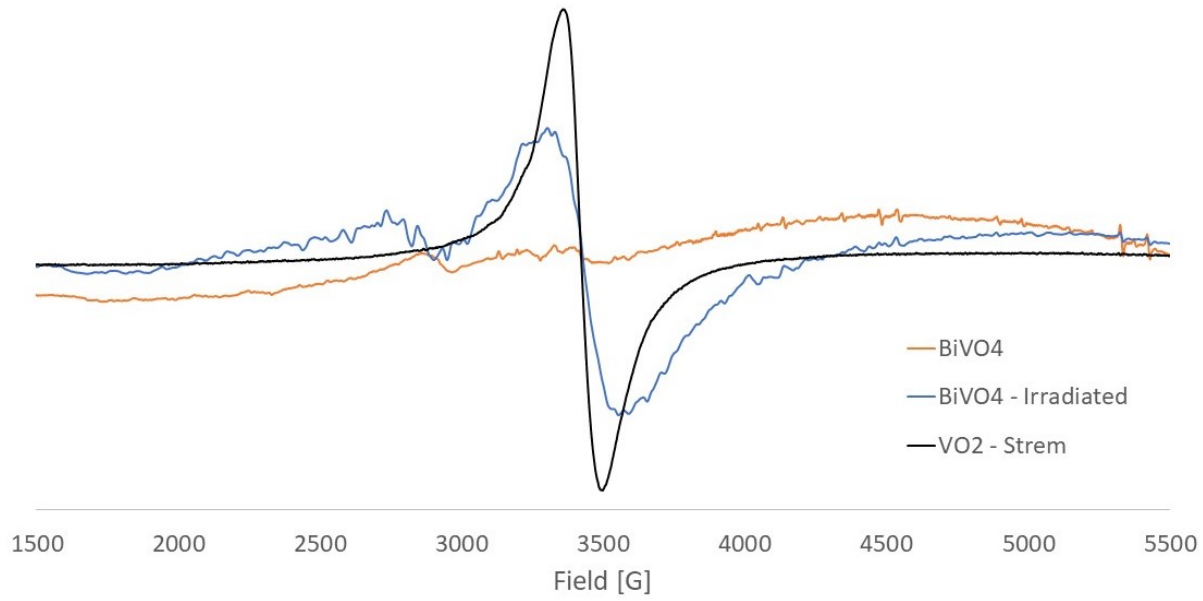

Figure 2.6. EPR experiment of VO_2, *m*-$BiVO_4$ and *m*-$BiVO_4$ irradiated.

The photo-irradiation of *m*-$BiVO_4$ clearly shows the appearance of para-magnetism implying that either vanadium(IV) or (III) might be formed thus supporting our initial hypothesis that a reduced vanadium species may have formed during the process. The close similarity of the *g*-factor with that of VO_2 indicates that a tetravalent vanadium is most likely to be formed. It is interesting to observe that the trivalent V_2O_3 is EPR-silent at room temperature. Therefore, it becomes apparent that the EPR spectrum showed the presence of a reduced vanadium.

Since the presence of trivalent vanadium could not be conclusively excluded, attempts to synthesize bismuth vanadate in lower vanadium oxidation state were performed. The first methodology we

followed was that reported in the literature for $Bi_2V_2O_7$.[236] By following this methodology however, we only obtained *m*-$BiVO_4$. Our results make more sense since the heating in air of the reaction mixture, as prescribed by the preparation of $Bi_2V_2O_7$, oxidizes vanadium(IV) and affords *m*-$BiVO_4$ as presented in Figure 2.4 (black line). In fact, several methodologies to obtain conventional diamagnetic $BiVO_4$ used vanadium in lower oxidation state as precursor and all of them require oxidation in air.[32,130,172,237,238]

Before attempting different protocols, we modified the conditions used for $Bi_2V_2O_7$ by performing the reaction under inert atmosphere. The resulting solid was analyzed by X-ray powder diffraction (Figure 2.7) showing that metallic bismuth and V_2O_3 were formed. This unexpected result indicates Bi^{3+} being reduced to metallic bismuth and V^{4+} affording V_2O_3. In conclusion, using the methodology presented by Khademinia S. *et. al*. in 2015 we were not able to reproduce the proposed structure but instead obtaining Bi and V_2O_3.

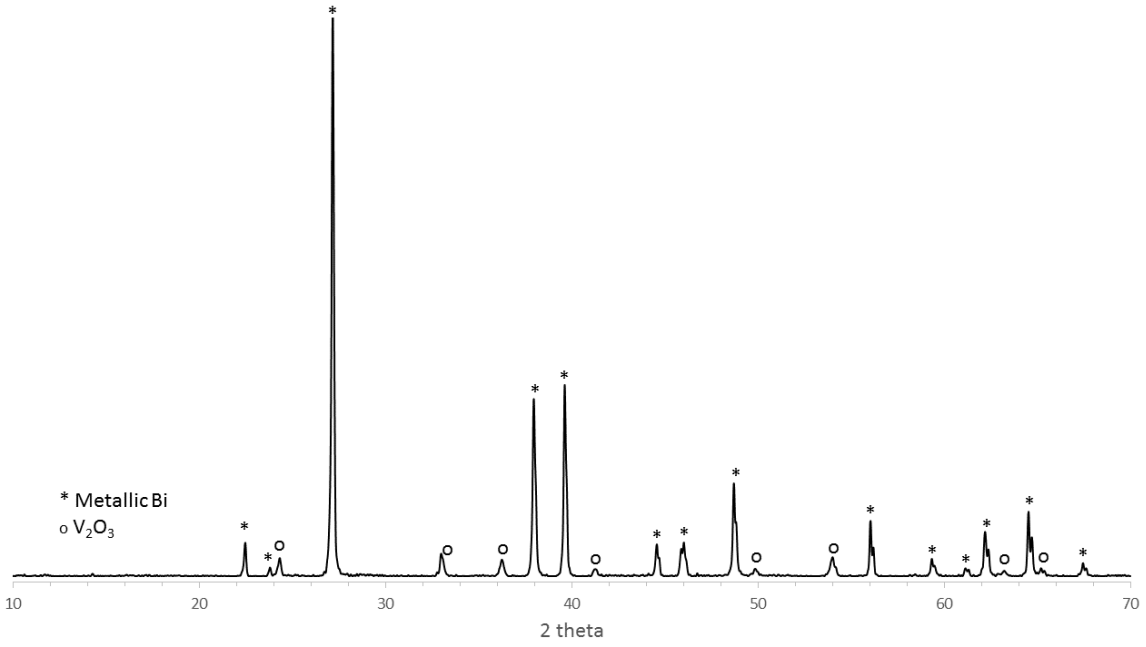

Figure 2.7. XRD pattern of the products of $Bi(NO_3)_3.5H_2O$ mixed with $VO(acac)_2$ and heated under Ar at 500°C for 8h.

We further attempted the preparation of $Bi_2V_2O_7$ by solid state technique at 400, 500, 600 and 700°C (Figure 2.8). Firstly, mixing Bi_2O_3 and VO_2 in molar ratio 1:2 and heating to 400°C and 600°C did not present a total conversion from the precursors into any oxo/bismuth vanadium compound with lower oxidation state of vanadium. The reaction was thus performed for longer periods and higher temperature. Longer time reaction at 500°C gave similar results to a 24 h-long reaction at 700°C. Still, the expected $Bi_2V_2O_7$ was not obtained, but a mixture of $Bi_4V_2O_{10}$ and Bi_2VO_5 was afforded with small crystalline impurities of unreacted VO_2. The susceptibility moment at room temperature for the mixture, assuming a formula of the major component $Bi_4V_2O_{10}$ was 2.02 BM. The dark-green paramagnetic solid had the expected value of magnetic susceptibility and it was EPR-silent at room temperature.

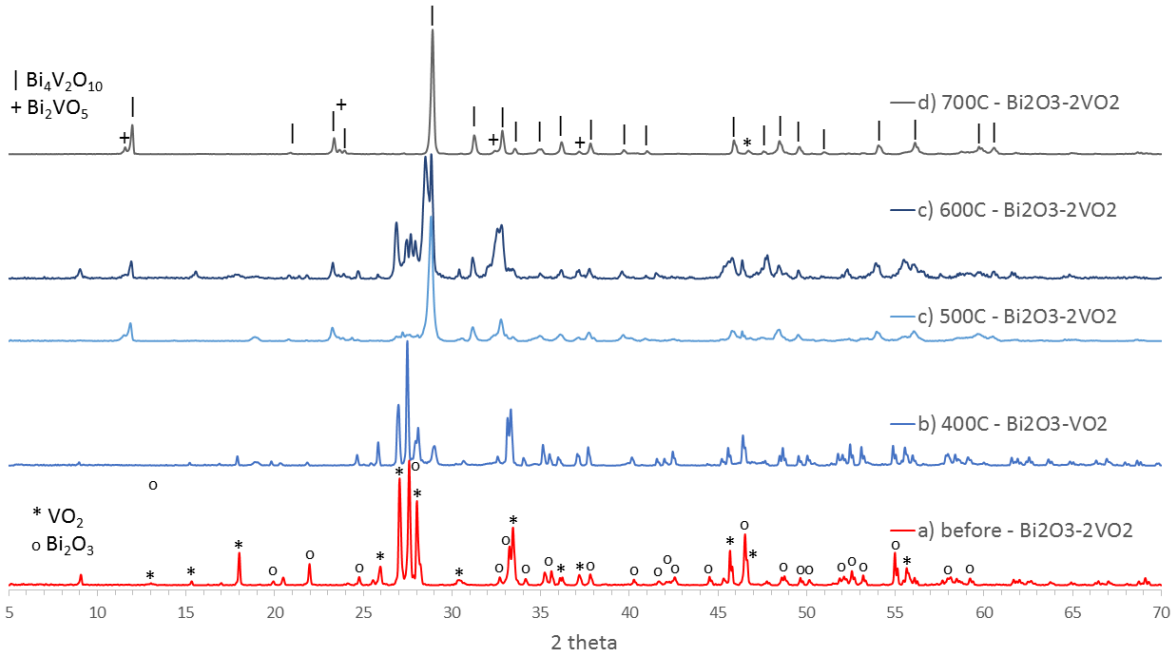

Figure 2.8. XRD powder patterns of $Bi_2O_3/2VO_2$ in the follow conditions: a) physical hand mixed before heating, b) 24h at 400°C, c) 24h at 500°C, d) 24h at 600°C and e) 24h at 700°C, mixture of Bi_2VO_5 – Orthorhombic a = 5.4704 Å, b = 17.2471 Å and c = 14.921 Å in Pnma (62) space group and $Bi_4V_2O_{10}$ – Orthorhombic a = 5.494 Å, b = 5.504 Å and c = 15.449 Å P21221 (18) space group.

2.6. Reverse combustion reaction with $Bi_4V_2O_{10}/Bi_2VO_5/VO_2$ mixture.

In a typical experiment where carbon dioxide was bubbled to a suspension of the solid in water during 15 minutes, the system remains under carbon dioxide atmosphere along the process. Upon irradiation with a mercury lamp in a quartz reactor, the gas mixture above the reaction mixture was analyzed every hour over 6 hours by GC-TCD and no gas other than carbon dioxide was detected. The suspension was then filtered to remove any solid from it and analyzed by GC-FID to determine possible formation of any possible organic water-soluble product. Unfortunately, no organic matter was detected. This demonstrate that our mixed-valent bismuth vanadate oxide is inactive. The use of NaOH did not modify the scenario.

2.7. Formaldehyde dehydrogenation on $Bi_4V_2O_{10}/Bi_2VO_5/VO_2$ mixture.

Having established the non-ability of reduced species to perform reverse combustion, the reactivity was explored with formaldehyde, one intermediate of the CO_2 reverse combustion. Upon irradiation of the suspension of the solid mixture with formaldehyde solution in water (0.10M) no activity was observed after 24h. Once NaOH (2.0 mL, 1M) was added to the system, hydrogen production began (Figure 2.9).

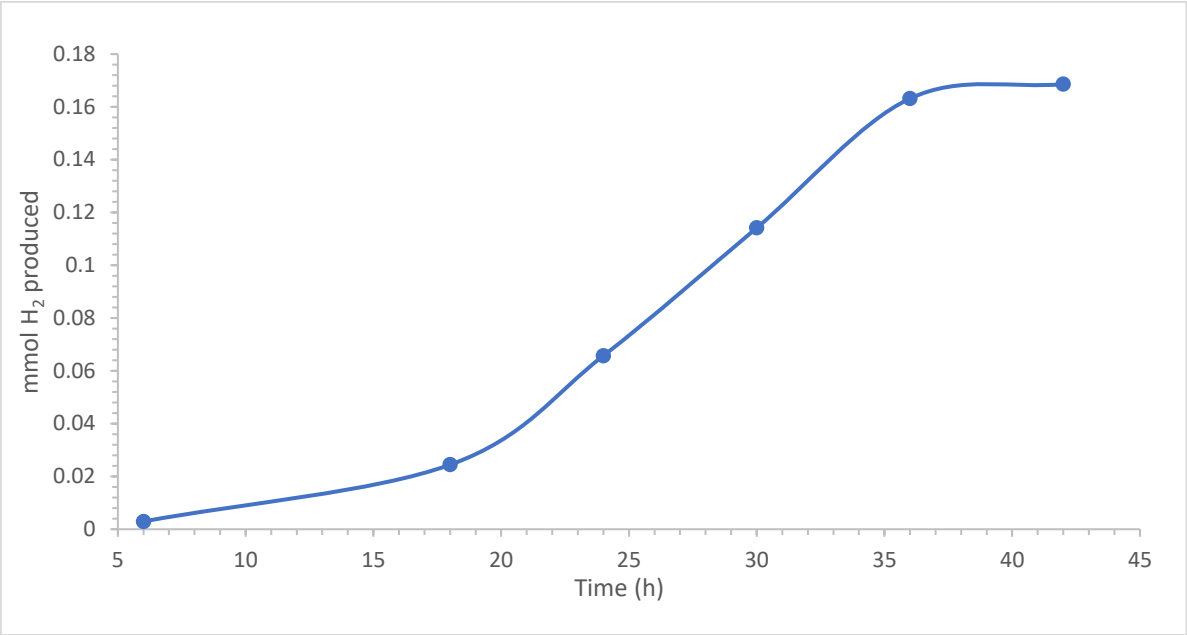

Figure 2.9. Hydrogen production from formaldehyde solution in water and NaOH in presence of vanadium(IV) solid mixture and under mercury lamp irradiation.

After 35 h of irradiation hydrogen production stops even when either more NaOH or formaldehyde was added. This was indicative of a poisoning of the surface of the catalyst possibly preventing light from interacting with the surface of the material. SEM analysis was thus performed before and after the reaction to show how the surface at the solid might be affected. As shown in Figure 2.8, the starting solid is a mixture of $Bi_4V_2O_{10}$ with a very small amount of other vanadium(IV) species (COMPO analysis in Figure 2.10b).

With these results, we have shown that bismuth vanadate in lower oxidation state is only capable to perform mild dehydrogenation of formaldehyde in basic media. The only byproduct in this reaction is the formate anion, in good agreement with previous observations from our group.[181]

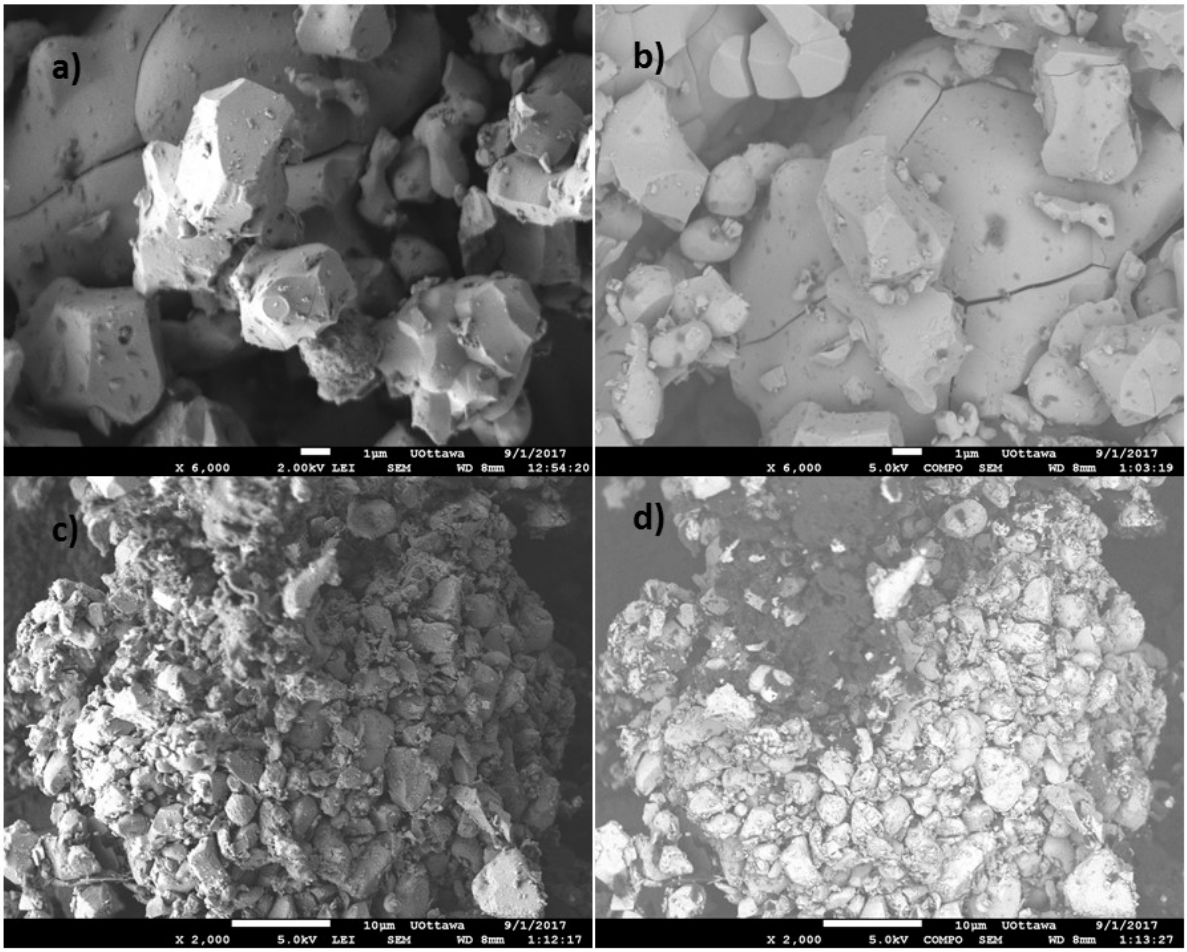

Figure 2.10. SEM analysis of a) $Bi_4V_2O_{10}/Bi_2VO_5/VO_2$ mixture before dehydrogenation of formaldehyde, b) COMPO analysis of $Bi_4V_2O_{10}/Bi_2VO_5/VO_2$ mixture before dehydrogenation of formaldehyde, c) post reaction solid and d) COMPO of postreaction solid.

By comparing the SEM analysis of Figure 2.10c/d, deposition of a new solid on the surface of the material is apparent. The bright material corresponds to the remaining $Bi_4V_2O_{10}$, while the dark solid is mainly a Na/C/O based material. We believe that this could be sodium formate produced as side product in the reaction as mentioned above. SEM-EDS analysis shows also that the bright material contains a surface atomic ratio Bi:V of 2:1 on average as in the initial formula $Bi_4V_2O_{10}$ used as major starting material. Residual nanoparticles that contain more Bi than V on SEM-EDS analysis were also observed. XRD of the material confirmed that the solid presented a new phase where vanadium is less

present in the structure (Figure 2.11). This could be an effect of vanadium being leached out from the structure because of the basic reaction conditions. This behavior was also observed when $BiVO_4$ was used as discussed later in this chapter. Instead, the dark solid contained a very low amount of vanadium comparing to the Na/C/O composition.

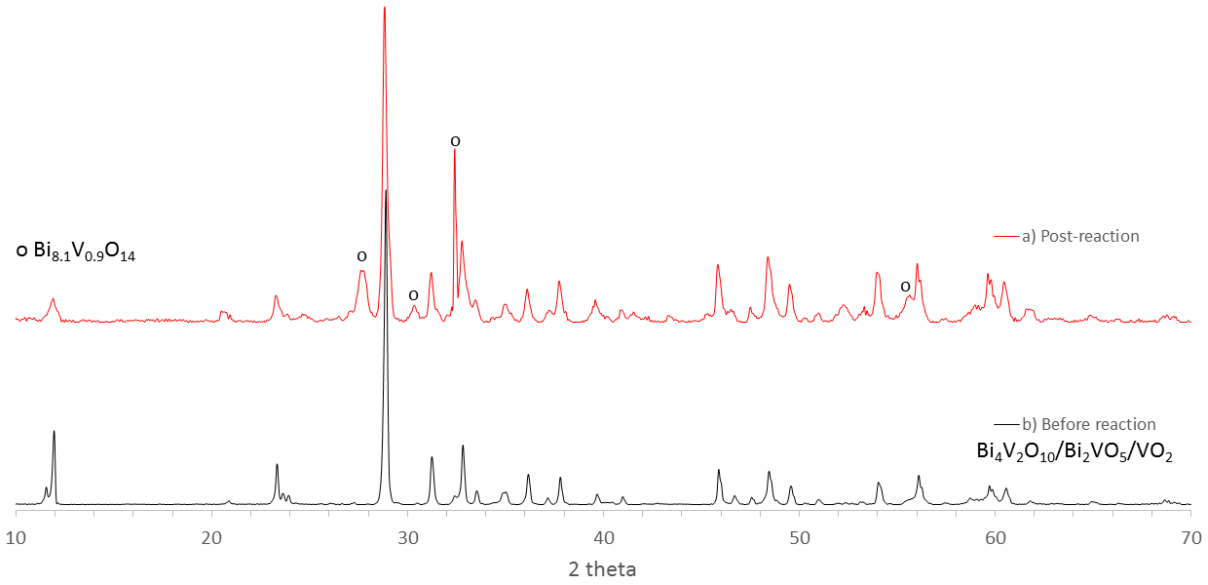

Figure 2.11. XRD powder pattern of solid mixture $Bi_4V_2O_{10}/Bi_2VO_5/VO_2$ b) before and a) after dehydrogenation of formaldehyde in basic media.

The optical properties of *m*-$BiVO_4$, were examined using UV-vis diffuse reflectance analysis showing a band gap in agreement with the values reported for this solid.[124] This confirms that *m*-$BiVO_4$ is in fact a semiconductor able to be photo-excited by using visible light irradiation (Figure 2.12).

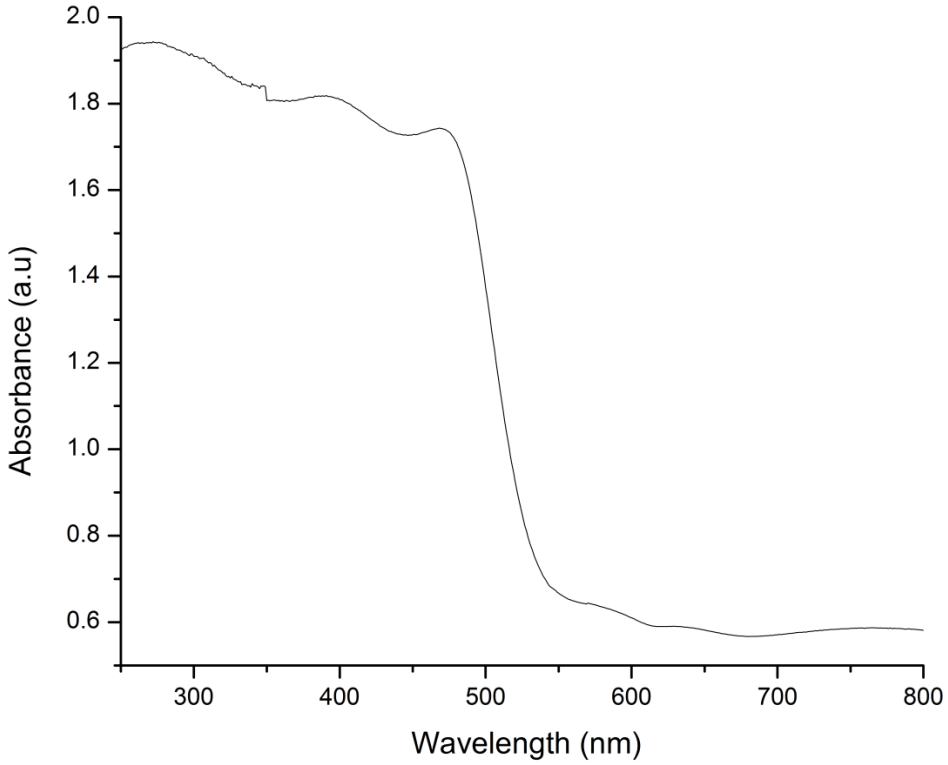

Figure 2.12. UV-vis diffuse reflectance of polyhedral *m*-$BiVO_4$ with an apparent experimental band gap of 560.2 nm (2.21eV).

2.8. Reverse combustion reaction on *m*-$BiVO_4$.

Upon irradiation under reverse combustion conditions, CO_2 is transformed into MeOH while the shape of the crystalline *m*-$BiVO_4$ was modified (Figure 2.13c). The postreaction solid clearly shows the presence of two phases in the XRD spectrum. The main phase present is still *m*-$BiVO_4$ while the second pattern is attributable to Bi_2O_3 (Figure 2.4 red line). The same phenomenon may be better observed in the "polyhedral" *m*-$BiVO_4$. The sample was analyzed by SEM before (Figure 2.13d) and after (Figure 2.13e) the reverse combustion reaction. The corrosion and deposition of microcrystalline material is now more evident. Also, of interest is the fact that two opposite faces of each polyhedron seem to be principally affected. Questions arise from the meaning of the etching of the crystals and the deposition of Bi_2O_3, implying that vanadium has been somewhat leached out of the structure.

Literature data indicated that the methanol production reaches a maximum with no catalyst decomposition.[116] In all of our experiments, we observed both a decrease in methanol concentration after 200 minutes of catalytic testing and a permanent deactivation of the catalyst after reactivation by heating. This is in contrast to other published work where a linear production of methanol was observed with little loss of activity after an alleged "regeneration" carried out upon heating at 80°C.[125] In an attempt to clarify these discrepancies, further investigation of the intermediate products and catalyst composition was performed with pristine and reactivated *m*-$BiVO_4$.

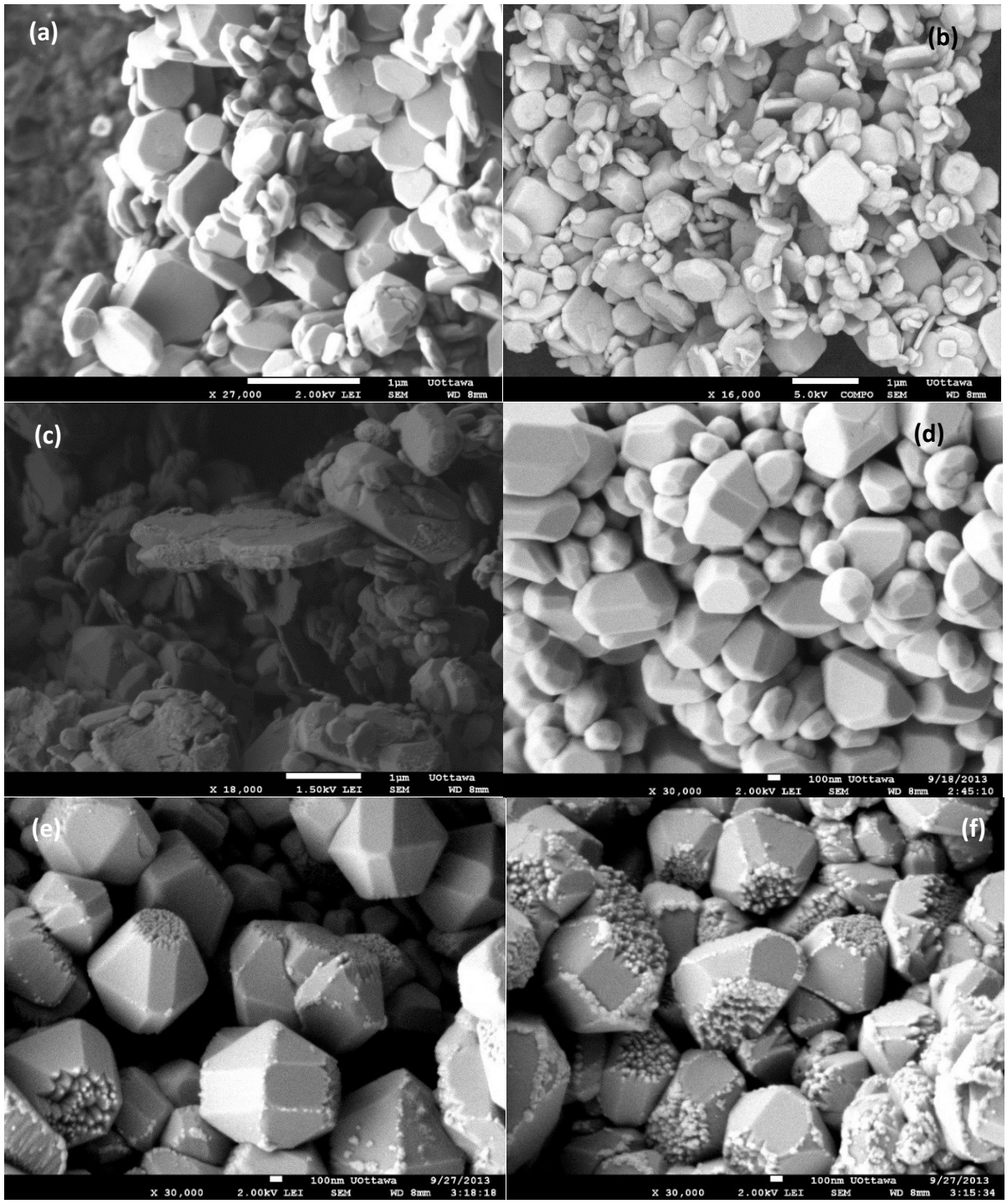

Figure 2.13. SEM (a) analysis of pure *m*-$BiVO_4$ before reverse combustion process, (b) SEM-COMPO, (c) SEM analysis of the solid after the process, (d) SEM analysis of polyhedral *m*-$BiVO_4$ before the reverse combustion process, (e) SEM analysis of polyhedral *m*-$BiVO_4$ after reverse combustion process and (f) SEM analysis of *m*-$BiVO_4$ with no carbon dioxide.

While we could not reproduce the formation of EtOH as claimed in the literature,[124] both formate anion and formaldehyde, along with methylformate were generated during the catalytic runs. Formate concentration appears to stabilize after 3 hours without loss of activity. Formaldehyde and methanol production decreases after recovery of the $BiVO_4$ catalyst, although the activity in formate formation does not appear to be affected by catalyst recovery. In all cases, no methane was detected confirming that the methanol loss after initial formation is not due to further reduction. We attribute the loss of methanol to the re-oxidation into lower value organics, including formaldehyde and formate by either *m*-$BiVO_4$ or the quartz reactor. As mentioned in the introductory part, the oxidation of several alcohols, including methanol into formaldehyde, has been shown to occur in glass and quartz reaction vessels upon irradiation with no need for a catalyst.[239] No other small organic molecules were detected. This perhaps could be taken as evidence for CO_2 photoreduction to initiate via monodentate binding, with stepwise proton-coupled electron transfers producing methanol as a final product. Potential oxidation products of methanol, formaldehyde, and sodium formate (Table 2.1) in a 1 M solution of NaOH were studied to help decipher the pathway for methanol re-oxidation. In all cases methane, carbon monoxide or other organic products were not observed.

Table 2.1. Quantitative analysis of oxidation and reduction of intermediates and products with *m*-$BiVO_4$ after 24 h

Starting material	MeOH (μmol)	CH_2O (μmol)	HCOO (μmol)	H_2 (μmol)
Methanol		28	13	3.6
Formaldehyde	460		71	25
Sodium formate	300	n.d.		n.d.

To observe the effect of formaldehyde on *m*-$BiVO_4$, an experiment was performed with formaldehyde as the starting organic material. Interestingly, when this *m*-$BiVO_4$ catalyst was analyzed by XRD and SEM, large amounts of Bi_2O_{4-x} nanoparticles were detected over the starting $BiVO_4$ (Figure 2.14). This effect is also seen during methanol production but to a lesser extent. The heavy coating of the active surface of $BiVO_4$, which is present only in inactive samples, suggests that this coating is at least partially responsible for the deactivation of the catalyst. This likely occurs due to blocking of the active surface by the coating of bismuth oxide, which can be partially removed by regenerating the catalyst during heating.

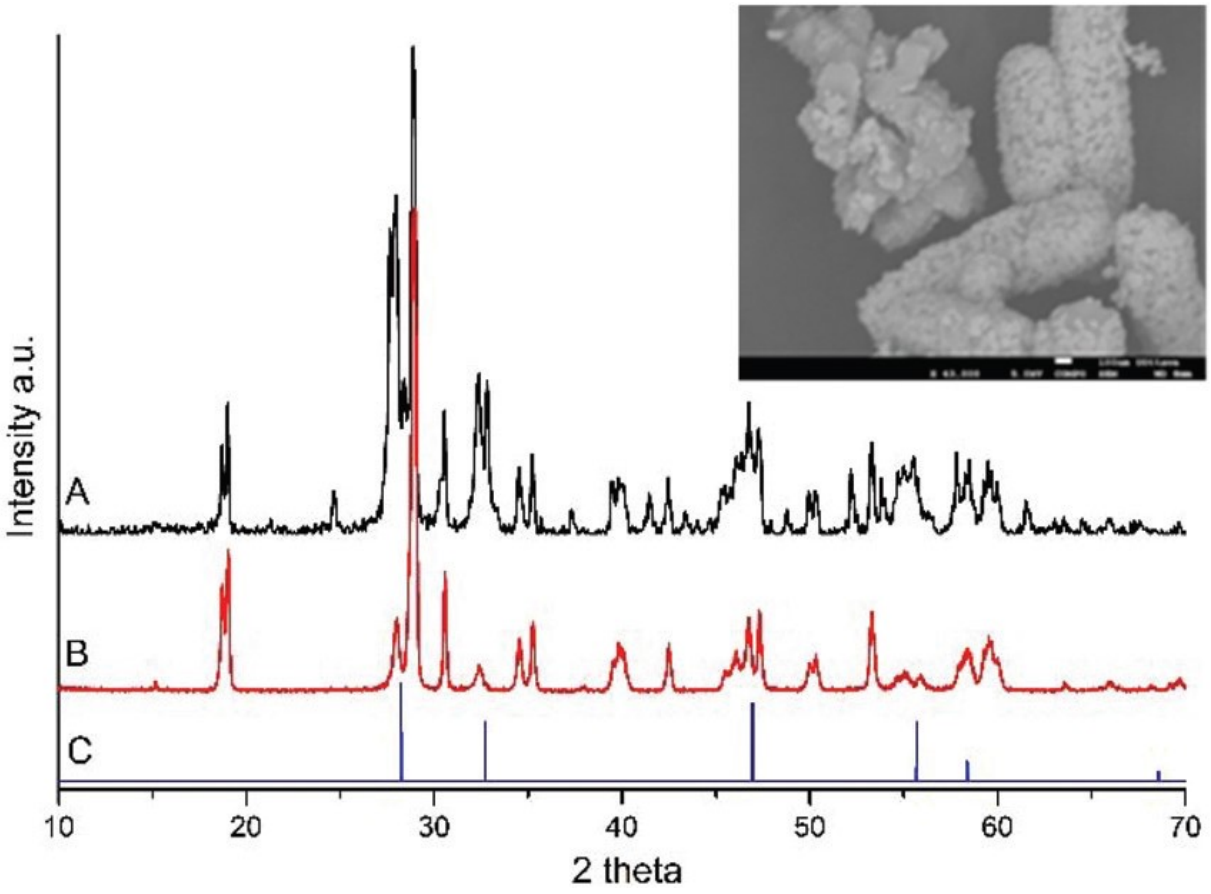

Figure 2.14. Comparison of powder XRD patterns of (A) inactive hyperbranched *m*-$BiVO_4$ from reaction with formaldehyde (B) inactive hyperbranched *m*-$BiVO_4$ from CO_2 photoreduction and (C) literature spectrum of Bi_2O_{4-x}. SEM micrograph of hyperbranched *m*-$BiVO_4$ from formaldehyde-spiked conditions is inset.

From the experiments of $BiVO_4$ with formaldehyde, we observe that the deposition of Bi_2O_{4-x} is caused at the surface of the catalyst by a reaction with formaldehyde, one of the key intermediates in the reduction to methanol. In turn, this indicated irreversible loss of vanadium from the original *m*-$BiVO_4$ structure. Several unsuccessful attempts were performed to try to reinsert the vanadium back into the etched *m*-$BiVO_4$ structures by illuminating with various vanadium sources in water (NH_4VO_3 or etched vanadium solution).

2.9. Catalyst deactivation

The activity of $BiVO_4$ towards CO_2 photoreduction necessarily requires the use of base.[124] However we have found that in 1 M NaOH aqueous solutions, both with and without 1 atmosphere of CO_2, *m*-$BiVO_4$ will become etched and Bi_2O_{4-x} nanoparticles are deposited on the surface of the catalyst (Figure 2.15b/e). By using a backscatter filter to determine surface electron density, deposited nanoparticles are revealed to be very dense, compared to bulk *m*-$BiVO_4$. In this state, the catalyst has become deactivated and shows limited CO_2 reduction activity. The etching has also been shown to occur without illumination.[240]

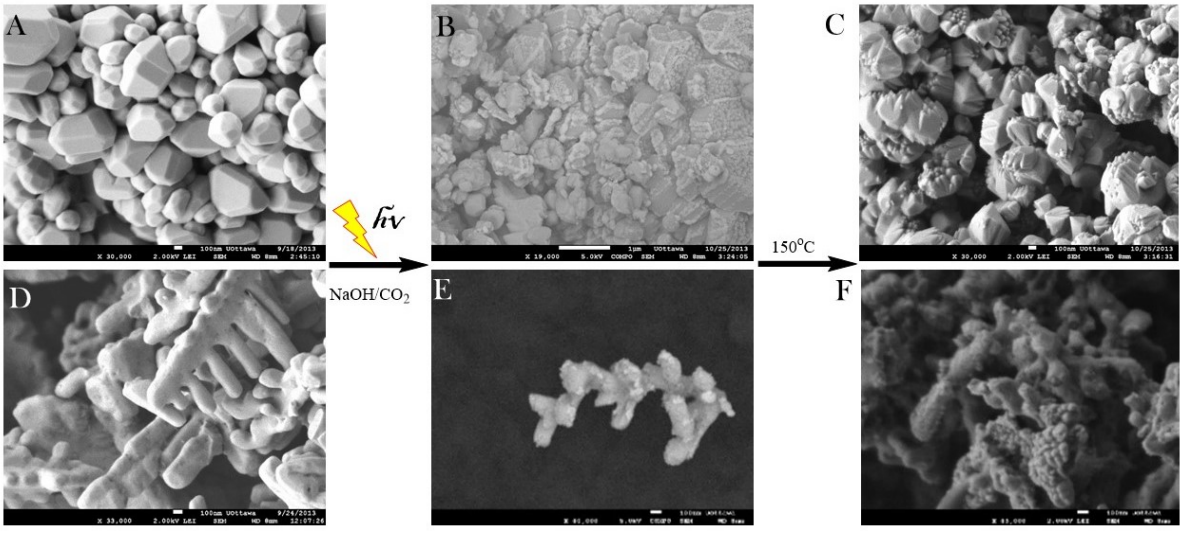

Figure 2.15. SEM images of (a) polyhedral, (b) inactive, and (c) reactivated polyhedral *m*-$BiVO_4$, and (d) hyperbranched, (e) inactive and (f) reactivated hyperbranched *m*-$BiVO_4$.

The catalyst can be reactivated by heating at 150°C which removes the electron rich deposits from the surface by drawing vanadium density from the inner $BiVO_4$. Although the catalyst can be reactivated, it remains irreversibly etched (Figure 2.15c/f). The reactivated catalyst was tested for CO_2 reduction under the same conditions and was shown to have reduced activity compared to pristine $BiVO_4$ (Figure 2.16). Composition of the $BiVO_4$ surface was analyzed during all stages of $BiVO_4$ regeneration (Figure 2.16).

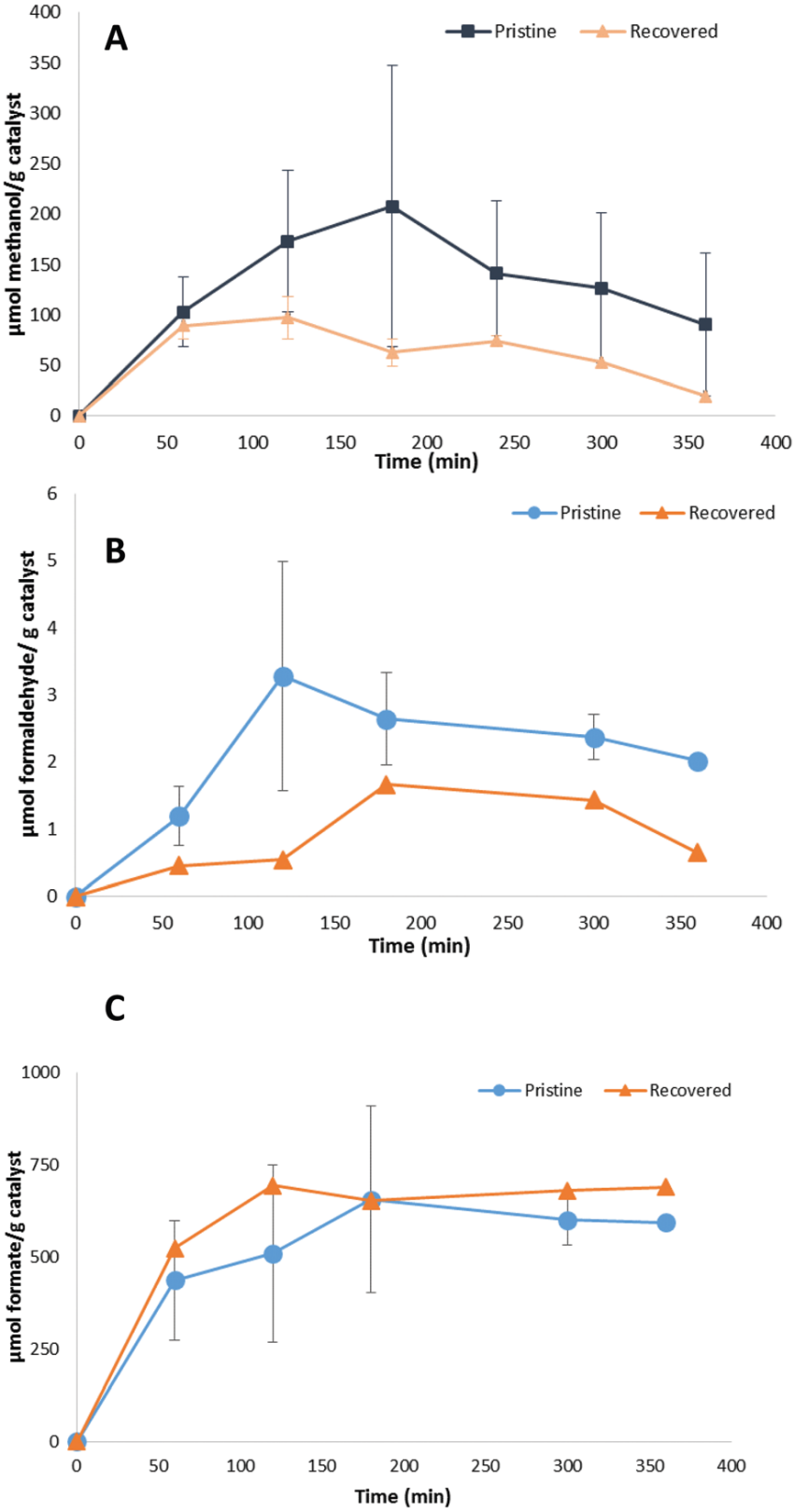

Figure 2.16. Concentration of (a) methanol, (b) formaldehyde and (c) formate during catalysis

Table 2.2. EDS derived molar % of bismuth, vanadium and oxygen on the surface of hyperbranched m-$BiVO_4$ averaged over three samples.

Sample	% Bi	% V	% O
Pristine hyp-$BiVO_4$	15.3 ± 1.4	15.2 ± 1.5	69.5 ± 2.7
Inactive hyp-$BiVO_4$	17.6 ± 0.7	13.52 ± 0.4	69.4 ± 1.1
Reactivated hyp-$BiVO_4$	16.7 ± 0.3	13.92 ± 0.02	68.8 ± 0.4
Dried hyp-$BiVO_4$ filtrate	0.00	19.0 ± 2.4	81.0 ± 2.4

XRD data (Figure 2.17) reveals the formation of a new, crystalline, material contaminating the sample of $BiVO_4$. The contamination peaks correspond with literature samples of a mixed valence bismuth oxide, denoted as Bi_2O_{4-x}.[241] Attempts to separate this contaminant from the bulk $BiVO_4$ have been unsuccessful. We assign the electron rich surface deposits to Bi_2O_{4-x}. The molar percent of oxygen does not change significantly between samples (Table 2.3), although bismuth and vanadium percentages are greatly altered in post-reaction.

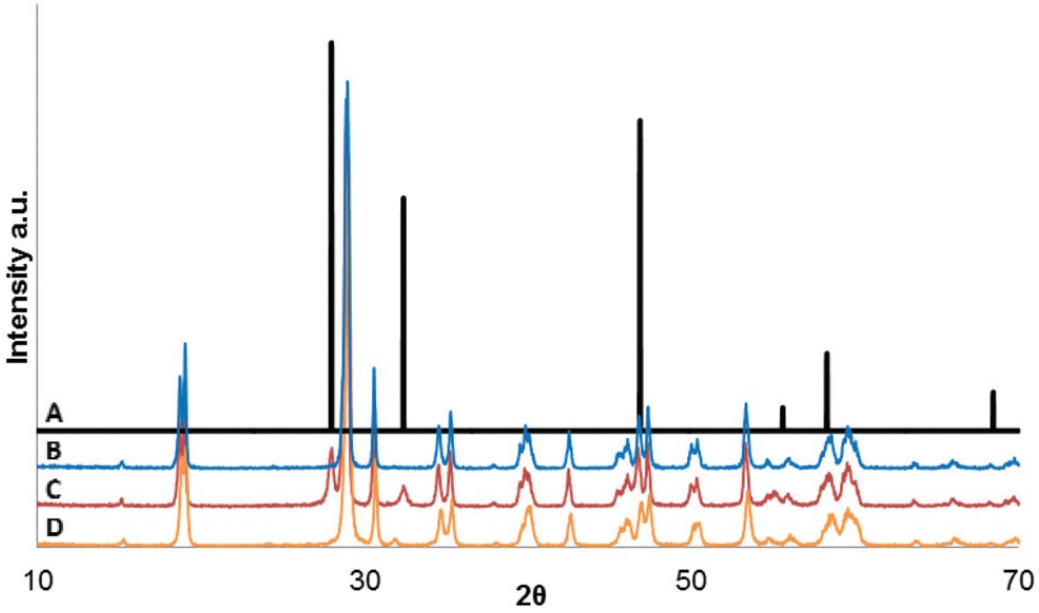

Figure 2.17. XRD patterns of (A) literature pattern of Bi_2O_{4-x}. (B) Pristine hyperbranched *m*-$BiVO_4$, (C) inactive hyperbranched *m*-$BiVO_4$ and (D) reactivated hyperbranched *m*-$BiVO_4$.

Pristine hyperbranched *m*-$BiVO_4$ has a ratio of 0.99 V/Bi, by surface molar percentage. This is compared to the inactive ratio of 0.77 and the recovered ratio of 0.83. This confirms that a large amount of surface vanadium is irreversibly lost during the reaction, likely caused by leaching in the alkaline conditions. Similar losses of vanadium were observed from the structure by XRF measurements (Table 2.3).

Table 2.3. Comparison of XRF data of as-synthesized and post-reaction polyhedral $BiVO_4$.

Sample	Bi mass %	V mass %	O mass % (balance)	Change in V (mass %)
$BiVO_4$ before testing	50.26	14.47	35.27	-
$BiVO_4$ after testing	57.35	14.2	28.45	0.27

To confirm that vanadium was lost to the filtrate, a sample of the filtrate was dried and EDS measurements of the filtrate taken which shows only vanadium in solution (Figure 2.18). This is further confirmed by ^{51}V NMR of the filtrate which shows multiple peaks, characteristic of a mixture of aqueous vanadium oxides (Figure 2.18c).

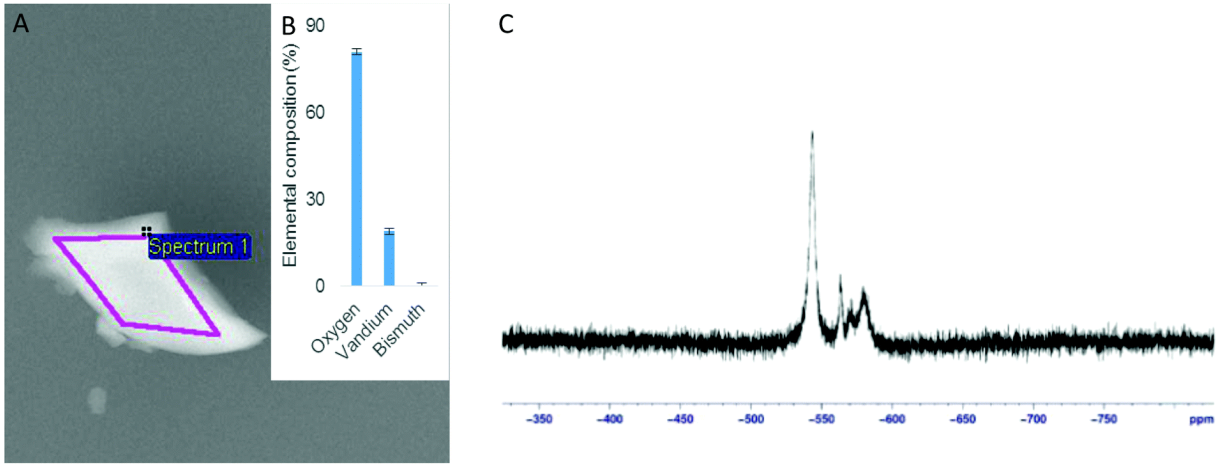

Figure 2.18. A) SEM image of dried filtrate after etching, B) elemental composition of particle obtained by EDS, and C) ^{51}V NMR of post-reaction filtrate.

2.10. Conclusions

In conclusion, *m*-$BiVO_4$ is indeed able to perform reverse combustion in basic conditions. In our experiments, only methanol was formed. Different from the literature claims, decomposition of the catalyst after the process was always clearly detected. The solid deposited on the surface of the solids corresponds to mixture of bismuth oxides that can be removed by heating the sample at 150°C. The vanadium leached out of *m*-$BiVO_4$ consists of a mixture of V(IV) and V(V). Also, this work has provided new insight into the mechanism of $BiVO_4$ as a photo-catalyst for CO_2 photo-reduction. A major deactivation pathway appears to be caused by the re-oxidation of its own products. Furthermore, $BiVO_4$ will rapidly decay with loss of vanadium and deposition of bismuth oxides and will require constant recovery by heating. However, vanadium leaching and catalyst etching are irreversible processes, and after every catalytic cycle of photo-reduction/recovery, a portion of the initial catalyst is irreversibly lost.

The major and minor products formed in this reaction provide some new insight into the mechanism of CO_2 photo-reduction for $BiVO_4$. While formaldehyde, formate and methanol are all possible products in all three proposed CO_2 reduction pathways, the lack of other key intermediates detected (CO, glyoxal, etc.) suggests that the formaldehyde pathway is the most likely pathway for CO_2 reduction promoted by *m*-$BiVO_4$.

By lowering the oxidation state of vanadium in bismuth vanadate specie ($Bi_4V_2O_{10}$) aiming to mimic the intermediate vanadium(IV-III) formed after the photo-irradiation, reverse combustion was evaluated at neutral and basic pH with no conversion to any organic or gas observed during the process. On the other hand, it presented mild reactivity for dehydrogenation of formaldehyde in basic media.

2.11. Experimental Section

2.11.1. Preparation of polyhedral m-$BiVO_4$: $Bi(NO_3)_3.5H_2O$ (10 mmol, 4.85 g) was suspended in 50 mL of distilled water in a 100 mL glass pressure vessel. Na_2SO_4 (7.04 mmol, 1.00 g) was dissolved in 20 mL of water and added to the Bismuth nitrate suspension. After stirring the solution for 30 minutes, NH_4VO_3 (10 mmol, 1.17 g) was added and the vessel was closed and heated at 180^{o}C for 24h. After this time, the vessel was cooled down to room temperature. The resulting yellow solid was filtered and washed five times with 45 mL of boiling water to ensure all remaining salts were removed from the final yellow solid. Once the solid was washed out, it was dried under vacuum at 100^{o}C for 12h. The yellow solid was characterized by powder X-ray crystallography, XRF, SEM and UV-vis diffuse reflectance and agreed with the published monoclinic bismuth vanadate.[125]

2.11.2. Catalytic testing

In a typical reaction, 0.4 g of catalyst and 200 mL of a 1.0 M NaOH solution were placed in a quartz flat bottom flask adjacent to a 350W Xe arc-lamp. Prior to light irradiation, the reaction mixture was thoroughly degassed and allowed to equilibrate under a CO_2 atmosphere for 30 minutes. Methanol was detected with an Agilent 7820A GC with a FID, using a Restek Rt-U-Bond column and helium carrier gas. ^{51}V NMR spectra were recorded on a Bruker Avance II 300 MHz spectrometer using neat $VOCl_3$ as a standard. Chemical shifts are reported in ppm and spectra were recorded at 298 K. Powder XRD diffractograms were obtained on a Rigaku Ultima IV diffractometer. X-ray Fluorescence (XRF) measurements were performed on a Rigaku Supermini-200. UV-Vis spectra were obtained on a Specmate UV-1100 spectrometer. Scanning electron microscopy and energy dispersive X-ray analysis were performed with a JSM-7500F SEM instrument by JEOL, Inc. The concentration of formaldehyde was determined by a colorimetric procedure by Nash.[242] Concentration of dissolved formate was determined by a colorimetric procedure by Sleat and Mah.[243]

This work was published in: **Camilo J. Viasus**, Nicholas P. Alderman, Virginie Peneau, Bulat Gabidullin, Balamurugan Vidjayacoumar, Khalid Albahily and Sandro Gambarotta, *International Journal of Hydrogen Energy*, **2019**, 44, 3, 1534-1543.

Chapter 3. Two-Step Catalytic Dehydrogenation of Formic Acid to CO_2 via Formaldehyde

CJV: All work was done by me and all experimental part was carried out by me. Dr. Gabidullin carried out the single crystal X-ray analysis. Dr. Alderman and Peneau helped with paper editing and catalytic tests. Dr. Balamurugan Vidjayacoumar and Dr. Khalid Albahily were funds providers and consulted during the development of the paper.

3.1. Preamble

After evaluating the behaviour and characteristics of *m*-$BiVO_4$ in chapter 2 vis-a-vis reverse combustion, and given the limitations discovered during our work, an alternative material was considered by replacing vanadium with chromium in a similar metal oxide extended structure. Considering the impossibility for *m*-$BiVO_4$ to retain the V atoms in the structure during longer-time reverse combustion, higher oxidation states were expected to be beneficial for improved resiliency and performance. The fact that $Bi(OH)CrO_4$ is a semiconductor with an appropriate band-gap and band-edge to perform radical reverse combustion was advising its utilization. In this material, the transition element is in its highest oxidation state, Cr(VI), which was expected to be capable of releasing oxygen during the oxidizing half reaction path. The following chapter describes the preparation, characterization and reactivity of this species.

3.2. Introduction

Small organic molecules (C1) may be employed as hydrogen shuttles in catalytic water-splitting binary systems. For example, the selective dehydrogenation of formaldehyde in basic conditions to formate anion, along with the inverse reaction where water is used as hydrogen source, can be used, in combination with appropriate catalysts and in homogeneous phase, for formaldehyde/formate mediated water splitting (Scheme 3.1).[181]

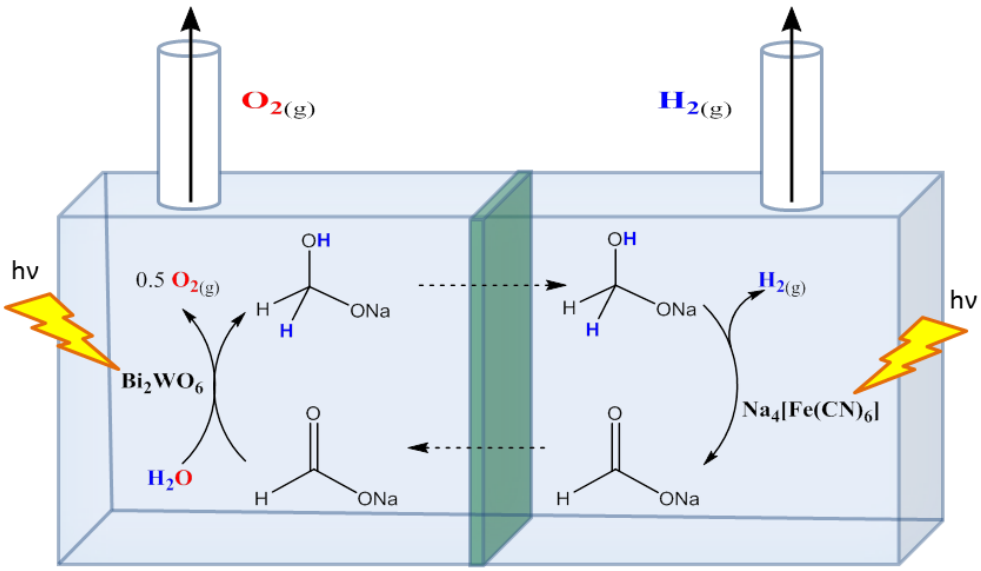

Scheme 3.1. Photochemical water splitting in a two-stage system. Reproduced from ref #[181] with permission by The Royal Society of Chemistry.

The redox pair CO_2/formic acid could be in principle another candidate for this purpose but there are some caveats. The use of formic acid as a hydrogen carrier has become an attractive route for redox reactions of practical use.[244] Efficient hydrogen release[1–5] and the relative ease of carbon dioxide hydrogenation to recover the starting feed,[6–8] including reverse combustion techniques,[9–11] makes formic acid and its corresponding anion viable precursors for water splitting via shuttle catalysis.

However, in all examples of the dehydrogenation of formic acid both hydrogen and carbon dioxide are produced at the same time. Therefore, a costly and energy-intensive gas separation step must be performed to have a clean stream of hydrogen unless a two-step system could be found.

The dehydrogenation of formic acid to hydrogen and carbon dioxide has been performed by numerous catalysts. These include catalysts based on silver[252,253], palladium[254–257], iron[247,258], iridium[259–262], cobalt[263], ruthenium[264], zinc[265] and boron.[266] However, in all of these reactions both hydrogen and carbon dioxide are produced simultaneously.

Numerous possible decomposition pathways of formic acid have been widely studied in the last decade.[246,251,254,267,268] Although hydrogen and carbon dioxide are the primary products, other by-products may also be present. Carbon monoxide, for example, is formed by dehydration of formic acid in the presence of a catalytic amount of sulfuric acid.[269] Metal oxides at high temperatures also perform decarbonylation.[270] Molecular compounds containing ruthenium and iridium among others, can afford disproportionation to methanol, water and carbon dioxide.[244,267,270–272]

Even if we restrict the C1-mediated water-splitting to the formaldehyde/formic couple, the multiple decomposition pathways of formic acid pose some serious challenges. The disproportionation of formic acid into a mixture of formaldehyde, carbon dioxide and water is in fact a thermodynamically permissible process.[270]

$$2\ HCOOH_{(g)} \rightarrow 2\ CO_{2\,(g)} + 2\ H_{2\,(g)} \qquad \Delta G^{o}_{(273K)} = -86.8\ kJ/mol \qquad (Eq.\ 1)$$

$$2\ HCOOH_{(g)} \rightarrow 2\ CO_{(g)} + 2\ H_2O_{(l)} \qquad \Delta G^{o}_{(273K)} = -46.2\ kJ/mol \qquad (Eq.\ 2)$$

$$2\ HCOOH_{(g)} \rightarrow CO_{(g)} + H_2O_{(l)} + CH_2O_{(aq)} \qquad \Delta G^{o}_{(273K)} = -60.0\ kJ/mol \qquad (Eq.\ 3)$$

As mentioned above, we have previously reported highly efficient hydrogen production from para-formaldehyde and sodium hydroxide by using the $[Fe(CN)_6]^{4+}$ photocatalyst.[181] The reaction produces formate as a by-product, but the reverse transformation of formic acid/formate to formaldehyde using

water as a hydrogen source, although possible under photochemical conditions, has not yet been achieved with comparable activity and selectivity. Even the simple stoichiometric reduction of formic acid to formaldehyde is problematic since it leads directly to methanol instead.[273]

In a search for catalysts to a methanol-free transformation of formic acid into formaldehyde, we have previously studied the ability of $BiVO_4$ to act as a photo-semiconductor for the hydro-reduction of CO_2 (reverse combustion) in Chapter 2. The key feature of that system was the presence of a low-valent bismuth and high valent vanadium which, upon irradiation, exchange their redox roles, with bismuth oxidizing water and vanadium reducing CO_2. This led us to consider the combination of bismuth(III) and chromium(VI) oxides, as in $Bi(OH)CrO_4$.

The presence of a more strongly oxidizing hexavalent chromium was expected to facilitate oxygen release and hopefully provide a better catalyst for reverse combustion.[274] In other words, the behavior of this material could be two-fold. On one hand, it may catalyze the dehydrogenation of formic acid to CO_2, while in combination with a reverse combustion catalyst, use formic acid as a water splitting shuttle.

On the other hand, it might reduce formic acid to formaldehyde with the input of water as hydrogen source. In this case, the water splitting could be shuttled by the formic/FA couple.

The combination of trivalent Bi and hexavalent Cr gives rise to interesting bimetallic oxo-aggregates whose structure can be tailored by the synthetic protocol.[275] The resulting bismuth chromate hydroxide material has photo-semiconducting properties with a band edge position

and light-harvesting capacity (band gap 2.21 eV) which was successfully used for the degradation of Methylene Blue (MB).[192]

The thermal degradation of $Bi(OH)CrO_4$ releases oxygen affording an ill-defined paramagnetic mixture of bismuth and chromium.[276] This species displays a different reactivity from that of Cr_2O_5 oxide, thus indicating that the presence of Bi might affect its chemical behaviour.[277]

In this Chapter, we present the synthesis and characterization of a new $BiCrO_4$ species obtained from thermolysis of $Bi(OH)CrO_4$ and its use as a catalyst for the disproportionation of formic acid to formaldehyde and carbon dioxide under mild conditions. Even though the possibility of obtaining a new shuttling system for water splitting was not achieved, various catalysts, such as MCl_3 [M = Ir(III) and Ru(III)], have been also investigated to complete a two-step tandem catalytic dehydrogenation of formic acid to H_2 and CO_2. These two-step processes have the advantage of forming carbon dioxide and hydrogen in two different stages, which means that no gas separation needs to be performed to obtain a clean stream of each product. This is the first time to our knowledge that a two-step process for the decomposition of formic acid has been presented.

3.3. Results and Discussion

We have analyzed the problem of formic acid decomposition in two separate steps: the release of carbon dioxide from formic acid in one step and formation of hydrogen in a second step (Scheme 3.2). This gives a clean, single product gas stream in each step.

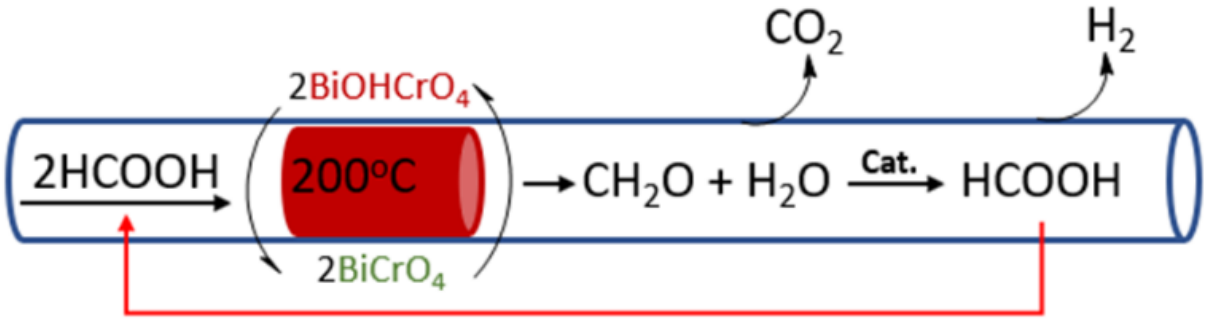

Scheme 3.2. Shuttle system using the couple formic acid/formaldehyde. Cat. = MCl_3 [M = Ir(III) and Ru(III)].

In the first step, bismuth chromate is used thermally to reduce formic acid to formaldehyde, water and carbon dioxide at low temperatures (200-300°C). In a second step, the formaldehyde is dehydrogenated in basic conditions with iridium or ruthenium catalysts at room temperature.

3.3.1. Formic acid reduction

Scheme 3.3 highlights the four steps of the reduction of carbon dioxide to methanol. It should be reiterated that formic acid can be catalytically oxidized to carbon dioxide and hydrogen[5,29–31] but selective reduction to formaldehyde has been reported only once.[181] It is worth reminding that in acidic media, the degradation of formic acid could follow a different path leading to carbon monoxide and water.[281,282]

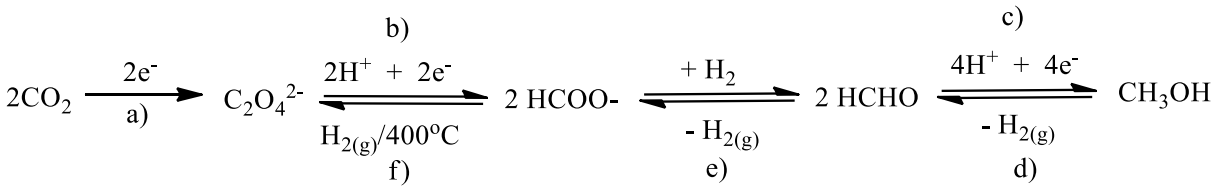

Scheme 3.3. Carbon dioxide redox, steps a[148,150,151], b[284], c[475], d[188], e[181] and f[476].

We have investigated the reactivity of formic acid with both monoclinic and orthorhombic forms of bismuth hydroxo-chromate $Bi(OH)CrO_4$ (Figure 3.1). To our initial disappointment, this photo-semiconductor does not perform reverse combustion under irradiation (i.e. formation of formaldehyde with water with oxygen release). However, it thermally catalyzes a clean disproportionation of formic acid to a mixture of formaldehyde and CO_2.

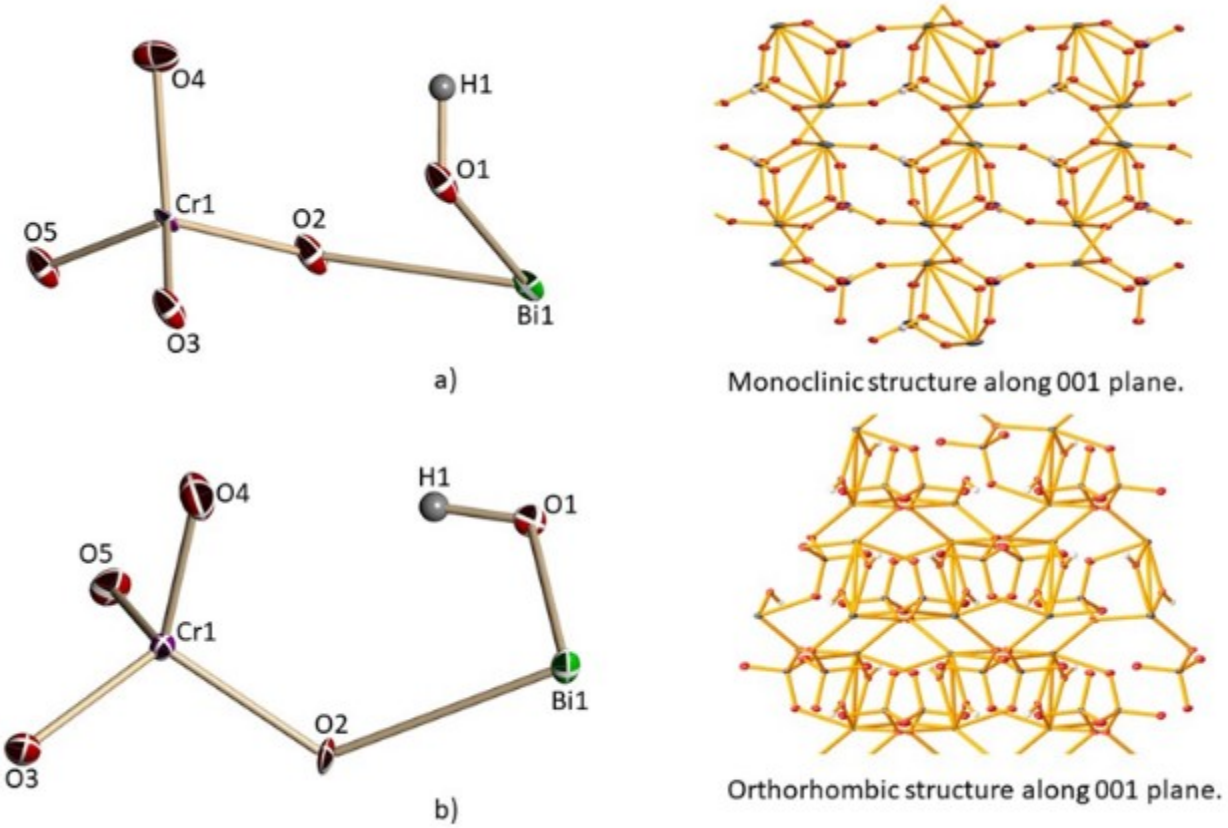

Figure 3.1. Crystal Structures of (a) *m*-$Bi(OH)CrO_4$ and (b) *o*-$Bi(OH)CrO_4$. Selected bonds for monoclinic and orthorhombic isomers respectively: Bi(1)-O(1) 2.254 Å, Bi(1)-O(2) 2.258 Å, Cr(1)-O(2) 1.717 Å, Cr(1)-O(3) 1.639 Å, Cr(1)-O(4) 1.636 Å, Cr(1)-O(5) 1.593 Å, Bi(1)-Cr(1) 3.619 Å and Bi(1)-O(1) 2.192 Å, Bi(1)-O(2) 2.420 Å, Cr(1)-O(2) 1.723 Å, Cr(1)-O(3) 1.610 Å, Cr(1)-O(4) 1.676 Å, Cr(1)-O(5) 1.630 Å, Bi(1)-Cr(1) 3.628 Å. Selected angles for monoclinic and orthorhombic isomers respectively: Bi(1)-O(2)-Cr(1) 121.31°, O(1)-Bi(1)-O(2) 75.99°, O(1)-Bi(1)-O(2)-Cr(1) -70.87° and Bi(1)-O(2)-Cr(1) 130.65°, O(1)-Bi(1)-O(2) 80.08°, O(1)-Bi(1)-O(2)-Cr(1) -17.33°.

The two forms of $Bi(OH)CrO_4$ have been structurally investigated using powder diffraction techniques by Aurivillius *et. al.*[283] We managed to grow single crystals of sufficient size to undertake crystal structure analysis for both forms, thus authenticating a previous structural proposal. Of the two monoclinic and orthorhombic forms, the monoclinic displays a much higher thermal resiliency and therefore, was preferred for the thermal degradation of formic acid.

In a standard experiment, a catalytic amount of *m*-$Bi(OH)CrO_4$ was placed in a glass tube surrounded by a furnace with formic acid being injected at constant rate. Catalytic runs were carried out at different temperatures in the range 200°C and 300°C (Table 3.1). As expected, temperature increases resulted in faster formic acid decomposition to carbon dioxide and hydrogen but also a substantial amount of carbon monoxide, water and oxalic acid.[284] The temperature of 200°C was instead found to be the optimum for maximizing the production of formaldehyde and minimizing formation of by-products. It should be reminded that thermodynamically-allowed side reactions such as water-gas-shift[111] as well as formaldehyde decomposition into syn-gas (CO + H_2) may also occur under thermal conditions. Temperatures lower than 180°C afford very low production of formaldehyde and the usual decomposition of formic acid into the above-mentioned by-products.

Table 3.1. Reactivity of formic acid using different catalyst and supports.

Entry	Metal Oxide	Temp °C	HCHO (μmol)	μmol		
				CO_2	H_2	CO
1	$Bi(OH)CrO_4$	200	97.9	4594	3143	1561
2		250	200	11601	7613	13054
3	$Bi(OH)CrO_4/SiO_2$	200	87.5	5123	4360	2575
4		250	608	32535	30165	22067
5	SiO_2	200	0.015	----	----	83194
6	$Bi(OH)CrO_4/Al_2O_3$	200	0.430	288	50	419
7	Al_2O_3	200	0	1069	169	31337
8	$Bi(OH)CrO_4/C$	200	4.60	1576	258	884
9		300	45.3	6760	4089	6747
10	C	200	0.510	936	159	1800
11		300	0.780	1857	343	4394
12	Cr_2O_3	200	0	1418	173	398
13	Bi_2O_3	200	15.1	4865	122	----

To increase the surface area and to disperse the catalyst, we have attempted to support $Bi(OH)CrO_4$. Different solids were investigated such as SiO_2, Al_2O_3 and carbon. While Al_2O_3 and

carbon acted as inhibitors (Table 3.1, entry 9-11), formaldehyde production had a threefold increase when SiO_2 was employed as support. It was previously reported that silica can afford mainly formic acid dehydration whilst other metal oxides MO (M = Mg and Zn) favor its dehydrogenation.[270] However, this was not the case in this work. The results presented in Table 3.1 (entry 3 and 4), show that the overall catalytic activity can be increased *up to seven times* with increasing temperatures.

To understand the catalytic activity of $Bi(OH)CrO_4$ with formic acid we have separately examined Bi_2O_3 and CrO_3. These oxides did not produce detectable amounts of CH_2O. Lower-valent Cr_2O_3, did not catalyze the formic acid disproportionation to formaldehyde either. Instead, it catalyzed the decomposition of formic acid into carbon monoxide, carbon dioxide, hydrogen and water.[270] On the other hand, reaction of Bi_2O_3 with HCOOH at 200°C affords metallic bismuth with parallel formation of water, carbon dioxide and carbon monoxide.

The robustness of the $Bi(OH)CrO_4/SiO_2$ catalytic system was assessed with a long term experiment under the optimal reaction conditions (Table 3.1, entry 4) finding a steady production of formaldehyde (Figure 3.2).

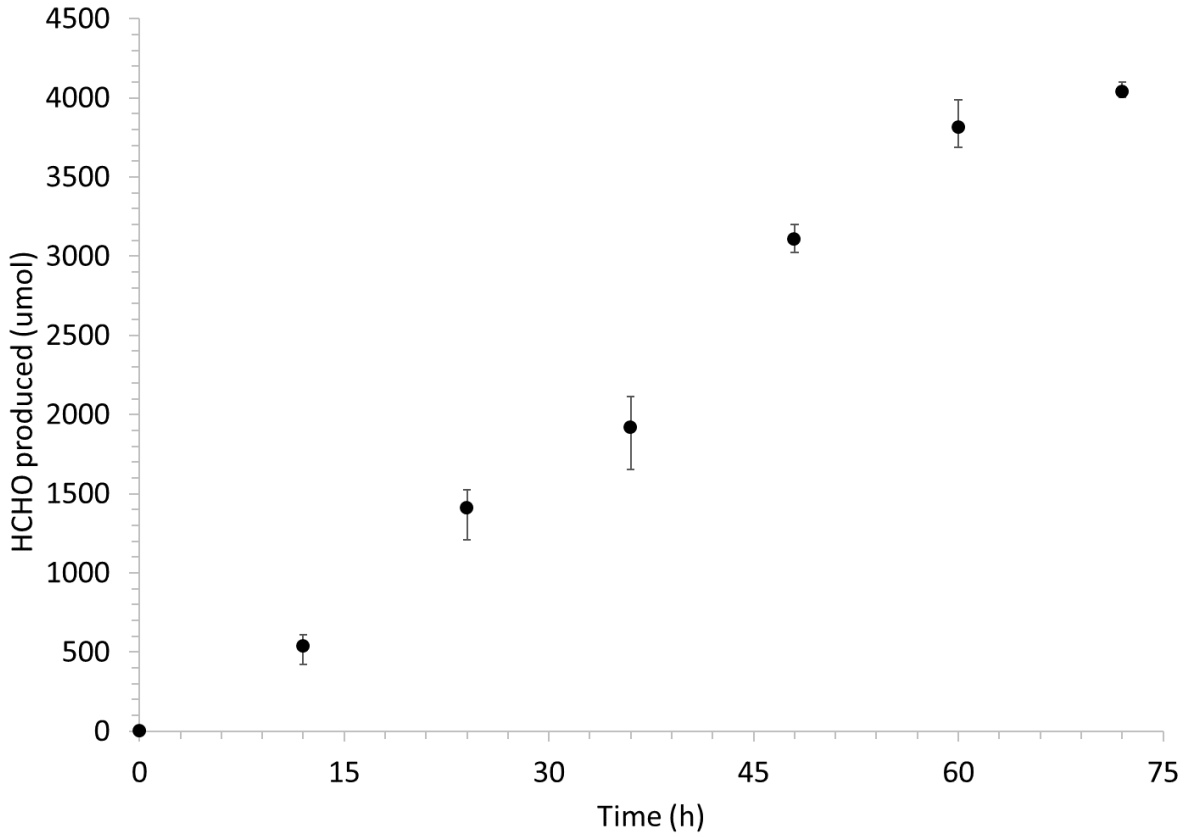

Figure 3.2. Formaldehyde produced over time from formic acid using $Bi(OH)CrO_4$ on SiO_2 at 250°C.

The production of formaldehyde remains linear for more than 60 hours, with a formaldehyde production rate of 0.065 mmol/mmol cat/hr. This rate can be increased by increasing the reaction temperature, however this also increases the amount of thermal decomposition of formic acid (and produced formaldehyde) into hydrogen and carbon dioxide.

As shown in equation 3, in the ideal disproportionation process, only 50% of the formic acid used is being transformed into formaldehyde. However, we observed amounts of carbon dioxide higher than formaldehyde as well as hydrogen being produced at the beginning of the reaction (Table 3.1, entry 4). We attribute this behavior to the initial stoichiometric transformation of $Bi(OH)CrO_4$ into $BiCrO_4$ which

consumes one equivalent of HCOOH (Eq. 4). Once $BiCrO_4$ is formed, the catalytic disproportionation towards formaldehyde starts.

$$HCOOH + 2\ Bi(OH)CrO_4 \rightarrow 2\ H_2O + CO_2 + 2\ BiCrO_4 \qquad \text{(Eq. 4)}$$

SEM analysis (Figure 3.3) shows the morphology of *m*-$Bi(OH)CrO_4$ before and after reaction when the $BiCrO_4$ was formed. Although the color of the material changed from orange to dark green, the surface morphology/shape and size of the particles remained similar. The bismuth chromate particle sizes appear to be in the 1-3 μm range, and contain a well-defined polyhedral morphology.

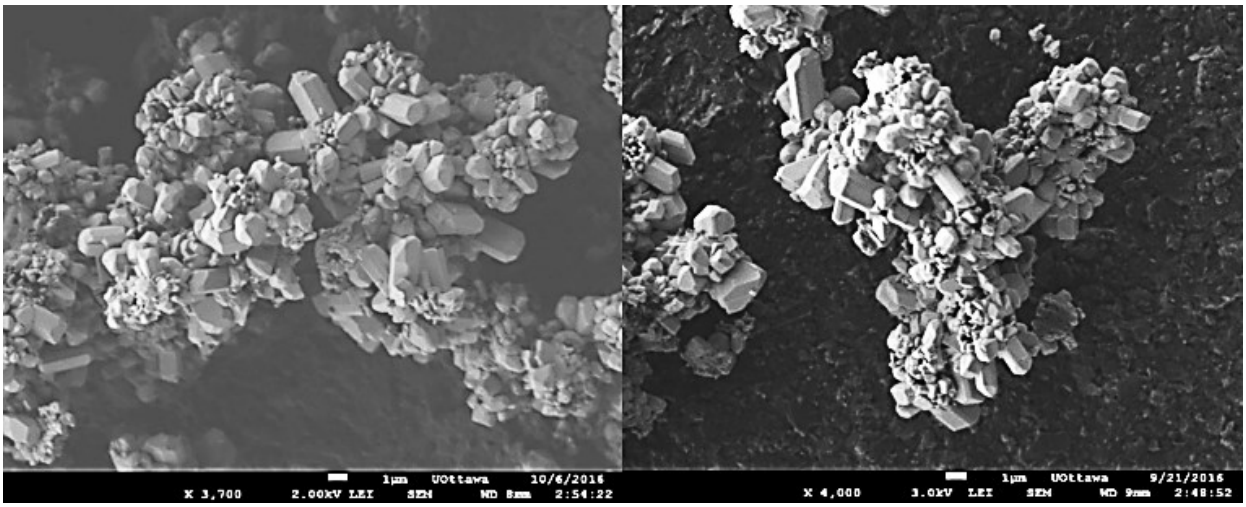

Figure 3.3. SEM analysis of $Bi(OH)CrO_4$, Left) $Bi(OH)CrO_4$ before reaction, right) After reaction $BiCrO_4$

XRF analysis did not show any significant change in the molar ratio of Bi:Cr at 1.04 before and 1.09 after reaction. However, a noticeable change of the oxygen/hydrogen ratio was observed suggesting the release of hydroxyl groups (Table 3.2). Additionally, the new material formulated as $BiCrO_4$ is paramagnetic with a magnetic moment of 1.86 BM in agreement with the d^1 electronic configuration of chromium(V). In other words, chromium(VI) has been reduced to chromium(V) with consequent release of OH from the structure.

Table 3.2. XRF results for the reaction of $Bi(OH)CrO_4$ at 200°C with HCOOH

Metal Oxide /Composition	% Bi	% Cr	% O/H bal.	Cr / Bi Ratio
Before – $Bi(OH)CrO_4$	58.32 +/- 0.48	15.13 +/- 0.12	26.55 +/- 0.60	1.04 +/- 0.01
After – $BiCrO_4$	64.19 +/- 0.42	17.40 +/- 0.13	18.41 +/- 0.55	1.09 +/- 0.01

XPS analysis was performed on $Bi(OH)CrO_4$ and $BiCrO_4$ samples to confirm the change in the binding energy in Bi and Cr environments (Figure 3.4). A comparison before and after reaction shows a similar intensity ratio for bismuth. The position of Bi 4f peaks located at binding energies of 157.20 eV and 162.52 eV for $Bi(OH)CrO_4$ shifted to 156.79 eV and 162.11 eV for $BiCrO_4$. Such low difference in energy suggests no change in the bismuth oxidation state during the cycle but indicated a rearrangement of the oxygen atoms around the trivalent Bi cation.[285] Chromium and oxygen instead showed a significant variation of the binding energy. A difference of 2.98 eV binding energy for chromium (from 577.20 eV to 574.22 eV) suggests a variation in the oxidation state from +6 to +5.

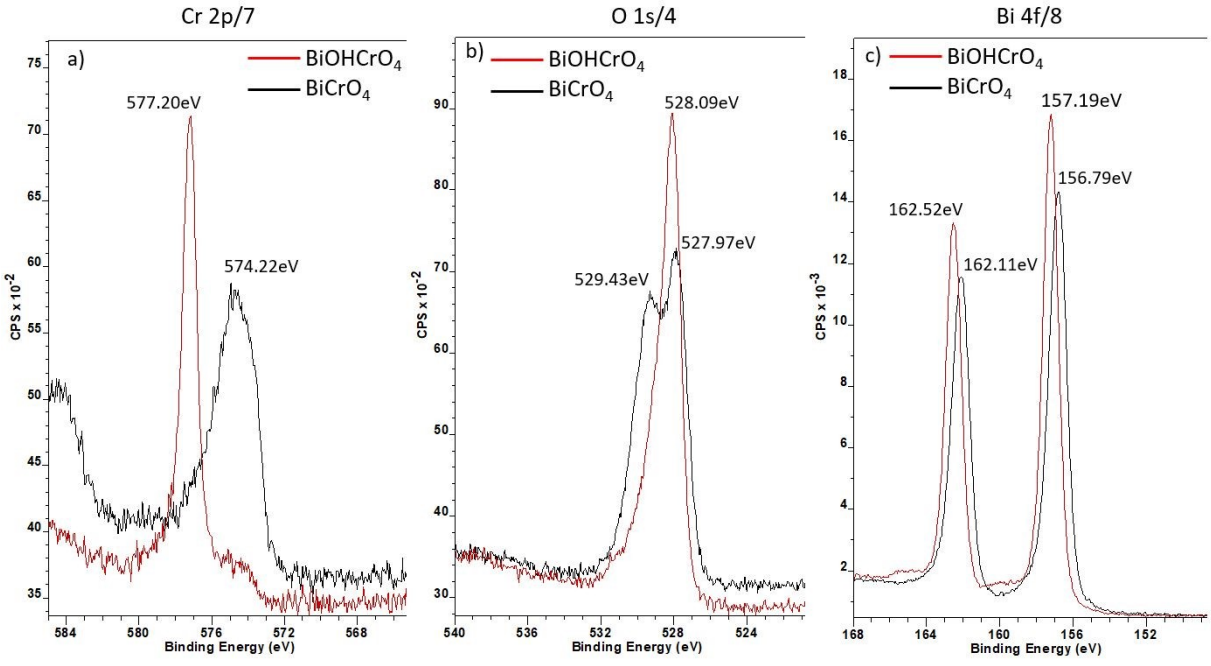

Figure 3.4. XPS analysis of $Bi(OH)CrO_4$ and $BiCrO_4$ involved in the cycle. a) Cr 2p/7, b) O 1s/4 and c) Bi 4f/8

In the case of oxygen, the band at 528.09 eV splits into 527.97 eV and 529.43 eV. Oxygen binding at 528.09 eV suggests bonding to Bi^{3+} and the binding energy at 529.43 eV suggests the oxygen bound to the chromium(V) species. Unfortunately, several attempts to obtain a single crystal of $BiCrO_4$ suitable for X-ray were unsuccessful.

The formation of the new $BiCrO_4$ compound and the analysis of the products indicate that Cr(VI) of $Bi(OH)CrO_4$ is (unsurprisingly) oxidizing formic acid to CO_2 at temperatures above 200°C. In turn, the so-formed Cr(V) species acts as a reducing agent (surprisingly) for a second molecule of formic acid. The water necessary for the reduction to formaldehyde is in fact present *in situ* as a result of the previous oxidation. As a consequence, $Bi(OH)CrO_4$ is being regenerated for another cycle of reaction with formic acid in an overall disproportionation to formaldehyde, CO_2 and water (Scheme 3.4). This transformation is unprecedented for $Bi(OH)CrO_4$ and was previously reported only for TiO_2 at 600K[286] and by our group using Bi_2WO_6.[181]

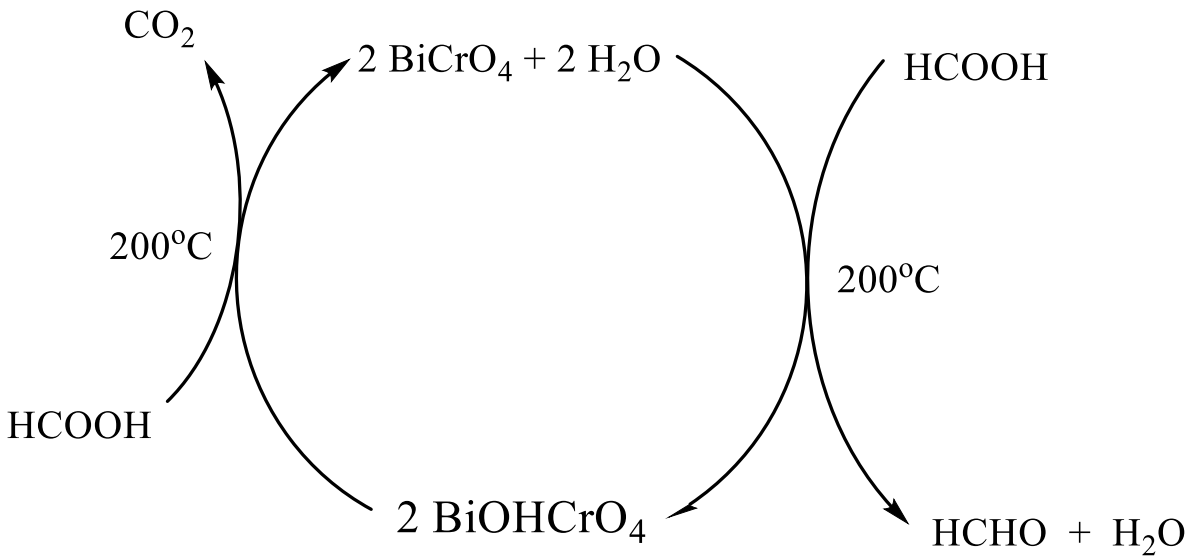

Scheme 3.4. Two-step reaction for the formic acid disproportionation

TGA of the orthorhombic and monoclinic precursor as well as the TGA of the post reaction catalyst are shown in Figure 3.5. Both forms display an initial thermal decomposition between 200°C and 400°C. At a T of about 350°C, the orthorhombic form loses both oxygen and water while the monoclinic only water. This remarkable difference of behavior between the two forms is probably the basis of the negligible reactivity of the orthorhombic form towards formic acid disproportionation. By further increasing the temperature to 600°C, bismuth is reduced to its metallic form and chromium to some ill-defined paramagnetic solid. The two processes are accompanied by further oxygen release for both monoclinic and orthorhombic forms.

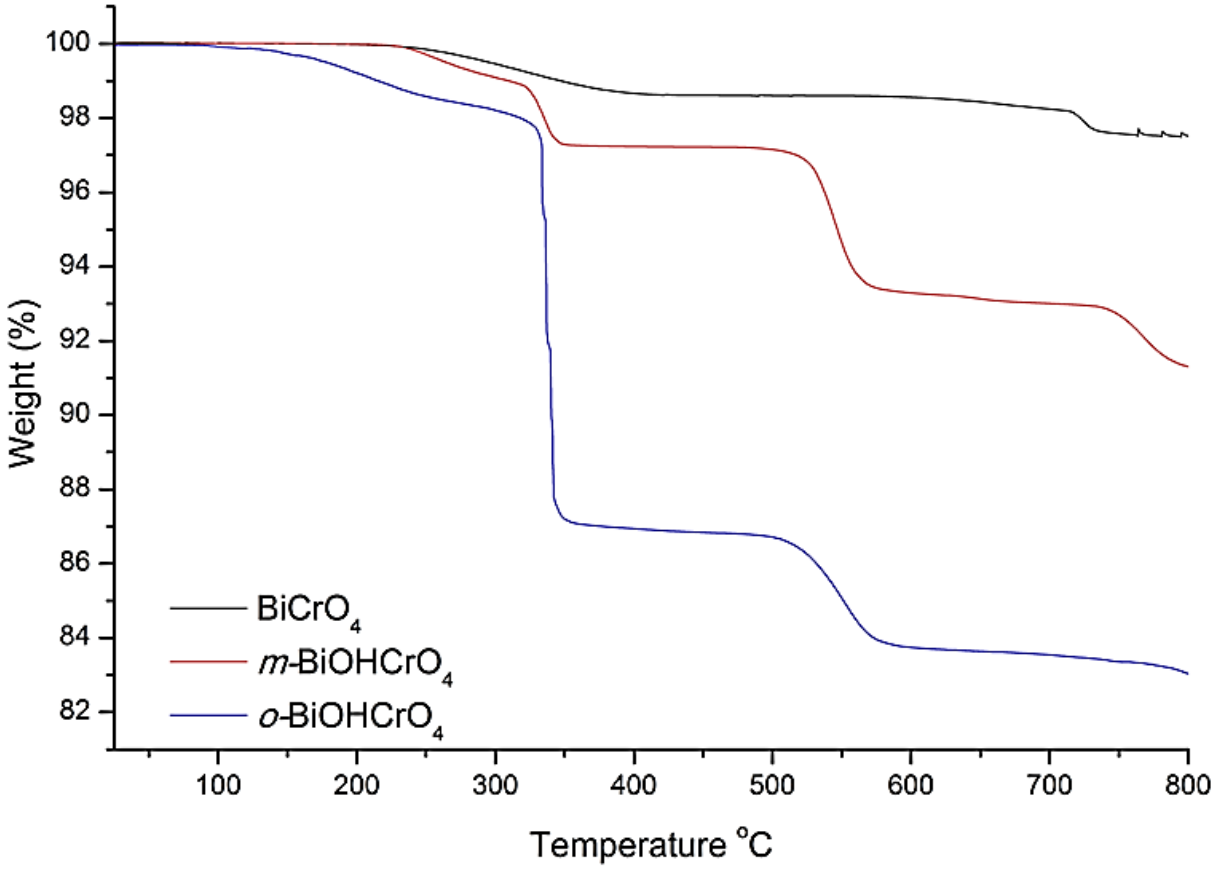

Figure 3.5. TGA of *o*-Bi(OH)CrO_4, *m*-Bi(OH)CrO_4 and post reaction solid, $BiCrO_4$.

The monoclinic form of $Bi(OH)CrO_4$ is clearly more resilient to thermal decomposition. The water release affords a new diamagnetic solid formulated as $(BiO)_2Cr_2O_7$ on the basis of the mass loss measured with TGA. This behavior has a close similarity to that of lanthanide chromate oxides.[287,288] Around 600°C, only oxygen was evolved and the resultant paramagnetic solid was determined to be a mixture of metallic Bi and Cr oxides. The TGA of $BiCrO_4$ instead showed a remarkable robustness of this material, showing little decomposition with the solid losing less than 2% in mass at temperatures up to 800°C. As expected, only oxygen was released from the decomposition of $BiCrO_4$.

3.3.2. Hydrogen evolution from pFA

To maximize the evolution of hydrogen gas from formic acid and complete the transformation to CO_2, a catalytic system for a rapid dehydrogenation of formaldehyde was needed. This system should not produce CO, but could reform formic acid ready for another cycle of disproportionation, ultimately producing only CO_2 and completing the release of hydrogen. Even though this cannot be used for water splitting purposes, it would provide a new way to use formic hydrogen as a hydrogen storage medium.

We have previously demonstrated that $Na_4Fe(CN)_6.10H_2O$ is a highly performing photocatalyst for formaldehyde dehydrogenation. Problems however arise about the longevity of this catalyst. Since we previously suggested that the M-OH moiety is ultimately responsible for catalyzing the hydrogen evolution from formaldehyde,[181] we have now analyzed the behavior of a large series of transition metal salts (M = Ir, Ru, Cu, Ag, Ni, Ti, Fe, Os, Rh, Pd) in basic solutions of formaldehyde and measured the rate of dehydrogenation. The most rapid and efficient hydrogen evolution was observed with $IrCl_3$. The reaction in turn produces the formate anion through a very selective reaction, since no traces of other products could be detected. Figure 3.6 shows that hydrogen evolution occurs rapidly in the first 2 hours. After this time, the concentration of formaldehyde is decreased not only for the natural

consumption due to the dehydrogenation but also because of the Cannizzaro aldehyde disproportionation. After 350 hours, no formaldehyde was detected in solution and no further hydrogen evolution was observed. To maximize the production of hydrogen, additional amounts of formaldehyde and base could be added at regular intervals to keep the reaction rate as high as during the first hour.

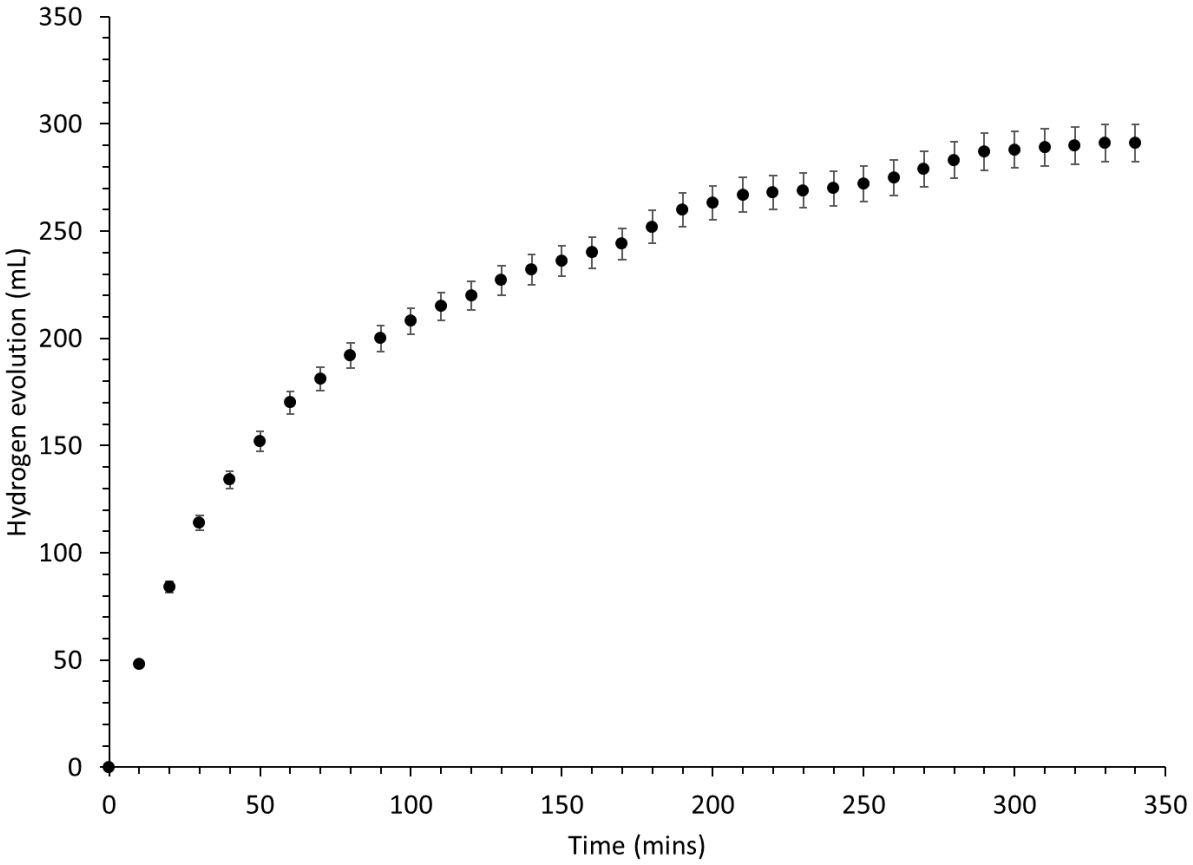

Figure 3.6. Hydrogen evolution from a mixture of pFA (67 mmoles), NaOH (250 mmoles), water (100 mL) and $IrCl_3$ (330 μmoles) at room temperature.

In an attempt to reduce the impact of the parasitic Cannizzaro reaction in decreasing hydrogen yield, the reaction was repeated over multiple days at both room temperature and 0°C (Figure 3.7). Lower temperatures increase the production of hydrogen due to the slowing of the parasitic Cannizzaro

reaction. The rate in reduction of this reaction is larger than the reduction in the hydrogen evolution reaction, giving a net increase in productivity.

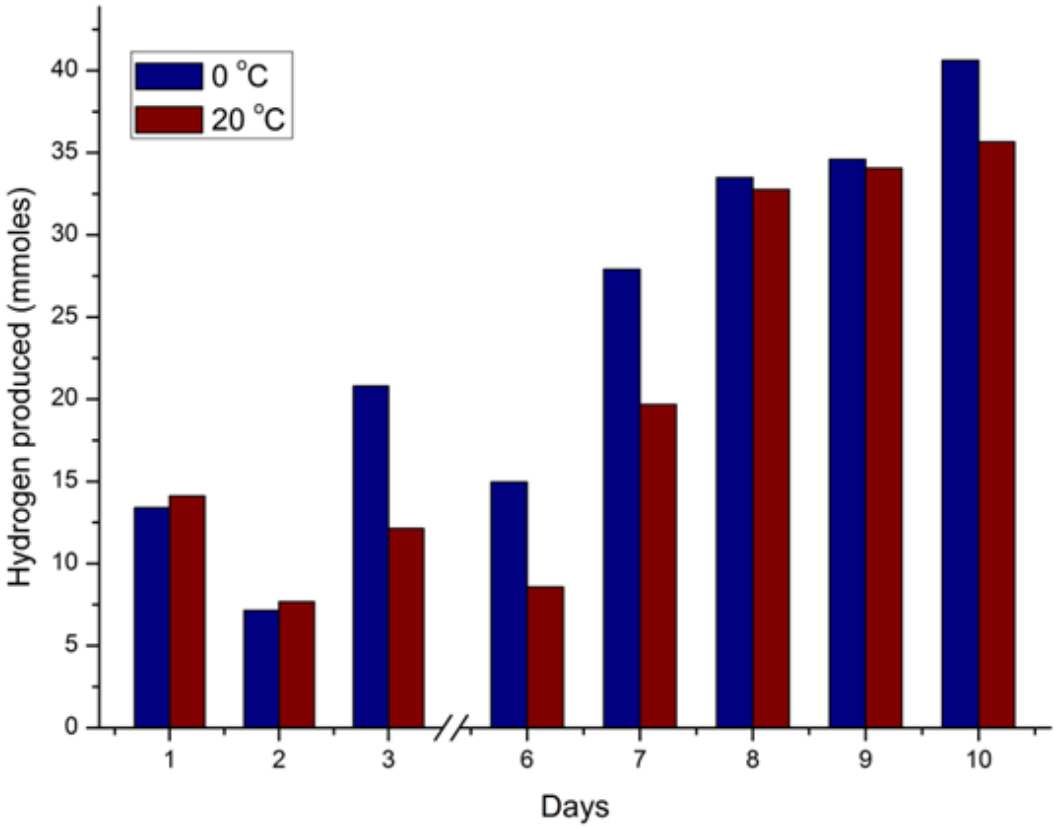

Figure 3.7. Daily hydrogen evolution from a mixture of pFA (67 mmoles), NaOH (250 mmoles initial, followed by 75 mmoles daily), water (100 mL) and $IrCl_3$ (330 μmoles) at room temperature and 0°C.

With this system, high daily yields can be obtained up to 61% (Table 3.3) with an overall productivity yield of 25%. However, even with the high 61% yield, 39% of the formaldehyde in this reaction mixture is being disproportionated into methanol and formate, of which methanol is lost from the cycle (the formate can be recycled back into formaldehyde). Therefore, to increase the viability of this reaction the Cannizzaro reaction should be minimized. This could possibly be achieved through the use of

additives, using different bases, using a mixture of solvents or decreasing the reaction temperature further.

Table 3.3. Hydrogen evolution (mmoles) and yield (%) for the dehydrogenation of formaldehyde by $IrCl_3$. Daily addition of pFA (67 mmoles), NaOH (250 mmoles initial, followed by 75 mmoles daily), water (100 mL) and $IrCl_3$ (330 μmoles) at room temperature and 0°C.

	Day									
Temp (°C)	1	2	3	4	5	6	7	8	9	10
0	13.4 (20%)	7.1 (11%)	20.8 (31%)	15.0 (22%)	27.9 (42%)	33.5 (50%)	34.6 (52%)	40.6 (61%)	13.8 (21%)	19.2 (29%)
20	14.1 (21%)	7.7 (12%)	12.1 (18%)	8.6 (12%)	19.7 (30%)	32.8 (49%)	34.1 (51%)	35.7 (54%)	26.6 (40%)	32.6 (49%)

Having found two separate catalytic system for reduction of formic acid to formaldehyde and for dehydrogenation of formaldehyde, we have attempted to combine them in one overall tandem catalytic system (Scheme 3.5). In the first stage, an experiment was run using the best conditions for formaldehyde production (Table 3.1, entry 4). After collecting 643.1 μmol of formaldehyde in water over 12 h, that solution was basified to pH = 13.0 using sodium hydroxide. After addition of $IrCl_3$ (100 mg, 330 μmol) and stirring for 24h the hydrogen produced was analyzed by CG-TCD and gave 159.12 μmol of H_2 for a yield of 25 %. This confirms that the catalytic decomposition of formic acid into hydrogen and carbon dioxide in a two-step process, releasing carbon dioxide in one step and hydrogen in a second step, is indeed possible.

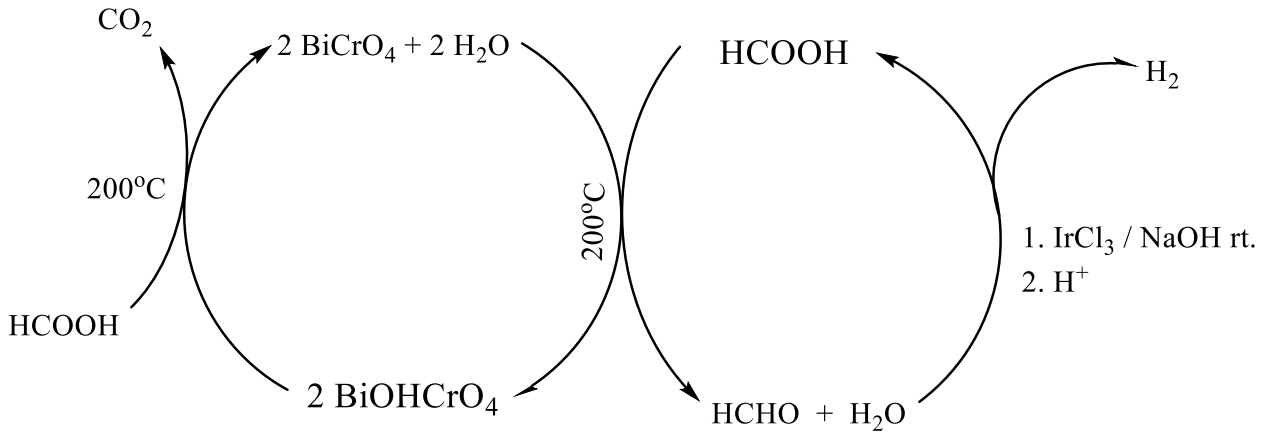

Scheme 3.5. Overall proposed tandem catalysis of disproportionation of formic acid into formaldehyde and carbon dioxide.

3.4. Conclusions

Formaldehyde was produced from formic acid and subsequent formaldehyde dehydrogenation with a *m*-$BiOHCrO_4$ and $M^{n+}Cl_n$ (M = Ir, Ru) catalysts respectively. This is the first example of a two-step process for the decomposition of formic acid, resulting in carbon dioxide emission in one step and hydrogen evolution in a second step. We have presented a novel $BiCrO_4$ material capable of disproportionating formic acid into formaldehyde, carbon dioxide and water. Single crystal X-ray analysis was obtained for the *m*-$BiOHCrO_4$ and *o*-$BiOHCrO_4$ precursors for the first time. A SiO_2 support was used as a dispersing agent for this material which shows higher activity.

To dehydrogenate formaldehyde, we searched for a catalyst capable of transforming formaldehyde back to formic acid, ready for another cycle of disproportionation. Iridium chloride in basic conditions gave good dehydrogenation rates which remained active after 10 days of reaction. This catalyst has a higher rate and resilience than has previously been published for this reaction. Overall this tandem catalytic system provided an efficient catalytic dehydrogenation of formic acid to CO_2.

3.5. Experimental Part

Data for single crystal X-ray structure determination were obtained with a Bruker diffractometer equipped with a 1K Smart CCD area detector. Powder XRD diffractograms were obtained on a Rigaku Ultima IV diffractometer set to 2 2θ°/min from 10-70 2θ°. An XRF diffractometer (Rigaku Supermini200) was used on sample holders of 40mm diameter and 3mm thick, with the powder pressed in an internal 12mm diameter and 2mm thick inner chamber, determination of the elements was obtained against a standard calibration curve by using a mixture of metal oxides of interest. UV-Vis analysis was obtained on a Specmate UV-1100 spectrometer. Infrared spectra were obtained on a Nicolet 6700 FTIR with a diamond ATR between 650-4000 cm^{-1}, at 128 scans with a resolution of 4 cm^{-1}. For the Elemental Analysis, the capsules were loaded with standards into an Isotope Cube elemental analyser made by "elemental", Germany. Samples are flash combusted with oxygen at about 1200°C with a helium carrier. $Bi(NO_3)_3.5H_2O$ 99.5%, CrO_3 99.99% and $IrCl_3.H_2O$ were purchased from Strem Chemicals, HCOOH 99% was purchased from Sigma Aldrich. Acetamide was purchased from Fluka. Citric acid was purchased from Fisher Scientific. Acetic anhydride was purchased from VWR. All other chemicals were used without further purification. If not specifically mentioned, all reactions were carried out in distilled water without degassing or other modifications.

In a homemade tube furnace, $Bi(OH)CrO_4$ was placed (0.35 g, 1 mmol) in a 1 cm ID quartz (1.1 cm OD) tube of 40 cm length. The tube furnace was heated using heating tape around a stainless-steel pipe with a welded thermocouple and a PID controller. $Bi(OH)CrO_4$ (0.35g, 1.0 mmol) was used by grinding with SiO_2 (3.00 g, 49.9 mmol) and placing inside the tube reactor as described above. Argon was used as carrier gas. The carrier gas was passed over formic acid before entering the tube furnace, to allow the formic acid vapor to flow through the system. The products were collected by bubbling the gas outlet through water to collect the liquid products, and the gas was collected using an up-turned

measuring cylinder. Every 12 h, liquid and gas samples were taken and analyzed. The experiment was performed 3 times and the average taken.

In the dehydrogenation of formaldehyde studies, paraformaldehyde (67 mmoles) was placed in a 150 mL round bottomed flask. To this, water (100 mL) was added and allowed to stir. After 5 minutes, sodium hydroxide (250 mmoles) and the appropriate catalyst (330 μmoles) were added. The gas-based products were collected in an up-turned measuring cylinder, and liquid samples were taken from the round bottomed flask at regular intervals.

H_2, CO_2 and CO gas identification and detection were carried out with an Agilent 7820A GC equipped with a TCD, using an Agilent GS-CarbonPlot column (for CO_2) or Agilent HP-Molesieve column (for all other gasses).

Formaldehyde concentrations for dilute samples were determined through a colorimetric reaction with acetyl acetone. To a solution of ammonium acetate (15.4 g) in water (50 mL), acetyl acetone (0.2 mL) and glacial acetic acid (0.3 mL) were added whilst stirring. This was further diluted with water (49.5 mL) and stored in the fridge for up to 3 days. To determine the formaldehyde concentration, 1.5 mL of the sample were mixed with 1.5 mL of the acetyl acetone solution and heated to 60^{o}C for 10 minutes. After cooling for 10 minutes, the absorbance of the solution was measured at 412 nm and compared to a calibration curve.

3.5.1. Preparation of monoclinic-$Bi(OH)CrO_4$ (1). $Bi(NO_3)_3.5H_2O$ (6.33 g, 13.0 mmol) was suspended in 100 mL of water and CrO_3 (1.30 g, 13.0 mmol) was dissolved in 50 mL of water. The chromium(VI) oxide solution was added drop wise into the bismuth(III) nitrate suspension in an ultrasonic bath. Once the solutions were combined, an insoluble orange precipitate formed. The system was refluxed for 2 h, and the resultant orange solid was separated by filtration and washed with 25 mL of cold water three

times and dried for 24h at 100°C. Powder XRD confirmed the pure monoclinic species (JCPDS 16-0681). Single yellow crystals suitable for X-ray analysis were obtained from a saturated solution of $Bi(OH)CrO_4$. The average yield of the reaction was (4.27 g, 12.5mmol, 96.2%). E.A. found (Calcd), Bi 58.32(61.11), Cr 15.13(15.20), H 0.26 (0.29). FTIR (v:cm^{-1}), (3352,b) –OH. The crystals were analyzed by single crystal X-ray and TGA.

3.5.2. Preparation of orthorhombic-$Bi(OH)CrO_4$ (2). To obtain the orthorhombic species, the same solution prepared for the mono- species was reacted under hydrothermal conditions at 180°C for 6 days. The orthorhombic crystal phase of Bi(OH)CrO4, indexed in the JCPDS cards (16-0592) confirm the presence of the complex. To obtain a single crystal, the system was allowed to cool down from 180oC to room temperature over 2 days. The average yield of the reaction was (0.86 g, 2.51mmol, 19.3%). E.A. found (Calcd), H 0.30 (0.29). FTIR (v:cm-1), (3382, b) –OH. The crystals were analyzed by single X-ray and TGA.

The work has been published in part in: **Camilo J. Viasus,** Nicholas P. Alderman, Sebastiano Licciulli, Ilia Korobkov and Sandro Gambarotta, *Chem*. *Eur. J.,* **2017**, 23, 17269-17278.

Chapter 4. Reactivity of carbon dioxide with vanadium aryloxo compounds.

CJV: All work was done by me and all experimental part was also carried out by me. Dr. Gabidullin and Dr. Korobkov carried out the single crystal X-ray analysis. Dr. Alderman helped with the paper editing. Dr. Licciulli assisted the first preliminary steps of vanadium complexes synthesis

4.1. Preamble

In chapter 2, we have shown that *m*-$BiVO_4$ can perform reverse combustion affording methanol from carbon dioxide and water under visible light irradiation. Important questions remain about the detailed mechanism of reduction, namely how electrons are delivered to carbon dioxide. Although our work has highlighted discrepancies about the integrity and stability of the photo-semiconductor we have shown that vanadium(III-IV) species might be generated as possible intermediates. These oxidation states might be primarily responsible for the reduction of CO_2.

In order to further support this hypothesis, we embarked on a modelling study by preparing molecular vanadium complexes mimicking as closely as possible the environment of vanadium in m-$BiVO_4$. Characteristics such as coordination geometry, coordinating atoms and oxidation state of the metal center were of course central to the validity of the models to be built. Given the extended structure of *m*-$BiVO_4$ oxygen-based ligand systems with established ability to give bridging interactions such as mixed alkoxide/oxo derivatives were the natural choice. Aryloxides were particularly handy due to stability, resiliency and their convenient solubility properties. The choice of vanadium aryloxides was also advised by the lower tendency of the V-O bond to perform migratory insertion reactions and in turn providing better substrates for studying the extent of electron transfer from the metal to CO_2. In addition, the aryloxides ligands are readily available with an ample choice of molecular frameworks, thus enabling the fine tuning of steric environment.

We have hypothesized that reduced vanadium centers are being generated during the photo-irradiation of *m*-$BiVO_4$. The extent of electron transfer from the metal to CO_2 was the main issue to be clarified along with how this might determine the type of reactivity.

We have therefore prepared and characterized selected vanadium aryloxide complexes and studied their reactivity with CO_2, obtaining both two- and one-electron transfer depending on ligand selection which resulted in a remarkable variety of reactivity patterns.

In this chapter, we have studied how carbon dioxide can interact with vanadium aryloxide compounds and how two different oxidation states for vanadium can generate different reactivity patterns. DFT calculations were performed to analyze the viability of several vanadium compounds as well as possible nature of intermediate species. Electronic and structural parameters were also evaluated and analyzed.

4.2. Introduction

A wide variety of molecular compounds using early transition metals in different oxidation states and ligand systems have been published in the literature where carbon dioxide reduction has been the main target.[289] Because vanadium is an early transition metal, it presents high oxo-philicity as one of its main characteristics. Nevertheless, it has been examined in less detail than other metals like titanium. Several applications as polymerization,[290,291] epoxidation,[292,293] sequestration/activation[294] among others[227,295] shows that vanadium compounds may be capable of intriguing and surprising behavior.

The high thermodynamic stability of CO_2 makes any catalytic transformation and activation particularly challenging. The main *foci* on this chemistry remain for its reduction,[77,78,302–307,157,166,296–301] incorporation,[141,301,316–320,308–315] sequestration-storage[321,322,331,323–330] and recycling[332–337] with the number of electrons transferred to the CO_2 carbon atom (either one or two) being the factor determining the type of reactivity.[81,92,344–349,112,164,338–343] Therefore, being capable of controlling the extent of electron transfer is central to drive the reactivity towards specific transformations. Due to this, less energy demanding molecules such CS_2[350] and COS[351] have been studied as a starting point to understand the coordination behavior using vanadocene. Unfortunately, vanadocene does not reduce carbon dioxide on its own, notwithstanding its rich electronic configuration.

A two-electron transfer to carbon dioxide causes three sorts of possible events. The first is a simple deoxygenation during which an oxygen atom is extracted by a low/mid-valent metal to afford a metal oxide and CO (Scheme 4.1).[342,352–354] Even though this reaction is potentially useful, the high stability of metal oxides formed as by-products makes their further reduction to the original state energy-intensive, and therefore likely unsuitable for making the transformation catalytic.[355,356]

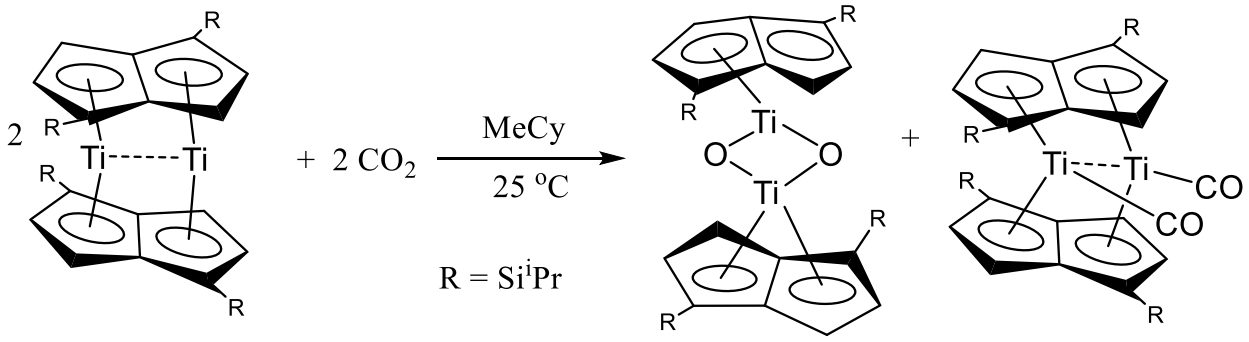

Scheme 4.1. Deoxygenation of carbon dioxide to form metal oxide and carbon monoxide using Ti(II). Reproduced from ref #[352] with permission by The Royal Society of Chemistry.

The second possibility is a disproportionation to CO and carbonate dianion (Scheme 4.2).[75,76,342,357–359] Again, the formation to a metal carbonate suffers from the same limitations as the oxo species. Finally, reversible coordination to electron-rich elements, MOF's and metal-free systems is also a possibility.[313,360–362]

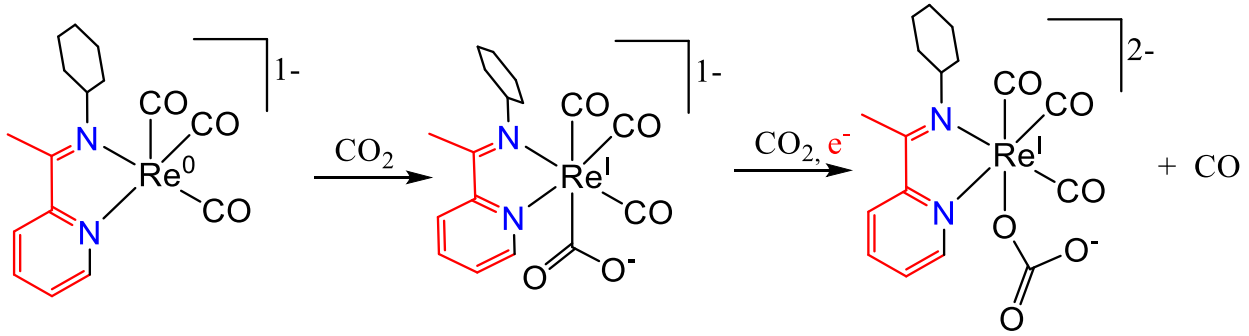

Scheme 4.2. Disproportionation of carbon dioxide into carbonate and carbon monoxide. Reproduced from ref #[359] with permission by The American Chemical Society.

Although this phenomenon is conceptually very appealing, it might preclude any realistic possibility for further incorporation of CO_2 into substrates (Scheme 4.3). Any given reagent expected to attack the coordinated CO_2 (either electro- or nucleophile) may simply revert the coordination, likely to be labile, and attack the metal center instead.[317,363] Ligand migratory insertion, as in the case of organometallic

derivatives, may generate organic functions (carboxylates, carbonates, carbamates, etc)[91,364,365] and not necessarily through stoichiometric transformations.[77,140,366,367]

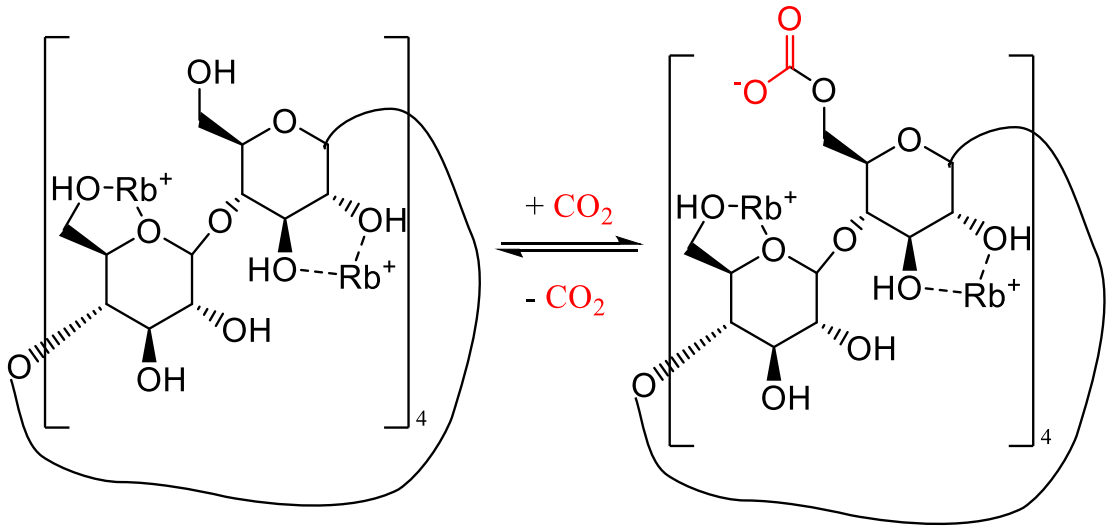

Scheme 4.3. Reversible binding of carbon dioxide in MOF's. Reproduced from ref #[362] with permission by The American Chemical Society.

When the electron transfer can be limited to only one electron, the reaction initially transforms the coordinated $CO_2^{(\bullet-)}$ into a radical anion, which, by mainly being carbon centered, eventually may dimerize to form the oxalate dianion.[367] However, the utilization of complexes acting as a one electron donor is a necessary but non-sufficient condition since two electrons, leading to a deoxygenation or disproportionation, may also be obtained via cooperative attack of two metals on the same CO_2 unit.[145] Thus, one-electron reducing complexes need to provide a sufficiently long lifetime to the intermediate CO_2 radical-anion to enable head to head coupling and consequent irreversible C-C bond formation.[368] It is conceivable to expect that for this purpose, the type of initial coordination of CO_2 (end-on, side-on, mono- or bi-nucleating, etc.) is of pivotal importance.

Low-valent, early transition metals are normally highly oxophilic and therefore unlikely to embark in overall one electron transfers to CO_2. Even in the case of purely one electron reductants, the enhanced

stability of the M-O bond is the drive for subjecting CO_2 to a two-electron cooperative attack by two metals.[369–371] However, this might be moderated or perhaps prevented by tuning the redox potential of the transition metal, via the judicious choice of the ligand field, and by increasing the steric bulk around the metal center.

4.3. Results and discussions

4.3.1. Evidence for reversible reactivity/interaction of vanadium(IV) aryloxide with CO_2.

The initial task of this work was to verify the idea that a one-electron reducing agent in a relatively high oxidation state, such as tetravalent vanadium, could have the ability to react with CO_2. To prevent dynamics leading to unwanted transformations such as disproportionation to carbonates, we have selected aryloxide ligands listed below bearing large steric hindrance (Scheme 4.4).

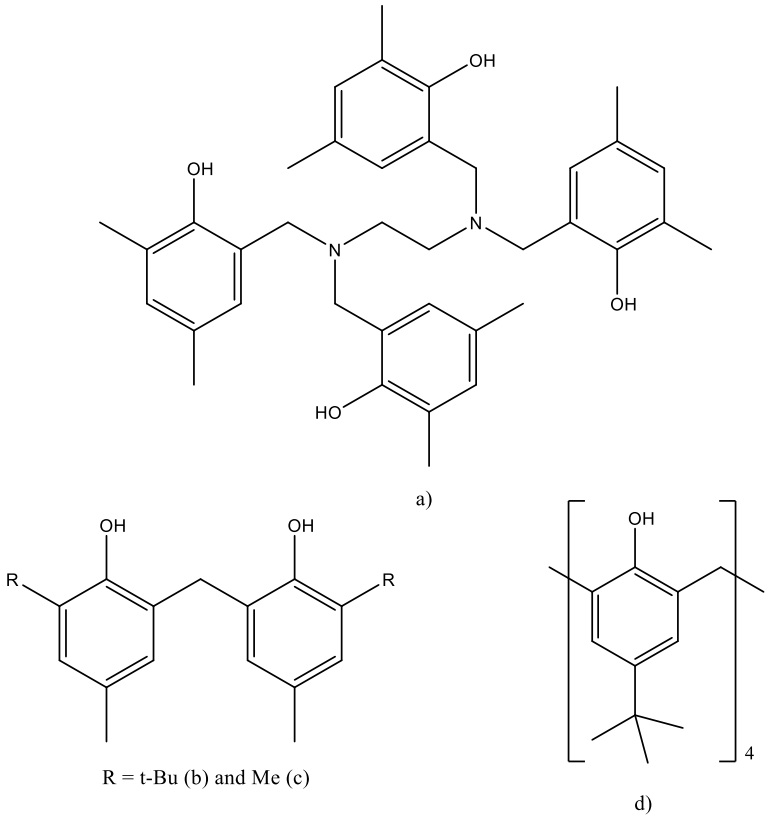

Scheme 4.4. Ligands a,[372] b,[373] c and d used for vanadium(IV) compounds.

Vanadium complexes of the four ligand systems were prepared using standard procedures by reacting the deprotonated form of the ligands with a simple vanadium salt. All compounds were isolated and fully characterized. The structures were authenticated by X-ray analysis (Figure 4.1). The reactivity with carbon dioxide was tested in both THF and toluene. The structure of complex 1 shows the metal center secluded in an octahedral ligand field. The space filling model indicates that the metal center is in fact hardly accessible. Accordingly, compound **1** is a very stable material that, even in air, does not give sign of any apparent decomposition and no reactivity was observed towards carbon dioxide.

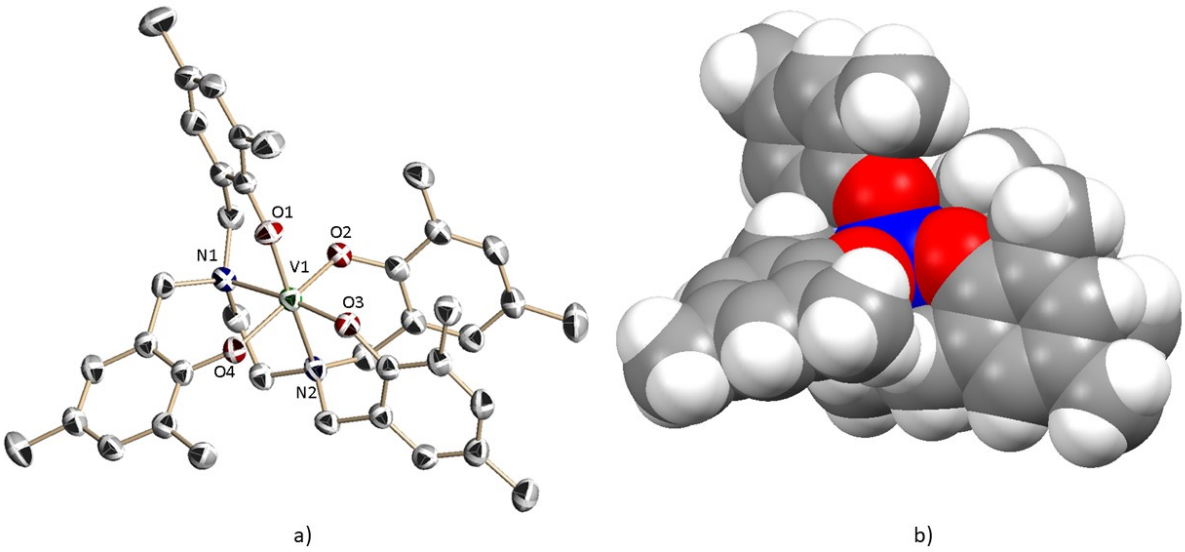

Figure 4.1. a) ORTEP diagram of compound 1 with ellipsoids drawn at 50% of probability level. Hydrogen atoms are omitted for clarity. Selected bond distances [Å] and angles [°] for compound 1: V1-N1 = 2.184, V1-N2 = 2.220, V1-O1 = 1.850, V1-O2 = 1.880, V1-O3 = 1.849, V1-O4 = 1.876, N1-V1-O1 = 89.86, N2-V1-O3 = 89.53, N1-V1-O2 = 84.31, N1-V1-O4 = 84.73, N1-V1-N2 = 83.45, N2-V1-O3 = 89.53, N2-V1-O4 = 88.00, N2-V1-O2 = 81.89, O1-V1-O2 = 90.39, O1-V1-O3 = 98.11, O3-V1-O4 = 92.89 and O2-V1-O3 = 96.88. b) space filling of compound 1, blue = vanadium; grey = carbon; red = oxygen and white = hydrogen.

Modifying the reaction conditions by increasing the temperature up to 70°C in an autoclave with 100 psi of carbon dioxide did not modify the outcome.

The commercially available 2,2'-methylenebis(6-tert-butyl-4-methylphenol) was purchased from Sigma and dried under vacuum at room temperature for 24h prior to use. The corresponding vanadium complex possesses a distorted tetrahedral vanadium(IV) geometry (Figure 4.2). However, the metal center appears to be deeply buried in the organic framework of the ligand system. Therefore, it comes as no surprise that it does not react with carbon dioxide. Only at 120°C and 100 psi CO_2 pressure conditions, compound 2 reacts with carbon dioxide affording carbon monoxide and, possibly, pentavalent vanadium. Any attempt to isolate and characterize the vanadium product failed, but EPR experiments indicated that paramagnetic material was still present in the reaction mixture. ^{51}V NMR

spectra of the solution showed a mixture of vanadium(V) compounds including vanadyl derivatives. Broad chemical shifts at 479.07 and 518.62 ppm are attributable to pentavalent vanadium surrounded by aryloxide ligands in mixture with other vanadium complexes visible at 420.03 and 427.02 ppm.

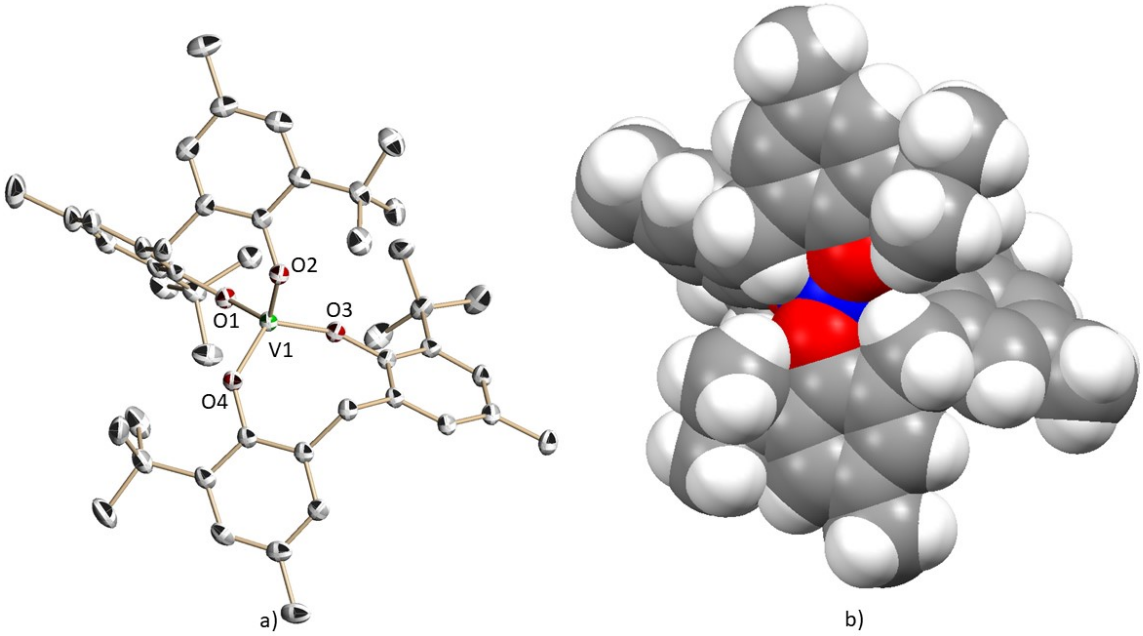

Figure 4.2. a) ORTEP diagram of compound 2 with ellipsoids drawn at 50% probability level. Hydrogen atoms are omitted for simplicity. Selected bond distances [Å] and angles [°] for compound 2: V1-O1 = 1.778, V1-O2 = 1.800, V1-O3 = 1.782, V1-O4 = 1.796, O1-V1-O2 = 119.71, O1-V1-O3 = 101.69, O1-V1-O4 = 108.14, O2-V1-O3 = 107.49 and O3-V1-O4 = 118.65. b) space filling of compound 2, blue = vanadium; grey = carbon; red = oxygen and white = hydrogen.

In a third attempt to find a proper ligand for the vanadium(IV) metal center, and after the observation of how the bulk steric effect may affect the reactivity, a less sterically hindered di-phenol as ligand was prepared (compound **3** - Figure 4.3c). Replacing the t-Bu substituent by -Me group should allow for the vanadium(IV) atom to have better chances to interact with carbon dioxide (Figure 4.3). The dimeric structure of **4** was somehow expected considering that non-oxovanadium(IV) compounds display in general high coordination numbers.[233,374] Analyzing the space filling model of compound **4** in its

dimeric form, it is doubtful that carbon dioxide might find accessibility to the vanadium atom. However, the asymmetric unit presented in Figure 4.3d will have more probability.

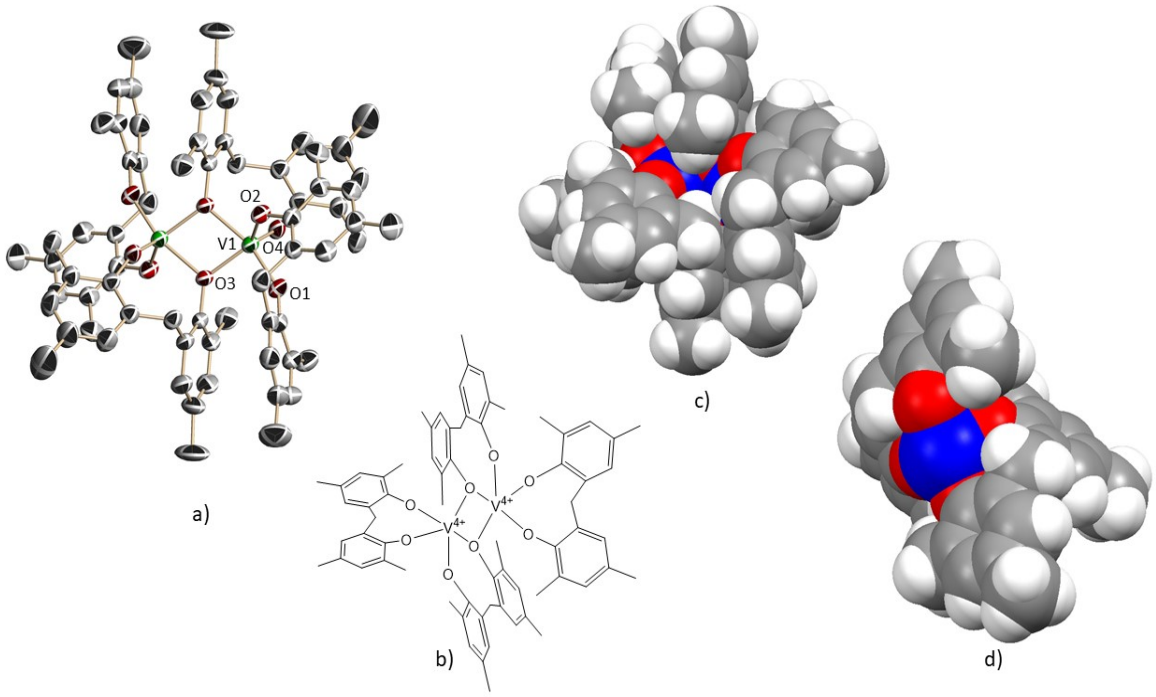

Figure 4.3. a) ORTEP diagram of compound 4 with ellipsoids drawn at 50% probability level. Hydrogen atoms are omitted by clarity. Selected bond distances [Å] and angles [°] for compound 4: V1-O1 = 1.830, V1-O2 = 1.804, V1-O3 = 2.029, V1-O4 = 1.732, O1-V1-O2 = 92.52, O1-V1-O3 = 160.75, O1-V1-O4 = 101.72, O1-V1-O3' = 93.17, O2-V1-O3' = 127.88, O2-V1-O4 = 112.72, O3-V1-O4 = 116.62 and O2-V1-O3 = 86.48. b) Schematic drawing of compound 4 shown for clarity., c) space filling of compound 4 in its dimer form., d) space filling of compound 4 in its monomer form. Blue = vanadium; grey = carbon; red = oxygen and white = hydrogen.

Regrettably, compound **4** doesn't react with carbon dioxide. Same negative outcome was obtained under pressure at high temperature. In all cases presented above for compounds **1**, **2** and **4**, the reaction was monitored by EPR and head space gas analysis by GC-TCD.

Obviously the three complexes analyzed above do not provide the correct steric environment. We have therefore turned our attention to the calixarene tetra-anions to support the vanadium center in a rigid

structure where the metal center could have a better exposure to CO_2. Complex **5**, was prepared, and crystallized (Figure 4.4). Due to an open coordinative vacancy, the solid-state structure presented is dimeric. Similar core structure was published by Floriani *et. al.*[375] and was obtained with the procedure presented for compound **5** at the end of this chapter. A vanadium(IV) dimer was obtained in good agreement with those previously reported.

The structure analysis and the space filling model confirmed a larger exposure of the vanadium(IV) center possibly more available to interact with carbon dioxide. One significant difference of compound **5** compared to compound **4** is the shorter V-O distance in the dimer (V1-O3 = 2.029 Å for compound **4** and V1-O3 = 2.200 Å for compound **5**). The chelate effect of the calixarene ligand is being affected by the additional coordination of one of its oxygen atoms to another vanadium calixarene unit. This suggests that in solution, **5** will have more probability to dissociate into a monomeric unit. Once a dark blue toluene solution of compound **5** was exposed to carbon dioxide, a promising color change to dark green was observed. This reaction was monitored by EPR and UV-vis.

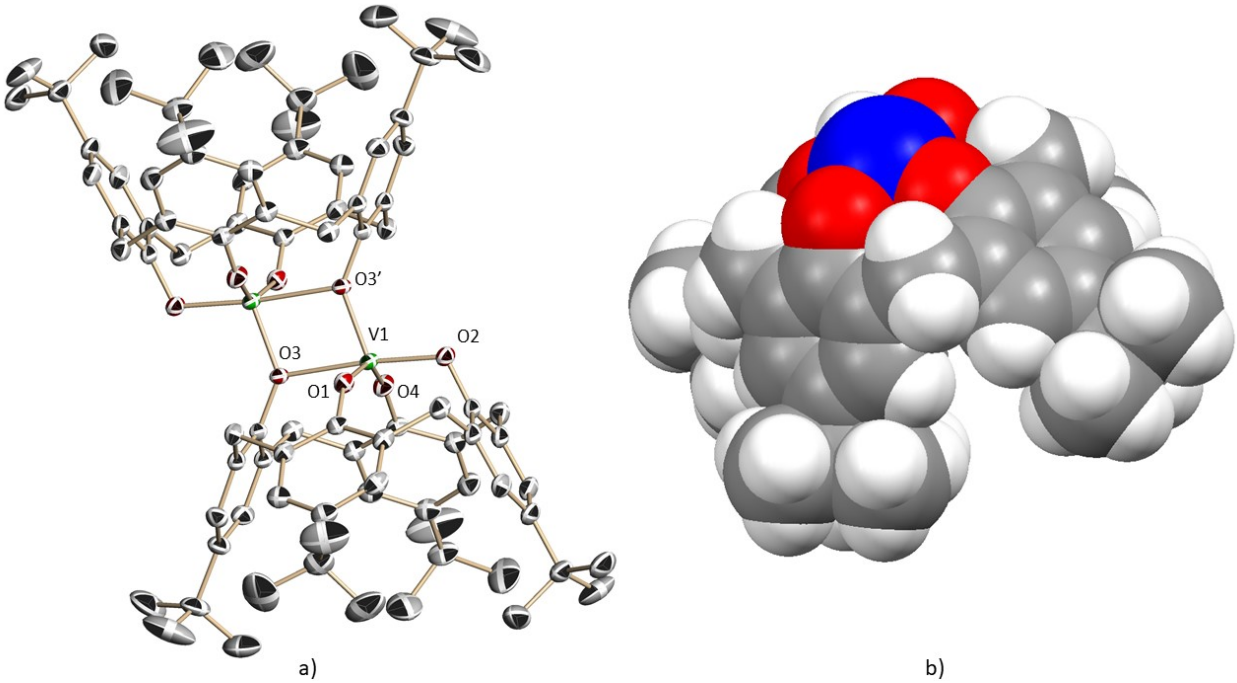

Figure 4.4. ORTEP diagram of compound 5 with ellipsoids drawn at 50% probability level. Hydrogen atoms are omitted by clarity. Selected bond distances [Å] and angles [°] for compound 5: V1-O1 = 1.771, V1-O2 = 1.843, V1-O3 = 2.200, V1-O4 = 1.766, V1-O3' = 1.864, O1-V1-O2 = 95.45, O1-V1-O4 = 144.41, O1-V1-O3 = 83.34, O2-V1-O3 = 174.82, O2-V1-O4 = 95.00 and O3-V1-O4 83.23. b) space filling of compound 5 in its monomer form. Blue = vanadium; grey = carbon; red = oxygen and white = hydrogen.

EPR experiments show a variation in the hyperfine coupling due to the vanadium(IV)-carbon dioxide interaction (Figure 4.5). The variation in the *g* factor before and after carbon dioxide addition is presented in Table 4.1.

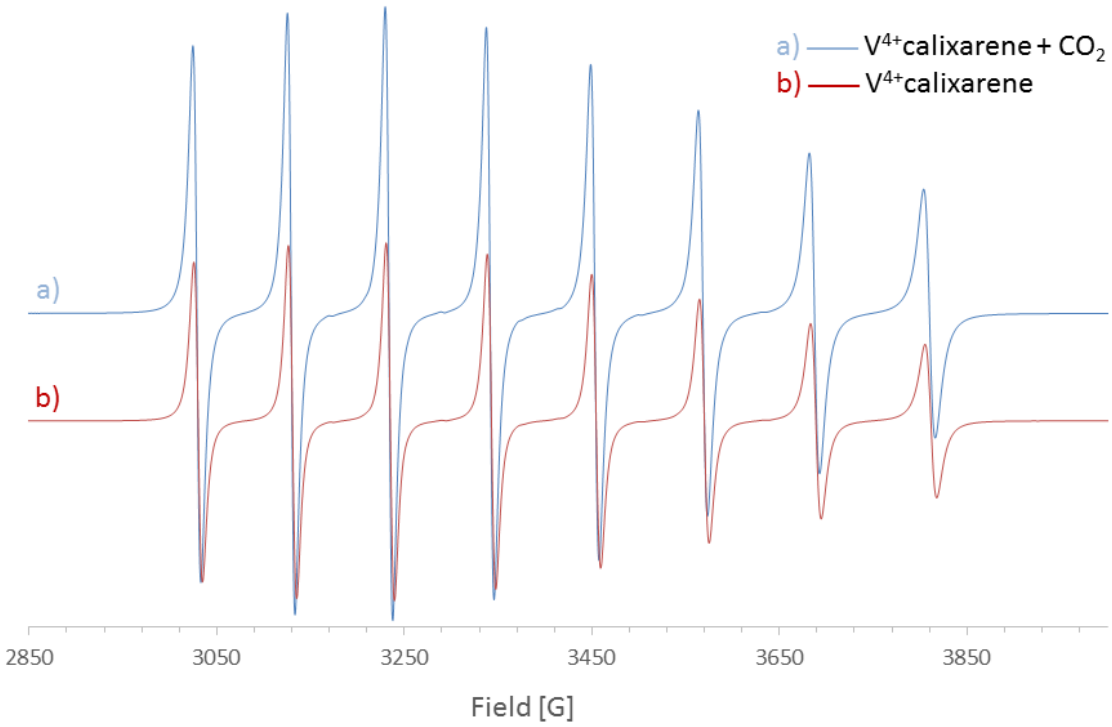

Figure 4.5. EPR spectra of compound 5 before and after carbon dioxide addition.

Table 4.1. g factor determines for compound 5 and its CO_2 interaction.

EPR line (x)	Compound 5		After CO_2 addition	
	g_x factor	Field [G]	g_x factor	Field [G]
1	2.20797	3030.2	2.20565	3028.8
2	2.13678	3130.8	2.13475	3129.4
3	2.09693	3234.8	2.09484	3233.6
4	2.05710	3343.0	2.05516	3341.6
5	2.01766	3454.6	2.01580	3453.2
6	1.97891	3569.8	1.97689	3568.5
7	1.94068	3688.8	1.93847	3687.4
8	1.90303	3811.4	1.90064	3810.0

The head space of the sealed-glass reactor was monitored by GC-TCD and no gases other than CO_2 or N_2 were found during the experiment. After compound **5** had been exposed to CO_2 for 36 hours, the color changed from dark blue to dark green. However, when carbon dioxide was removed from the

system by applying vacuum, the blue color returns. This was a clear indication for the presence of a CO_2 association/dissociation equilibrium. Further attempts to crystallize any product aiming for a compound 5-CO_2 adduct in a carbon dioxide atmosphere did not afford characterizable compounds. EPR experiments did not provide sufficiently clear evidence to characterize the carbon dioxide adduct. A UV-vis spectrum was taken with and without CO_2 (Figure 4.6).

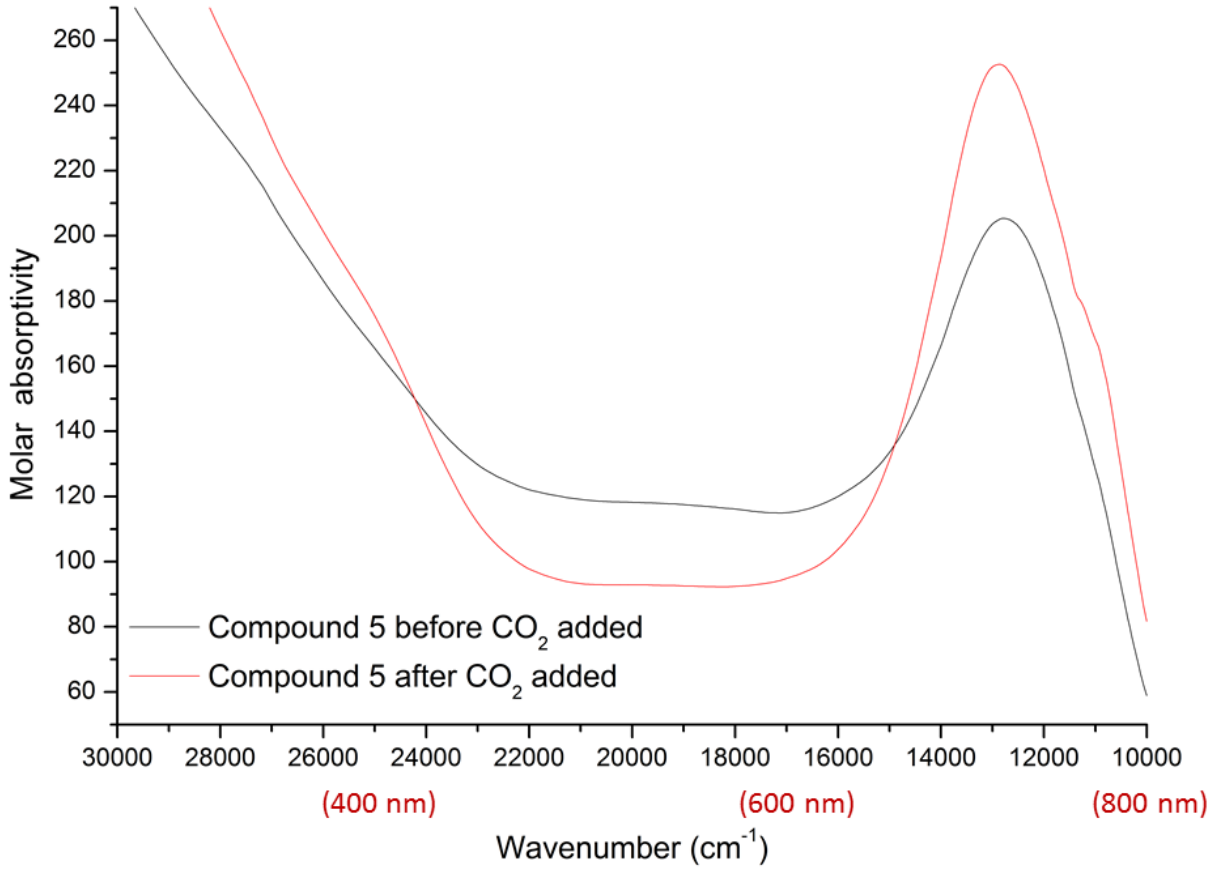

Figure 4.6. UV-Vis spectra of compound 5 before and after carbon dioxide addition.

The slightly hypsochromic shift (blue shift) from 12,789 to 12,854 cm^{-1} for compound 5 observed before and after carbon dioxide exposure might agree with the modification of the molecular symmetry due to carbon dioxide coordination (Figure 4.6).

DFT calculations were performed to analyze this possible interaction between compound **5** and carbon dioxide. They were kept into consideration and the structure reported below was the best stable result. The low reducing power of the metal center prevented electron transfer to carbon dioxide. The resulting interaction shows carbon dioxide being slightly bent because of the only partial electronic transfer from the vanadium metal. Whilst this interaction seems promising, the low reducing power of vanadium(IV) makes this interaction unstable and reversible. In fact, when the system is exposed to vacuum to remove any residual carbon dioxide, the EPR spectrum transforms into that of **5**. This proposed structure presents a shorter distance between an oxygen in carbon dioxide than its dimer form (V1-O3 = 2.200 Å), which lends further credibility to the possibility of the presence of this adduct in solution. As a result, more electronic density located on vanadium may lead to a better chance to bind CO_2.

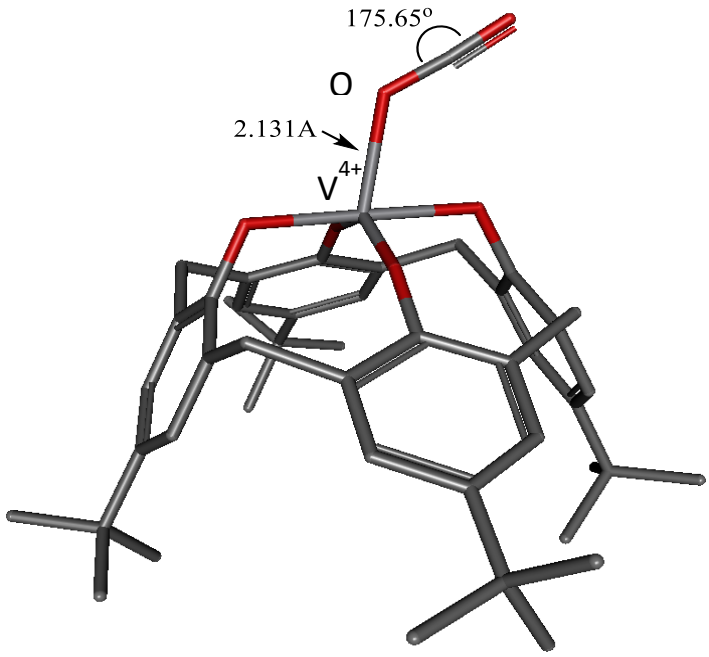

Figure 4.7. Possible interaction between compound 5 and carbon dioxide using DFT calculations in Gaussian 09 package.

At this stage, with the preliminary structures investigated, it's clear that the reduction power of vanadium(IV) aryloxide compounds is not sufficiently strong to transfer electron density to carbon dioxide. There are two different possibilities to explain this behavior. The first could be inherent to the ligand system used which for either steric or electronic reasons simply does not support a sufficiently robust interaction with CO_2. The second could be that the metal oxidation state is not sufficiently reducing. We have therefore considered the employment of lower vanadium oxidation states.

4.3.2. Deoxygenation and carbon dioxide insertion using vanadium(III) aryloxides

The d^2 trivalent state of vanadium was selected as a starting point for this part of the work. It was argued that higher oxidation states would have too weak reducing power and lower oxidation states would have too strong reducing power. It is worth reminding that simple homoleptic V(III) complexes already are sufficiently reducing to attack N_2.[224,376] Thus, homoleptic vanadium complexes both neutral $[(2,4,6\text{-}Me_3C_6H_2O)_3V(THF)_2]$ (**6**) and anionic $\{[(2,4,6\text{-}Me_3C_6H_2O)_2V](\mu\text{-}2,4,6\text{-}Me_3C_6H_2O)_2[Li(THF)_2]\}$ (**7**) and $\{[(2,4,6\text{-}Me_3C_6H_2O)_2V](\mu\text{-}2,4,6\text{-}Me_3C_6H_2O)(\mu\text{-}\eta^6\text{-}2,4,6\text{-}Me_3C_6H_2O)Li]\}_2$ (**8**) have been prepared (Scheme 4.5) for the purpose of reacting with CO_2. Complex **6** was previously reported by Thiele.[377]

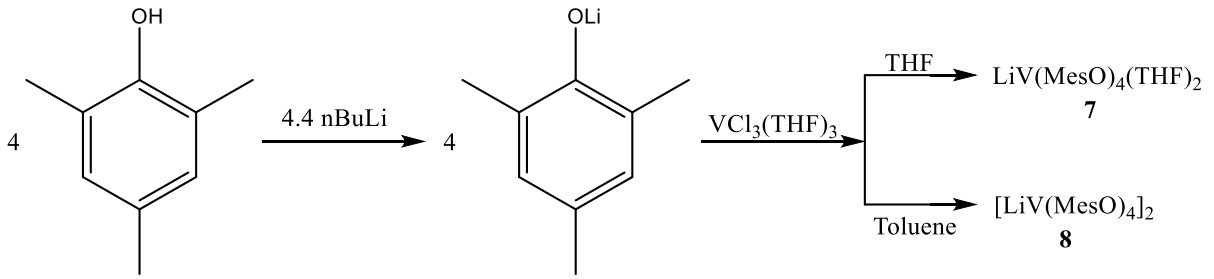

Scheme 4.5. Preparation of compounds **7** and **8**.

Complexes **7** and **8** are instead unknown and therefore we have authenticated their structures by X-ray diffraction methods (Figure 4.8). Exposure of toluene solutions of the above complexes to

anhydrous CO_2 at atmospheric pressure afforded a simple deoxygenation with formation of CO and the corresponding vanadyl derivative $(2,4,6\text{-}Me_3C_6H_2O)_3V(O)$ (**9**). The formation of CO was monitored and quantified by GC-TCD analysis of the gas mixture. The reaction appears to be the result of a much expected two-electron attack of CO_2 by V(III) with consequent extraction of the oxo-atom, release of CO and oxidation of the metal center to the pentavalent state (Scheme 4.6).

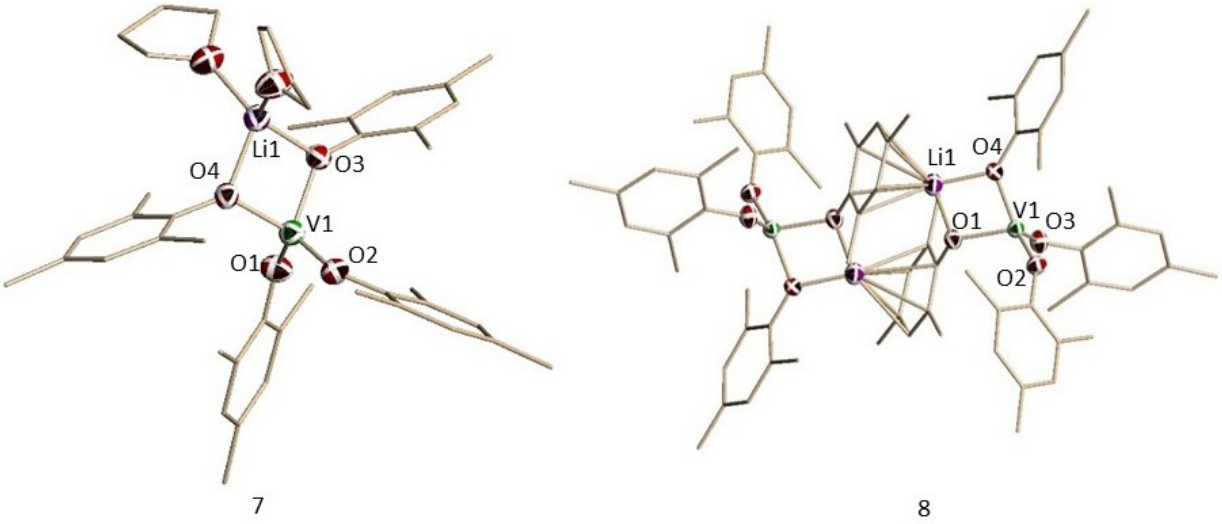

Figure 4.8. Thermal ellipsoids plot of **7** and **8** with ellipsoids drawn at the 50% probability level. Hydrogen atoms were omitted for clarity. Selected bond distances [Å] and angles [°] for compound 7: V1-O1 = 1.832, V1-O2 = 1.845, V1-O3 = 1.923, V1-O4 = 1.926, O1-V1-O2 = 118.32, O1-V1-O3 = 113.29, O1-V1-O4 = 111.44, O2-V1-O3 = 109.51, O2-V1-O4 = 114.87 and O3-V1-O4 84.61. Selected bond distances [Å] and angles [°] for compound 8: V1-O1 = 1.952, V1-O2 = 1.841, V1-O3 = 1.809, V1-O4 = 1.917, O1-V1-O2 = 95.54, O1-V1-O3 = 114.44, O1-V1-O4 = 84.61, O2-V1-O3 = 114.47 and O2-V1-O4 = 126.43.

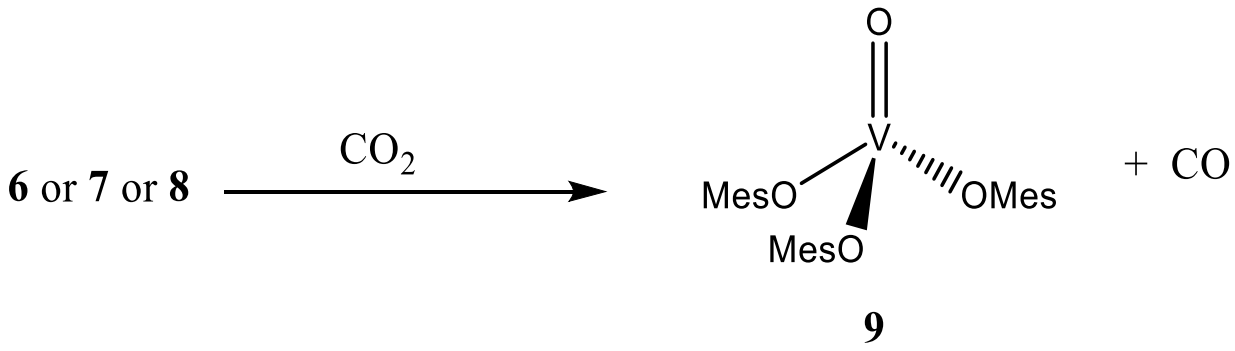

Scheme 4.6. CO_2 reactivity with compounds **6**, **7** and **8**.

Assuming that the reaction proceeds via an intermediate V-CO_2 adduct, DFT calculations have been performed to elucidate the possible structure of this elusive intermediate. Calculations were performed at B3LYP level using TZVP basis set for all atoms with Gaussian 09 package. Berny algorithm was performed to find a transition state using the QST3 method. The possible presence of residual THF in the metal coordination sphere has been evaluated by computing CO_2 adducts with and without THF. Convergence could be obtained only in the case of a THF-free adduct. In this event, the calculation revealed that the optimal geometry adopted by the coordinated CO_2 is a bent end-on mode. It should be reminded that this is a unique bonding mode, observed in the sole case of one trivalent uranium compound.[378] The deviation from linearity appears to be caused by the transfer of electronic density, roughly corresponding to one electron, from the metal to the CO_2 carbon atom (Chart 4.1). The effective valence electron configuration (Natural Electron Configuration) in terms of the Natural Population Analysis (NPA) indicates that in the orbitals of V there is the equivalent of 0.97 electrons which roughly corresponds to the d^1 configuration of V(IV). The electron transferred by vanadium to CO_2 is mostly located on its carbon atom displaying 0.67 electrons in an orbital of mainly p-character. Therefore, this intermediate is formally composed of a tetravalent vanadium and a CO_2 radical anion.

Furthermore, the two electrons (one on vanadium and one on the CO_2 C atom) appear to be decoupled since the frequency analysis presents the triplet state as the higher energy state.

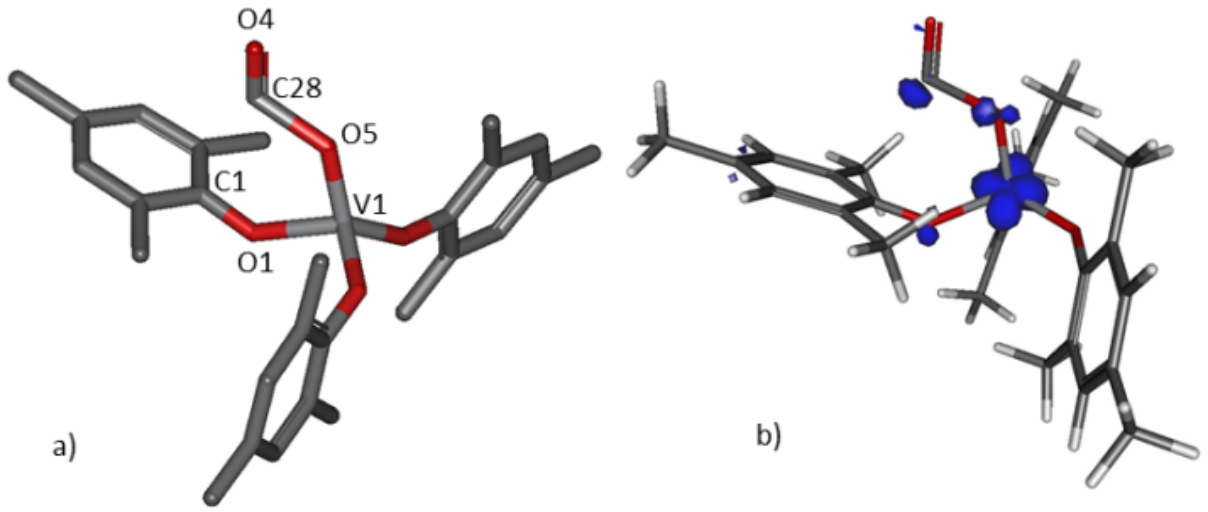

Chart 4.1. a) Carbon dioxide interaction with vanadium(III) tris-(2,4,6-trimethylphenoxide). V1-O5 = 1.720Å, C1-C28 = 2.729Å, V1-O1 = 1.888 Å, C1-O1 = 1.308 Å, V1-O5-C28 = 128.9°, O5-C28-O4 = 115.8° and O1-V1-O5 = 93.8°. b) HOMO-Spin density contours.

The end-on orientation of the coordinated CO_2 molecule in combination with its bending, predicted by the calculations, is somewhat unique. It appears as the transition from the linearity of the observed end-on labile coordination on a sterically encumbered trivalent uranium atom[378] to the well-established side-on coordination on zerovalent Ni complexes.[379] In the present case, the predicted angle in the O=C=O unit is close to a sp^2 configuration [V1-O5-C28 = 128.9°]. The incipient formation of the vanadyl function (V1-O5 = 1.720Å) is accompanied by the expected elongation of the O5—C28 bond (1.729 Å). The residual C-O multiple bond instead undergoes further shortening [C(28)-O(4) = 1.152 Å] implying an increase of the CO bond multiplicity prior to the final release of CO. The peculiar bonding mode of CO_2 indicated by DFT calculations implies, from the formal point of view, that substantial spin density is transferred from the d^2 vanadium with consequent formal oxidation of the metal center.

Accordingly, Mulliken analysis (Table 4.2) shows that the carbon atom gathers a significant spin density (0.260989), even larger than that of the two oxygen atoms (0.027629 and 0.113987 respectively).

Table 4.2. Mulliken charges and spin density for V-CO_2 adduct.

Atom	Mulliken charges	Atomic-atomic spin density
V1	1.331914	1.010518
O1	-0.481092	0.116675
C28	0.153548	0.260989
O4	-0.159974	0.027629
O5	-0.527752	0.113987

Alternative bonding modes of CO_2 to the metal center (structures A-E, Chart 4.2) have been also analyzed by DFT. Calculations evaluated the lowest energy and eventually the most probable transition/ground state for the pathway of carbon dioxide reduction by vanadium(III) homoleptic compound (Chart 4.3).

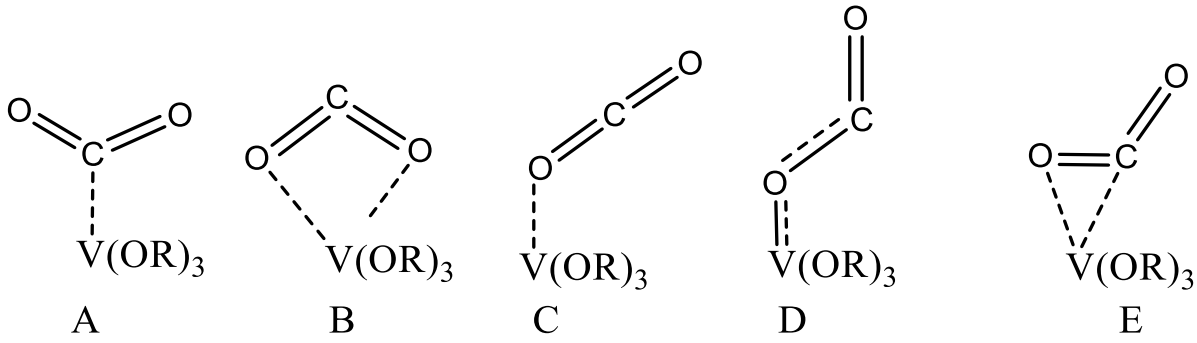

Chart 4.2. Binding modes calculated as possible intermediates during the reduction of carbon dioxide.

It was found that the linearity of CO_2 in the bonding mode C is almost unaffected by the multiplicity (gs4 and gs5, Chart 4.3). As expected, higher multiplicity only results in lower energy. Once the bonding mode A is input, calculations show the structure is energetically unstable, shifting towards the D or E bonding modes. The binding mode B with a multiplicity of 3 also initially leads to C and then eventually to D while attempting to obtain a transition state. With a multiplicity of 1, B remains instead unchanged but with high energy (gs 8 and 9, Chart 4.3). The linear bonding mode C (gs4 and 5, Chart 4.3) is the starting point for reaching the transition state D as the final coordination mode (ts1 and 2, Chart 4.3) prior to product formation. Energetically speaking, the binding mode E (gs6 and 7 with multiplicity of 1 and 3 respectively) is more stable than D. However, not a single imaginary frequency was found implying that no transition state could be reached while using E as a starting point. In this case, the complex with a multiplicity of 3 (ts2) was found higher in energy than 1. This implies that either the electrons in the d^2 configuration on vanadium(III) are being paired because of the CO_2 coordination, or the two electrons are transferred to CO_2 thus generating a diamagnetic species, ts1.

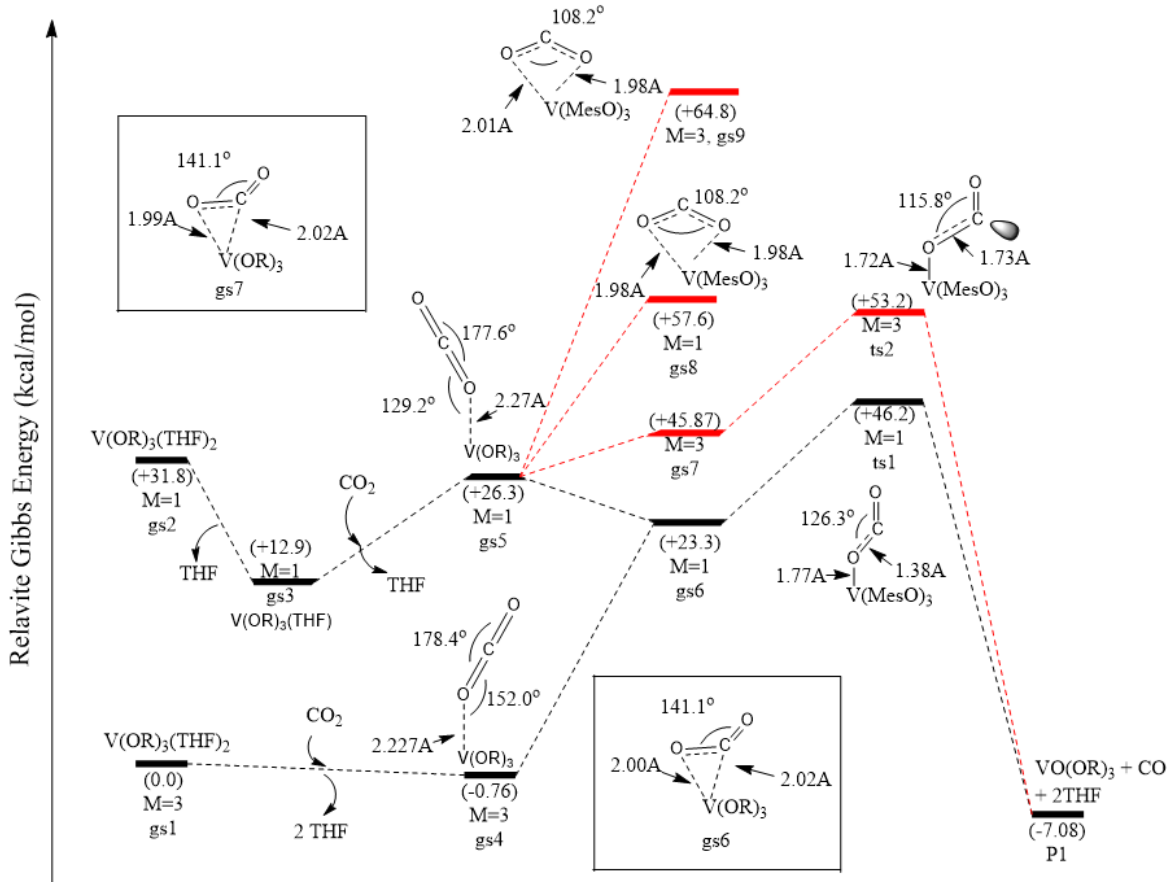

Chart 4.3. Proposed mechanism of the reduction of carbon dioxide to carbon monoxide mediated by vanadium(III) homoleptic compound.

An Intrinsic Reaction Coordinate diagram was calculated as a function of the relative Gibbs energy, thus verifying that reagents and products can indeed be connected via the intermediate active CO_2-adduct sited at the highest energy point. The progress of the reaction nicely shows the change of all the geometrical parameters in synchrony with the increase of CO_2 bending until the final deoxygenation. The calculated relative Gibbs free energy for the overall reaction is -7.08 kcal/mol (Chart 4.4).

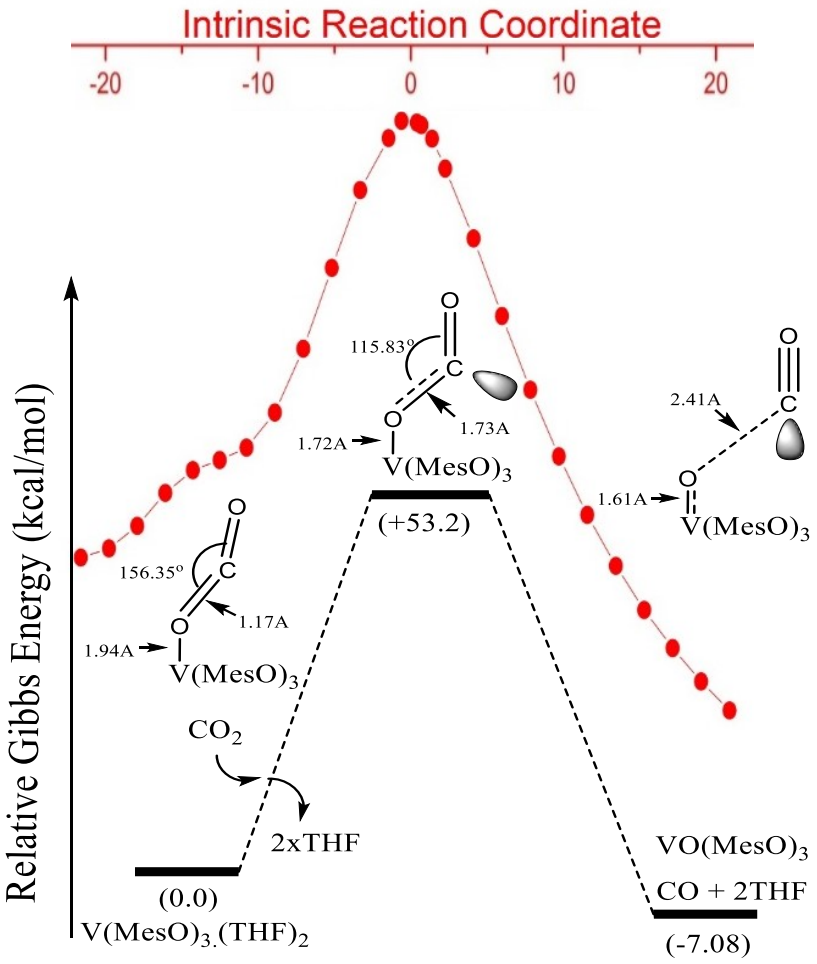

Chart 4.4. Energy profile and Intrinsic Reaction Coordinate diagrams.

The deoxygenation of CO_2 to form a pentavalent $(RO)_3V{=}O$ function and CO was somewhat expected for a relatively oxophilic element such as vanadium. We reason that by increasing the steric hindrance around the metal center and creating a pocket, where the bending of the coordinated CO_2 could be moderated similarly to the case of uranium[378], potentially an adduct could be trapped and isolated. In an attempt to simulate such an environment, we have probed the reactivity of a sterically encumbered

trivalent vanadium tris(2,6-bis-phenylaryloxide) complex. The complex (2,6-$Ph_2C_6H_3O)_3V$(THF) (**10**) was prepared and analyzed (Figure 4.9).

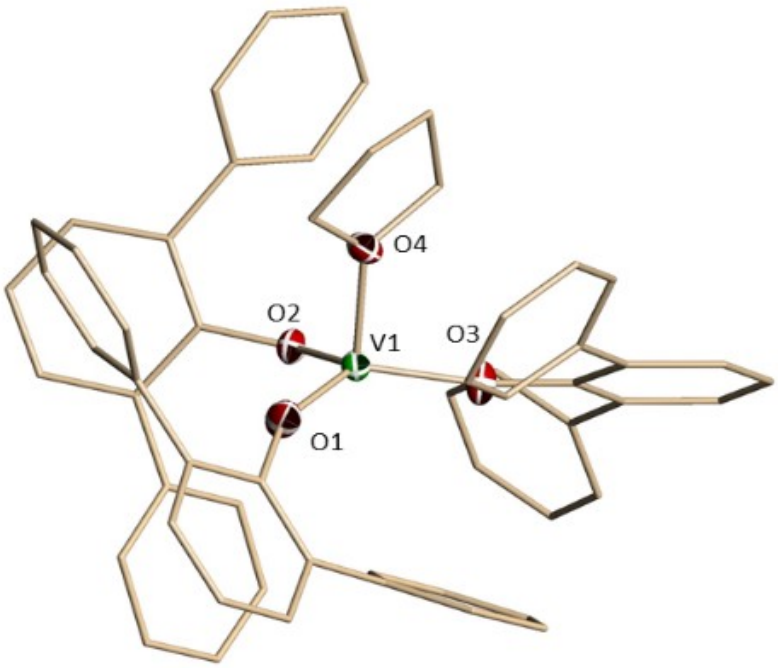

Figure 4.9. Thermal ellipsoids plot of **10** with ellipsoids drawn at the 50% probability level. Hydrogen atoms were omitted for clarity. Selected bond distances [Å] and angles [°] for compound 10: V1-O1 = 1.832, V1-O2 = 1.845, V1-O3 = 1.923, V1-O4 = 1.926, O1-V1-O2 = 118.32, O1-V1-O3 = 113.29, O1-V1-O4 = 111.44, O2-V1-O3 = 109.51, O2-V1-O4 = 114.87 and O3-V1-O4 = 84.61.

The connectivity and composition were confirmed by an X-ray crystal structure. Even in this case, the reaction of (2,6-$Ph_2C_6H_3O)_3V$(THF) (**10**) with CO_2 afforded deoxygenation with the formation of the corresponding pentavalent (2,6-$Ph_2C_6H_3O)_3V$(O) (**11**) and CO albeit through a substantially slower reaction. In addition, the reaction seems to proceed through initial formation of intermediates given that the original green color of the reaction solution slowly turned blue within the next two hours and eventually red after twelve (Scheme 4.7). When the reaction was halted at the initial stage by degassing

the reactor after the color turned decisively blue, a different species was isolated as a paramagnetic, blue crystal. The crystal structure confirmed the analytical data and revealed a monomeric tetravalent complex formulated as $(2,6\text{-}Ph_2C_6H_3O)_2V(O)(THF)_2$ (**12**).

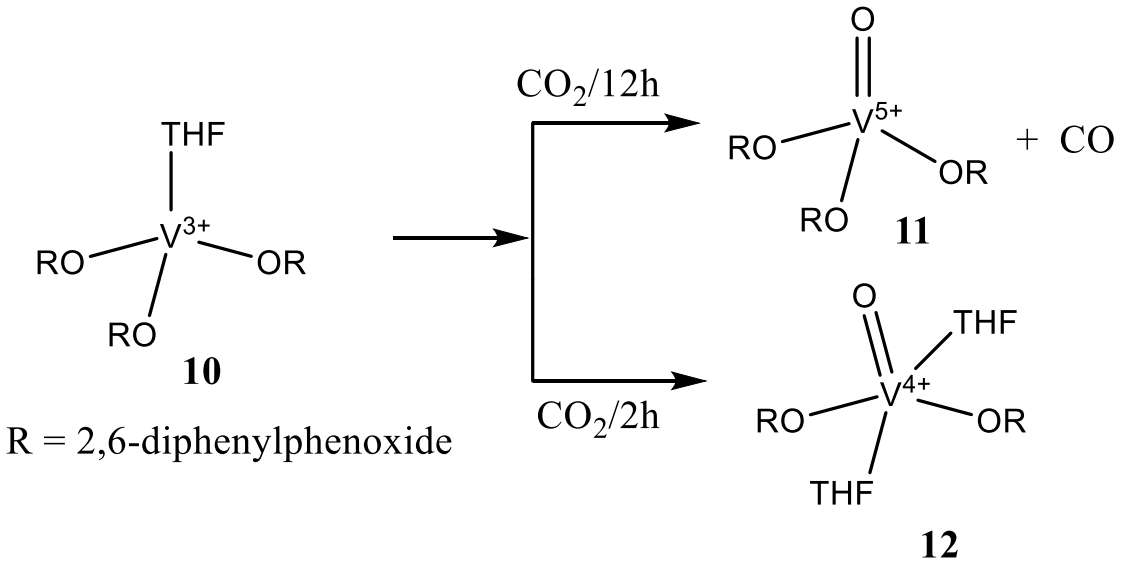

Scheme 4.7. Synthesis of compounds 11 and 12.

The formation of **12** does not have a straightforward explanation since it implies a one-electron transfer and the loss of one ligand anion. It is thus unlikely to be the intermediate for the formation of **11** (Figure 4.10). In any event, it hints at the occurrence of a reactivity alternative to simple deoxygenation. Unfortunately, attempts to isolate other species or to identify other products failed. We have therefore examined a trivalent vanadium aryloxide complex containing a terminally bonded electron-withdrawing chlorine atom in the hope of moderating the electron transfer to CO_2, and to arrest the vanadium oxidation to the tetravalent state. In turn, this implies that only one electron may indeed be provided by the metal for CO_2 reduction.

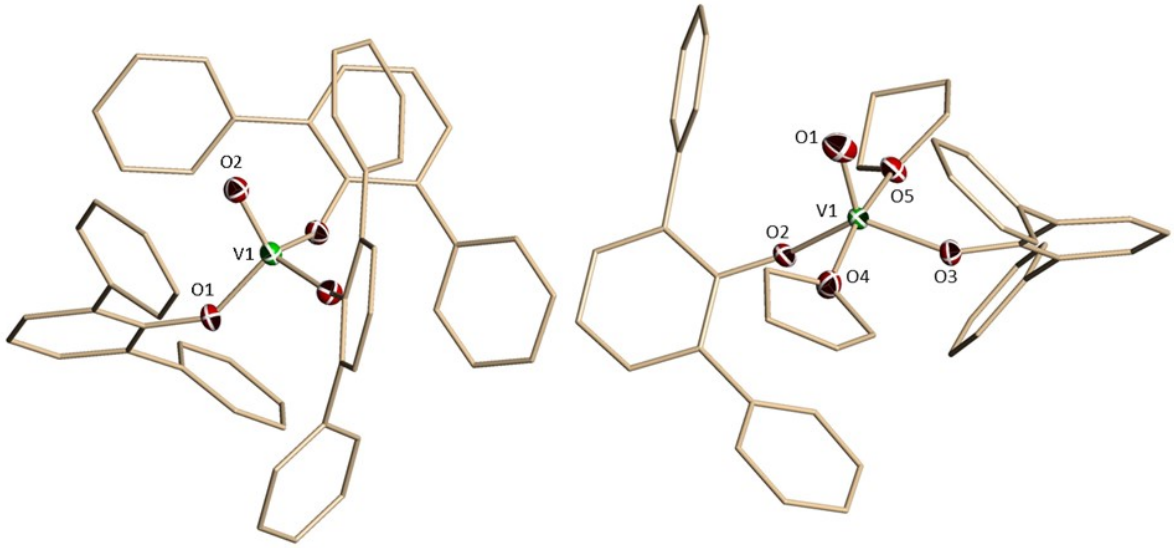

Figure 4.10. Thermal ellipsoids plot of **11** and **12** with ellipsoids drawn at the 50% probability level. Hydrogen atoms were omitted for clarity.

After the strong reducing power that vanadium(III) homoleptic compounds can generate over CO_2, and the labile interaction vanadium(IV) compounds presented, to find an intermediate reducing power was the next challenge to be evaluated. Compound **13** then was evaluated.

The reaction of $(2,4,6\text{-}Me_3C_6H_2O)_2V(Cl)(THF)_2$ (**13**)[377] with CO_2 was performed under the previous reaction conditions. After 48 hours exposure to CO_2 at atmospheric pressure, blue crystals of a new compound formulated as the tetravalent $[(2,4,6\text{-}Me_3C_6H_2O)V(O)Cl]_2(\mu\text{-}2,4,6\text{-}Me_3C_6H_2O)_2$ (**14**) were obtained at room temperature. The dimeric nature of this paramagnetic complex, along with the composition and connectivity, were determined by an X-ray crystal structure (Figure 4.11). Since even in this case its formation implies loss of one ligand and one-electron, the reaction mother liquor was also analyzed.

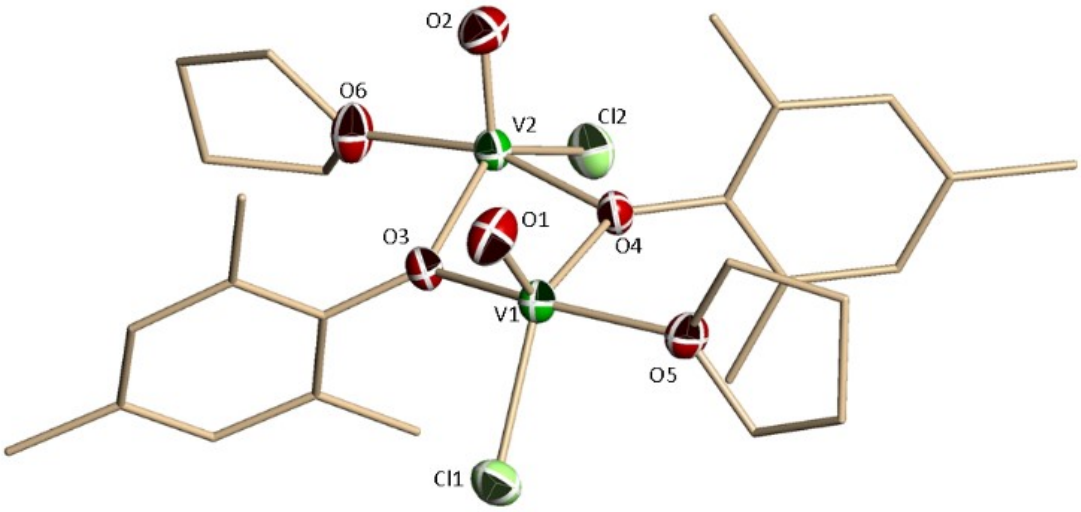

Figure 4.11. Thermal ellipsoids plot of **14** with ellipsoids drawn at the 50% probability level. Hydrogen atoms were omitted for clarity.

The accurate mass was calculated on the product+Na^+ (305.1492 m/z) peak using lock Mass Accuracy on a micromass TOF-MS-ESI spectrometer. The analysis indicated the presence in solution of an organic molecule whose molecular mass corresponds to the ester depicted in Scheme 4.8. This structure was confirmed as mesityl ester ($C_{19}H_{22}O_2$) by ^{1}H-NMR in $CDCl_3$ and fragmentation pattern by MS-EI.

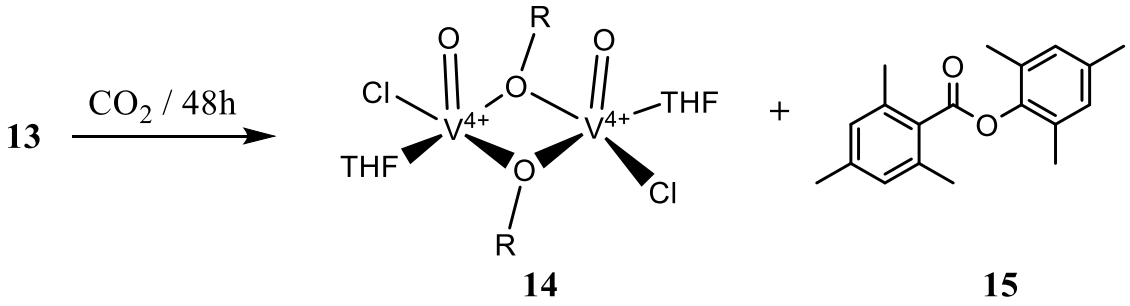

Scheme 4.8. Reactivity of compound **13** with carbon dioxide.

Although the formation of the ester via coupling of the ligand aryl residues and CO_2 looks surprising, it may have in fact a simple rationalization (Scheme 4.9), but other are also possible. In one of the several possible mechanistic scenarios, one-electron transfer from vanadium to CO_2 is followed by a two-electron attack of the CO_2 oxygen atom to one ligand aryl moiety.

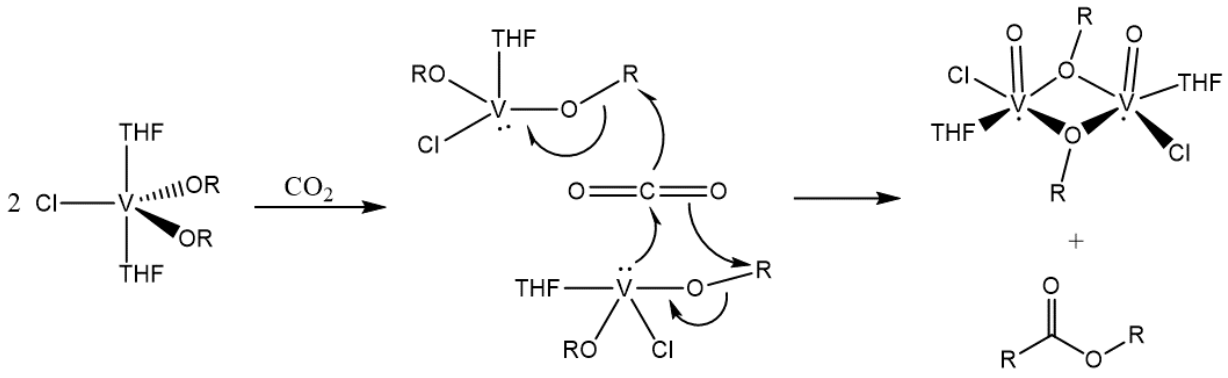

Scheme 4.9. Proposed rationalization for the formation of the ester.

Under any mechanistic scenario however, the formation of the tetravalent **14** clearly indicates that only one electron has been transferred by vanadium to CO_2. On the other hand, the overall reaction requires for CO_2 undergoing a two-electron reduction as in the case of the simple de-oxygenation. The striking difference of the product (ester instead of CO) possibly indicates that the two electrons have been delivered at two different stages and, very possibly, by the cooperative interaction of two metal centers. In any event, it is conceivable that the preliminary interaction of the V(III) center of chlorine containing **13** with CO_2 is more limited in term of charge transfer. To probe the likelihood of this assumption, as well as obtaining information on the mechanistic pathway for ester formation, DFT calculations were performed.

The geometrical parameters as obtained from the crystal structures have been recalculated, obtaining a good match with the experimental values (Chart 4.5). This lends credibility to the appropriateness of the selection of the functional and basis set. Berny algorithm was used to find a possible initial interaction/transition state. The result indeed confirmed the formation of an adduct but with some striking differences from the case of the homoleptic(III) adduct.

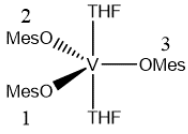

Compound 6

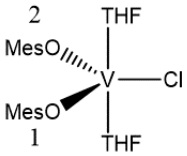

Compound 13

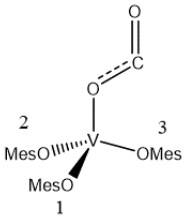

6-CO_2 adduct

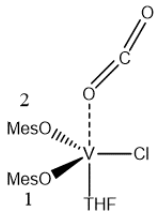

13-CO_2-THF adduct

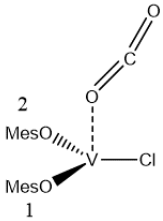

13-CO_2-noTHF adduct

Measurement/ Compound	X-ray		DFT				
	6	13	6	13	6-CO_2	13-CO_2-THF	13-CO_2-noTHF
V-OMes1	1.864	1.845	1.892	1.870	1.890	1.842	1.828
V-OMes2	1.860	1.854	1.891	1.871	1.828	1.853	1.823
V-OMes3	1.866	--	1.891	--	1.805	--	--
V-Cl	--	2.288	--	2.326	--	2.311	2.283
O--Mes1	1.351	1.372	1.351	1.354	1.308	1.341	1.348
O--Mes2	1.339	1.366	1.349	1.354	1.357	1.360	1.363
O--Mes3	1.359	--	1.347	--	1.354	--	--
V-O-Mes1	134.1	128.9	136.1	134.1	139.3	172.5	157.9
V-O-Mes2	160.1	129.3	140.9	136.8	138.9	136.1	136.8
V-O-Mes3	130.0	--	147.2	--	153.8	--	--

Chart 4.5. Comparative table of experimental and computed bond distances and angles.

Firstly, in the homoleptic case the preliminary dissociation of THF is energetically downhill and the CO_2 adduct does not contain THF. With the partly chlorinated compound instead, the presence of THF does not seem to influence the stability of the structure, as well as geometry of the activated complex. The THF and THF-free CO_2-adducts show in this case almost identical arrangements of the coordinated CO_2. Secondly, the linearity of carbon dioxide remained almost unaffected by the coordination as a result of

a minimal electron transfer from the metal center (Chart 4.6). This means that the chlorine atom is interfering in the coordination and preventing the two-electron transfer to carbon dioxide by limiting the charge transfer to only one electron. The NPA indicated that the electron density is mostly on the vanadium atom. Accordingly, the Mulliken charges shows the carbon of the CO_2 molecule remains more positive than in the case of the trisaryloxo vanadium(III)-CO_2 adduct. The longer distance for V—O4 (Chart 4.6) compared to V1—O5 (Chart 4.1) and the minor perturbation of the C=O bond are all in agreement with a minimum extent of CO_2 reduction.

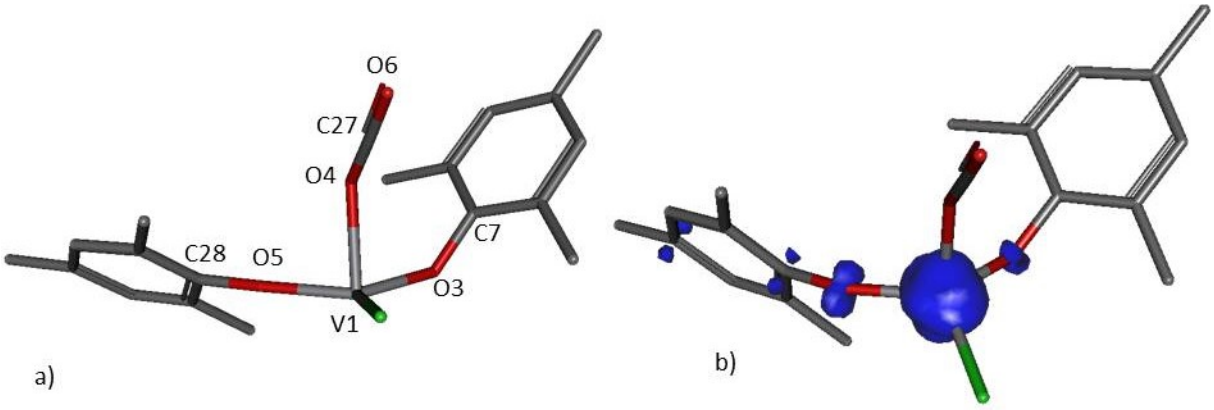

Chart 4.6. a) Computed carbon dioxide interaction with compound 13. V1-O4 = 2.190 Å, V1-O5 = 1.827 Å, C28-O5 = 1.348 Å, V1-O5-C28 = 157.9°, O4-C27-O6 = 178.3° and O5-V1-O4 = 100.08°. b) HOMO-Spin density for adduct compound13-CO_2.

Surprisingly, the spin density distribution on the HOMO of 13-CO_2 clearly indicates that one of the two aryloxide oxygen atoms of **13** has gained a considerable amount of charge as a result of the CO_2 coordination (Chart 4.7).

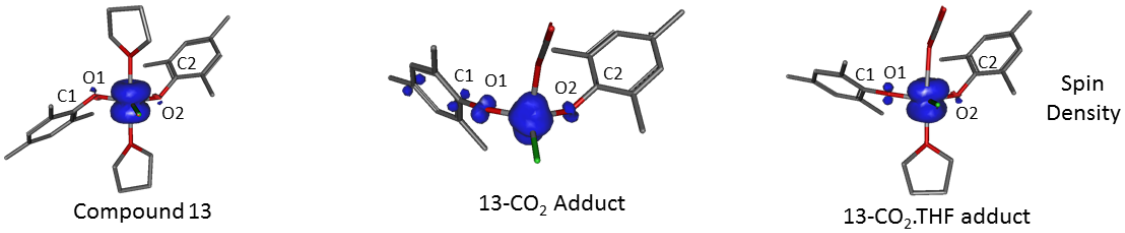

Atom\ properties	Compound 13		13-CO_2 adduct		13-CO_2.THF adduct	
	Mulliken Charges	Spin Density	Mulliken Charges	Spin Density	Mulliken Charges	Spin Density
V	1.113467	2.085459	1.182954	2.038353	1.194344	2.024294
O1	-0.560999	-0.035449	-0.621613	0.015934	-0.611908	0.011567
C1	0.295719	0.013708	0.649851	0.008555	0.288959	-0.015647
O2	-0.575802	-0.032372	-0.398998	-0.032141	-0.548355	-0.031358
C2	0.225084	0.011247	0.244159	0.018407	0.208565	0.016780

Chart 4.7. HOMO-spin density of compound 13 and 13-CO_2 adducts with and without THF.

Whether this may or may not lead to a radical attack by the ligand, instead of the metal, to the coordinated or free CO_2 to generate a ROC(O) radical species is impossible to establish at this stage. For this reason, we decided to probe a possible mechanism by DFT by following the rationalization proposed in Scheme 4.9. Chart 4.8 presents two pathways for the formation of an ester.

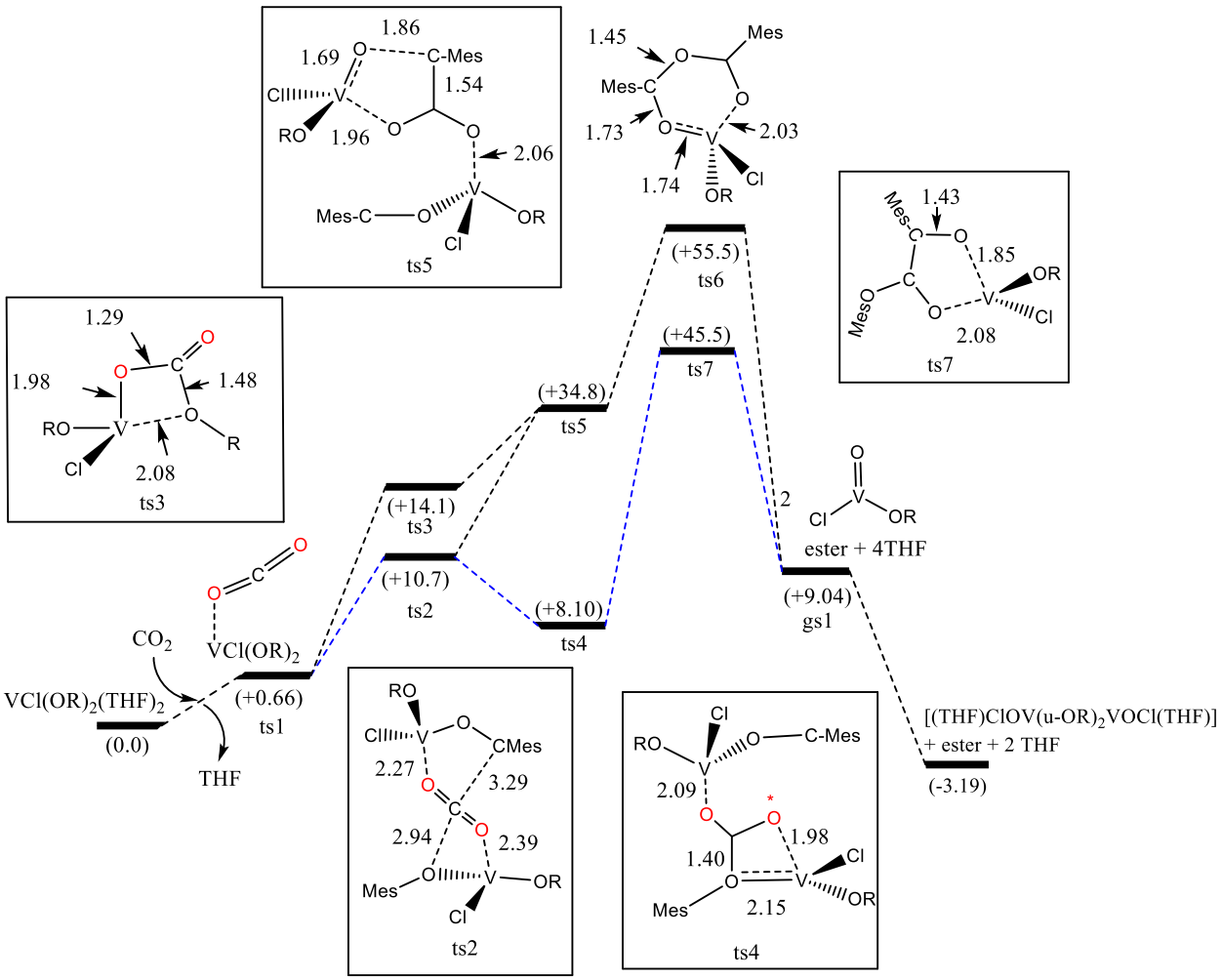

Chart 4.8. Gibbs energy profile in kcal/mol on the pursuit of the mechanism for ester formation using compound 13. Blue dash line presented the lower energy profile. All distances are in Å.

The proposed pathway towards ester formation shows a few possibilities in terms of transition states. After the first interaction proposed for the 13-CO_2 adduct, the transition state ts1 could undergo an extended two metal center interaction with carbon dioxide affording ts2. The initial state ts1 can also evolve into a higher energy structure, ts3, because of a single intramolecular migration required to form the carbonate, ts3. From ts2, the lower energy path is to afford an intramolecular carbonate ts4 where one of the oxygen atoms acquire a radical type of character because of charge transfer from one of the two metal centers. This of course does not imply that ts5 cannot be obtained from ts2. Indeed,

geometry analysis of ts2 shows a longer distance present when the CO_2 carbon atom attempts coupling with an identical molecule to form a carbon-carbon bond (O_2C---C_{Mes} = 3.29Å). This makes the pathway less favored (red line) compared to carbonate formation (dash-line, C---O = 2.94Å) This highest path started with a C—C formation between the ligand system and CO_2. The transition state ts5 is reached when the C-O bond of the phenoxide residue starts breaking and vanadyl=O forming. Also, the geometries of ts4 and ts5 show some interesting comparative features. In ts4, the distances V—OMes and V—O*CO are 2.15 and 1.98 and 1.69 and 1.86 Å respectively. This implies that it would be difficult to determine where the oxygen is contributed from (either directly from the ligand system or carbon dioxide). If the oxygen is coming from the carbon dioxide, vanadyl formation will present V=O* (Scheme 4.9). If the oxygen is coming from the ligand system, vanadyl formation will present V=O since the distance in ts5 of V—O is shorter (1.69Å). This mechanistic approach suggested an initial release of a VOCl(MesO) fragment and the formation of ts6. Similar as in ts5, the second VOCl(MesO) fragment is released and the ester is formed, gs1. The lower-energy mechanistic path was obtained when ts7 is formed. In conclusion, the energy profile presented suggested a vanadyl formation in both cases using oxygen from the ligand system. The lower energy profile indicates that the oxygen might come from the carbon dioxide at the first stage and from the ligand system at ts7. Further experiments using CO_2 with oxygen-18 labeled will elucidate this step.

Regrettably, CO_2-adducts could not be isolated and chemically characterized in spite of reiterated attempts. To probe at least that the metal reduction potential is indeed substantially modified by replacing one aryloxide ligand with chlorine. Cyclic voltammetry measurements have been carried out on THF solutions of both **6** and **13**. In both cases only irreversible vanadium oxidations could be detected. However, for compound 6, the two stages of oxidation, due to formation of tetra and pentavalent states are clearly visible at +0.23V and +0.42V. In compound **13** there is only a single broad oxidation at substantially higher potential +0.77V (Chart 4.9). The observed difference in oxidation

potentials is in line with the computed lower ability of 13 to transfer electrons to CO_2 and which explains the different reaction outcome.

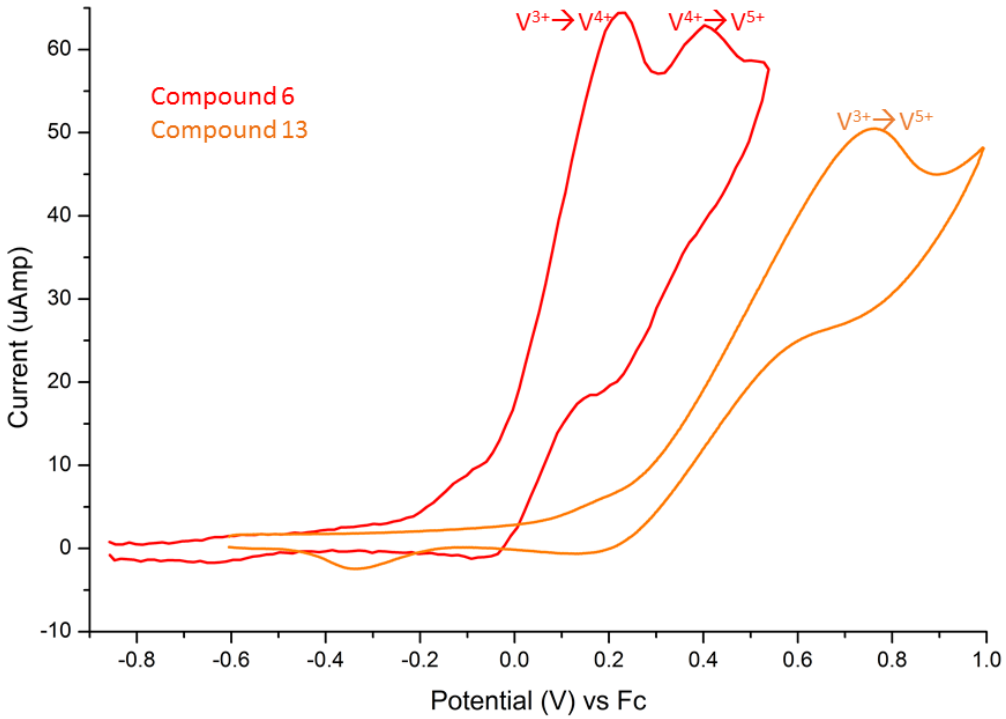

Chart 4.9. Cyclic voltammetry diagrams for 6 and 13.

4.4. Conclusions

In conclusion, vanadium(IV) aryloxo compounds present weak/negligent reducing power towards carbon dioxide reduction. When a Lewis base is used such amino function contained in the ligand system (compound **1**), vanadium(IV) presented unusual air stability. This might be explained by the closed-shell environment on vanadium(IV) metal center.

Steric hindrance was evaluated by preparing compounds **2** and **4** with no positive results towards carbon dioxide reduction. Only carbon monoxide is generated by using high temperature and pressure that generates decomposition on vanadium(IV) compound. A mixture of vanadium(IV) and (V) was found by ^{51}V NMR by the assumption of vanadyl(V) oxo bridge might be formed.

Only a weak interaction was found, characterized by EPR and UV-vis, when calix[4] was used as ligand system (compound **5**). The nature of this interaction seems reversible since the EPR analysis shown that once carbon dioxide is removed with vacuum, the EPR spectra returns to its original result.

Lowering the oxidation state, vanadium(III) aryloxide compounds present strong reducing power towards carbon dioxide, performing partial deoxygenation and ultimately producing vanadyl-oxo species. The occurrence of linear end-on coordination, instead of the commonly observed side-on, is the starting point of the reactivity. Electron-transfer from the metal bends the coordinated CO_2 and triggers the reaction. During this stage, the extent of charge transfer, as determined by the selection of the ligands, affects the bending of the coordinated CO_2. A larger amount of electron transfer severely bends the coordinated CO_2, leading to CO. Simple coordination with less charge-transfer enhances instead the radical nature of the adduct, in the end triggering ligand fragmentation and attack of the CO_2.

Questions remain about why one-electron transfer from vanadium afforded the ester instead of an oxalate. It is tempting to speculate at this stage that this could be again ascribed to the particular bonding mode adopted by CO_2 with these complexes. The formation of oxalates with one-electron reductants has also been related[145,148,368,369] to an inward bending of coordinated CO_2, instead of outward observed in this work, in an overall chelating bonding mode with two oxygen atoms both pointing towards the same metal center. Identifying the factors determining the type of bending (inward versus outward) of linearly coordinated CO_2 would be obviously the next challenge.

4.5. Experimental Part

All vanadium precursors used were non-oxovanadium compounds. For this study, we were using vanadium(IV) and vanadium(III) chloride purchased from Sigma. VCl_4 was used without further

purification, instead $VCl_3(THF)_3$ was prepared from VCl_3 using a standard procedure.[380] All manipulations were performed under a nitrogen/argon atmosphere with rigorous exclusion of oxygen and water by using standard Schlenk and glovebox techniques. n-Heptane, ether, toluene and THF were dried with an activated Al_2O_3 column and deoxygenated prior to use by several vacuum/nitrogen purges. Pyrene 98%, mesitylphenol 97%, 2,6-diphenylphenol 98% were purchased from Aldrich. Carbon dioxide (grade 4.0) was passed through a P_2O_5 column prior to use. Complexes **6** and **13** were prepared according to published procedures.[377] The formation of CO was monitored by gas chromatography using an Agilent Technologies 7820A GC-TCD system with a Molsieve column. All other chemicals used were purchased from Sigma-Aldrich and used as received. Magnetic susceptibilities were measured using a Johnson Matthey magnetic susceptibility balance at room temperature. NMR experiments were performed with either Bruker 300 or 400 MHz instruments using $CDCl_3$ or C_6D_6 as solvents. Mass spectrometric analysis for compound **15** was carried out using a Micromass QToF I ESI Mass Spectrometer, with Lock Mass HRes Exact Mass Calculation and Kratos Concept 1S, HRes EI Mass Spectrometer and for compounds **9**, **10** and **11**, in a Bruker UltrafleXtreme MALDI-TOF/TOF mass spectrometer interfaced to an MBraun glovebox for anaerobic analysis using pyrene as matrix. Sample preparation: a 100 mM solution of pyrene in C_6H_6 was prepared and mixed with 3.1 mM analyte solutions to give a ratio of ca. 500:1 (molar) pyrene: analyte, spotted ca. 1-2 μL on the MALDI target, allowed solvent to evaporate via the dried droplet method before inserting. TOF spectra collected in positive reflection mode, with the accelerating voltage (IS1) fixed at 20.16 kV. To minimize fragmentation, laser energy maintained at minimum intensity required to observe a signal within 1000 shots; samples were analyzed promptly to prevent matrix evaporation.[381,382] Single crystal X-ray data were obtained using a Bruker diffractometer equipped with a Smart CCD area detector and a Bruker Kappa APEXII CCD diffractometer. The magnetic moments were measured at room temperature from samples sealed in calibrated tubes prepared inside a dry-box. Preliminary ground state geometries were

optimized using semi-empirical PM7 method implemented in MOPAC2016.[383] DFT calculations have been performed at the B3LYP[384–387] level by using TZVP[388,389] basis set for all atoms with Gaussian 09® suite package. Berny algorithm was performed to find a transition state using QST3 and standard methods.[390,391] Vibrational frequencies analysis was performed to characterize the nature of the transition state, one imaginary frequency. All most probable transition states were probed by performing an intrinsic reaction coordinate (IRC) procedure[392,393] to confirm that the two minima are connected. Solvation effects were also considered using PCM solvation model.[394,395] Natural population analysis was performed to obtain the electronic distribution in the transition state. The graphical user interface Gabedit[396] and Avogadro[397] were used for input/output and structure handling. All cyclic voltammetry experiments have been carried out in a three-neck round bottom flask. All experiments were done in a N_2 filled glovebox. Cyclic voltammetry was performed using a VersaSTAT 3 (Princeton Applied Research) potentiostat. A conventional three electrode system was employed. A glassy carbon electrode (diameter = 0.4 cm) was used as the working electrode, a Pt wire as the auxiliary electrode, and an Ag wire was used as a pseudo-reference electrode. Ferrocene was added as an internal reference. Tetrabutylammoniumhexafluorophosphate ($(n\text{-}Bu)_4NPF_6$, TBAHFP), the supporting electrolyte, was crystallized two times with dried methanol and dried in vacuum at 90 °C for 24 h before use. The electrolyte solution, 0.1 M $(n\text{-}Bu)_4NPF_6$ in THF was used in each experiment. The concentration of compounds 6 and 13 were 1.1 mM and 1.4 mM (10 mL THF) in each experiment.

4.5.1. Preparation of vanadium(IV) compounds.

Preparation of [($C_{38}H_{44}N_2O_4$)V] (1). 2, 2', 2'', 2'''-[1,2-ethanediylbis[nitrilobis(methylene)]]tetrakis[4,6-dimethylphenol[372] (2.31 mmol, 1.38g) was dissolved in THF. KH (10.16 mmol, 0.41 g) was added slowly to deprotonated the phenol groups and the mixture was stirred overnight. VCl_4 (0.300 mL, 2.38 mmol)

was added drop wise. Once the addition is done, the mixture was stirred 24 hours. The resultant solution was then centrifuged and the obtained solid was removed. After 2 weeks, from a dark blue solution, blue crystals were obtained. The yield of the reaction was 69.1% (1.60 mmol, 1.03 g) based on the ligand used. μ_{eff}= 1.81 BM.

Preparation of [$(C_{23}H_{30}O_2)_2V$] (2). 2,2'-Methylenebis(6-tert-butyl-4-methylphenol) purchased from Sigma was dissolved in 20mL of THF. KH was slowly added (0.258 g, 6.45 mmol) and the solution was stirred for 24h. Once the reaction is complete, the solvent was removed under vacuum and the resultant solid was dissolved in 15 mL of cold toluene. Then, VCl_4 (0.291 mL, 2.93 mmol) was added drop wise. Once the addition is done, the mixture was stirred overnight. The mixture was then centrifuged and the obtained solid was removed. The remained solution was dried out with vacuum and the obtained sticky dark red solid was dissolved in fresh n-heptane. From that solution and after 1-week dark blue crystals were obtained. The yield of the reaction was 89.1% (0.329g, 0.527mmol) based on vanadium salt used. μ_{eff}= 1.68 BM.

Preparation of 2,2'-Methylenebis(4,6-dimethyl-phenol) (3). In a 250 mL round bottom flask, 2:1.1 molar ratio of 2,4-dimethylphenol (10.0 mL, 82.8 mmol) and *p*-formaldehyde (45.5 mmol, 1.37 g) were added. Methanol was used (100 mL) as solvent in this reaction and a few drops of concentrated sulfuric acid were added to catalyze the condensation. The system was stirred under reflux during 24 h. After that, a beige-white sticky solid was obtained when the methanol was removed using a rotatory evaporator. The solid was washed three times with 20mL of a mixture 1:1 methanol water to remove any excess of sulfuric acid and unreacted chemicals. The solid was then purified by crystallization in boiling ethanol and allowing to cool to room temperature in a water bath. The crystals were filter under vacuum and analyzed by ^{1}H, ^{13}C NMR and ^{13}C NMR DEPT135 analysis. ^{1}H NMR (22°C., 300 MHz, $CDCl_3$) δ: 6.99 (s, 2H), 6.84 (s, 2H), 6.33 (s, 2H), 3.90(s, 2H), 2.28 (s, 3H) and 2.21 (s, 3H). ^{13}C NMR (22°C., 300 MHz, $CDCl_3$) δ: 148.74, 130.13, 129.98, 128.81, 126.38, 123.99, 31.21, 20.49 and 15.99 ppm. ^{13}C NMR

DEPT 135 (22°C., 300 MHz, $CDCl_3$) δ: 129.98, 128.81, 31.21 (down), 20.49 and 15.99 ppm. The yield of the reaction was 61.2% (25.1 mmol, 6.42 g).

Preparation of $[(C_{17}H_{18}O_2)_2V]_2$ (4). 2,2'-Methylenebis(4,6-dimethyl-phenol) was dissolved (0.751 g, 2.93 mmol) in 25 mL of THF. KH was slowly added (0.258 g, 6.45 mmol) and the solution was stirred for 24h to ensure no more hydrogen was evolved and both phenols were deprotonated. Once the reaction is done, the solvent was removed under vacuum and the solid was suspended in 20 mL of toluene. Then, VCl_4 (0.291mL, 2.93mmol) was added drop wise to the deprotonated ligand in toluene. Once the addition is done, the mixture was stirred overnight. The mixture was centrifuged and the solid (KCl as byproduct) was removed. The remaining solution was dried out under vacuum and the obtained sticky dark red solid was dissolved in fresh toluene. After a new centrifuge step, tiny amount of KCl was removed and from the solution dark red crystals were obtained over 2 weeks. The yield of the reaction was 35.9% (0.329 g, 0.527 mmol) based on vanadium salt used. μ_{eff}= 1.79 BM.

Preparation of $[(C_{44}H_{52}O_4)V]_2$ (5). 4-tert-Butylcalix[4]arene was partially dissolved (0.561g, 0.864mmol) in THF (25 mL), then KH was added slowly as powder (0.152 g, 3.81 mmol) to deprotonate the phenols. The reaction produced hydrogen gas and was allowed to react for 36h in a glass vial. Once the reaction was completed, the THF was removed under vacuum. The resultant white solid was suspended in 25 mL of dry toluene and stirred for 2 more hours. After that time, VCl_4 (0.091 mL, 0.872 mmol) was added drop wise. The mixture was stirred for 36 hours and then centrifuged. From the resultant solution, and after 3 weeks, dark blue crystals were obtained. The yield of the reaction was 49.5% (0.376 g, 0.428 mmol) based on vanadium salt used. μ_{eff}= 1.52 BM.

4.5.2. Preparation of vanadium(III) aryloxides.

Preparation of $[Li(THF)_2V(OMes)_4]$ (7). MesOH (mesitylphenol) (0.375 g, 2.75 mmol) was dissolved in 15 mL of n-heptane, and the solution cooled to -35°C. n-BuLi (2.5 M, 1.2 mL) was added drop wise. The

mixture was stirred for approximately 12 hours and the solvent evaporated in vacuo. The resulting solid was re-dissolved in THF (20 mL) and $VCl_3(THF)_3$ (0.257 g, 0.70 mmol) added and stirred for 24 hours. The initial color of the solution turned purple and then green. The resulting solution was centrifuged to remove the lithium salt produced and allowed to stand undisturbed at -30°C for 4 days. Green crystals of 2 were obtained (0.104 g, 0.22mmol., 31 %). μ_{eff} = 2.83 BM. E.A. found (Calcd) C 70.91 (71.14), H 8.22 (8.14).

Preparation of $[LiV(OMes)_4]_2$ (8).

Method A. A similar procedure was used as for complex 2, but using toluene instead of THF. From the reaction 3 was isolated as a blue crystalline material (0.481 g, 0.80 mmol, 96 %). μ_{eff} = 2.65 BM. E.A. found (Calcd) C 72.46(72.23), H 7.38(7.41).

Method B. A procedure identical to the formation of 1 was followed. However, the reaction mixture was not centrifuged, but dried under vacuum instead. Hot heptane was used to extract the complex from the solid residue and the extracts filtered to get a clear blue solution. After slow cooling, blue crystals of 3 were obtained (0.144 g, 0.24 mmol, 35%).

Preparation of $VO(2,4,6\text{-}Me_3C_6H_2O)_3$ (9). Exposure of a toluene solution of complexes **6**, **7** or **8** to carbon dioxide changed the color of the solutions to dark-red. In all three cases, the presence of CO as byproduct was determined by GC-TCD. After the reaction was completed (no more CO released) the solvents were removed with vacuum. The resulting dark solid was re-dissolved in 5 mL of pure toluene and centrifuged to remove small amount of insoluble residue. After one week at -35°C, red crystals were obtained (0.223 g, 0.472 mmol. 94 %). HRES-MALDI-TOF-TOF $[M]^{\bullet+}$ m/z calculated for $VO_4C_{18}H_{33}$ 472.182, found 472.203. ^{51}V NMR (22°C., 300 MHz, C_6D_6) δ: -485.5 ppm. $VOCl_3$ was used as reference. ^1H NMR (22°C., 300 MHz, C_6D_6) δ: 6.68 (s, 6H), 2.43 (s, 18H), 2.10 (s, 9H). ^{13}C-NMR (22°C., 300 MHz, C_6D_6) δ: 151.62, 129.52, 129.10, 122.93, 20.61 and 15.81 ppm (Appendix T4.7).

Preparation of V((2,6-C_6H_5)$_2$$C_6H_3O$)$_3$(THF) (10). 2,6-diphenylphenol (0.50 g, 2.03 mmol) was dissolved in 15 mL of THF and treated with KH (0.089 g, 2.22 mmol). The mixture was stirred for a further 12 h before addition of $VCl_3(THF)_3$ (0.251 g, 0.67 mmol). The resulting solution was stirred for 24h and centrifuged to remove insoluble material. Dark green crystals of 5 were obtained from THF (0.235 g, 0.40 mmmol. 60 %). μ_{eff}=2.64 BM. HRES-MALDI-TOF-TOF $[M\text{-}THF]^{\bullet+}$ m/z calculated for $VO_3C_{54}H_{39}$ 786.234, found 786.283.

Preparation of VO(2,6-C_6H_5)$_2$$C_6H_3O$)$_3$ (11). Complex 10 (0.250 g, 0.291 mmol) was dissolved in 15 mL of a 1:1 mixture of toluene:THF. The mixture was stirred and placed under carbon dioxide atmosphere. The color of the solution changed from green to dark red passing through an intermediate blue color. The formation of CO as byproduct was monitored by GC-TCD. The solvents were evaporated in vacuo and a dark solid was obtained. 5 mL of pure toluene was used to dissolve the solid and after one week at -35^{o}C, red crystals were collected (0.088g, 0.102 mmol, 35 %). HRES-MALDI-TOF-TOF $[M\text{-}H]^{\bullet+}$ m/z calculated for $VO_4C_{54}H_{39}$ 801.221, found 801.118. ^{51}V NMR (22^{o}C., 300 MHz, C_6D_6) δ: -521.1 ppm. $VOCl_3$ was used as reference. ^{1}H NMR (22^{o}C., 300 MHz, C_6D_6) δ: 7.58 (d, J=7.1Hz, 4H), 7.49 (t, J=7.4Hz, 4H), 7.40 (t, J=7.2 Hz, 2H), 7.30 (d, J=7.6Hz,2H), 7.08 (t,J=7.6 Hz, 1H). ^{13}C NMR (22^{o}C., 300 MHz, $CDCl_3$) δ: 149.45, 137.72, 130.10, 129.50, 128.98, 128.89 and 122.79 ppm.

Preparation of VO((2,6- C_6H_5)$_2$$C_6H_3O$)$_2(THF)_2$ (12). Similar procedure as for compound **11** was followed with the reaction being stopped after 2h, when the color of the solution was blue. No formation of carbon monoxide was observed at this stage. The solution was degassed to remove carbon dioxide. The blue solution was cooled to -30^{o}C and after filtration blue crystals were obtained. (0.068 g, 0.100 mmol. 19 %). μ_{eff}=1.46 BM.

Preparation of [(2,4,6-$Me_3C_6H_2O$)V(O)Cl]$_2$(μ-2,4,6-$Me_3C_6H_2O$)$_2$ (14). Complex 13 (0.451 g, 0.900 mmol) was dissolved in 25 mL of toluene and exposed to carbon dioxide for 48h. The solution was concentrated

to ½ of the volume by gentle vacuum and then filtered. Layering crystallization technique using n-heptane (3 mL) was used and as result blue crystals were obtained. The crystals were collected by filtration. (0.30 g, 0.05 mmol. 11.1%). μ_{eff}= 2.39 BM. E.A. found (Calcd) C 55.01(55.51), H 6.66(6.75).

Mesityl ester ($C_{19}H_{22}O_2$) purification (15). The filtrate from the isolation of complex **9** was quenched with 2 mL of HCl 1M. 5 mL of ethyl acetate was used to extract the mesithylphenol and the mesityl ester. The mixture was isolated by using amorphous silica gel 60 mesh with 8:2 hexanes:ethyl acetate as mobile phase. After solvent evaporation of the first fraction, it was analyzed by ^{1}H NMR, MS-ESI and MS-EI (SI).

Appendix T4.1 Supporting information

Appendix T4.2. Crystallographic Experiment Details

	1	**2**	**4**	**5**	**7**	**8**	**9**
Formula	$C_{38}H_{44}N_2O_4V$	$C_{48.1}H_{64.90}O_4V$	$C_{19.45}H_{20.80}O_2V_{0.5}$	$C_{29}H_{34}O_2V_{0.5}$	$C_{88}H_{120}Li_2O_{12}V_2$	$C_{36}H_{44}LiO_4V$	$C_{27}H_{33}O_4V$
fw	643.69	758.04	312.03	440.03	1485.6	598.59	472.47
a (Å)	8.6051(14)	31.824(2)	10.7513(11)	12.4805(3)	19.9205(8)	10.3694(5)	28.0337(11)
b (Å)	25.756(4)	11.3267(6)	11.7566(12)	13.4294(3)	20.9328(10)	12.8043(6)	17.9273(7)
c (Å)	14.910(3)	27.9824(16)	14.3660(15)	18.2986(4)	22.1770(9)	12.8815(5)	4.8537(2)
α (deg)	90	90	105.862(2)	100.9426(13)	90.00	85.942(3)	90
β (deg)	98.407(3)	114.8963(13)	95.806(3)	101.9859(13)	111.223(2)	77.113(3)	90
γ (deg)	90	90	97.171(3)	108.3448(13)	90.00	85.726(3)	90
cryst syst	Monoclinic	Monoclinic	Triclinic	Triclinic	Monoclinic	Triclinic	Orthorhombic
space group	P2(1)/c	C 2/c	P-1	P-1	P2(1)/c	P-1	Pna2(1)
V ($Å^3$)	8269.0(10)	9149.1(9)	1715.5(3)	2737.95(11)	8620.4(6)	1660.02(13)	2439.32(17)
Dc (g cm^{-1})	1.308	1.101	1.208	1.067	1.145	1.198	1.287
Z	4	8	4	4	4	2	4
no. of refl. measured	7790	38654	20197	30298	89147	18841	15508
Unique of refl. [*I>2 σ(I)*]	5139	11243	8317	13461	7705	5601	2925
R_{int}	0.0706	0.0429	0.0685	0.0366	0.0852	0.0707	0.0898
R_1 [*I>2 σ(I)*]	0.0550	0.0596	0.0747	0.0764	0.0706	0.0580	0.0477
wR_2[*I>2 σ(I)*]	0.1283	0.1542	0.1675	0.2084	0.1784	0.1377	0.1105
GOF	1.025	1.019	1.029	1.032	1.044	1.028	1.014

Appendix T4.3 - Crystallographic Experiment Details …continue

	10	**11**	**12**	**14**
Formula	$C_{58}H_{47}O_4V$	$C_{44}H_{42}O_5V$	$C_{56.4}H_{43.8}O_{4.6}V$	$C_{26}H_{38}Cl_2O_6V_2$
fw	858.9	701.72	846.05	619.34
a (Å)	42.1043(11)	12.1702(5)	16.0007(5)	14.4157(4)
b (Å)	11.6416(3)	17.0881(7)	16.0007(5)	16.1677(4)
c (Å)	19.4509(6)	19.5515(9)	15.6229(7)	14.0267(3)
α (deg)	90	71.7168(11)	90	90
β (deg)	109.5040(10)	88.3800(12)	90	114.7063(11)
γ (deg)	90	69.5795(11)	120	90
cryst syst	Monoclinic	Triclinic	Trigonal	Monoclinic
space group	C2/c	P -1	R 3H	P 21/c
V ($Å^3$)	8987.0(4)	3603.1(3)	3463.9(3)	2969.93(13)
Dc (g cm^{-1})	1.27	1.294	1.217	1.385
Z	8	8	3	4
no. of refl. measured	58321	47527	13045	42949
Unique of refl. [$I>2\ \sigma(I)$]	11132	20969	3076	7324
R_{int}	0.0455	0.0494	0.0642	0.0281
R_1 [$I>2\ \sigma(I)$]	0.0475	0.0525	0.0488	0.0397
wR_2[$I>2\ \sigma(I)$]	0.1067	0.1032	0.1030	0.109
GOF	1.023	1.009	1.001	1.036

Appendix T4.4. xyz geometry of vanadium complex with carbon dioxide obtained by QST3 method

V	0.20041	-0.42477	0.63158
O	-0.55759	0.86425	-0.52353
O	1.77517	-0.99228	-0.04345
O	-0.93992	-1.85190	0.69950
C	-0.76895	2.15405	-0.56615
C	3.12718	-1.05202	-0.08778
C	-2.17316	-2.19677	0.25072
C	3.73965	-1.19259	-1.34562
C	3.88989	-1.01552	1.09132
C	5.12850	-1.27238	-1.39889
C	5.91995	-1.22586	-0.25036
C	5.27712	-1.10390	0.98042
C	3.22642	-0.90113	2.43615
C	7.42422	-1.28315	-0.34149
H	5.87024	-1.08284	1.88882
C	2.90378	-1.26885	-2.59428
H	5.60468	-1.38350	-2.36778
C	-2.34961	-2.62371	-1.07576
C	-3.62632	-3.00850	-1.48269
C	-4.72054	-2.98682	-0.61804
C	-4.50531	-2.57353	0.69717
C	-3.24938	-2.18064	1.15432
C	-1.18262	-2.67018	-2.02517
H	-3.76512	-3.34339	-2.50577
C	-6.09787	-3.37501	-1.09538
H	-5.33756	-2.56301	1.39387
C	-3.02835	-1.76489	2.58351
C	-2.12942	2.61722	-0.57886
C	0.30899	3.08845	-0.73472
C	-2.36472	3.97060	-0.70682
C	-1.32105	4.89876	0.84611
C	0.00010	4.42873	-0.86430
H	-3.38879	4.32705	-0.70632
C	-1.61352	6.36740	-0.94907
H	0.80811	5.14054	-0.99168
C	1.72683	2.60511	-0.78158
C	-3.24215	1.62223	-0.45738
H	-6.65514	-2.50283	-1.45212
H	-6.68439	-3.82818	-0.29396
H	-6.04709	-4.08743	-1.92069
H	7.86422	-1.66475	0.58126
H	7.84846	-0.28977	-0.51884

H	7.74950	-1.92531	-1.16222
H	-2.56584	6.55100	-1.44861
H	-0.82742	6.89547	-1.49004
H	-1.67955	6.81384	0.04897
H	-0.80401	-1.66862	-2.24787
H	-1.47182	-3.13404	-2.96863
H	-0.35012	-3.23731	-1.60311
H	-3.96742	-1.77092	3.13760
H	-2.59261	-0.76553	2.65210
H	-2.33007	-2.43958	3.08583
H	3.96228	-0.98157	3.23615
H	2.48263	-1.68950	2.58414
H	2.70406	0.05126	2.55616
H	2.20591	-2.10835	-2.55291
H	3.53604	-1.39159	-3.47384
H	2.30086	-0.36799	-2.73218
H	2.39771	3.41140	-1.07532
H	1.84325	1.78066	-1.48657
H	2.05573	2.23877	0.19478
H	-4.21097	2.11969	-0.48200
H	-3.16622	1.05629	0.47349
H	-3.20341	0.88833	-1.26548
C	-0.53981	2.18687	2.15254
O	-0.69182	2.59011	3.22112
O	-0.00519	0.54700	2.03537

Appendix T4.5. Mulliken charges and spin densities

Atom		Mulliken charges	Atomic-Atomic spin densities
1	V	1.331914	1.010518
2	O1	-0.481092	0.116675
3	O	-0.582346	-0.018358
4	O	-0.549049	0.001158
5	C	0.192269	0.076018
6	C	0.286961	0.001595
7	C	0.287792	0.01372
8	C	0.014494	-0.006968
9	C	0.003426	-0.004761
10	C	-0.217958	0.004097
11	C	0.176207	-0.008853
12	C	-0.223987	0.004509
13	C	-0.446416	-0.003452

14	C	-0.444595	-0.000174
16	C	-0.424368	0.00066
18	C	0.013239	-0.003203
19	C	-0.202777	0.00292
20	C	0.161605	-0.003431
21	C	-0.201593	0.002529
22	C	0.008318	-0.005561
23	C	-0.44492	-0.00011
25	C	-0.448838	-0.000021
27	C	-0.413922	-0.000494
28	C	0.084733	0.164395
29	C	0.111681	0.175466
30	C	-0.187318	-0.090558
31	C	0.19298	0.244674
32	C	-0.181435	-0.092176
34	C	-0.440615	0.008274
36	C	-0.435758	0.003788
37	C	-0.403798	0.004517
65	C28	0.153548	0.260989
66	O4	-0.159974	0.027629
67	O5	-0.527752	0.113987

Appendix T4.6. Compound 5 xyz geometry after carbon dioxide interaction, DFT calculation using B3LYP and TZVP basis set.

V 0.0421652453 -0.1215111136 0.0027120478
O -2.5539069349 2.8415405053 -0.2187903354
O -0.4208886319 1.9544231114 -0.1170960285
O 0.0796164177 -0.6873854001 -1.6579902176
O -1.9068282209 -0.1920472217 -0.0421929476
O 1.9414245405 -0.0621559100 0.0487523514
O -0.0057529242 -0.5141694434 1.7127690241
C -1.5219619641 2.3593413752 -0.1668462272
C -2.5076310191 -1.3342237594 2.5705648833
C -5.6111102014 -5.2708340051 0.8079724021
C -4.3328816850 -6.1008161923 -1.1459359775
C -3.3486083460 -6.3376460575 1.1469285313
C -4.1981291039 -5.4236625451 0.2202354215
C -2.7534863584 -2.0327475874 1.2458798073
C -3.3018311381 -3.3031226454 1.2655555724
C -3.5629228907 -4.0356475462 0.1126694640
C -3.2448292045 -3.4307753079 -1.0911005769
C -2.6914467081 -2.1571032315 -1.1712377769

C -2.4433280814 -1.4335207782 0.0068302790
C -2.3778201501 -1.6013527521 -2.5479366393
C 1.0635398850 -3.9276565528 -6.9586273034
C 1.0900041533 -5.7687894863 -5.2594113552
C -1.0548775970 -5.0059730064 -6.2464742626
C 0.3190532205 -4.5387582584 -5.7619791802
C -1.0754034630 -2.1109434130 -3.1225814527
C -0.9992850698 -3.0548268292 -4.1388243678
C 0.2206764503 -3.5035946243 -4.6373499200
C 1.3920406402 -2.9772960147 -4.0852718731
C 1.3680350620 -2.0353512146 -3.0734189583
C 0.1198066751 -1.6207064075 -2.6174034638
C 2.6036597205 -1.4473781576 -2.4312268530
C 5.7581312995 -5.0511988068 1.1919897674
C 4.7516719364 -5.8204701076 -0.9420677529
C 3.5090870282 -6.1532275889 1.1805723238
C 4.4387970021 -5.1964985510 0.4193143129
C 2.8686488465 -1.9916074556 -1.0394059473
C 3.4770299644 -3.2367201321 -0.9300881475
C 3.7663111336 -3.8281500642 0.2885903166
C 3.4160304329 -3.1095285517 1.4262727067
C 2.8086725625 -1.8666873859 1.3787743423
C 2.5265931077 -1.2831975224 0.1254987063
C 2.4741041856 -1.1795971312 2.6903390662
C 0.8104101165 -5.1782810634 5.8832574730
C 0.6971250706 -3.1666293705 7.3726978584
C -1.3822976301 -4.3245405764 6.6702793294
C 0.0155535941 -3.9052266886 6.2109739014
C 1.2057910500 -1.6996460877 3.3273583605
C 1.1760776288 -2.5280302320 4.4339807059
C -0.0230114642 -2.9961543574 4.9788560267
C -1.2149298978 -2.6065202708 4.3741124583
C -1.2369521095 -1.7765495426 3.2604553785
C -0.0165316084 -1.3397695476 2.7668107283
H -4.7788374352 -7.0886330500 -1.0196909656
H -4.9761178237 -5.5333339452 -1.8202070589
H -3.3621545069 -6.2337021182 -1.6261303867
H -3.9261390022 -6.6824422494 2.0060809651
H -3.0032455371 -7.2241927044 0.6140552305
H -2.4663184174 -5.8268749689 1.5275666049
H -5.5825191802 -4.8261215115 1.8030195899
H -6.2294151677 -4.6330920159 0.1741427007
H -6.0959902738 -6.2462113038 0.8900833801

H -3.3511024046 -1.5346039092 3.2323614324
H -2.4708224369 -0.2580033576 2.4041459473
H -3.5322193329 -3.7371552829 2.2324983456
H -3.4254305271 -3.9523401244 -2.0215515308
H -3.1876164212 -1.8721970994 -3.2266481661
H -2.3459378928 -0.5134915928 -2.4942039196
H 1.1397640438 -4.6561912289 -7.7685219511
H 0.5362426653 -3.0510551843 -7.3381597909
H 2.0744324984 -3.6195159711 -6.6922423211
H 0.5827172037 -6.2243945000 -4.4076575772
H 1.1655844618 -6.5170698952 -6.0511608069
H 2.1020845693 -5.5122511364 -4.9467903633
H -1.6453148316 -4.1819690867 -6.6497373914
H -0.9289765876 -5.7409388425 -7.0427910345
H -1.6270955357 -5.4806738572 -5.4480782857
H -1.9248336187 -3.4356061232 -4.5471563744
H 2.3549758389 -3.3043898986 -4.4578468826
H 2.5022839395 -0.3638002836 -2.3769170099
H 3.4654967029 -1.6673283852 -3.0625310726
H 5.5971829790 -4.6537392028 2.1941526097
H 6.2480882532 -6.0221192452 1.2932930003
H 6.4408992383 -4.3775583748 0.6717790325
H 5.2269622642 -6.7920196085 -0.7979191999
H 3.8476589942 -5.9795445140 -1.5317721007
H 5.4365902789 -5.2013308984 -1.5235298256
H 3.2814113362 -5.7838711848 2.1805344113
H 2.5642296599 -6.2801733230 0.6500016032
H 3.9767753408 -7.1347974083 1.2850392068
H 3.7292332829 -3.7466890701 -1.8500525966
H 3.6234448665 -3.5266438550 2.4049716064
H 2.3788291861 -0.1080714439 2.5168238215
H 3.3020548739 -1.3293961925 3.3843262850
H 0.8436824742 -5.8375926272 6.7531296961
H 0.3481542671 -5.7243620181 5.0595780518
H 1.8378064408 -4.9519110964 5.5985022514
H 0.1513763437 -2.2572178753 7.6289036562
H 0.7306604671 -3.8044868028 8.2584234054
H 1.7207126021 -2.8836072962 7.1277059070
H -1.2988552503 -4.9703544769 7.5455489007
H -1.9920669246 -3.4650934912 6.9526978653
H -1.9125014590 -4.8838231609 5.8980764562
H 2.1179970642 -2.8101523700 4.8881466850
H -2.1609389561 -2.9441447952 4.7734193279

Appendix T4.7. ^{51}V NMR of $VO(2,4,6\text{-}Me_3C_6H_2O)_3$ (9) in C_6D_6.

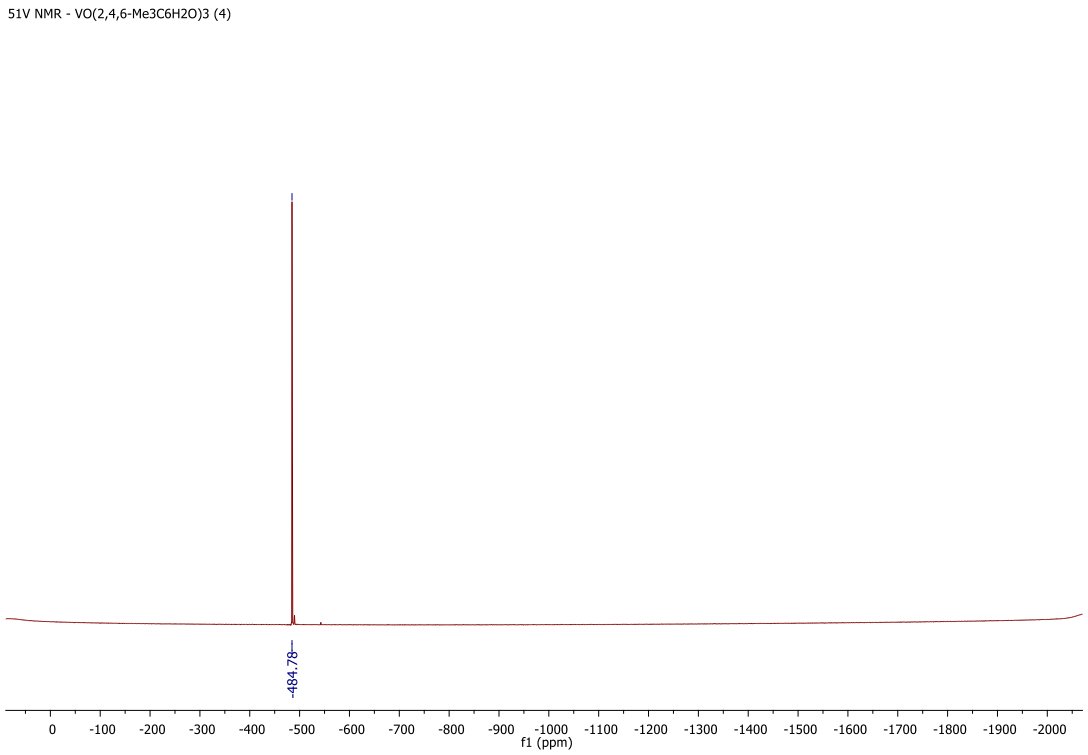

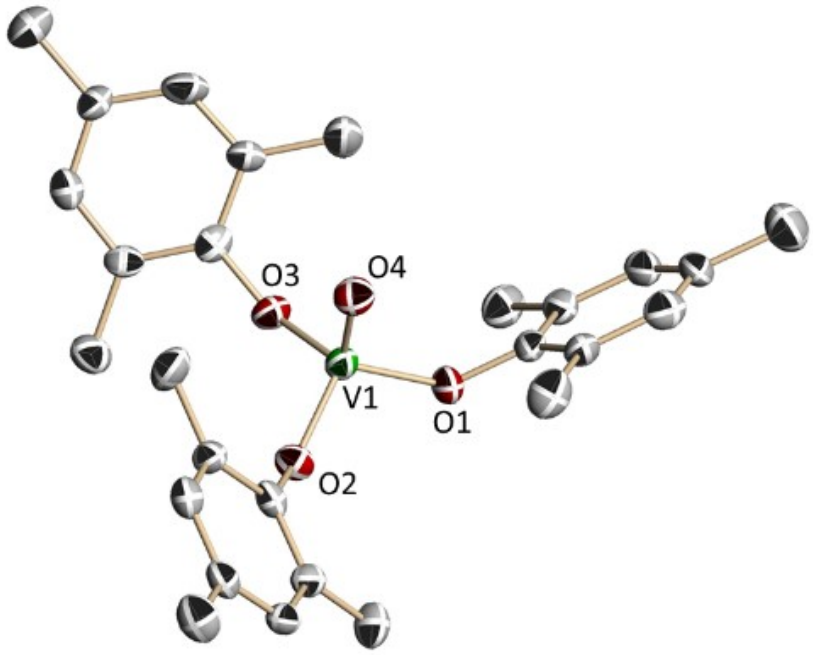

Thermal ellipsoids of compound 9 drawn at 30% of probability level. Hydrogen atoms are omitted for clarity. Selected atom distances and angles are as follows: V1-O4 = 1.571 Å, V1-O1 = 1.768 Å, V1-O2 = 1.782 Å, V1-O3 = 1.784 Å, O1- V1- O4 = 107.35°, O2- V1- O4 = 108.68° and O3- V1- O4 = 107.41°.

Appendix T4.8. ^{1}H NMR, ^{13}C NMR and ^{13}C NMR DEPT 135 of compound **3**. ^{1}H NMR of (**12**) (22^{o}C., 300 MHz, $CDCl_3$) δ: 6.99 (s, 2H), 6.84 (s, 2H), 6.33 (s, 2H), 3.90(s, 2H), 2.28 (s, 3H) and 2.21 (s, 3H).

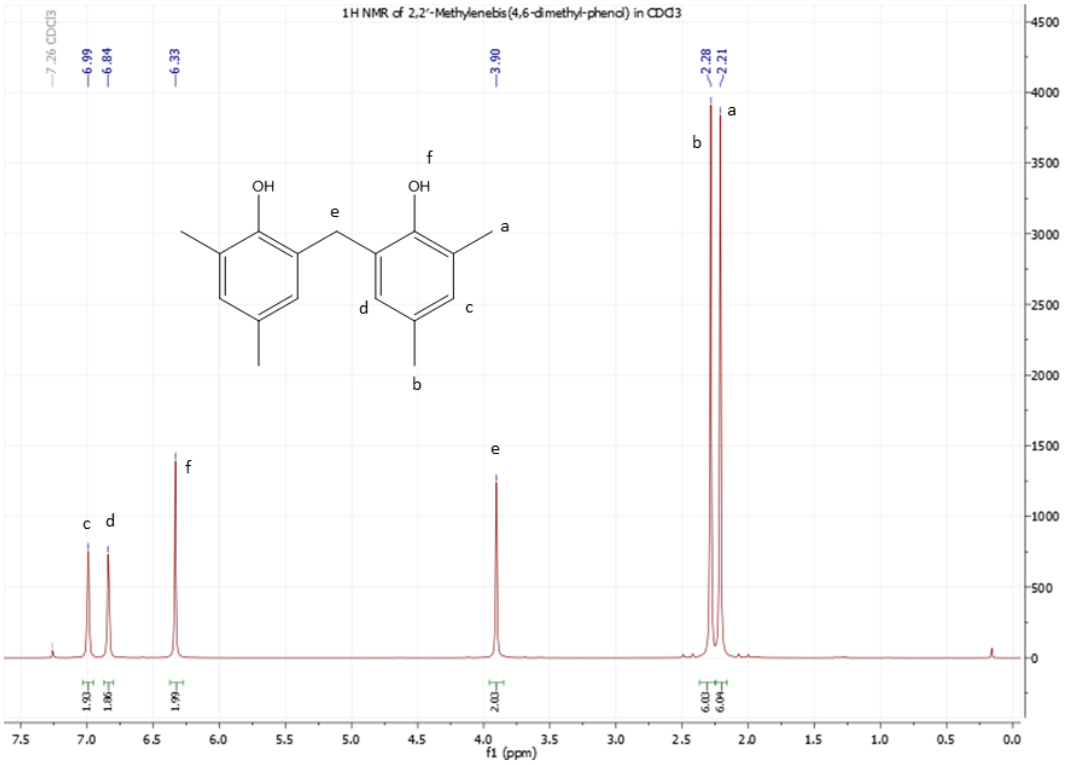

^{13}C NMR of (**12**) (22^{o}C., 300 MHz, $CDCl_3$) δ: 148.74, 130.13, 129.98, 128.81, 126.38, 123.99, 31.21, 20.49 and 15.99 ppm.

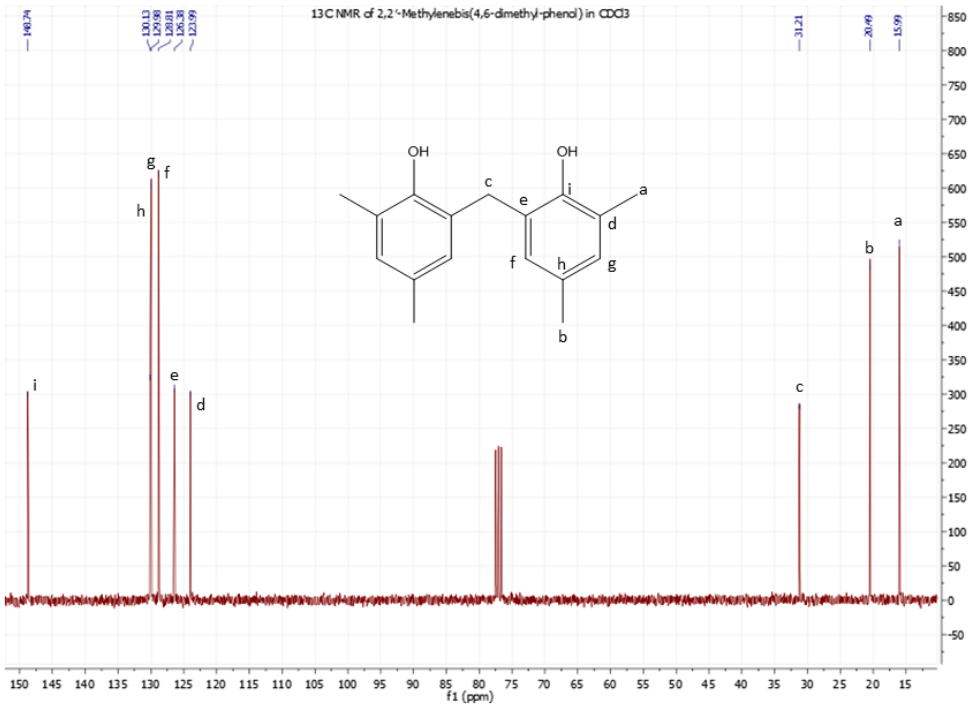

^{13}C NMR DEPT 135 of (**12**) (22°C., 300 MHz, $CDCl_3$) 129.98, 128.81, 31.21 (down), 20.49 and 15.99 ppm.

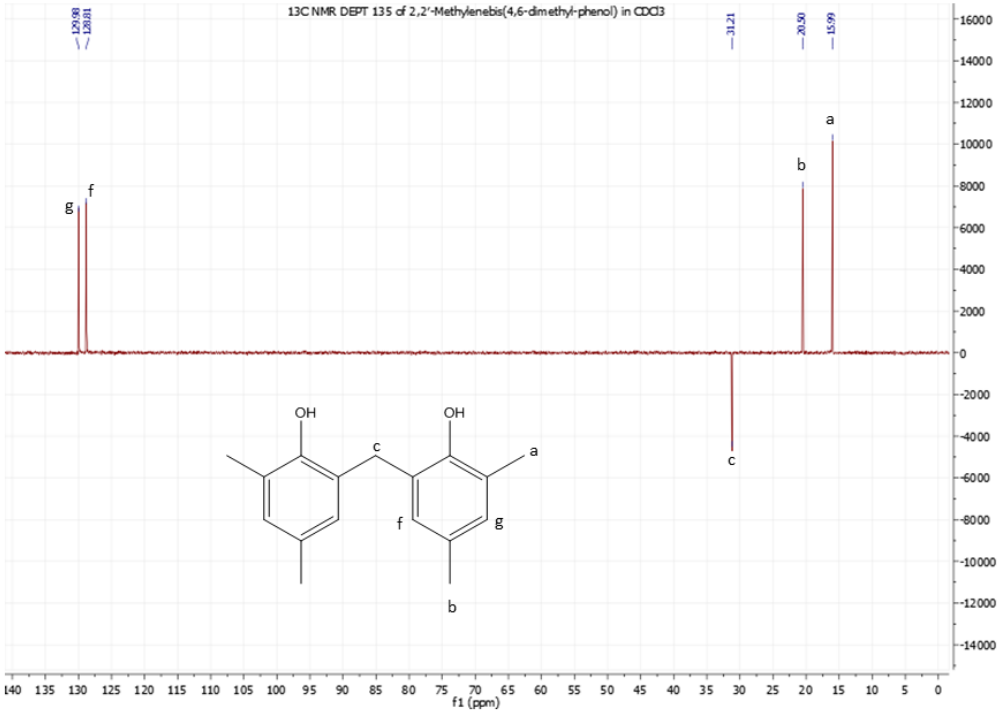

Appendix T4.9. ^{1}H NMR of mesityl ester (benzoic acid 2,4,6-trimethylphenylester) in $CDCl_3$. (**15**). ^{1}H NMR (400MHz, $CDCl_3$, 21°C) 6.940, 6.939 (s, 2H), 6.928, 6.927 (s, 2H), 2.526 (s, 6H), 2.324 (s, 3H), 2.290 (s, 3H) and 2.237 (s, 6H).

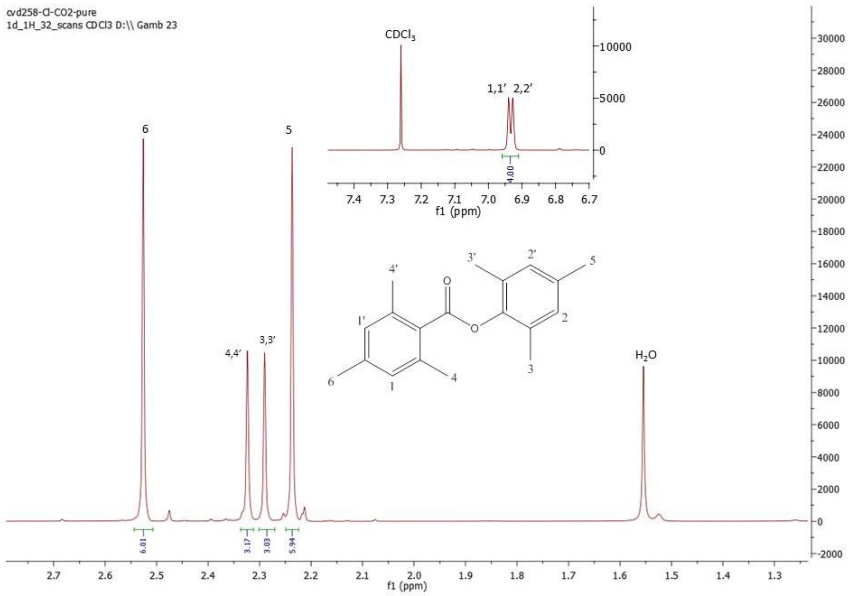

Appendix T4.10. TOF-MS-ESI of byproduct (**15**): M+Na = 305.1492

Elemental Composition Report **Page 1**

Single Mass Analysis
Tolerance = 50.0 mDa / DBE: min = -1.5, max = 50.0
Isotope cluster parameters: Separation = 1.0 Abundance = 1.0%

Monoisotopic Mass, Odd and Even Electron Ions
5 formula(e) evaluated with 3 results within limits (up to 50 closest results for each mass)

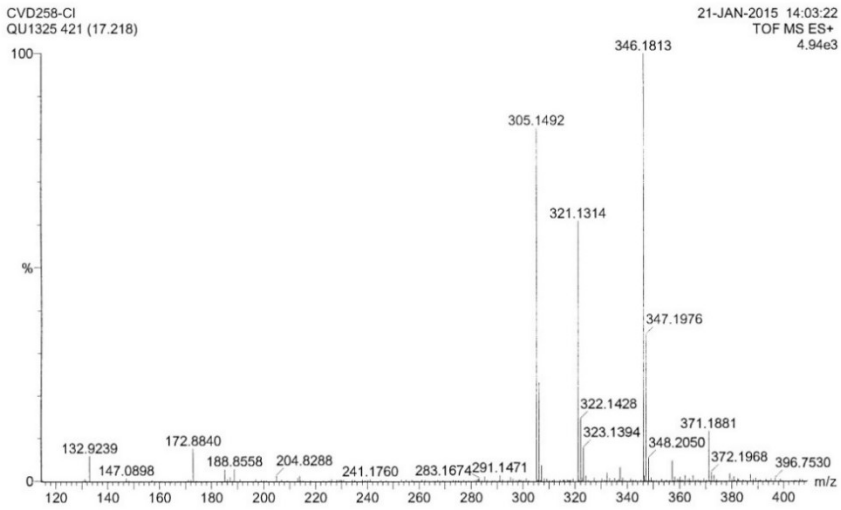

Minimum:				-1.5		
Maximum:		50.0	5.0	50.0		
Mass	Calc. Mass	mDa	PPM	DBE	Score	Formula
305.1492	305.1517	-2.5	-8.4	8.5	2	C19 H22 O2 Na
	305.1729	-23.7	-77.6	3.5	3	C16 H26 O4 Na
	305.1881	-38.9	-127.6	7.5	1	C20 H26 O Na

Appendix T4.11. MS-EI direct probe of benzoic acid 2,4,6-trimethylphenylester (**15**).

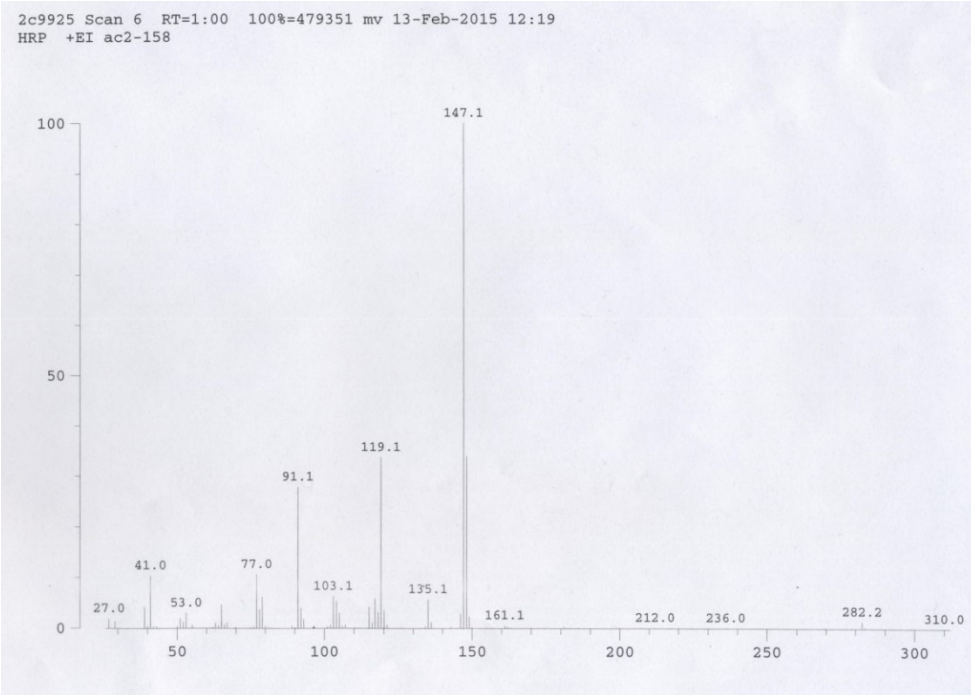

This work has been published in part in: **Camilo J. Viasus,** Nicholas P. Alderman, Bulat Gabidulin and Sandro Gambarotta, *Angew. Chem. Int. Ed.* **2018,** 57, 10928-10932.

Chapter 5. Reaction of CO_2 with a Vanadium(II) Aryloxide: Synergistic Activation of CO_2/-oxo Groups towards H-Atom Radical Extraction.

CJV: All work was done by me and all experimental part was also carried out by me. Dr. Gabidullin carried out the single crystal xray analysis. Dr. Alderman helped with the paper editing.

And in: **Camilo J. Viasus**, Bulat Gabidulin and Sandro Gambarotta, Linear end-on coordination of CO_2 using vanadium aryloxide. Submitted **2019**.

CJV: All work was done by me and all experimental part was also carried out by me. Dr. Gabidullin carried out the single crystal xray analysis.

5.1. Preamble

The reactivity of carbon dioxide with aryloxide vanadium(III) compounds has been explored. The idea behind this was, once again, to favor the elusive end-on bonding mode of CO_2 and possibly prevent the direct involvement of the ligand system in the reactivity of CO_2. Thus, by modulating the metal redox potential, we hoped to enhance radical behavior of CO_2 towards new paths of reactivity.

5.2. Introduction

The reactivity patterns of CO_2 are remarkably affected by the extent of electron-transfer performed by the attacking reagents.[74,107,289]

Floriani's pioneering work more than four decades ago demonstrated that a two-electron transfer may result in CO_2-coordination, either mono- or bimetallic (Scheme 5.1).[317,342,398,399] However, when the two electrons are provided by two one-electron donors via cooperative attack, a CO_2 deoxygenation to oxo- or carbonato-bridged dimetallic compounds occurs, with simultaneous evolution of CO.[76,342,359,400,401]

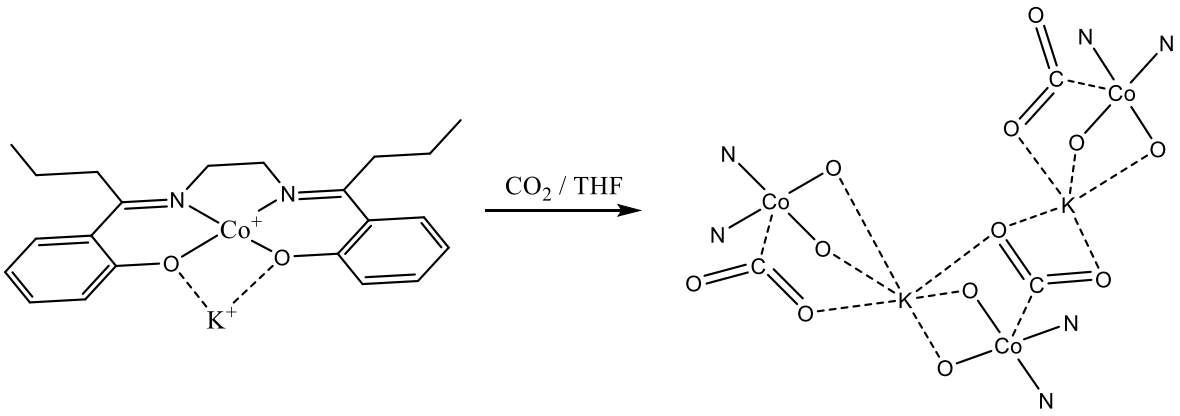

Scheme 5.1. Representative unit of the polymeric $[Co(pr\text{-}salen)KCO_2.THF]_n$. Ligand fragments were omitted for clarity.

Being able to limit and control one-electron transfers and extending the lifetime of the resulting $CO_2^{(\cdot-)}$ radical anion is central to subsequent coupling and formation of C-C bonds.[149,151] This process, documented in the CO_2 chemistry of lanthanides and TM, is so far exclusively limited to formation of the oxalate dianion.[73,148,149] Albeit a stoichiometric process, this remains a quite noticeable aspect of CO_2 chemistry. Once performed in a catalytic fashion, it can be regarded as the first step towards

carbohydrate synthesis, a much-wanted process and, so far, exclusive domain of naturally occurring photosynthesis.[8,140,153,184,402,403]

The possibility of successfully obtaining one-electron transfer is obviously related to both the reducing power of the metal (i.e. oxidation state)[404] and the nature of the ligand system[405,406], altogether extending the lifetime of the intermediate carbon-centered radical-anion.

Another critical factor for driving the reactivity is the coordination mode of CO_2 to the metal center.[407] The widely observed side-on coordination to one, two or even more metal centers preludes to either reversibility of the coordination or two-electron transformations.[408] The geometry of the ligand systems, however, may affect the initial bonding mode of CO_2 to the metal center. For example, the end-on coordination mode has long eluded proof until the characterization by Meyer of the sole and unique case of end-on bonded CO_2 complex to a sterically encumbered uranium moiety.[378] On the other hand, lanthanide complexes afford one-electron reduction and form oxalate derivatives.[145,318,409] Whether or not this behavior is the consequence of an initial end-on bonding mode remains unclear. Thus, we became interested in probing the possibility that sterically bulky ligands might favor, while in combination with strongly reducing metals, end-on bonding modes and which in turn might be the starting point for successful C-C or even C-H bond-forming one-electron reductions.

For this purpose, we have recently used low-valent vanadium, a strong reductant, in combination with bulky aryloxide ligands and investigated its reactivity with CO_2 (Chapter 4). While the much-anticipated deoxygenation to oxo-species and CO was still observed, the work also featured the occurrence of the rare end-on coordination mode. Furthermore, by tuning the electronic properties of the metal via judicious ligand replacement, it was possible to switch from the two-electron transfer to one-electron reduction, entering into a radical pattern of reactivity similar to the presented by Nicholas

et. al. later in 2018[410] (i.e. radical attack to the ligand system forming dimers or in our case with incorporation of CO_2 forming organic esters).

In this chapter, we describe the reaction of d^2 V(III) *and* d^3 V(II) complexes of a tetradentate ligand environment with CO_2. The use of vanadium(III) complexes transformed CO_2 to formate, a process which can be normally carried out with various electrochemical techniques.[161,411–413] In this part of the thesis however, we found that the formate anion can be generated by H-atom abstraction from the solvent through a reaction pattern unprecedented for CO_2.

5.3. Results and Discussion

5.3.1. Reactivity with CO_2 of a [(TMEDA)V(II)(ONNO)] complex

The ligand selected for this work was the tetradentate $[2,4\text{-}Me_2\text{-}2\text{-}(OH)C_6H_2CH_2]_2N(CH_2)_2NMe_2$ (H_2ONNO)[290] containing two phenolic oxygen and two aliphatic amine nitrogen donor atoms. The selection of this ligand was advised by the presence of the two phenolic functions and which, upon deprotonation, form the corresponding dianion necessary to provide electro-neutrality to the V(II) metal center. The aryloxide function was deemed important for the enhancement of the vanadium radical behavior and to prevent insertion reactions, otherwise unavoidable with organometallic or amide derivatives. The tetradentate geometry was also regarded as important for favoring the initial end-on coordination of CO_2 while the presence of the two amino residues could provide additional stability to vanadium due to their hard nature.[414,415]

The deprotonation of H_2ONNO was carried out with KH in THF through a very rapid and vigorous reaction. Subsequent reaction with $VCl_2(TMEDA)_2$[228,416] was also rapid affording the corresponding (ONNO)V(TMEDA) (**1**) previously reported in the literature (Scheme 5.2).[290]

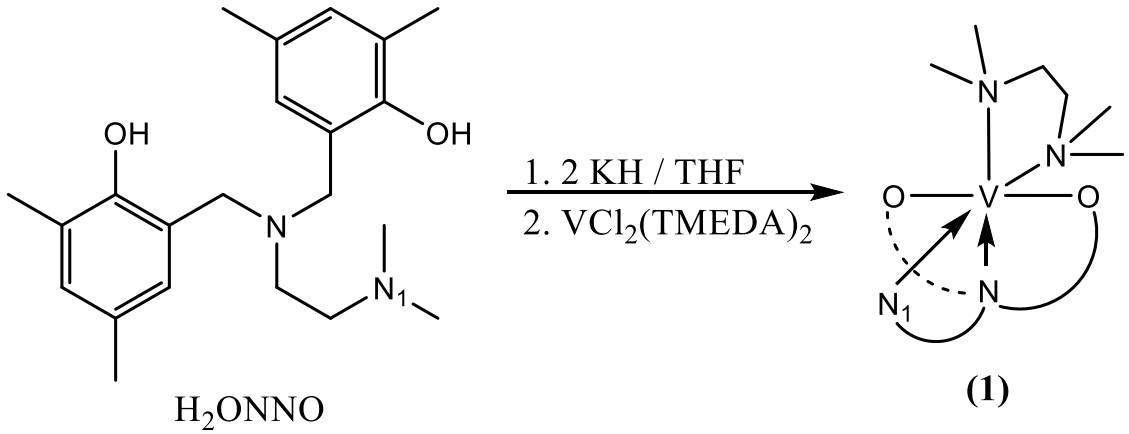

Scheme 5.2. Preparation of compound 1.

When a solution of **1** in toluene was exposed to CO_2 at 35 psi, in a steel reactor with a Pyrex liner and left undisturbed for 48 hours at room temperature, a color change occurred. Employment of lower pressures gave incomplete reactions. The GC analysis of the gas phase indicated that a substantial amount of CO was formed. The GC-MS of the solution phase indicated the presence of organic products identified as 2,10-Me_2diphenyl as the main component along with isomers. A crystalline solid, formulated as [(NONO)V]$_2$(μ-OH)(μ-formate) (**2**) was obtained upon layering the reaction solution with heptane (Scheme 5.3).

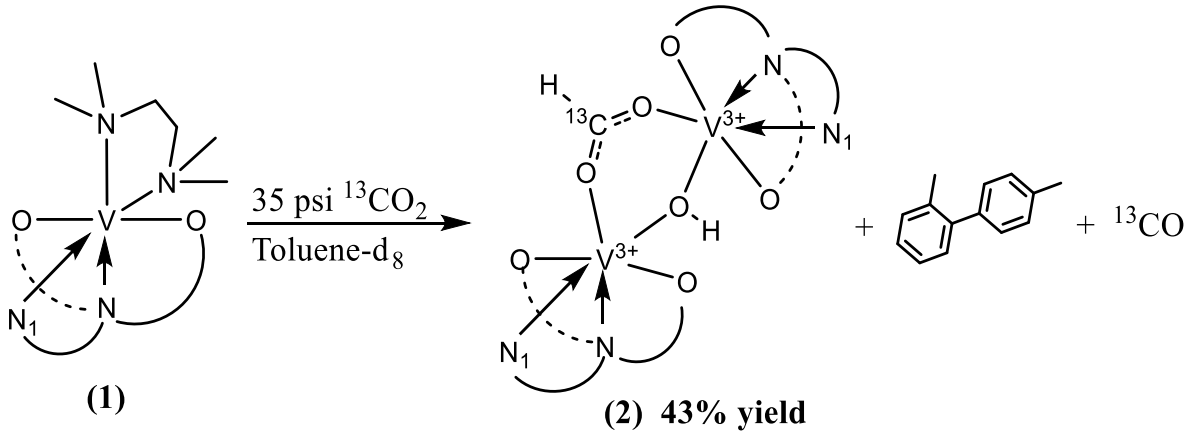

Scheme 5.3. Reactivity of compound 1 with CO_2.

The ESI-MS was consistent with the proposed formulation. The spectrum of the product obtained under identical conditions using $^{13}CO_2$ indicated that the formate residue was indeed generated by CO_2. Experiments carried out in deuterated toluene could not conclusively identify the masses of the deuterated formate and hydroxo fragments but gave the expected molar mass. IR spectra of the products obtained in toluene and d^8-toluene showed the expected isotopic shift of the OH and formate groups (Figure 5.1). The formulation of (**2**) was authenticated by an X-ray crystal structure (Figure 5.2). The structure did not display any particularly noticeable feature with the two metal centers each wrapped by the ligand with the expected geometry. The two bridging hydroxo- and formate groups occupy *cis*- coordination sites on each vanadium center. The positions of the two hydroxo and formate hydrogen atoms were identified by difference Fourier maps and their refinement gave noticeable improvement of the refinement factors. Bond distances and angles for the V-O(H)-V unit agreed with the proposed formulation.

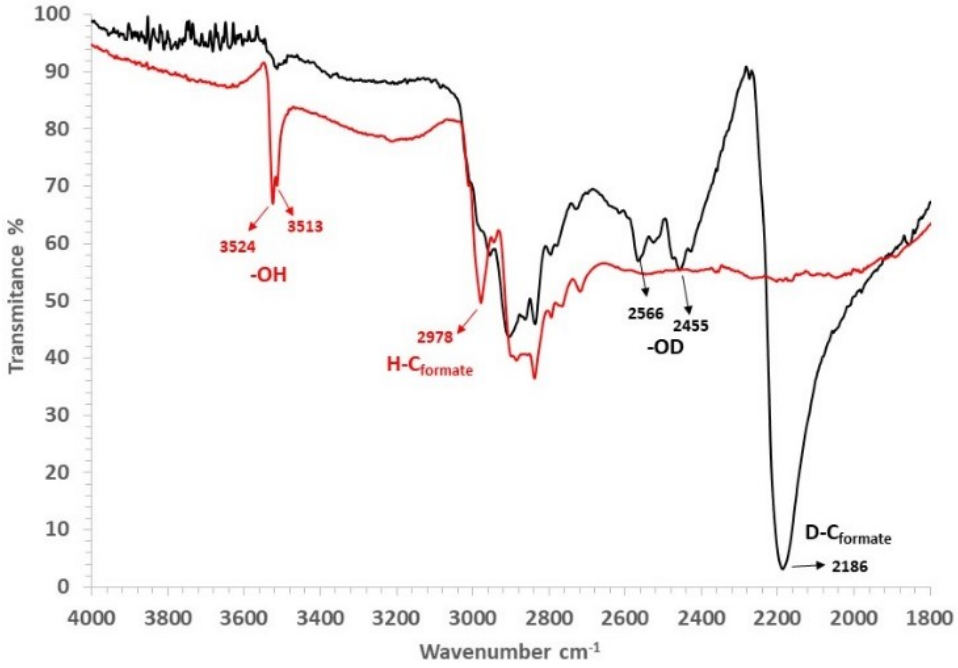

Figure 5.1. ATR FT-IR spectrum of compound (2) obtained in toluene (Red line) and in toluene-d8 (Black line).

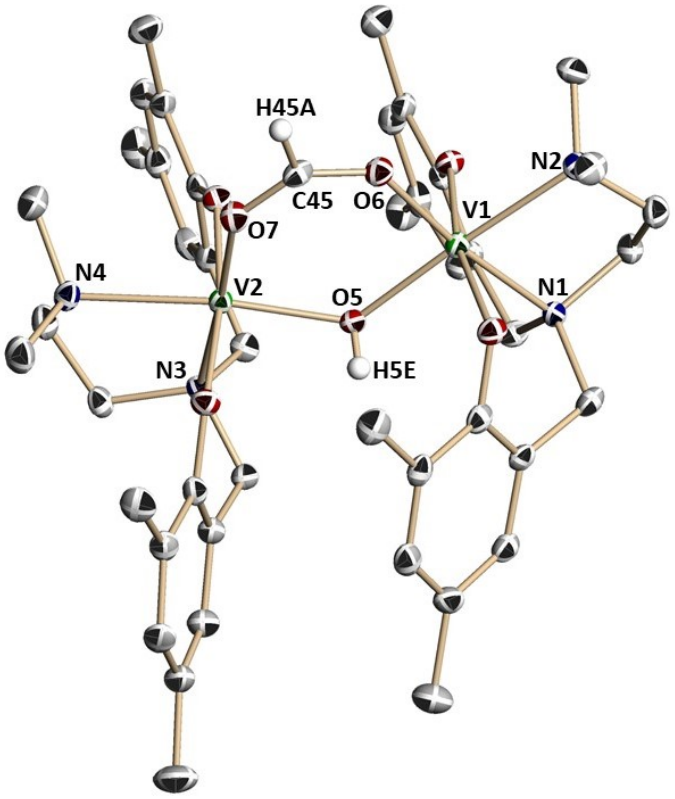

Figure 5.2. ORTEP diagram of compound **2** with ellipsoids drawn at 40% probability level. Selected distances and angles are as follows: V1 – O5 = 2.024 Å, V2 – O5 = 1.994 Å, V1 – O6 = 2.021 Å, V1 – O7 = 2.061 Å, V2 – O7 = 2.061 Å, O6 – C45 – O7 = 129.90o, V1 – O5 – V2 = 131.52^{o}, V1 – O6 – C45 = 134.89^{o} and V2 – O7 – C45 = 134.39^{o}.

The formation of **2** raises interesting mechanistic questions. The presence of the two different bridging units implies two separate events. One is a CO_2 deoxygenation with parallel formation of CO and a V-O-V moiety in a characteristic two-electron process. One has only to assume that the oxo formation is followed by H-atom extraction from the solvent. The formation of formate in the other step would imply a linearly end-on bonded CO_2 followed by its bending, one-electron transfer and one H atom extraction from the solvent. This radical behavior of linearly bonded CO_2 would be in line with our previous findings in the chemistry of V(III) aryloxides (Chapter 4).

What disconcerted us in this rationalization scheme was the possibility of an intermediate trivalent V-O-V unit to perform hydrogen atom abstraction with a consequent partial reduction to a mixed-valent

V(II)-(OH)-V(III) unit. Even in the event that the formation of formate would be the first step and CO_2 deoxygenation the second, the subsequent hydrogen atom extraction and partial reduction would be hard to explain.

To gather further insights, we have attempted the synthesis of $[(ONNO)V]_2(\mu\text{-}O)$ by careful oxidation of **1** which was reacted with CO_2 in an attempted step-by-step formation of **2**. While the reactions with O_2 gave the expected tetravalent $[(ONNO)VO]_2$ (**3**) *unreactive with* CO_2, the reaction with pyridine-oxide gave a more complex outcome. A pentanuclear species $\{[(ONNO)VO]_4[VO]\}$ (**4**) was formed containing five non-equivalent vanadium atoms in an average oxidation state of 3.6 (Scheme 5.4).

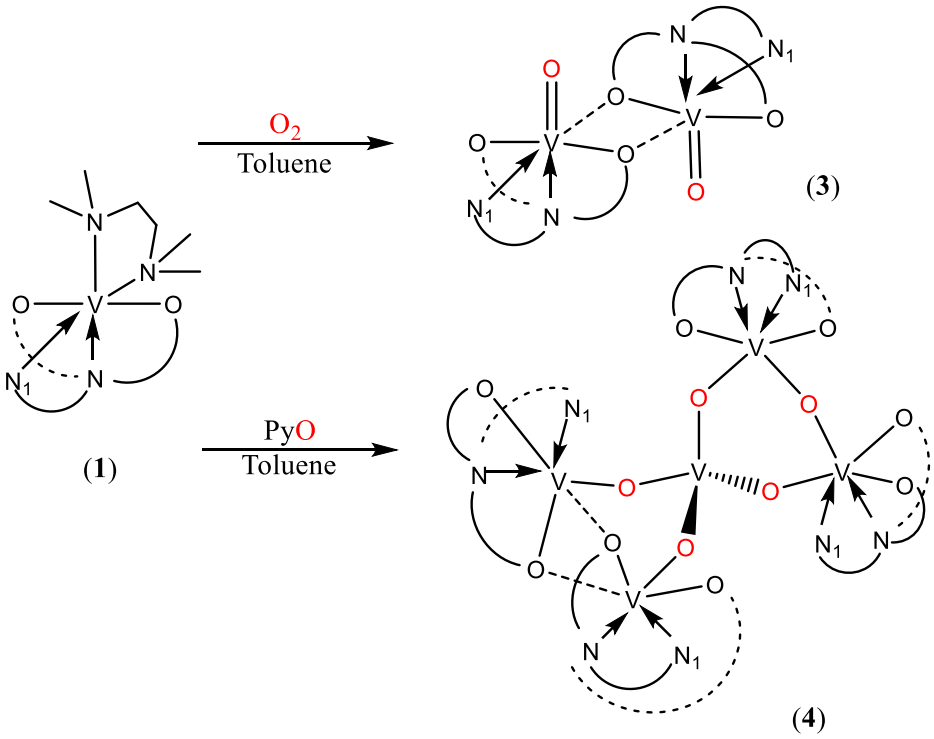

Scheme 5.4. Oxidation of **1** to produce **3** and **4**.

Regardless of the complex structure and the lower oxidation state of the metal, complex **4** *is also unreactive* with CO_2. The outcomes of the two reactions were both authenticated by X-ray analysis

(Figure 5.3). The absence of OH functions was indicated by the IR spectra. Bond distances and angles also were in the expected range for the proposed formulation.

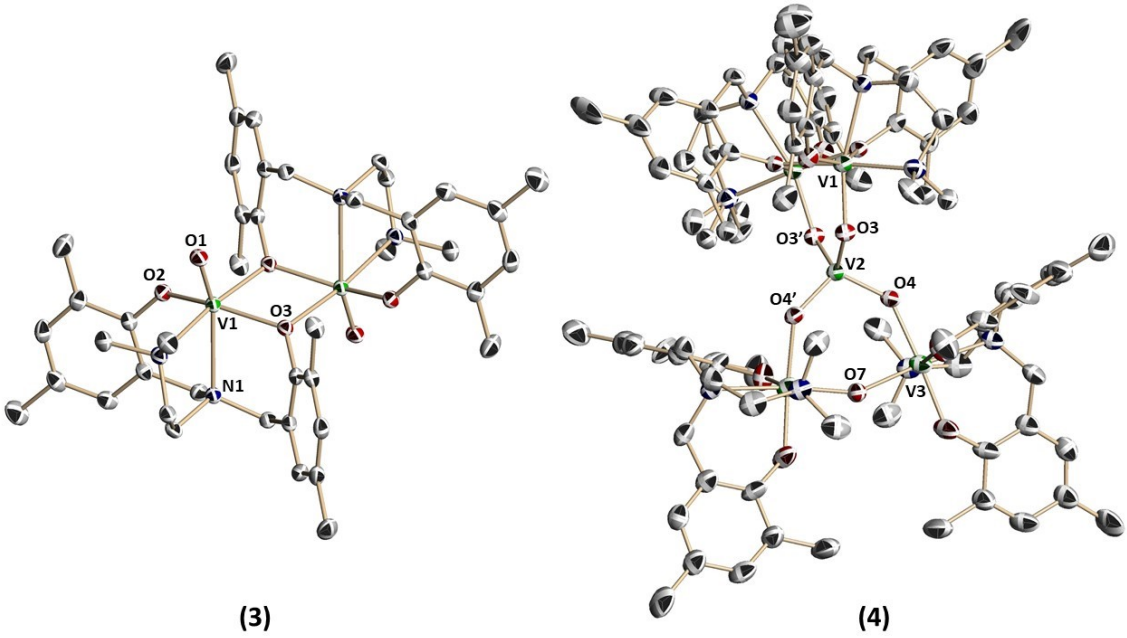

Figure 5.3. ORTEP drawings of **3** and **4** with ellipsoids drawn at 30% probability level. Hydrogen atoms were omitted by clarity. Selected bond distances for **3**: V1-O1 = 1.605 Å, V1-N1 2.443 Å, V1-O3 = 2.079 Å and V1-O2 = 1.899 Å. Selected bond distances and angles for **4**: V1-O3 = 1.908 Å, V2-O3 = 1.729 Å, V2-O4 = 1.711 Å, V3-O4 = 1.986 Å, V3-O7 = 1.929 Å, V3-O7-V3' = 151.71° and O4-V2-O3 = 110.13°.

The results of the oxidation reactions described above confirmed that tetra- and lower valent V-O-V units *do not perform* H atom extraction. Thus, the formation of the OH residue in (**2**) cannot be explained by assuming an initial CO_2 deoxygenation.

We have therefore performed DFT calculations on the reaction of (**1**) with CO_2. The calculations predict the initial formation of a transition state consisting of an adduct with CO_2 arranged end-on and possessing a significant bending [O-C-O = 131.3°]. Upon evolution of CO, the transition state evolves into an intermediate ground state (gs3) with a V-O-V framework. Natural population analysis (NPA) by DFT calculations for gs3 (Chart 5.1) indicates that this unit should adopt a bent geometry with a V-O-V angle of about 159.2 °. Not surprising for a ground state, the electron density distribution clearly

indicated that there is *no increase nor deficiency of electron density* on the atoms of the V-O-V core. In turn, this confirmed that no hydrogen abstraction and formation of -OH residues should be expected for this intermediate oxo- species. Further reaction with CO_2, however, revealed an intriguing and unexpected behavior. Once CO_2 is added to gs3, a dimeric transition state ts6 is assembled with CO_2 adopting a bridging bonding model (Chart 5.1).

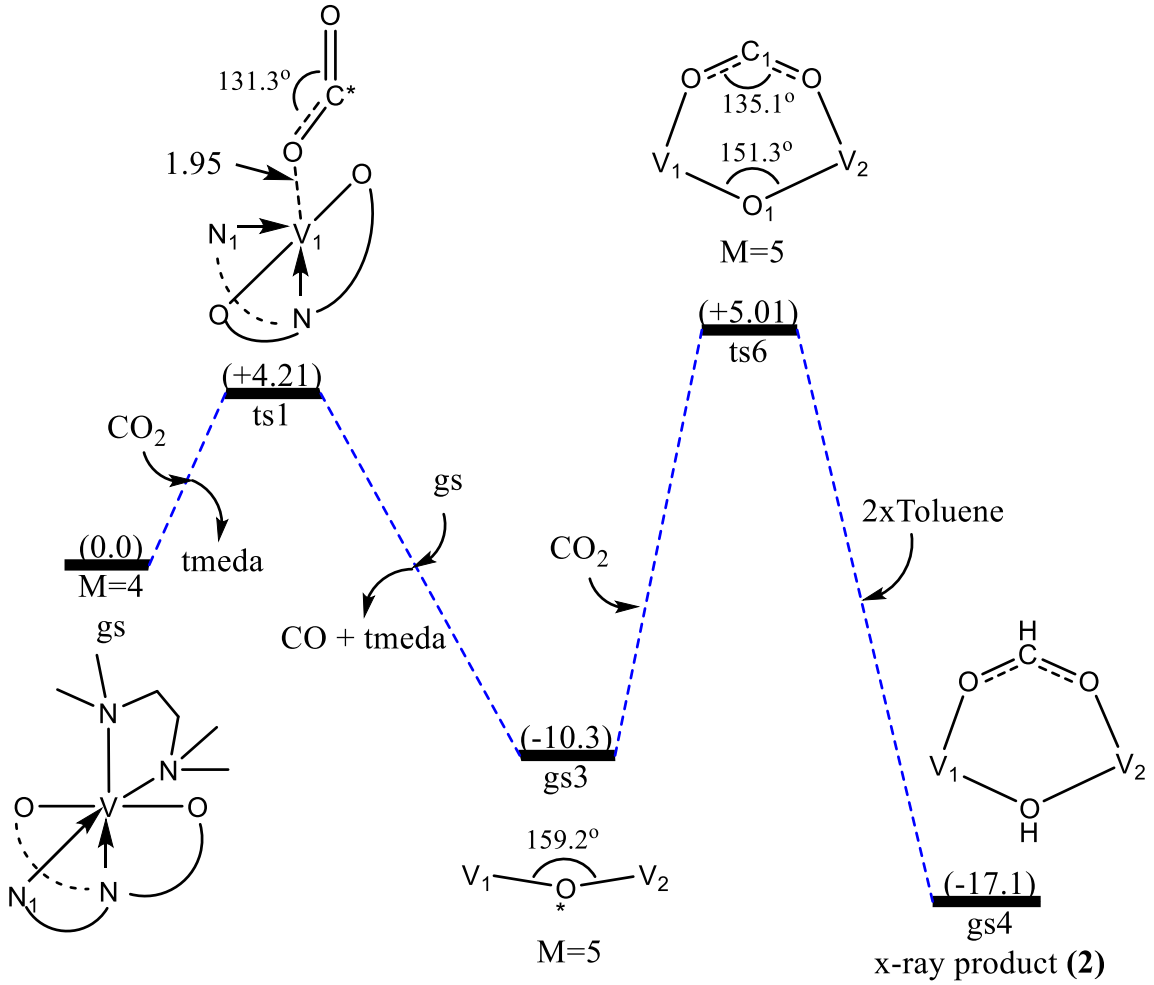

Chart 5.1. Relative Gibbs energy profile (kcal/mol) for the proposed mechanism in the reactivity of CO_2 using vanadium(II) compound.

An inspection of the Mulliken charges and spin density for the μ-oxo-, bridging CO_2 carbon and vanadium atoms revealed that the two vanadium centers slightly decrease their spin density with

respect to gs3 as a result of the acquired presence of CO_2 (Table 5.1). By the same token, the CO_2 carbon atom C1 shows an *increase of spin density* with respect to ts1, while the bridging oxygen atom instead *decreased its spin density* with respect to gs3.

We have also considered the possibility that the starting V(II) may afford a dianonic dinuclear CO_2 complex. While DFT predicts for this hypothetical complex the same bridging arrangement as observed by Maron, Okuda and Cummins,[417] the energy profile was less favorable with respect to the simple deoxygenation. The scenario provided by ts6 is therefore somewhat reminiscent of a frustrated Lewis pair, whose high reactivity is sufficient to perform dihydrogen activation[418–421] among other remarkable performances.[422,423]

Table 5.1. Mulliken charges and spin density of ts1, gs3 and ts6.

Atom	Mulliken charges	Spin Density	NPA
V1[a]	1.078475	2.101240	2.01
C*[a]	0.188108	0.734055	0.66
V1[b]	1.042943	2.094055	2.02
V2[b]	1.154588	2.075989	1.98
O*[b]	-0.821774	-0.059004	-0.02
V1[c]	0.980614	1.839976	1.75
V2[c]	0.950011	1.826881	1.73
O1[c]	-0.610253	-0.409999	-0.39
C1[c]	0.271552	0.784811	0.73

[a] ts1, [b] gs3, [c] ts6

In other words, by positioning CO_2 in a bent-bridging coordination mode on a pre-formed V-O-V unit (ts6 in Chart 5.1), it enhances electron density on the C at the expense of the oxo-O atom, thus creating

the perfect scenario for hydrogen extraction not only by C but also by the bridging oxide. We found remarkable that a minor increase of the formal oxidation state as from the trivalent state of gs3 to the 3.6 of (**4**) is sufficient to completely obliterate the reactivity with CO_2.

5.4. End-on linear coordination of CO_2 on a V(III) aryloxide compound

5.4.1. Introduction

Controlling the reactivity of CO_2 is doubtlessly a daunting task.[346] The work described above reiterates that the bonding mode adopted by CO_2 during preliminary coordination is central to determining its reactivity. The reader should be reminded that the most common is side-on, either on a monometallic system or on a bifunctional complex, where eventual charge separation between an anionic site and a Lewis acidic one is the key to reversible fixation.[73] More recently, the fixation of CO_2 by bifunctional systems has also been established with CO_2 adopting a linear coordination geometry with two different metals sited at the two edges of the linearly coordinated CO_2.[424] Instead, the linear end-on bonding mode remains so far unique, having been determined in the sole case of a trivalent uranium complex.[425] The reactivity that can be expected by this sort of bonding mode remains unknown.

In the system described above, theoretical work has clearly indicated that the linear end-on bonding mode of CO_2 is the key to understanding its radical behavior. We have therefore multiplied efforts and succeeded in isolating and characterizing the intermediate CO_2 complex adding a second example to the sole existing case of linear end-on bonding mode.[425] We further confirm that such species is indeed responsible for the unusual reactivity pattern and investigated further the reactivity of this rare bonding mode.

5.4.2. Results and Discussion

We have shown above that the reaction of (ONNO)V(TMEDA) with CO_2 affords an unusual deoxygenation and radical H atom extraction leading to the formation of $[(NONO)V]_2(\mu$-

OH)(μ–formate) (**3**) (Scheme 5.3). The reaction required employment of pressure and moderate heating. By carrying out the reaction at low temperatures and enabling sufficient time (1 atm of pressure and -10°C) a new species can be isolated in analytically pure form and significant yield (Scheme 5.5). The GC of the headspace of the vessel clearly shows the presence of CO produced after 12h of reaction.

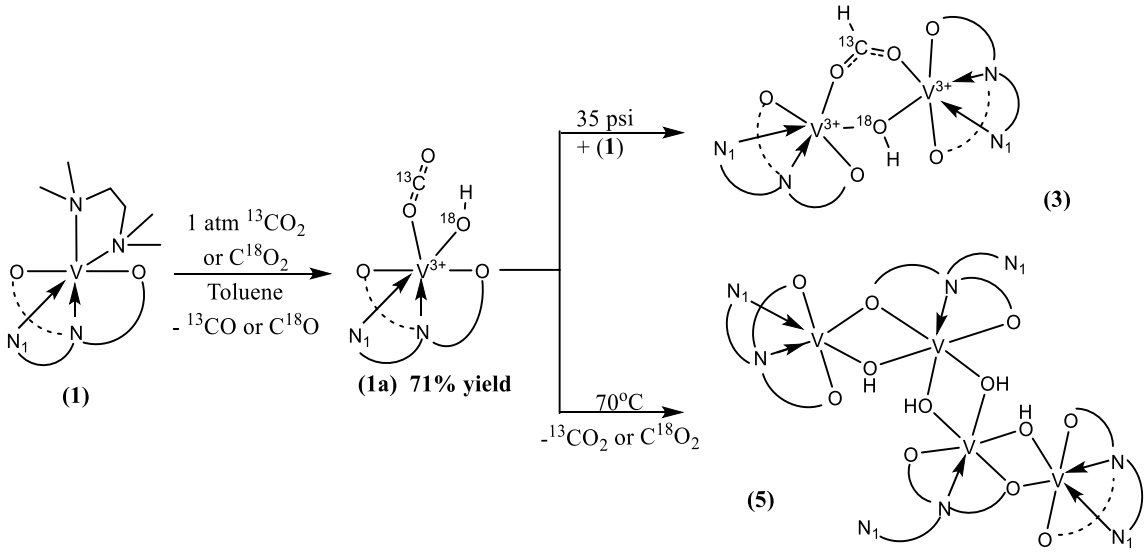

Scheme 5.5. Vanadium(II) schematic reactivity with $^{13}CO_2$/$C^{18}O_2$.

A red crystalline material, formulated as (ONNO)V(OCO)(OH) (**1a**) on the basis of its X-ray crystal structure, was obtained by slow diffusion of pentane (71%). The identity of the terminally bonded hydroxyl group was confirmed by difference Fourier maps, enabling the location of the H. Furthermore, FT-IR of isotopically labelled crystalline materials ($C^{18}O_2$, $^{13}CO_2$), showed the expected shifts for the OH group and coordinated CO_2 for a complex prepared in non-labelled and d^8-toluene, thus confirming that the H atom originated from toluene and the O atom and CO from CO_2. The GC-MS of the reaction mixtures allowed identification of the presence of a few isomeric dibenzyl species as observed in the case of the preparation of **3**. ESI-MS were in line with the above findings. The metric parameters of **1a**

are reported in Figure 5.4, indicating minimal deviation from the linearity and alteration of the C-O distance with respect to free CO_2. The visible bending of the V-O-C vector is clearly not the result of steric interaction within the complex but of the enhanced single bond character of the V-O bond. Curiously this does not result in significant alteration of the two C-O double bonds. The end-on coordination as observed in **1a** is the first case for the transition series and second to the sole example of a U(III) derivative reported by Meyer.[425]

We found it rather curious that **1a** does not further deoxygenate CO_2 through a cooperative attack by a second trivalent vanadium center to finally afford a binuclear oxo-bridged tetravalent complex. We previously showed that such a species is perfectly stable and can be obtained via direct reaction of **1** with strong oxidants. This behavior reiterated to us that the coordination of CO_2 might be sufficiently strong to attempt reactivity studies. The thermal stability of **1a** was probed by heating a toluene solution.

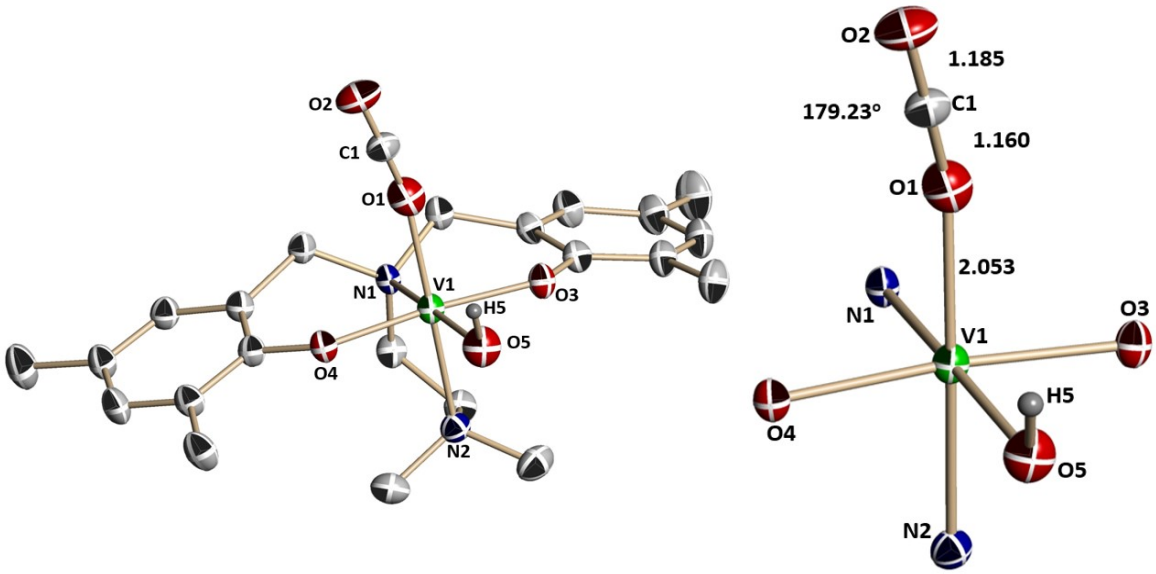

Figure 5.4. Thermal ellipsoid plot of **1a** with ellipsoids drawn at the 30% probability level. Hydrogen atoms, excepted for the V-OH unit, were omitted for clarity. Selected distances and angles of compound **1a** are as follows. V1 – O1 = 2.053 Å, V1 – O3 = 1.916 Å, V1 – O4 = 1.919 Å, V1 – O5 = 2.164 Å, V1 – N1

= 2.144 Å, V1 – N2 = 2.260 Å, V1–O1–C1 = 159.5°, O1–V1–N2 = 174.5°, O5–V1–N1 = 174.4° and O4–V1–O3 = 174.5°.

At the T of about 70°C a slight color change and the presence of CO_2 gas in the headspace of the reactor indicated that **1a** had decomposed. From the reaction mixture a new V(III) hydroxo-bridged tetranuclear complex **5** was isolated and fully characterized including X-ray (Figure 5.5). Exposure of **5** to CO_2 at high pressure reformed **1a** (Scheme 5.5). In contrast, reaction of crystalline **1a** in toluene solution with **1** afforded **3** in good yield in agreement with the reaction mechanism presented in Chart 5.1. It should be reminded that this reaction implied H-atom abstraction from the solvent. Accordingly, isomeric diphenyl derivatives were detected in the reaction mother liquor.

Single point DFT calculations on **1a** were carried out in Gaussian09 suite package at the CAM-B3LYP/6-311G level of theory. In order to determine electrophilic, nucleophilic and radical Fukui indexes for the compound **1a**, the calculations were performed on neutral, cationic and anionic structures. Hirschfeld charges on each of the atoms in the structure were obtained for the three mentioned states. Condensed reactivity Fukui indexes were determined and evaluated. Based on the equilibrium geometry of compound **1a**, the vanadium atom is the most susceptible to receive nucleophilic attack (CFI = 0.16) followed by O3, O4, O5, O2 and C1 with CFI 0.07, 0.06, 0.05, 0.04 and 0.02 respectively. To the contrary, O5 in -OH, O1 in CO_2 and C1 in CO_2 presented the highest probability to receive electrophilic attack with CFI 0.08, 0.05 and 0.03 respectively. By the same token, vanadium atom, O5, O2, O3, O4 and C1 have the highest probability of displaying radical behavior reactivity with CFI of 0.21, 0.07, 0.05, 0.04, 0.04 and 0.02 respectively. Clearly, these results suggest that using compound **1a** in an electrophilic or a radical reaction will have a better chance than with a nucleophilic reagent, where CO_2 would not be part of the reaction due to its lower chance to be activated (Appendix T5.3).

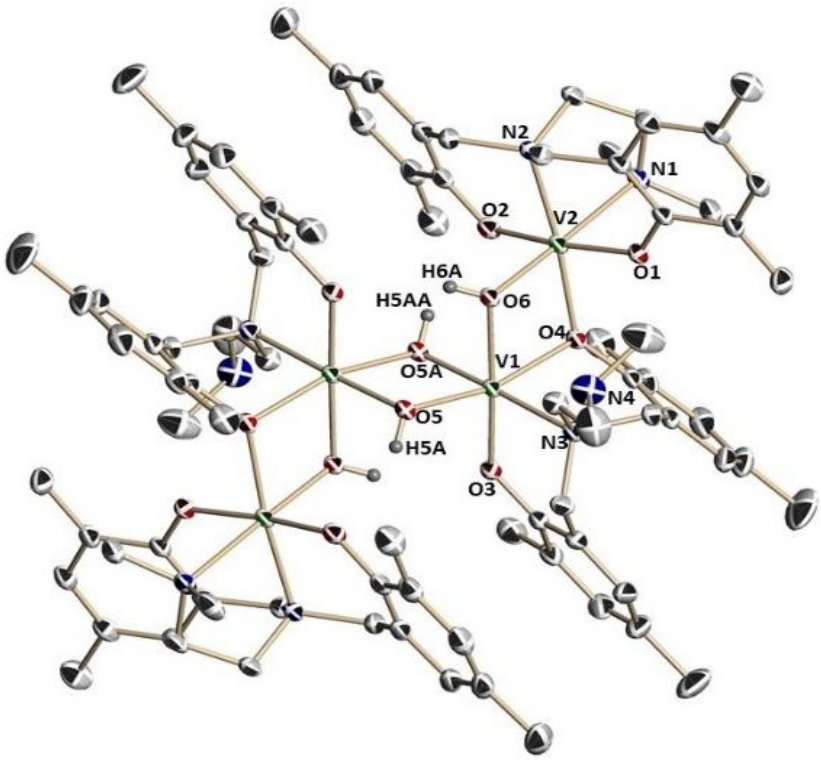

Figure 5.5. Thermal ellipsoid plot of **5** with ellipsoids drawn at the 30% probability level. Hydrogen atoms expected in the V-OH fragment were omitted for clarity. Selected distances and angles of compound **5** are as follows. V1 – O5 = 1.958 Å, V1 – O3 = 1.926 Å, V1 – O4 = 2.013 Å, V1 – O6 = 2.046 Å, V1 – N3 = 2.221 Å, V2 – O1 = 1.940 Å, V2 – O2 = 1.937 Å, V2 – O4 = 2.076 Å, V2 – O6 = 1.948 Å, V2 – N1 = 2.277 Å, V2 – N2 = 2.144 Å, V1 – O5 – V1A = 95.74°, V1 – O6 – V2 = 103.66° and V1 – O4 – V2 = 100.30°.

Besides the intriguing bonding mode of the coordinated CO_2 residue, both the presence and the origin of the OH group deserve attention. The isotope labelling experiments clearly demonstrated that the O atom was provided by CO_2 while the H atom arises from hydrogen-atom radical-abstraction from the solvent. In turn, this indicates that the initially formed vanadium oxo-derivative cannot contain the metal in its tetravalent state since the ONNOV(IV)O is a perfectly stable and CO_2-unreactive dimeric species. This leaves us with the only possibility that the initial deoxygenation is carried out by cooperative one-electron attack of two divalent vanadium centers on the same CO_2 molecule releasing

CO and affording a trivalent oxo-bridged vanadium complex. Unsurprisingly, this species, clearly capable of enhanced radical behavior in addition to being able of coordinate CO_2, has so far eluded isolation and characterization.

5.5. Reactivity with CO_2 of [V(III)(ONNO)X] complexes

The most valuable information emerging from the reactivity of ONNO divalent vanadium complex with CO_2 is that a V(III)-oxo species might be the true starting point for CO_2 one-electron activation. Naturally, multiple attempts were made to prepare vanadium(III) compounds as related as possible to the elusive oxo- species. The aim was to prevent the direct reduction of carbon dioxide to CO and the formation of inert vanadyl(V) derivatives. Given the versatility of the ligand system used before and considering the change from the divalent to trivalent state of the vanadium metal center, only a minor ligand modification was taken into consideration as a possible alternative. In addition to using the standard $(ONNO)H_2$ ligand, we have replaced the terminal tertiary amine pendant with another containing an ether oxygen (Scheme 5.6). We hoped that this modification would introduce only a slight change of electron density and of the reducing power of vanadium(III) with beneficial effects on CO_2 activation.

Following the previous protocol, the new selected ligand $(OONO)H_2$ was deprotonated with two equivalents of KH and the reaction mixture reacted *in situ* with $VCl_3(THF)_3$ to afford the corresponding (OONO)VCl(THF) (**6**).

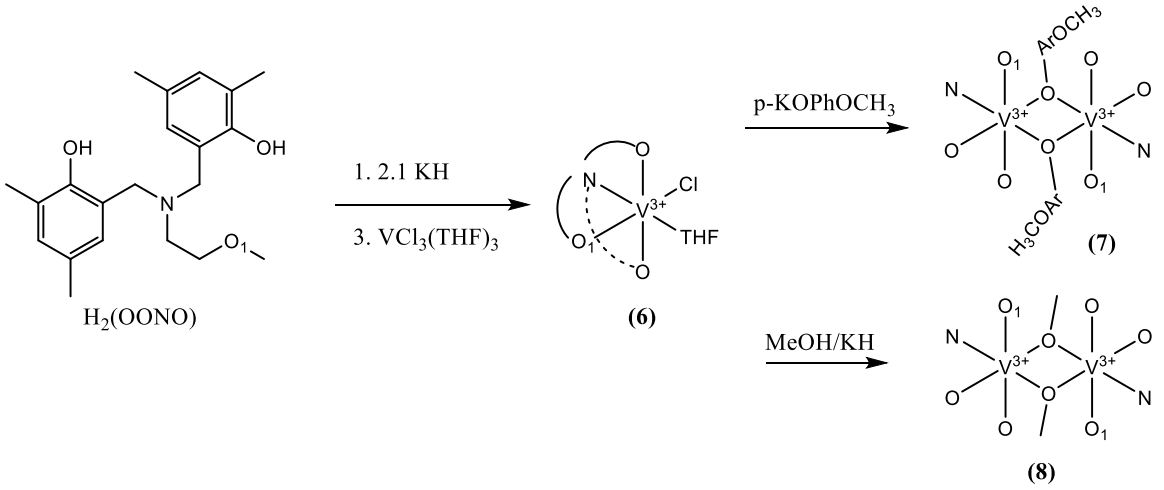

Scheme 5.6. Preparation scheme for compounds **6**, **7** and **8** using vanadium(III) precursor.

The structure of **6** was authenticated by X-ray diffraction analysis as well as analytical measurements.

Compound **6** was used as starting material for subsequent ligand replacement reactions (Figure 5.6).

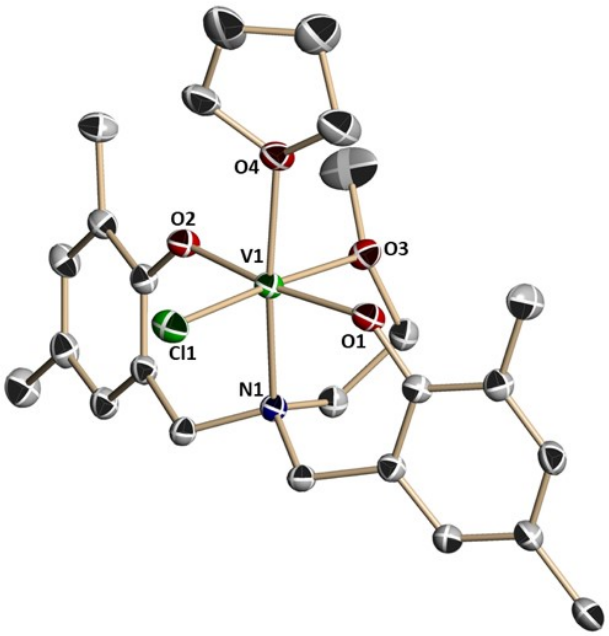

Figure 5.6. Thermal ellipsoid plot of **6** with ellipsoids drawn at the 30% probability level. Hydrogen atoms were omitted by clarity. Selected distances and angles of compound **6** are as follows. V1-N1 = 2.122 Å, V1-O1 = 1.908 Å, V1-O2 = 2.171 Å, V1-O3 = 1.903 Å, V1-O4 = 2.099 Å, N1-V1-O4 = 169.88°, O2-V1-Cl = 176.93°, O2-V1-Cl 176.93° and O1-V1-O2 = 171.63°.

Compound **6** did not react with CO_2. Temperatures up to 60 ^{0}C and CO_2 pressures up to 200 psi did not modify the outcome. The electron withdrawing presence of the Cl atom obviously had a negative quenching effect on the reactivity of the metal center.

Two new fully characterized dimeric compounds [(OONO)V(μ-*p*-OPhOCH$_3$)]$_2$ (**7**) and [(OONO)V(μ-OCH$_3$)]$_2$ (**8**) were obtained upon reaction of **6** with potassium *p*-methoxyphenol salt and potassium methoxide respectively. The reactivity of **7** was also examined (Figure 5.7). Again, and in line with the behavior of **6,** this compound was unreactive with CO_2.

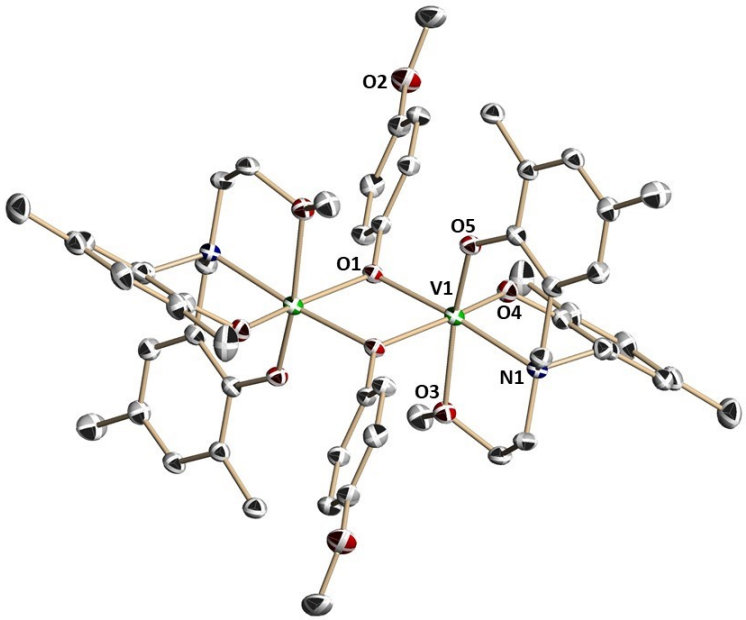

Figure 5.7. Thermal ellipsoid plot of **7** with ellipsoids drawn at the 30% probability level. Hydrogen atoms were omitted by clarity. Selected bonds and angles are as follows: V1 – V1' = 3.283 Å, V1 – O1 = 2.0282 Å, V1 – O3 = 2.1965 Å, V1 – O4 = 1.8955 Å, V1 – O5 = 1.8851 Å, V1 – N1 = 2.1722 Å, V1-O1-V1' = 105.79^o and V1-O5-CAr = 132.03^o.

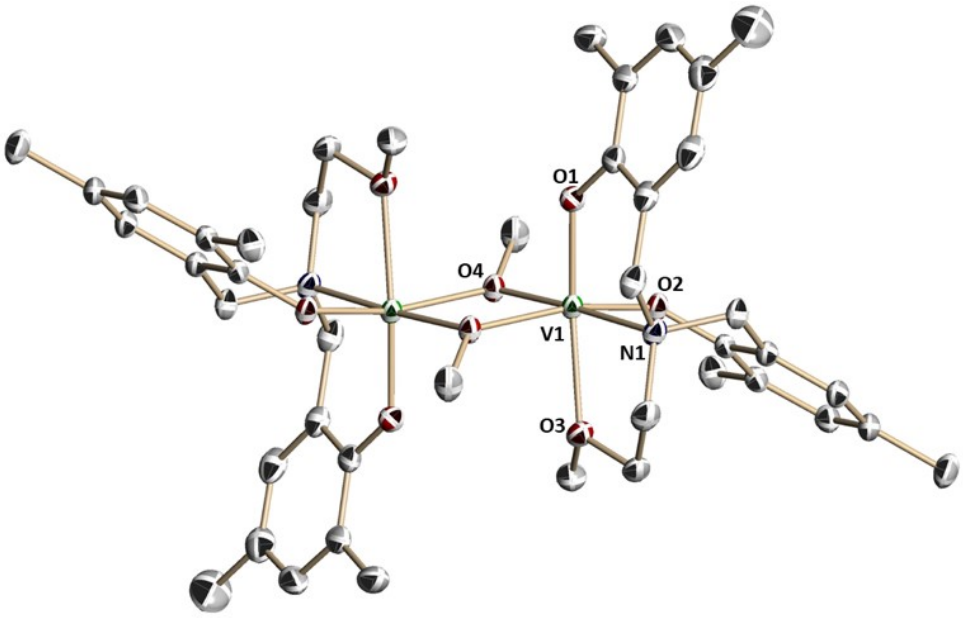

Figure 5.8. Thermal ellipsoid plot of **8** with ellipsoids drawn at the 30% probability level. Hydrogen atoms were omitted by clarity. Selected bonds and angles are as follows: V1 – V1' = 3.161 Å, V1 – O1 = 1.899 Å, V1 – O2 = 1.926 Å, V1 – O3 = 2.177 Å, V1 – O4 = 1.984 Å, V1 – N1 = 2.166 Å, V1-O4-V1' = 103.14° and V1-O4-C_{Me} = 131.39°.

To our growing concern, complex **8** (Figure 5.8) was also unreactive towards CO_2. We have therefore, reverted the ligand choice to the original ONNO successfully used above (Scheme 5.3). The preparation of the starting (ONNO)VCl(THF) (**9**) was carried out in the usual manner as well as its functionalization with aryloxide and methoxide (Scheme 5.7).

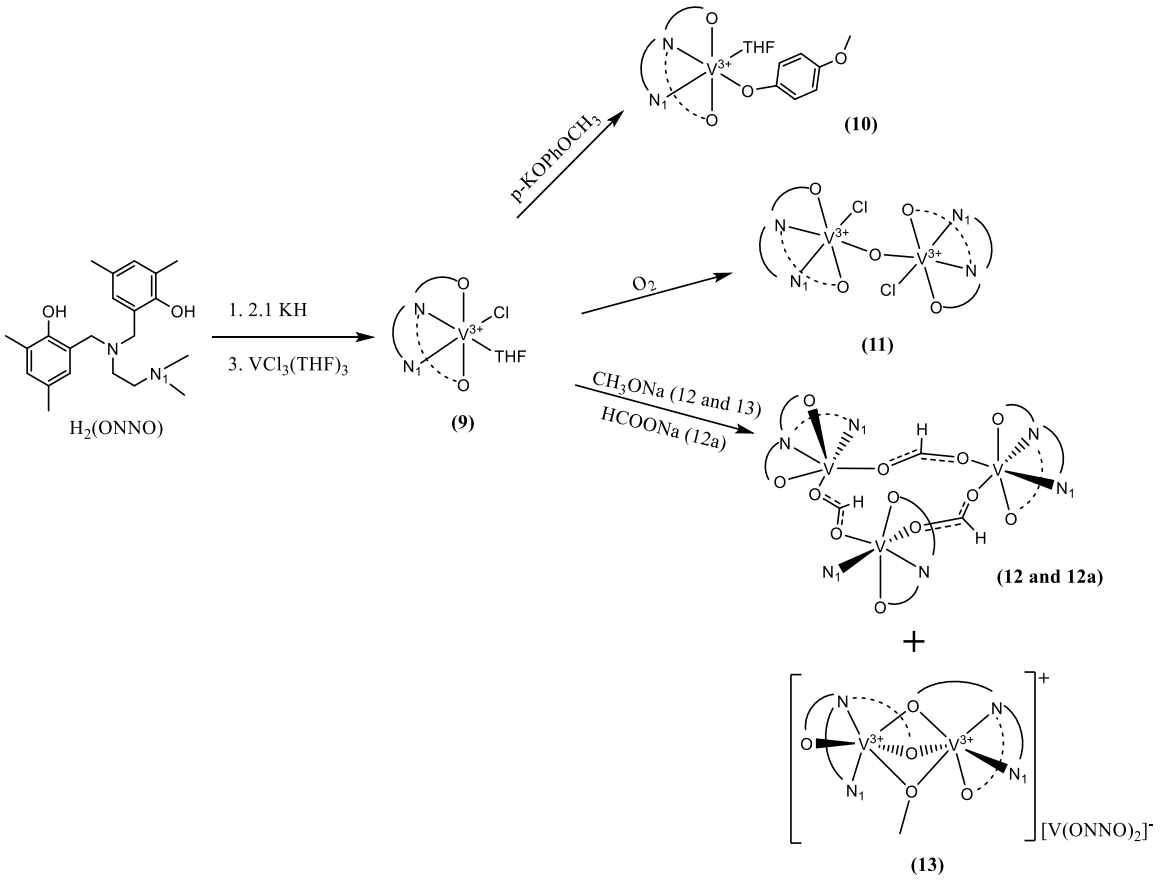

Scheme 5.7. Preparation scheme for compounds **9**,[290] **10**, **11**, **12**, **12a** and **13** using vanadium(III) precursor.

As before, the ligand $(ONNO)H_2$ was deprotonated with KH. Further in situ reaction with $VCl_3(THF)_3$ afforded (ONNO)VCl(THF) (**9**) (Figure 5.9A). As usual, the structure was authenticated by X-ray diffraction analysis confirming a previous literature assignment.[290] Compound **9** was unreactive with CO_2, but the presence of the residual chlorine made it a versatile starting material for ligand replacement reactions with more nucleophilic groups such as aryloxides and alkoxides. Compound **10** was obtained upon reaction with the aryloxide potassium salt (Figure 5.9B) and tested with CO_2 under the same conditions as **7** and **8.** Unfortunately, no reactivity was observed. Employment of harsher reaction conditions (70°C and 200 psi), did not modify the outcome of the reaction.

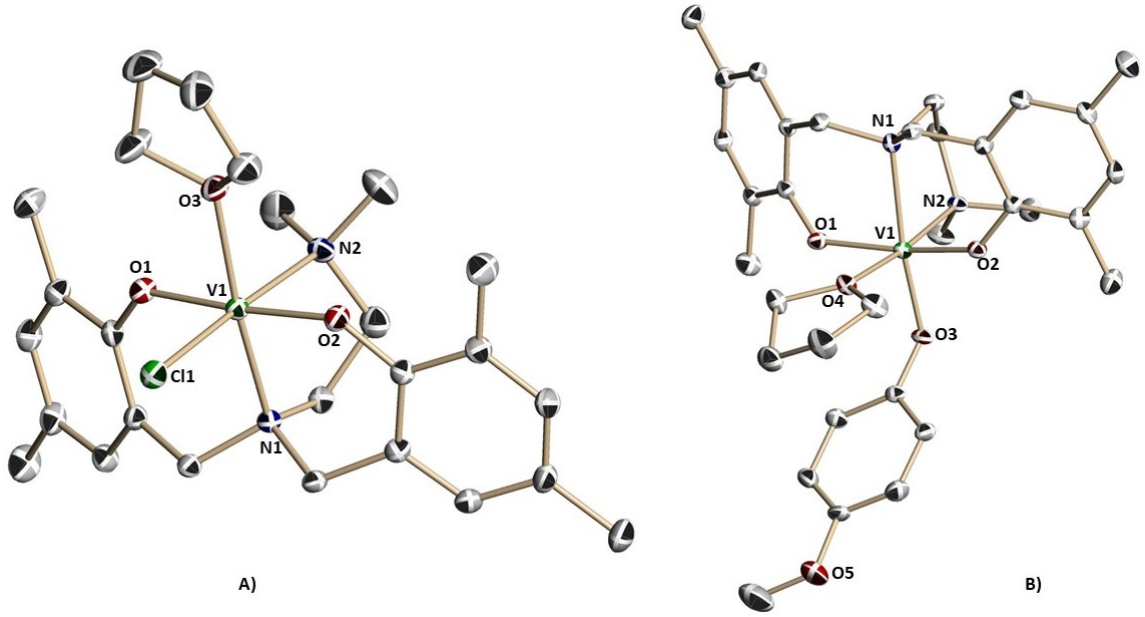

Figure 5.9. Thermal ellipsoid plot of **9**(A) and **10**(B) with ellipsoids drawn at the 30% probability level. Hydrogen atoms were omitted for clarity. Carbon atoms are in grey color. Selected distances of compound **9** and **10** are as follows. For compound **9**: V1-N1 = 2.134 Å, V1-N2 = 2.252 Å, V1-O1 = 1.901 Å, V1-O2 = 1.925 Å and V1-O3 = 2.130 Å. For compound **10**: V1-N1 = 2.2390 Å, V1-N2 = 2.1749 Å, V1-O1 = 1.9217 Å, V1-O2 = 1.9225 Å, V1-O3 = 1.9094 Å and V1-O4 = 2.1572 Å.

Albeit inert towards CO_2, compounds **9** and **10** were highly reactive with dry oxygen. In the case of **9,** a new oxo-bridged species [(ONNO)VCl(μ-O)] (**11**) was obtained (Figure 5.10). Similar reaction of **10** however, only afforded intractable materials. Looking at the possibility of obtaining the critical trivalent oxo-derivative discussed above, attempts to lower the oxidation state of **11** were carried out with metallic K with molar ratio 1:1. The reaction gave a red solution in THF, indicating reduction to V(III), but unfortunately only intractable materials were obtained once again.

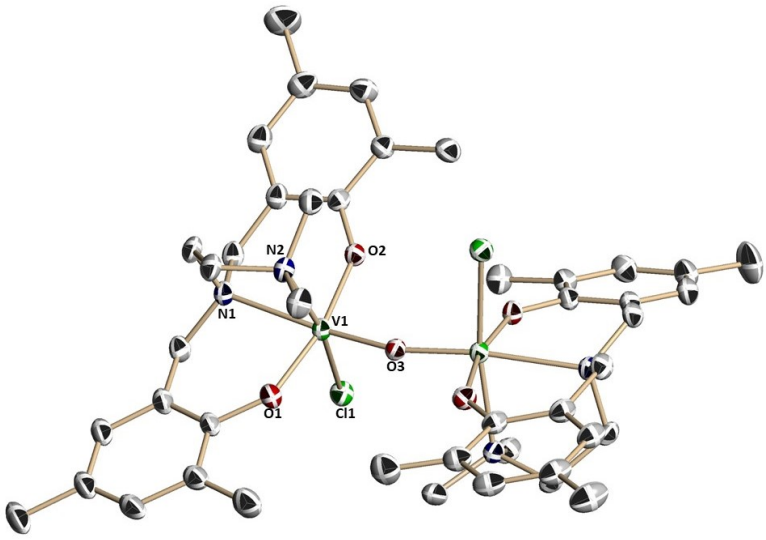

Figure 5.10. Thermal ellipsoid plot of **11** with ellipsoids drawn at the 30% probability level. Hydrogen atoms were omitted by clarity. Selected bond distances and angles are presented as follows. V1-O3 = 1.778 Å, V1-Cl1 = 2.390 Å, V1-O1 = 1.822 Å, V1-O2 = 1.814, V1-N1 = 2.273 Å, V1-N2 = 2.229 Å and V1-O3-V1' = 162.77°.

Because of the lack of reactivity observed with **9** and **10**, attempts were made to replace the Cl atom of **9** with a methoxide group. The reaction inexplicably afforded a trivalent formate derivative $[(ONNO)V(\mu\text{-}HCOO)]_3$ (**12**) (Figure 5.11).

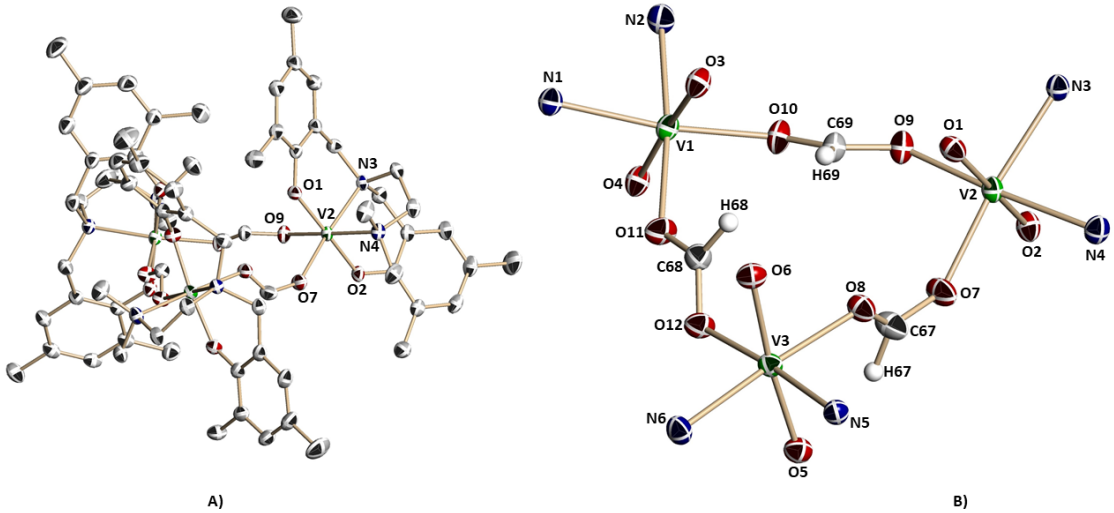

Figure 5.11. A) Thermal ellipsoid plot of **12** with ellipsoids drawn at the 30% probability level. Hydrogen atoms were omitted for clarity. B) Expansion of **12**. Selected distances and angles for compound 11 are as follows: V1-O10 = 2.049 Å, V1-O11 = 2.063 Å, V2-O7 = 2.044 Å, V2-O9 = 2.045 Å, V3-O8 = 2.086 Å, V3-O12 = 2.046, C67-O7 = 1.239 Å, C67-O8 = 1.229 Å, C68-O11 = 1.239 Å, C68-O12 = 1.256 Å, C69-O9 = 1.256 Å, C69-O10 = 1.238 Å, O7-C67-O8 = 129.22°, O11-C68-O12 = 124.75° and O9-C69-O10 = 124.32°.

Crystals of **12** are green but dissolve in toluene to generate an orange colored solution with greenish tint, probably indicative of a dissociative process. Compound **12** does react with carbon dioxide affording a red solution but, unfortunately, attempts to obtain a single crystal material from the resulting solution only gave intractable solids.

Once compound **12** was filtered off from its reaction mixture and the resulting solution concentrated, a new ionic compound $[(ONNO)_3V_2(\mu\text{-}OCH_3)][(ONNO)_2V]$ (**13**), (Figure 5.12) containing a methoxide group, was obtained in crystalline form upon slow evaporation. FTIR of **13** ruled out the presence of OH groups. Remarkably, when crystalline **13** was dissolved in toluene and exposed to CO_2 at constant pressure (35 psi), formaldehyde and formate were formed. No gases other than CO_2 were detected. Unfortunately, attempts to crystallize the product of the reaction of **13** with CO_2 were not met with success.

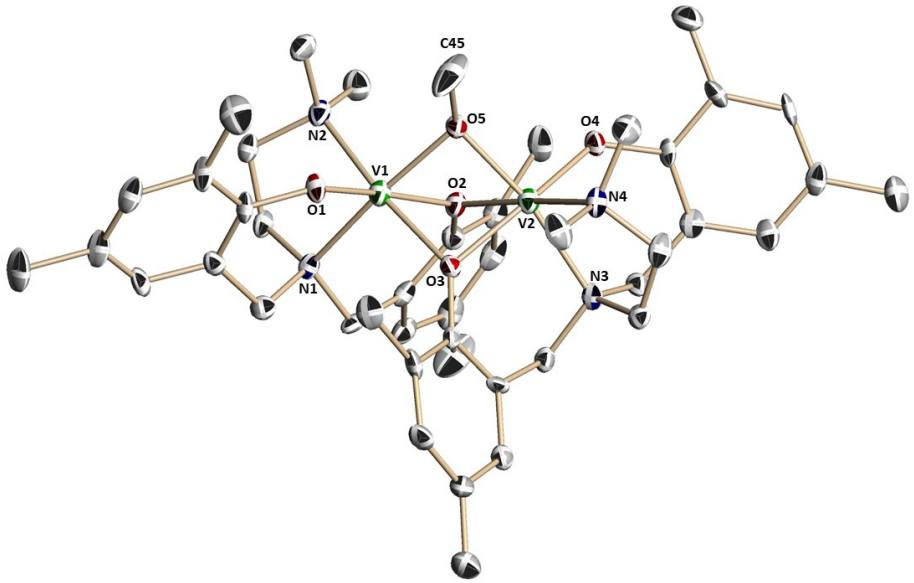

Figure 5.12. Thermal ellipsoid plot of **13** with ellipsoids drawn at the 30% probability level. Hydrogen atoms and $[V(ONNO)_2]^+$ co-crystallized fragment was omitted by clarity. Selected distances and angles of compound **13** are as follows: V1-V2 = 2.750 Å, V1-O5 = 2.009 Å, V1-O1 = 1.880 Å, V1-O2 = 1.979 Å, V1-O3 = 2.084 Å, V2-O5 = 1.971 Å, V2-O4 = 1.876 Å, V1-O2 = 2.116 Å, V2 – O3 = 1.991 Å, V1-N1 = 2.149 Å, V1-N2 = 2.169 Å, V2 – N3 = 2.153 Å, V2 – N4 = 2.179 Å, V1-O5-V2 = 87.39°, V1-O2-V2 = 84.29° and V1-O3-V2 = 84.82°.

The isolation of both **12** and **13** made us concerned about the quality of the commercially available NaOMe reagent employed for the preparation. Although the formation of **12** was clearly the result of large contamination by sodium formate in the commercial NaOMe, the possibility of synthesizing this trivalent formate derivative in a non-serendipitous manner was probed. We have thus reacted **9** with standard sodium formate to rationally afford pure **12**. Equimolar amounts of **9** and sodium formate afforded a new compound **12a** (Figure 5.13). Complex **12a** appears to be a different conformation of **12** due to a slightly different orientation of one of the bridging formate groups. Further reactivity with CO_2 gave the usual color change with formation of intractable materials with no gases other than CO_2 being detected.

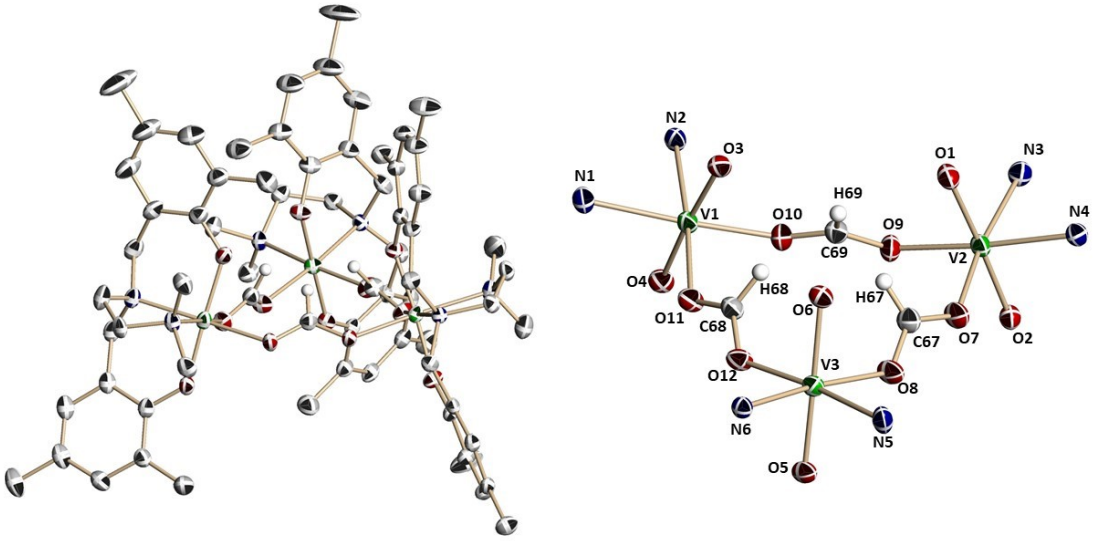

Figure 5.13. a) Thermal ellipsoid plot of **11a** with ellipsoids drawn at the 30% probability level. Hydrogen atoms were omitted by clarity. b) Expansion of **11a** metal core trimer with ellipsoids drawn at the 30% probability level. Carbon and hydrogen atoms were omitted by simplicity excepted in formate fragments.

A last step prior to attempt interpreting the fascinating conversion of CO_2 into formate and formaldehyde was to test the reactivity of anionic metallate derivatives. The idea about the use of

anionic derivatives was that an enhanced nucleophilic power could possibly promote reactivity with CO_2. To obtain a vanadium(III) anionic compound, reactions were performed using two equivalents of the deprotonated ligand $(ONNO)^{2-}$ (Scheme 5.8.). Compound $[(ONNO)_2V]K{\cdot}3THF$ **(14)** was then obtained and its structure confirmed by X-ray diffraction analysis.

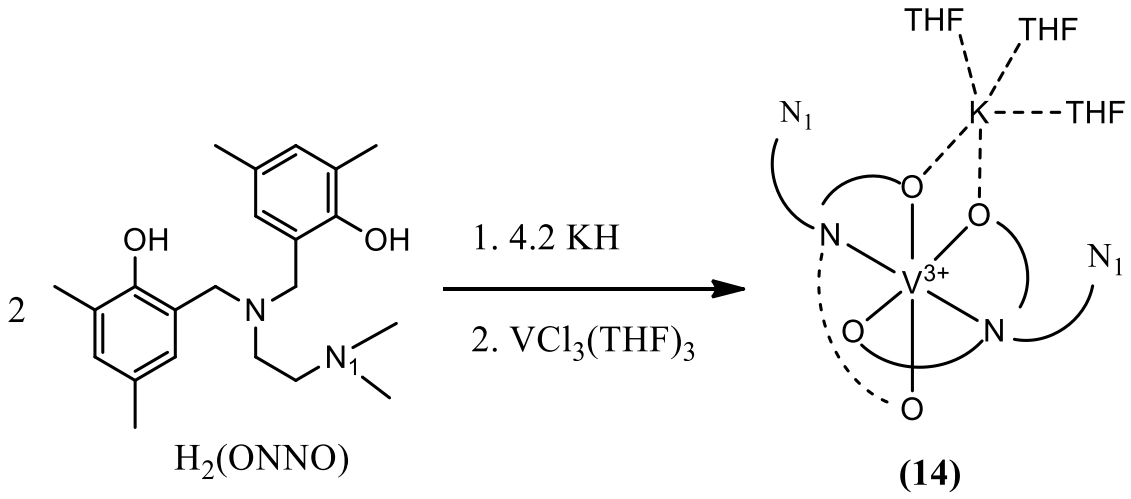

Scheme 5.8. Preparation of compound **14**.

The dimethylamine pendants in the ligand are dangling outside the coordination sphere of the vanadium center indicating coordinative saturation for vanadium. The encapsulation of the metal center and lack of ligand dissociation obviously is at the basis of the observed lack of reactivity of **14** with CO_2 (Figure 5.14), even at high temperatures and pressures.

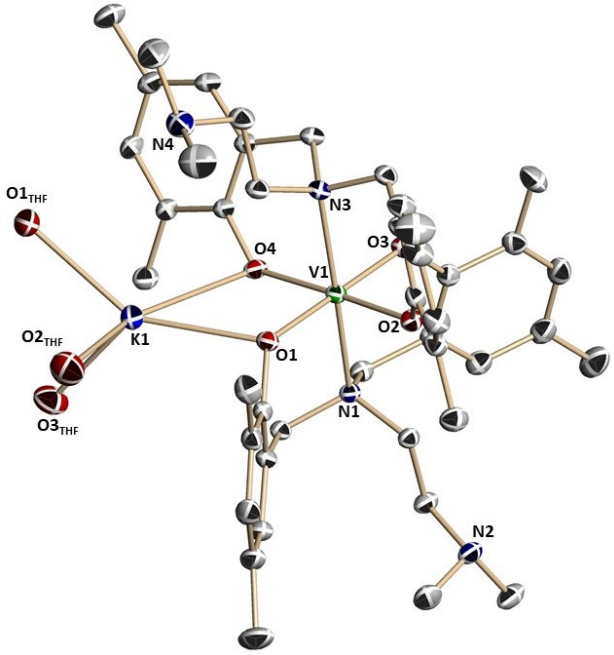

Figure 5.14. Thermal ellipsoid plot of **14** with ellipsoids drawn at the 30% probability level. Hydrogen atoms were omitted by clarity. Selected distances and angles of compound **14** are as follows: V1 – O1 = 1.990 Å, V1 – O2 = 1.952 Å, V1 – O3 = 1.949 Å, V1 – O4 = 1.988 Å, V1 – N1 = 2.216 Å, V1 – N3 = 2.223 Å, N1–V1-N3 = 175.02°, O2-V1-O4 = 176.80° and O1-V1-O3 = 179.86°.

The possibility of selectively obtaining formaldehyde from the reaction of aryloxide/methoxo derivatives with CO_2 was rather exciting. On the other hand, the interference from possible contamination by **9** could not be positively ruled out.

Since the collection of serendipitous results obtained from the use of impure NaOMe, albeit inspiring, was pointing towards the simple V-OMe function as responsible for the formation of formaldehyde, attempts to obtain a rational preparation were undertaken. Potassium methoxide was prepared by reacting anhydrous methanol 99%[426] with KH. Further reaction with **9** gave analytically pure **13**.

The possibility of comproportionating methoxide anions with CO_2 to a mixture of formate anion and formaldehyde is potentially a valuable reaction. In fact, the reaction does not require electrons

from the metal center and there is therefore potential for a catalytic transformation. Thus, assuming that (ONNO)V-OMe is responsible for such a transformation, we have performed DFT calculations to support this working hypothesis. Several mechanistic pathways were evaluated and the lowest energy profile is reported in Scheme 5.9. The pathway is in agreement with the previously discussed ability of vanadium(III) alkoxides to coordinate CO_2.

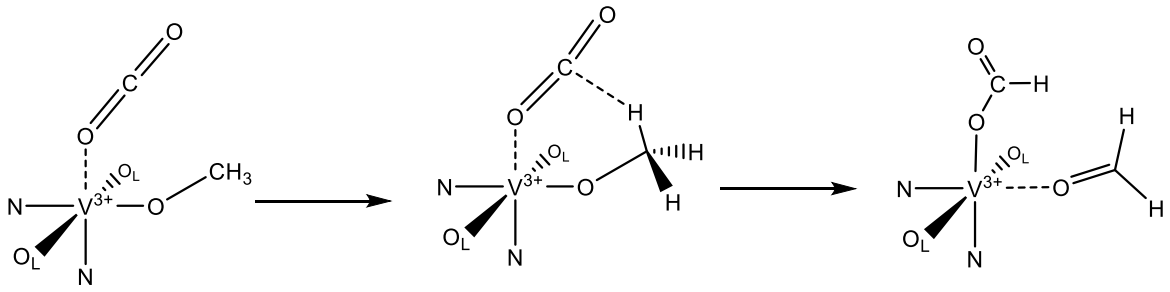

Scheme 5.9. Proposed computed pathway for the formaldehyde and formate production from **13.**

Computational DFT analysis was performed on the reaction pathway of **13** with vanadium in the trivalent state. The total charge of the dimeric unit is +1 with a total multiplicity of 5 (lower multiplicity was also evaluated). The initial dissociation of the dimeric unit of **13** by direct reaction with CO_2 requires a prohibitive energy input of +75 kcal/mol. This amount of energy is too large to make the process viable under ambient conditions implying that the dissociation may occur in solution with the critical assistance of solvation. If the hydrogen transfer to CO_2 from the methoxide group occurs when a dimeric vanadium(III) methoxy complex is used as starting material, the proposed path becomes permissible with only +31 kcal/mol being required (Scheme 5.10) to reach the transition state. We analyzed a structure similar to compound **10** (by replacing the substituent *p*-methoxiphenoxide by methoxide ligand – gs2 in Scheme 5.10) and also as a solvated THF product of **13** (Scheme 5.10).

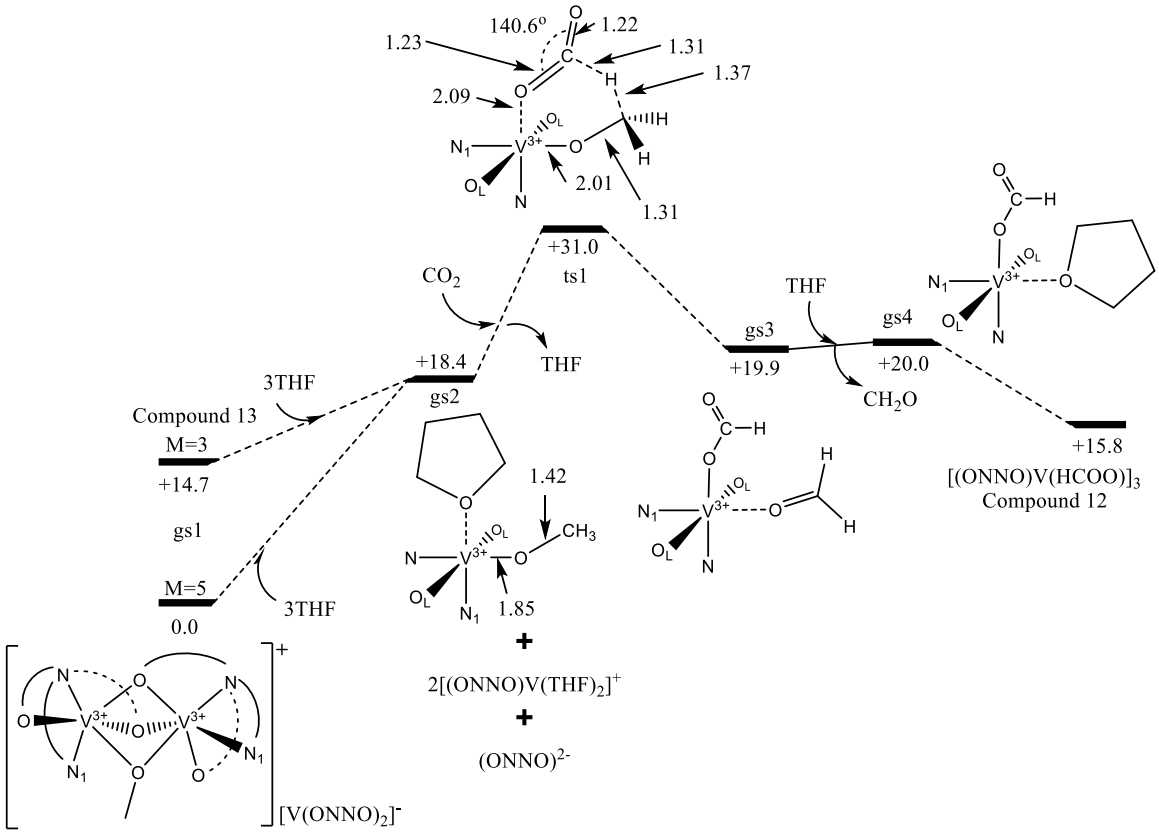

Scheme 5.10. Gibbs energy (kcal/mol and distances in Å) profile of proposed methoxide vanadium(III) compound reacting with CO_2.

The solvation energy in this case is only +3.7 kcal/mol making the process permissible. The transition state ts1 presented in Scheme 5.9 shows that comproportionation might occur between the CO_2 and methoxide unit. The proximity of the methoxide hydrogen atoms to the coordinated CO_2 (-*cis* position vacancy) is enforced by the ligand geometry. In the final step, formaldehyde is released from the coordination sphere affording gs4. Its trimerization further drops the energy to form compound **11** (+15.8 kcal/mol). Still, the energy in the predicted mechanism is uphill which indicates that due to the lack of information on the final structure, we might have to consider other vanadium(III) structures that could incorporate formaldehyde and formate in different manners.

5.6. Conclusions

In this chapter, we have presented a unique case of reduction of coordinated CO_2 to the formate anion performed by a transition metal and with the solvent acting as a H-atom source. The key to the appearance of radical behavior of the bridging coordinated CO_2 is the pre-existence in the molecular frame of a trivalent V-O-V unit, normally expected to be unreactive. We confirm our previous observation that this reaction proceeds via end-on linear coordination followed by bending prior to release of CO. To our surprise, the intermediate –oxo species coordinates CO_2 in a bridging fashion with a remarkable synergistic effect between coordinated CO_2 and oxo- atom for triggering a radical behavior. The charge displacement between the two centers is sufficient to enable H-atom abstraction (a typical radical process) and formation of the bridging hydroxo- and formate units of complex (**2**).

The initial step of the reaction of V(II) is a simple CO_2 deoxygenation with formation of a V(III) oxo species. This transient and elusive complex appears to be capable of coordinating CO_2 and to trigger a synergistic activation effect leading to radical H atom abstraction from the solvent. By modifying the reaction condition, we have prepared and fully characterized the V-CO_2 in an end-on coordination mode. This is the first example in literature when a transition metal can linearly coordinate a CO_2 molecule.

Trivalent vanadium complexes have been prepared and tested. Ligand modification and use of aryloxide gave no reaction. However, the combination of the $ONNO^{2-}$ ligand with the methoxide group gave rise to an interesting cationic unit, which reacted with carbon dioxide to afford disproportionation to formaldehyde and formate. The resulting vanadium(III) formate compound also reacts with CO_2, but its reactivity is not well understood. The pathway of a comproportionation of CO_2 with methoxide into formate and formaldehyde was elucidated by DFT.

5.7. Experimental part

Chemical and physical measurements. All manipulations were performed under argon atmosphere with rigorous exclusion of oxygen and water by using standard Schlenk and glovebox techniques. n-Heptane, pentane, ether, toluene and THF were dried over activated Al_2O_3 and deoxygenated prior to use by several vacuum/nitrogen/argon purges. VCl_3 98% was purchased from Aldrich and used as initial precursor for preparation of $VCl_3(THF)_3$. Carbon dioxide grade 5.0 was purchased from Linde. The organic compounds H_2ONNO, H_2ONOO, as well as complexes **1** and **9** were prepared according to published procedures.[228,290] The formation of CO was monitored by gas chromatography using an Agilent Technologies 7820A GC-TCD system with a Molsieve column. All other chemicals used were purchased from Sigma-Aldrich and used as received. Magnetic susceptibilities were measured using a Johnson Matthey magnetic susceptibility balance at room temperature. Mass spectrometric analysis were carried out using a Micromass QToF I ESI Mass Spectrometer, with Lock Mass HRes Exact Mass Calculation and Kratos Concept 1S, HRes EI Mass Spectrometer. Elemental analysis was performed by G.G. Hatch Stable Isotope Laboratory University of Ottawa in a VarioEL Cube analyzer.

Crystallography and magnetic measurements. The crystals were mounted on thin glass fibers using paraffin oil. Prior to data collection crystals were cooled to 200(2) K. Data were collected on Bruker APEX2 single-crystal diffractometers equipped with sealed Mo tube sources (wavelength 0.71073 Å) and APEX II CCD detectors. Raw data collection and processing were performed with APEX II software package from BRUKER AXS. Semi-empirical absorption corrections based on equivalent reflections were applied. Systematic absences in the diffraction data-set and unit-cell parameters were consistent with the assigned space groups. The structures were solved by direct methods, completed with difference Fourier synthesis, and refined with full-matrix least-squares procedures based on F^2. All non-H atoms were refined anisotropically. All hydrogen atoms positions were calculated based on the geometry of the related non-hydrogen atoms (riding model), except for the hydroxyl groups and formate anions in

compound 2 that were located from the Fourier difference map and were refined only with conventional bond distance restraints (SADI) applied. Compound 2 crystallizes in $\boldsymbol{P\bar{1}}$ space group with four molecules in the asymmetric unit. The C119…C122, N102 fragment was disordered over two positions with 0.582(8):0.418(8) occupancy ratio. The C341...C344, N304 fragment was disordered over two positions with 0.648(8):0.352(8) occupancy ratio. They were refined using enhanced rigid-bond restraints (RIGU) for ADPs and bond distance and angle restraints (SAME). Compound 3 crystallizes in $\boldsymbol{P\bar{1}}$ space group. The asymmetric unit contains two halves of complexes. No additional constraints or restraints were applied during refinement. Compound **4** crystallizes in $\boldsymbol{C2/c}$ space group with a half of the molecule in the asymmetric unit. The C21…C24,N2 fragment was disordered over two positions with 0.578(12):0.422(12) occupancy ratio. It was refined using enhanced rigid-bond restraints (RIGU) for ADPs and bond distance and angle restraints (SAME). It contained solvent molecules that were heavily disordered and could not be modelled properly. The SQUEEZE routine of PLATON was applied to remove their contribution to the scattering. It indicated two solvent regions per unit cell, 1926 Å3 each, containing approximately 432 electrons each. The crystals were small and gave relatively weak diffraction. After multiple trials the best dataset was used for this structure refinement. The high-resolution cut-off was set at 0.99A. The magnetic moments were measured at room temperature from samples sealed in calibrated tubes prepared inside a dry box.

Computational methods. Preliminary ground state geometries were optimized using semi-empirical PM7 method implemented in MOPAC2016 using, when available, the initial geometry obtained from the X-ray single crystal analysis.[383] DFT calculations have been performed at the CAM-B3LYP[427] level by using LANL2DZ[428–430] basis set for all atoms with Gaussian 09® suite package. Berny algorithm was performed to find a transition state.[390,391] Vibrational frequencies analysis was performed to characterize the nature of the transition state, one imaginary frequency. Natural population analysis was performed to obtain the electronic distribution in the transition state ts6 and gs3 with TZVP[388,389]

basis set for all atoms. The free graphical user interface Gabedit[396] and Avogadro[397] were used for input/output and structure handling. The initial geometry obtained from the X-ray single crystal analysis of compound **1a** was used to determine the Hirshfeld charges and spin density. Single point calculations were carried out at the CAM-B3LYP/6-311G level of theory.[9–11] In order to determine electrophilic, nucleophilic and radical Fukui indexes for compound 1a, single point calculations on neutral, cationic and anionic structures were carried out. Hirschfeld charges on each of the atoms in the structure were determined for the three states analyzed.

Isotopic experiments. A toluene solution of **1** was placed in a Parr® reactor and **1** atm of $^{13}CO_2$ or enriched O^{18}-labelled CO_2 from ICON Isotopes (enriched 95% ^{18}O) added**.** This was left unstirred for 24h at -10 degrees Celsius, after which the gasses were injected into the EI-MS and GC-TCD.

Preparation of H_2ONNO. Procedure reported by Lorber was followed.[431] ^1H NMR of H_2ONNO (22°C., 400 MHz, $CDCl_3$) δ: 6.91 (s, 2H), 6.73 (s, 2H), 3.62 (s, 4H), 2.59(s, 4H), 2.35 (s, 6H) and 2.26 (s, 12H). ^{13}C NMR of H_2ONNO (22°C., 400 MHz, $CDCl_3$) *δ:* 152.67, 131.24, 129.39, 127.39, 125.41, 121.61, 56.36, 56.06, 49.09, 45.00, 20.46 and 16.26 ppm. (Appendix T5.3).

Preparation of H_2ONOO. Procedure reported by Kerton was followed.[432] ^1H NMR of H_2ONOO ^1H NMR (22°C, 400 MHz, CDCl3) δ 8.47 (2H), 6.90 (H), 6.90 (H), 6.72(H), 6.72(H), 3.61 (t,2H), 2.75 (3H), 2.74 (t,2H), 2.26 (s,6H) and 2.24(s,6H). ^{13}C NMR of H_2ONOO (22°C., 400 MHz, $CDCl_3$) *δ:* 152.34, 131.24, 128.46, 127.93, 125.14, 121.19, 59.04, 57.06, 50.91, 20.42 and 16.08 ppm. Single crystal X-ray analysis was done in a quick run for structure determination purposes. All parameters were in agree with the published results. R1 = 0.0527, WR2 = 0.1497, Rint = 0.064, completeness = 1.00, GooF = 1.039 (Appendix T5.4).

Preparation of compound 1a. Crystalline material of (ONNO)V(TMEDA) (0.855 g, 1.64 mmol) was dissolved in 7 mL of d_8-toluene and cooled to -10°C. $^{13}CO_2$ was then used at atmospheric pressure and

left undisturbed for 12h. Red crystals of compound 1a were obtained and characterized by single crystal X-ray technique, (ONNO)V(OCO)(OH). μ_{eff} = 2.68 BM. Yield of the reaction was 71.1% (0.543 g, 1.16 mmol). EA found (calcd) C 59.09 (59.22), N 6.15 (6.01) and H 6.61 (6.70). ATR FT-IR of the single crystal material (ν, cm-1), (-OH) 3525s and 3516, (O=C=O) 2206 ms, (C=O) 1607 vs.

Preparation of compound 2. A crystalline sample of (ONNO)V(TMEDA) (0.241 g, 0.46 mmol) was dissolved in 10 mL of toluene. The solution was exposed to CO_2. The final pressure in the sealed vessel was 35 psi. The solution was stirred for 48 hours at room temperature. The head space of the reactor was analyzed by GC-TCD and CO was detected and quantified by using standard calibration curves. Layering the resulted solution with 6 mL of pentane allowed the formation of X-ray quality single crystals of $[V_2(\mu\text{-OH})(\mu\text{-HCOO})(ONNO)_2]$ (2) (43%, 0.098 mmol) after 4 days, MS-ESI [M-OH]+. m/z calculated for $V_2N_4O_7C_{45}H_{45}$ 872.350, found 872.492, [M-OH]+. 855.345, found 855.217 and [M-HCOO]+. 855.345, found 855.217. μ_{eff}= 4.51 BM. EA found (calcd) C 61.74 (61.92), N 6.38 (6.42) and H 7.21(7.16). ATR FT-IR of the single crystal material (ν, cm-1), ($^-$OH) 3528s and 3516, (-COO^-) 1607.8ms and 1575ms, (C-O) 1360.1vs.

Preparation of compound 3. A crystalline sample of (ONNO)V(TMEDA) (0.096 g, 0.18 mmol) was dissolved in 5 mL of toluene. The solution was stirred and then exposed to dry oxygen. The red solution turned immediately dark-blue and eventually purple after a few seconds. The reaction mixture was stirred for 6 hours and placed at -35^{o}C overnight. X-ray quality single crystals of $[VO(ONNO)]_2$ (3) (83%, 0.149 mmol) were obtained. μ_{eff} = 1.85 BM. EA found (calcd) C 62.81 (62.70), N 6.71 (6.65) and H 7.15 (7.18). ATR FT-IR of the single crystal material (ν, cm-1), (V=O) 985.1.

Preparation of compound 4. A Crystalline sample of (ONNO)V(TMEDA) (0.291 g, 0.56 mmol) was dissolved in 10 mL of toluene. The solution was stirred while PyO was added (11.7 mg, 0.149 mmol). The initial red solution turned to very dark red color passing through dark orange. The reaction mixture was stirred for 48 hours and then placed in a closed vessel to allow controlled slow evaporation with

activated molecular sieve. Single crystals suitable for X-ray diffraction were obtained after 48 hours, [(ONNO)V][VO_2][(ONNO)VO] (22.1%, 0.0247 mmol). EA found (calcd) C 57.91 (58.09), N 6.45 (6.65) and H 6.02 (6.16). KBr and ATR FT-IR of the single crystal material (ν, cm-1), (V=O) 965.1 and 981.3.

Preparation of compound 5. Crystalline material of 1a (ONNO)V(OCO)(OH) (0.255 g, 0.545 mmol) was partially dissolved in 3 mL of toluene. The mixture was heated up to 70°C. After complete dissolution of 1a, the color of the solution started to change from orange-red color to a light green solution. Vapor diffusion technique using pentane gave rise to single crystals of 5 [(ONNO)V(μ-OH)]$_2$ (22.1%, 0.0247 mmol) suitable for X-ray diffraction. Compound 5 can also be obtained by UV light irradiation of the solution of compound 1a in toluene. EA found (calcd) C 62.69 (62.55), N 6.61 (6.63) and H 7.49 (7.40).

Preparation of compound 6. Deprotonation of the (OONO)H_2[432] (0.601 g, 1.75 mmol) ligand was performed with KH (0.152 g, 3.81 mmol) in 10 mL of THF through a very rapid, exothermic and vigorous reaction. Subsequent reaction of $VCl_3(THF)_3$ (0.652 g, 1.75 mmol) was also rapid and a green solution was obtained and stirred overnight. The resultant solution was centrifuged and all solid was removed. The solution was put under vacuum to remove ½ of the total volume. To ensure that any inorganic salt was removed completely, the solution was centrifuged once more. From the THF solution, a slow vapor technique with pentane was used to obtained compound **6**. The solution was left undisturbed for several days and the formation of orange single crystals suitable for X-ray were obtained, (OONO)VCl(THF). The yield of the reaction was 69.1% (0.603 g, 1.21 mmol). The structure was elucidated by solid single crystal technique. μ_{eff} = 2.91 BM. EA found (calcd) C 60.55 (60.06), N 2.61 (2.80) and H 6.98 (7.06).

Preparation of compound 7. Crystalline material of **6** (0.691 g, 1.35 mmol) was dissolved in 5 mL of toluene. After the solid was totally dissolved, an orange color formed. Potassium salt of *p*-methoxyphenol (0.221 g, 1.36 mmol) was added. The mixture was stirred for 24 hours. The colour of

the solution changed from orange to green. The resultant solution was centrifuged and all precipitated solid was removed. Using gentle vacuum, ½ of the total volume of the solution was removed. To ensure that any inorganic salt was removed completely, the solution was centrifuged once more. Green crystals of **7** were obtained by a slow vapor diffusion technique with pentane. $[(OONO)V(\mu\text{-}OPhOCH_3)]_2$ was identified by single crystal X-ray analysis. The yield of the reaction was 47.2% (0.382 g, 0.637 mmol). μ_{eff} = 2.83 BM. EA found (calcd) C 65.55 (65.99), N 4.56 (4.66) and H 7.35 (7.55).

Preparation of compound 8. Crystallized compound 6 (0.210 g, 0.611 mmol) was dissolved in 5 mL of toluene. Premade MeOK was added in molar ratio 1:1.05 respectively. The light orange color solution turned to dark green and the NaCl produced was centrifuged and removed. Compound **8** crystallized after a week in a toluene/pentane mixture. X-ray single crystal technique allows the structural characterization of compound **8** as represented in Figure 5.8, $[(OONO)V(\mu\text{-}OCH_3)]_2$.THF. Red crystals were isolated by controlled slow evaporation in a sealed vessel. The yield of the reaction was 51.3% (0.155 g, 0.313 mmol).

Preparation of compound 9. Crystalline material was obtained as reported by Lorber et. al.[290] The structure was elucidated by analysis by single crystal X-ray. Yield 85.9% (2.56 g, 5.00 mmol).

Preparation of compound 10. Crystallized compound **9** (0.536 g, 1.56 mmol) was dissolved in 10 mL of THF. 4-methoxyphenol potassium salt solution in THF was previously prepared and added. The initial green color of the solution did change significantly. After stirring for 24 hours, the mixture was centrifuged and the KCl produced was removed. Compound **10** crystallized after one day under pentane vapor diffusion technique. X-ray single crystal technique allows the structural characterization compound **10** as represented in Figure 5.9B, $[(OONO)V(\mu\text{-}OPhOCH_3)]_2$THF. The yield of the reaction was 91.1% (0.391 g, 0.711 mmol).

Preparation of compound 11. Crystalline material of **9** (0.195 g, 0.381 mmol) was dissolved in 5 mL of toluene. The resultant orange solution was exposed to dry oxygen. The color of the solution turned blue after a few minutes. The reaction mixture was stirred for 12 hours where the blue color became darker. Layering the solution with 2 mL of pentane allowed growth of light blue single crystals to be analyzed by SC-XRD. The yield of the reaction was 71.3% (0.122 g, 0.134 mmol)

Preparation of compound 12. In a similar procedure to compound **10**, sodium methoxide bought from Sigma was used instead of *p*-methoxyphenol potassium salt. A saturated THF solution was settled overnight and dark green crystals were obtained suitable for SC-XRD. Yield of the reaction was 25.1% (0.855 g, 0.521 mmol). μ_{eff} = 6.83 BM.

Preparation of compound 12a. Same procedure where compound **12** was obtained. After filtration, the solution was concentrating till 1/3 of the initial volume. After 4 days by controlled slow evaporation in a sealed vessel with active molecular sieves allowed the growth of single crystals suitable for structural determination by SC-XRD. The yield of the reaction was 15.0% (0.095 g, 0.059 mmol).

Preparation of compound 13. In a similar procedure to compound **10**, sodium formate was used instead of potassium p-methoxyphenol salt. The mixture of **9** (2.23 g, 4.35 mmol) and sodium formate (0.304 g, 4.45 mmol) was stirred for 48 hours. After centrifugation, the saturated THF solution was settled overnight and dark green crystals were obtained suitable for structural determination. Yield of the reaction was 64.6% (0.855 g, 0.965 mmol). μ_{eff} = 6.25 BM.

Preparation of compound 14. Deprotonation of the (ONNO)H_2[432] (0.905 g, 2.54 mmol) ligand was performed with slow addition of KH (0.224 g, 5.58 mmol) in 7 mL of THF through a very rapid and vigorous reaction. Subsequent addition of $VCl_3(THF)_3$ (0.478 g, 1.28 mmol) generated a dark blue solution that was stirred overnight. The resultant solution was centrifuged and all solid was removed.

Gentle vacuum was applied until ½ of the volume was removed. Extra solid was removed upon centrifugation. From the THF solution blue crystals were obtained at -35 °C. Characterization by single crystal X-ray allows the determination of compound **14**. The yield of the reaction was 38.1 % (0.491 g, 0.488 mmol).

Appendix T5.2. DFT representation of the relevant structures in the proposed mechanism. Hydrogen atoms were omitted by clarity

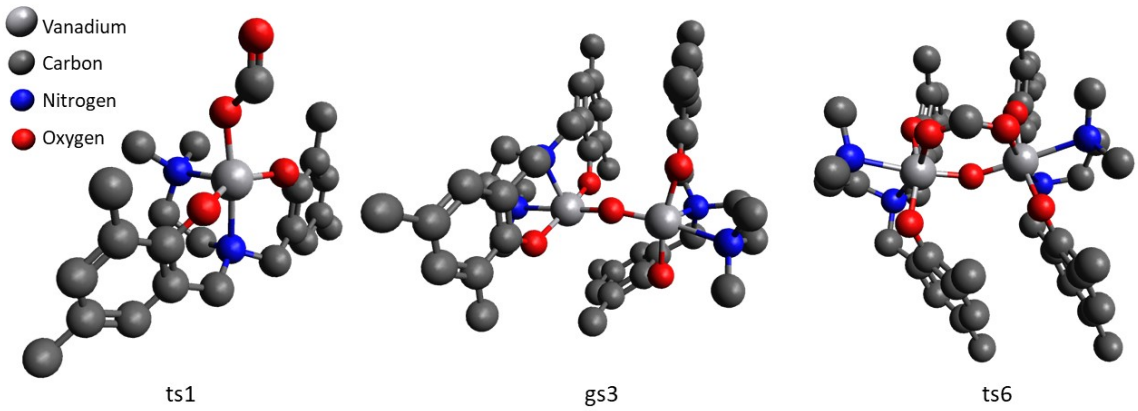

Appendix T5.3 Frontier MO for compound 1a, neutral specie. left: electrophilic susceptibility center: nucleophilic susceptibility and right: radicalic susceptibility

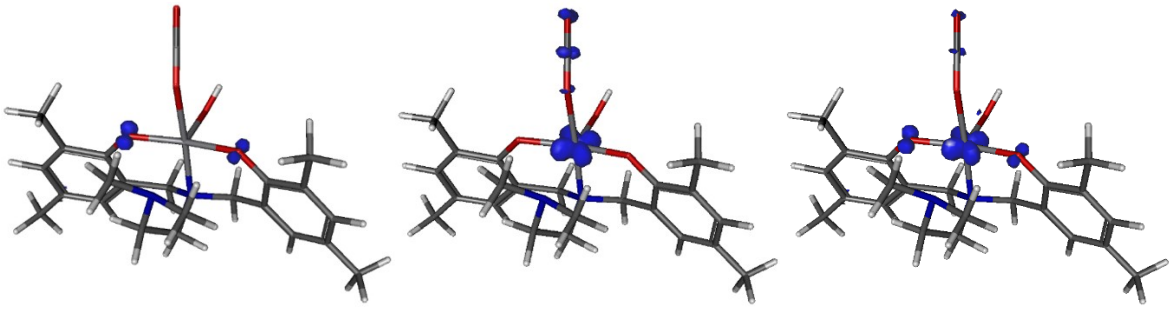

Appendix T5.3. ^{1}H and ^{13}C NMR experiments on H_2ONNO ligand.

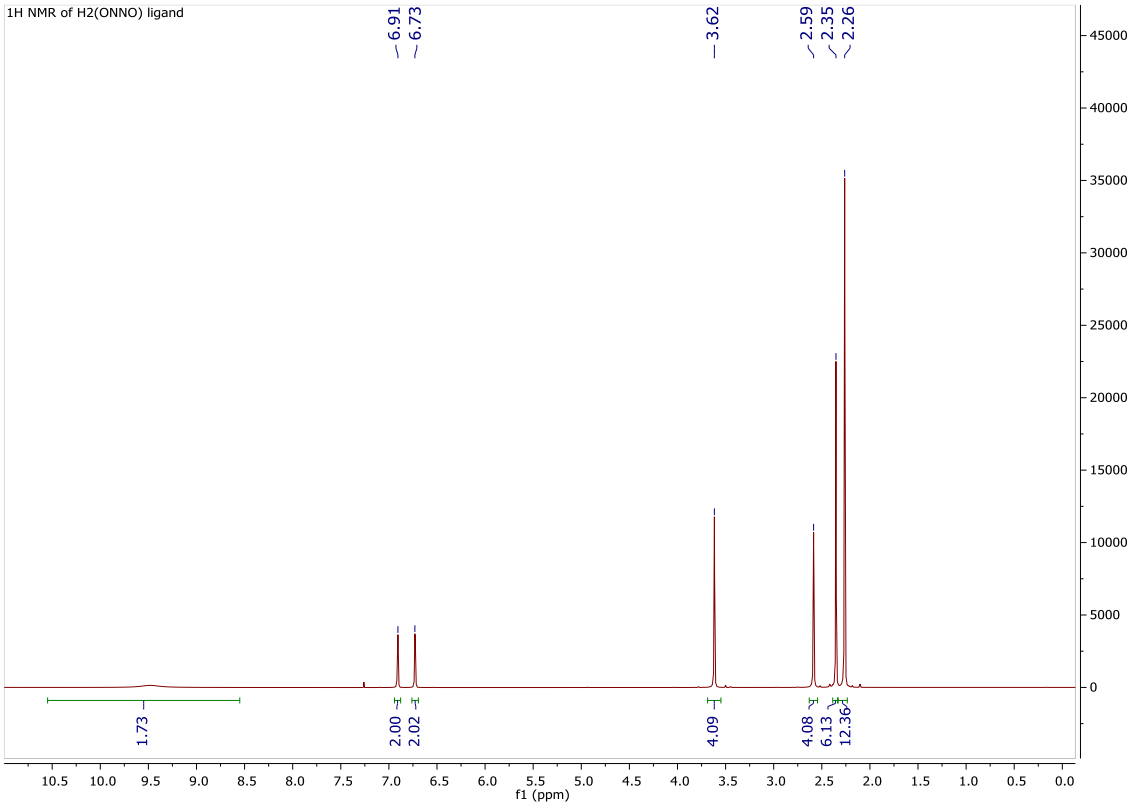

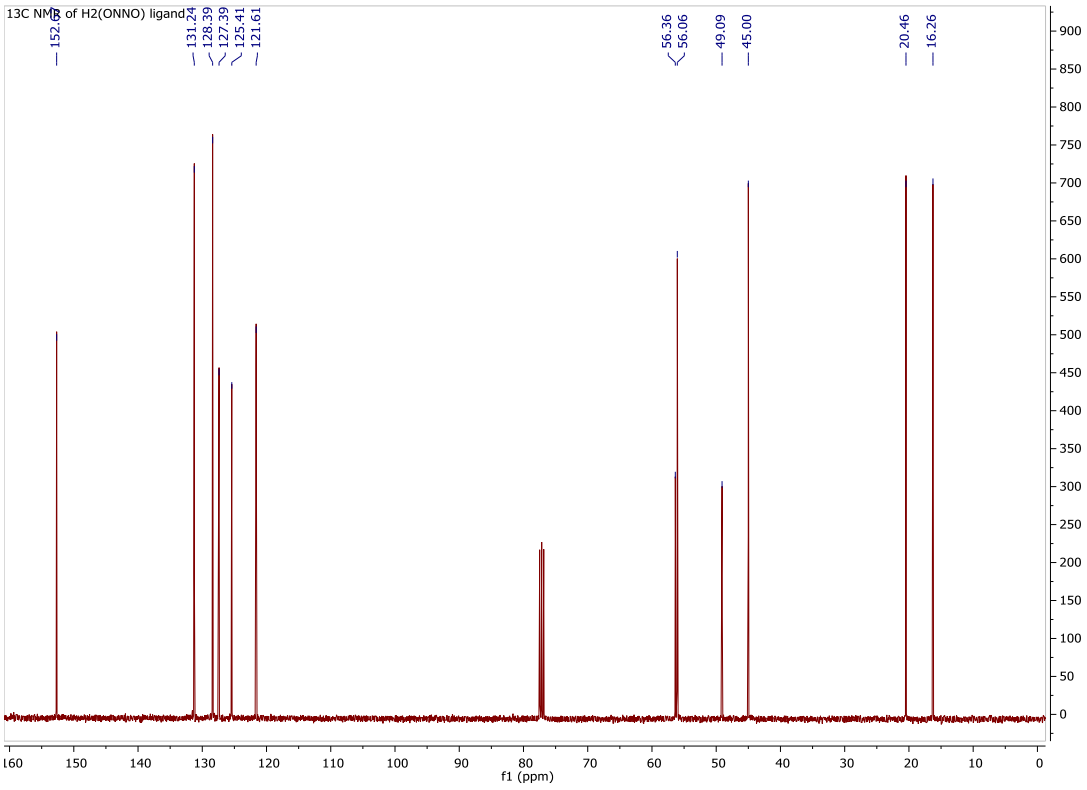

Appendix T5.4. ^{1}H and ^{13}C NMR experiments in $CDCl_3$ on H_2ONOO ligand respectively.

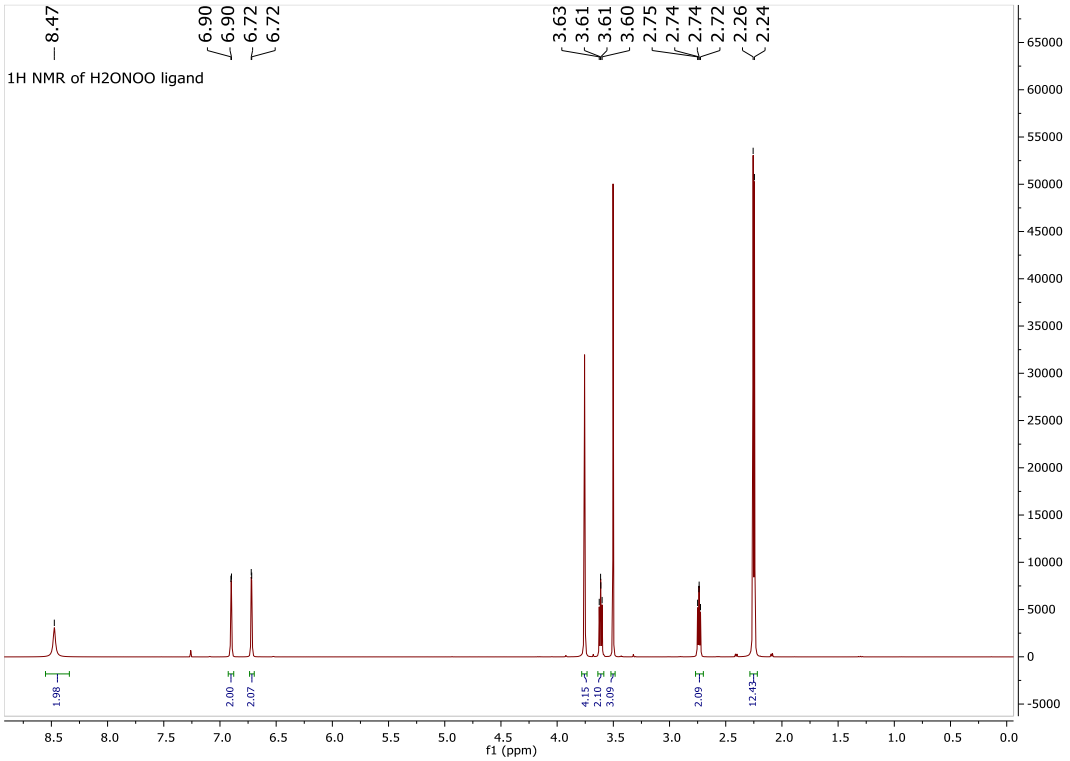

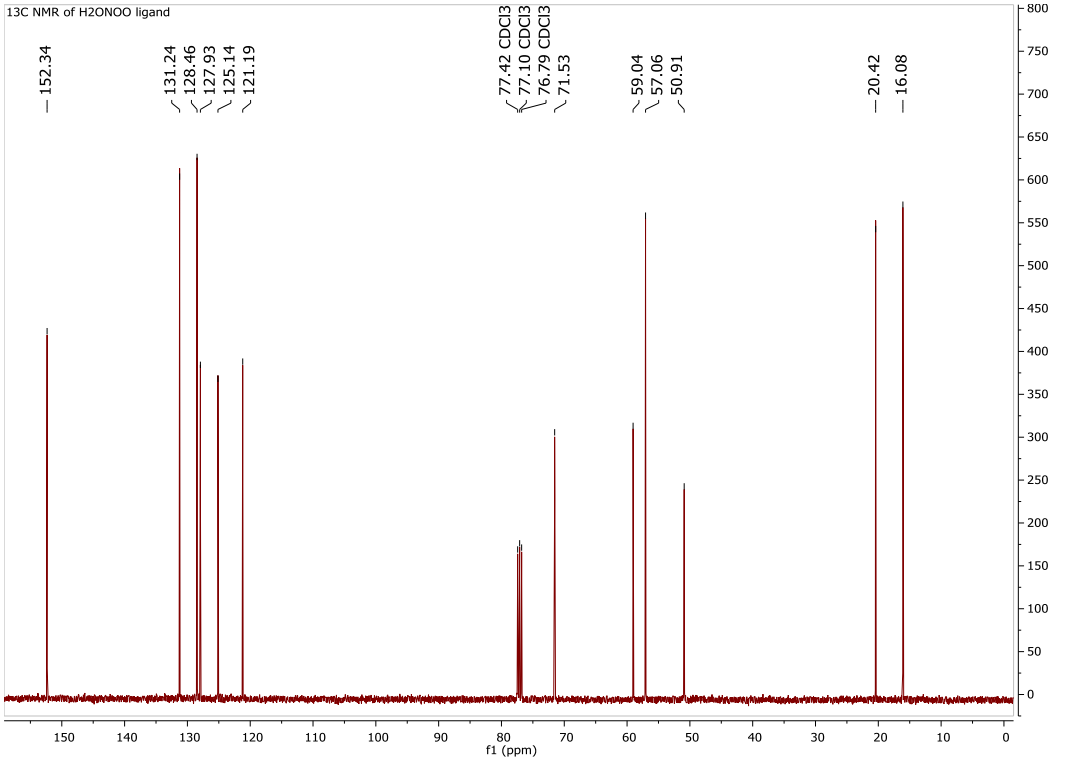

Appendix T5.4.1. Thermal ellipsoids of H_2ONOO ligand with 30% of probability level.

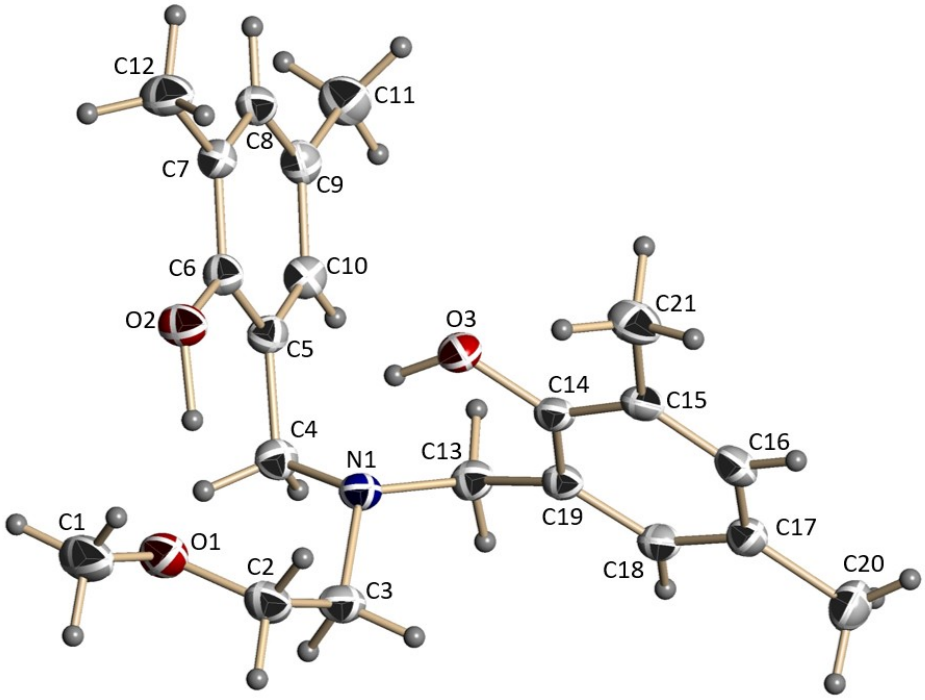

Chapter 6. Hetero-bimetallic compounds of vanadium and bismuth.

CJV: I have carried out all the experimental work and elaborated ideas.

6.1. Preamble

The work on $BiVO_4$ reported in chapter 2 has indicated that vanadium, in a trivalent state and surrounded by oxygen donor atoms, is capable of remarkable performance in terms of CO_2 fixation and activation. This has been further confirmed by the modeling studies carried out on vanadium aryloxides described in chapters 4 and 5 showing the trivalent metal as capable of directing the reactivity of CO_2 towards radical-type transformations. The role of bismuth, however, still remains ill-defined. If the hypothesis arising from the reverse combustion as promoted by $BiVO_4$ is correct (i.e. low valent vanadium and high valent Bi being formed by the irradiation), *in situ* generated pentavalent bismuth in an oxygen donor-based ligand environment is expected to perform water oxidation. To acquire additional information about the role played by bismuth, not only do homoleptic complexes need to be prepared but also heterobimetallic species ideally containing the two elements in the target oxidation states. In this chapter we describe the attempts we have carried out to prepare molecular heterobimetallic V/Bi compounds of oxygen donor ligand systems containing both elements in the critical oxidation states.

6.2. Introduction

Preparing heterometallic molecular compounds has been an important research topic over the past decades, allowing researchers to explore and demonstrate theories related to both catalysis, natural and synthetic systems. For example, most of the natural polymetallic systems have a critical limitation in their enormous complexity, typically frustrating meaningful synthetic work. However, mimicking natural systems by simplifying them may allow us to understand complex and much-wanted transformations. In turn, this enables procedures for the preparation of systems of even greater performance. A common strategy to contribute to the solution of these problems is the preparation of polymetallic systems in a ligand environment as close as possible to that of the target system.

Heterobimetallic systems may be considered as a subclass of the polymetallic or cluster compounds and have a broad range of applications. One of the most common is solid state chemistry with particular emphasis on preparation of magnetic, photovoltaic and photo-semiconducting materials. Semiconductors are probably the most popular class of hetero-polymetallic systems. Within this very large family of compounds, bismuth containing semiconductors are especially important in applications such as laser diodes,[433] organic pollutants removal,[434] magnetic luminescent materials[435,436] and photochemical catalysts among others[437,438].

The synthetic procedures for these materials mainly consist of solid-state reactions where the particle size is a critically limiting factor. A way around this problem consists of the recently discovered sol-gel (carboxylic acids, polyols, alkoxide among others as intermediates), Metal Organic Deposition (MOD), Metal Organic Chemical Vapor Deposition (MOCVD) and inkjet printing methodologies.[439,440] Among the most spectacular successes is the employment of molecular precursors for the production of thin-film transistors and organic semiconductors. These materials typically are hetero-polymetallic systems. In a classic example of heterobimetallic molecular material preparation (Scheme 6.1-i), the

metal alkoxide precursors are physically mixed at slightly higher temperatures than their melting points.[441] Reactions carried out in solvents but at the same temperature, may afford instead different products (Scheme 6.1-ii). Therefore, the synthetic protocol truly is pivotal for the preparation of a given heterobimetallic material.

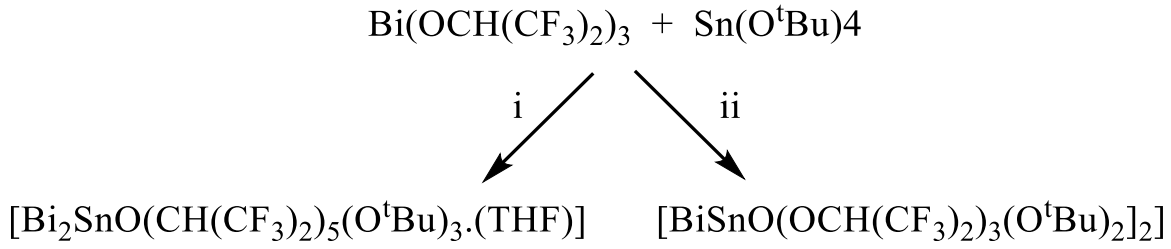

Scheme 6.1. Precursors in a heterobimetallic synthesis of Bi/Sn. Reproduced from ref #[441] with permission by The American Chemical Society.

In the broad range of application of the heterobimetallic structures now available with different functionalities we are particularly interested in CO_2 cooperative activation. Pillared compounds of cyclopentadienyl based ligands with two or more heavy atoms have been recently reported in the literature.[442] Applications are still under development, but the structural magnificence of these materials nowadays stimulates curiosity for their preparation with new ligand systems.[442] Heterobimetallic compounds containing Fe and Ru or Ti and Zr were characterized and the reactivity with CO_2 examined (Scheme 6.2).[443] Their subsequent degradation can form by-products containing the M-O-M' moiety.

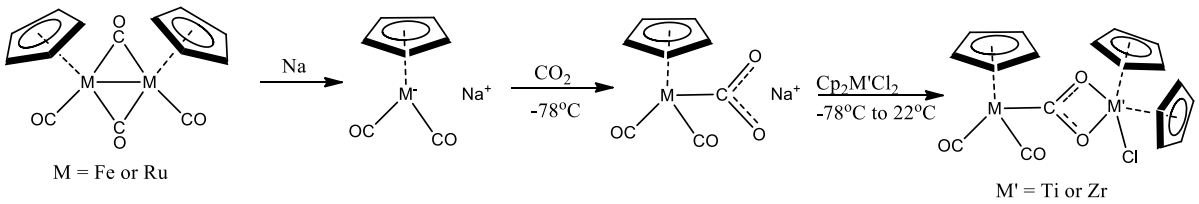

Scheme 6.2. Insertion of CO_2 using a bimetallic system. Reproduced from ref #[443] with permission by The American Chemical Society.

A few years later, the same authors presented CO_2 insertion performed in similar Cp ligand systems under mild conditions and where the heterobimetallic nature of the complex was demonstrated to be the main feature responsible for the CO_2 robust coordination.[444] Heterobimetallic compounds containing Ru and Mn (Figure 6.1) also were studied for the copolymerization reaction of epoxides with carbon dioxide.[445]

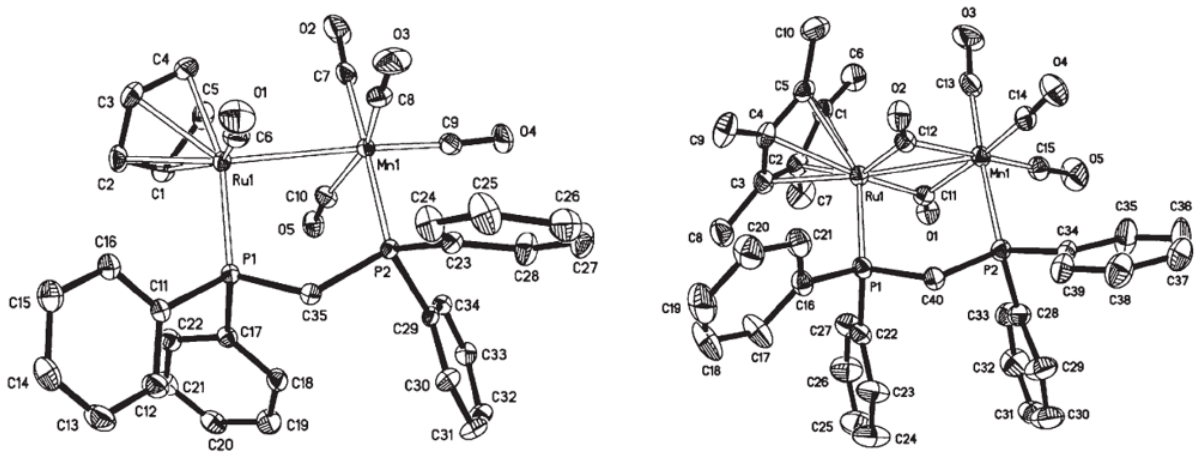

Figure 6.1. X-ray structure of $[(C_5H_5)Ru(CO)(\mu\text{-dppm})Mn(CO)_4]$ (left) and X-ray structure of $[\{C_5(CH_3)_5\}Ru(\mu\text{-}CO)_2(\mu\text{-dppm})Mn(CO)_3]$ where dppm = bis-diphenylphosphinomethane. Reproduced from ref #[445] with permission by John Wiley and Sons.

The reactivity of several substrates including propylene oxide, butadiene monoxide, 1,2-epoxyhexane and cyclohexene oxide were examined with excellent catalytic results.[445]

Using Zr-Co heterobimetallic compounds, a two-electron reduction of CO_2 into CO and Zr-O-Co oxo species was observed, and when a multi-electron reduction was attempted, a carbonate was produced. In addition, one-electron oxidation by H_2O can release hydrogen and form a Zr-hydroxide. At the same time, this metal-hydroxo might be deprotonated and act as nucleophile to attack different metals (Scheme 6.3).[446,447]

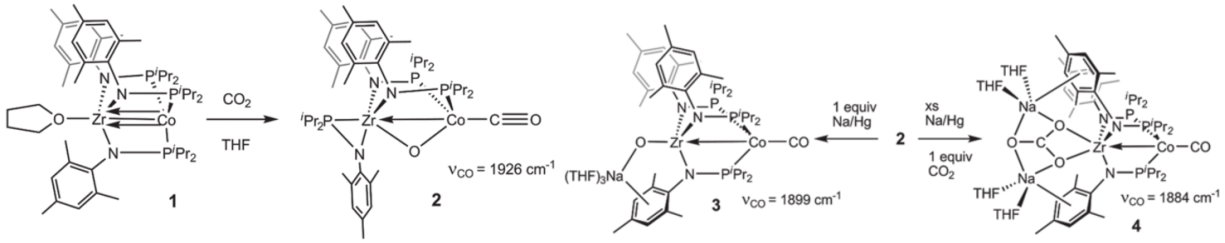

Scheme 6.3. Reduction of CO_2 using Zr and Co. Reproduced from ref #[446] with permission by The American Chemical Society.

More recently, heterobimetallic systems and multi-metallic structures have been studied for cooperative CO_2 activation,[448–452] a strategy pioneered by Floriani in the 70s.[453] On the same line, bimetallic Fe compounds were found to perform deoxygenation of CO_2 into CO and Fe-O-Fe bridges along with a remarkable reductive coupling to oxalate.[454] Unfortunately, CO_2 reduction into oxalate was only a low yield side process. More recently, the combination of U-K-Si atoms in the same molecular structure afforded C=O cleavage of the coordinated CO_2 molecule. As a result, a uranium(V) oxo species and CO were obtained.[452]

Other strategies for the synthesis of heteropolymetallic systems include usage of polydentate ligands, trans-metalation and one-pot reactions among others.[238,455] One of the most recent and remarkable achievement in this field is the preparation of heterobimetallic structures aiming at carbon dioxide absorption/insertion/activation (Figure 6.2).

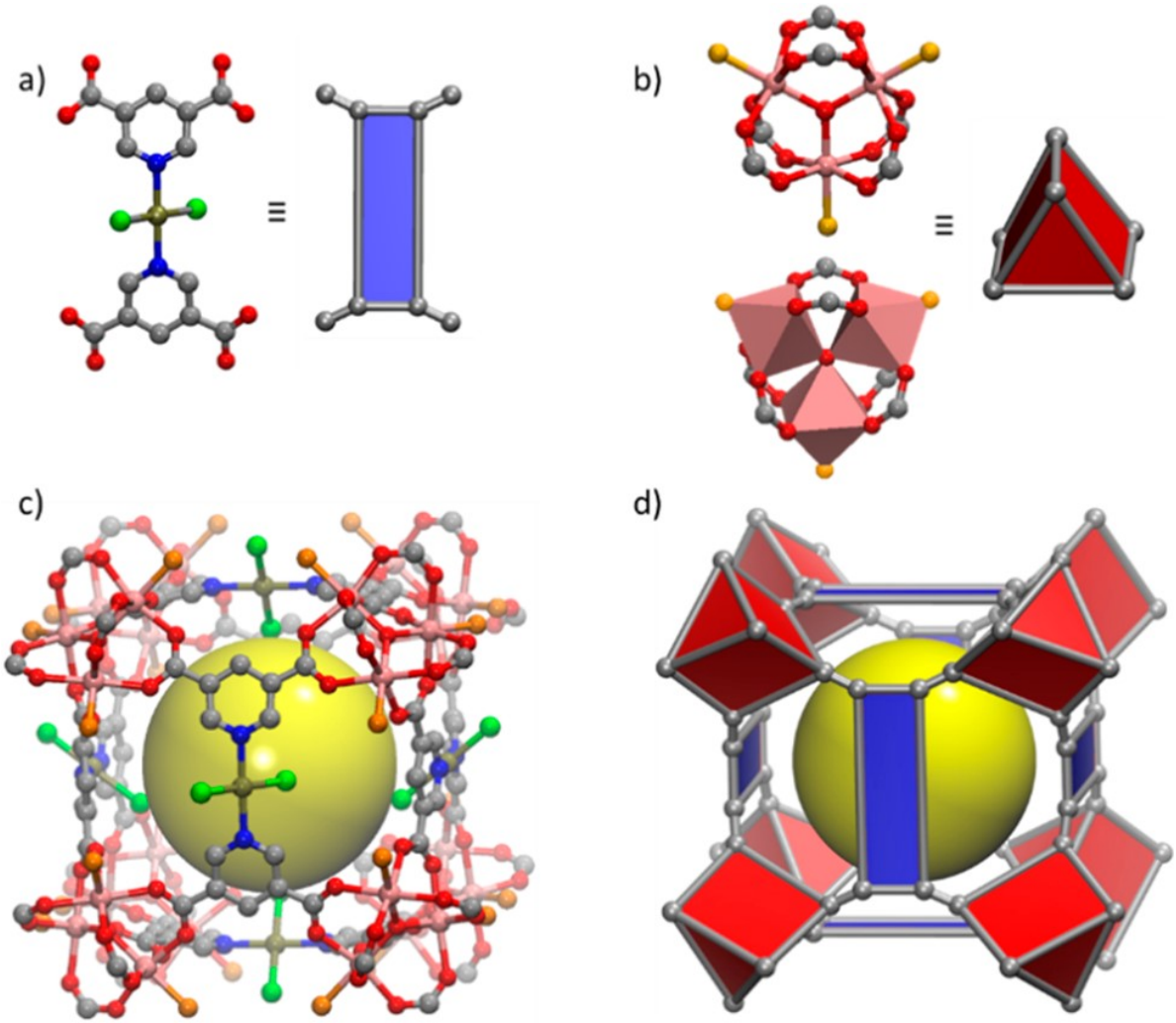

Figure 6.2. X-ray crystal structure of (a) metallo-ligand trans-$[PdCl_2(PDC)_2]$ (H_4L), representing a 4-connected rectangular planar node, (b) the oxo-centered indium carboxylate SBU, $[In_3O(COO)_6(H_2O)_2Cl]$ representing a 6-connected trigonal prismatic node and (c) ball-and stick and (d) polyhedral representation of the cuboidal cage (Color scheme: pink = In, gray = C, blue = N, red = O, tan = Pd, green = Cl, orange = 2/3 H_2O – 1/3 Cl^-; the large yellow spheres represent the cavity size). Hydrogen atoms are omitted for clarity. Reproduced from ref #[456] with permission by The American Chemical Society.

The heterobimetalic Pd/In structures presented in Figure 6.2 can remarkably uptake up to 9 mmol/g of CO_2 at 273 K and 1 bar. CO_2 activation still remains a challenge and these complexes are mainly used as CO_2 storage device.

Besides CO_2 activation, heteropolymetallic structures in general play an important role for interaction/storage/activation of small molecules and therefore an important research field is for preparing functional molecules with strong Lewis acidic sites and containing polar groups in the framework. In these cases, the geometry plays the usual central role as far as fixation/activation is concerned.[457–459] For our purposes, heterobimetallic systems that can reduce, activate or couple/incorporate carbon dioxide were desirable.[446,448,460] We have thus attempted the preparation of heterobimetallic molecular systems containing Bi and V linked by oxygen atoms. Precursors of bismuth aryloxide were prepared and precursors containing vanadium aryloxide in different oxidation states similar to those presented in Chapter 3 and 4 were used. For the purpose of modeling studies aiming at understanding the role of the two elements in reverse combustion promoted by $BiVO_4$, we were also interested in molecular compounds containing the two metals in various oxidation states. To our knowledge, the only example of a fully-characterized molecular heterobimetallic compound containing Bi and V was reported by J. W. Pell *et. al.* in 1996 (Scheme 6.4).[461]

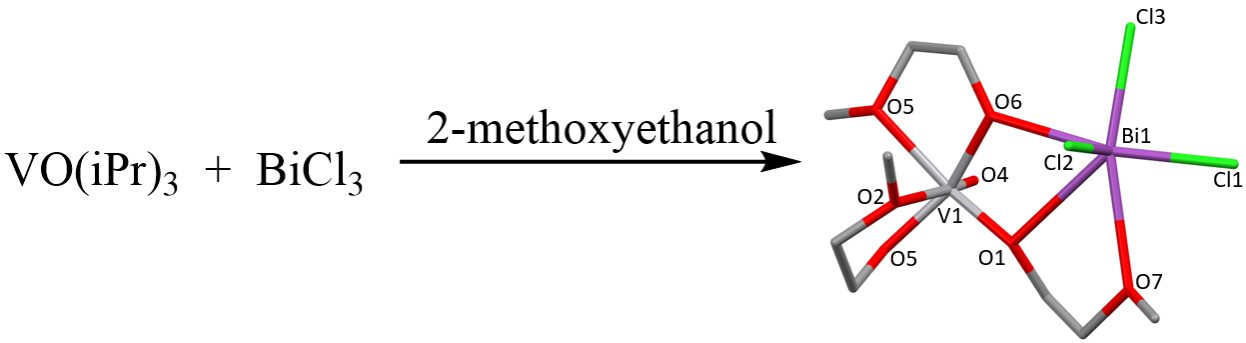

Scheme 6.4. Heterobimetallic Bi-V=O compound

Despite the large and diversified interest and several structures present in literature, there are no general procedures for preparing heterobimetallic compounds containing bismuth as one of its main

components. Several general procedures have been presented in order to obtain other heterobimetallic compounds by Whitmire and coworkers in 2003,[462] 2004[238], 2005[463], 2009[464] and applied in a few instances to the preparation of Bi-V compounds.[455,465–467] These procedures may provide a good starting point for our purpose of preparing model compounds of the *m*-$BiVO_4$ environment using molecular precursors in different oxidation states (Scheme 6.5).

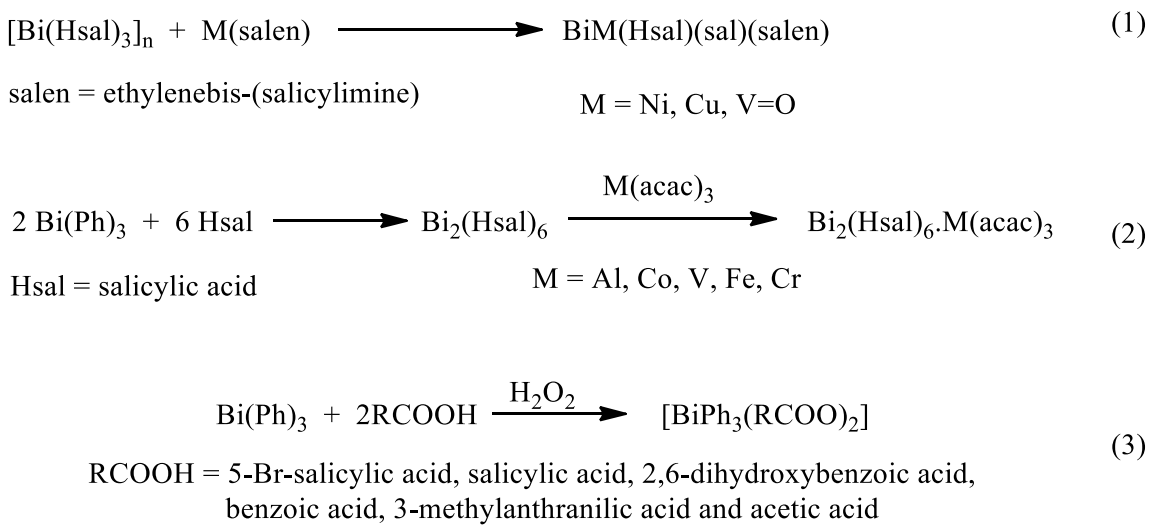

Scheme 6.5. Examples of heterobimetallic compounds and Bi(V) precursor respectively.

As highlighted below, anionic vanadium (III, IV or V) aryloxo metallate complexes containing an alkali cation can in principle be reacted with a bismuth salt such as $BiCl_3$ (Scheme 6.6).

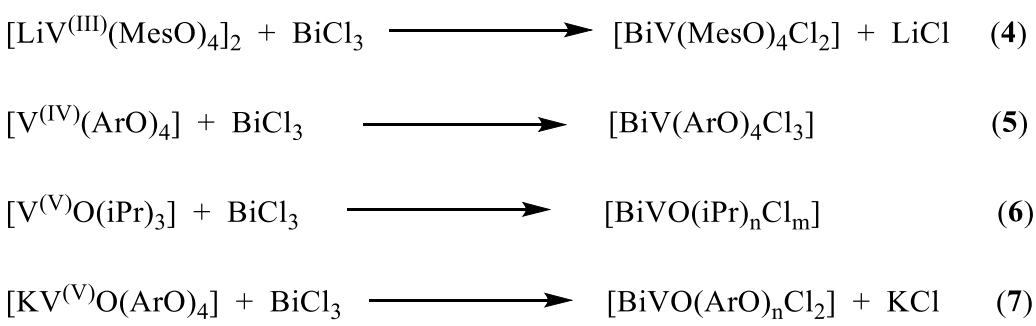

Scheme 6.6. Proposed interactions of vanadium compounds prepared in chapter 4 and commercially available vanadium(V).

In addition, anionic bismuth compounds containing alkali metals as counter cations (implying at least four ligands by one bismuth(III) metal center or six ligands by one bismuth(V)), could be used (Scheme 6.6 equations 4-7) for the reaction with vanadium salts in different oxidation states [e.g. $VOCl_3$, $VO(iPr)_3$, VCl_4 or $VCl_3(THF)_3$]. Furthermore, polydentate ligands with suitable geometries could also be versatile substrates for preparing heterobimetallic structures once they could coordinate to the first metal and use additional coordination sites for a second metallic element.

In this chapter, we describe our efforts for the preparation of heterobimetallic model compounds of *m*-$BiVO_4$. The schematic procedures highlighted above have been followed. After evaluating several possibilities of using individual precursors (Scheme 6.1), one pot syntheses (Scheme 6.4), have also been taken into consideration.

6.3. Results and discussion

We have previously mentioned that the oxidizing power of Bi(V) is sufficiently strong to oxidize water to oxygen (Chapter 2 – *m*-$BiVO_4$). Bi(III) has a non-significant reducing power when surrounded by only oxygen atoms but, it may be able to perform CO_2 insertions. Also, it was stated (Chapter 1) that the

valence band in *m*-$BiVO_4$ is mainly bismuth-contributed. We have thus tested Bi(III) and confirmed that there is no reactivity with CO_2 in term of fixation/coordination/activation while in combination with aryloxide ligands. Scheme 6.7 highlights the preparation of [{(Bi(MesO)$_2$}$_2$(μ-MesO)$_2$(μ-O)K$_2$(THF)$_2$] (**1**) that will be use as precursor to attempt the synthesis of an heterobimetallic structure.

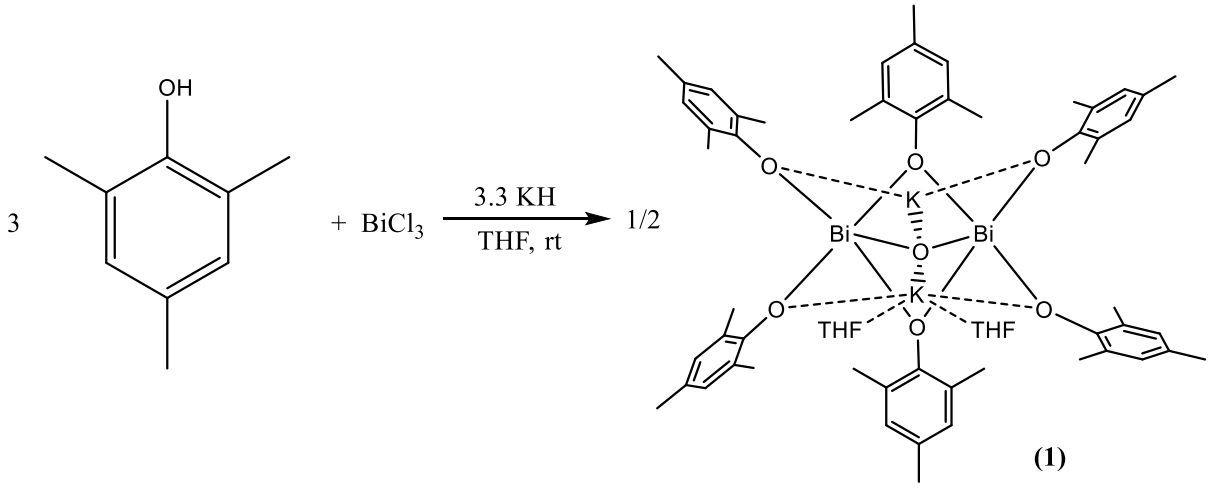

Scheme 6.7. Preparation of compound **1**.

The synthesis of **1** (Figure 6.3) follows the same procedure published by Turner L. E. *et. al.* in 2006 for the preparation of similar compounds of aminotris(phenoxide), alkoxide dimer and phenoxide cluster Bi complexes.[468–470] With **1** as starting material we have performed a direct reaction with $VOCl_3$ aiming at precipitating KCl (the driving force). Unfortunately, the only product crystallized from the resulting mixture was (2,4,6-$Me_3C_6H_2O)_3V(O)$, a known compound (Chapter 4 – compound 9) This result indicates that a transmetallation process occurs during the reaction driven by the oxophilicity of vanadium(V) aryloxide. Compound **1** was also reacted with other vanadium compounds in different oxidation states. For example, reaction with (2,4,6-$Me_3C_6H_2O)_2V(Cl)(THF)_2$[377] in molar ratio 1:1 in toluene gave a black precipitate. The solid was identified by powder X-ray analysis as metallic bismuth. In solution, only intractable material was present but the ^{51}V-NMR spectrum revealed the presence of a mixed-valence

+IV/+V vanadium species. This unexpected results implies that the reducing power of vanadium(III) is sufficient to reduce Bi^{3+} to the metallic state even in a non-stoichiometric reaction. The same behavior was observed when compound **1** was mixed with $[LiV(2,4,6\text{-}Me_3C_6H_2O)_4]_2$ (Chapter 3 – Compound 3), $VCl_3(THF)_3$ and VCl_4.

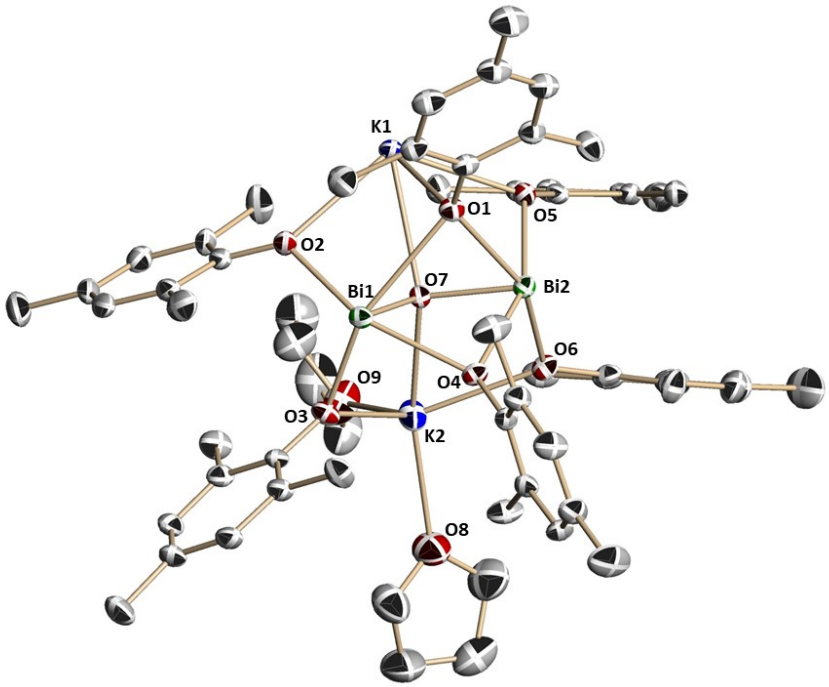

Figure 6.3. Thermal ellipsoid plot of **1** with ellipsoids drawn at the 30% probability level. Hydrogen atoms were omitted for clarity. Selected distances and angles of compound 1 are as follows. Bi1-O7 = 2.059 Å, Bi2-O7 = 2.063 Å, Bi1-O1 = 2.712 Å, Bi1-O2 = 2.235 Å, Bi1-O3 = 2.177 Å, Bi1-O4 = 2.442 Å, Bi2-O1 = 2.547 Å, Bi2-O4 = 2.386 Å, Bi2-O5 = 2.266 Å, Bi2-O6 = 2.210 Å, Bi1-Bi2 = 3.369 Å, Bi1-O7-Bi2 = 109.66°, Bi1-O1-Bi2 = 79.63° and Bi1-O4-Bi2 = 88.51°.

These results have clearly indicated that the reducing power of vanadium(III-IV) aryloxides and halides are too reducing to be compatible with trivalent bismuth. The last possibility was to decrease the ligand mobility by increasing its denticity. We thus decided to use a more rigid aryloxide system such as Calix[4]. The preparation of the bismuth derivative is summarized in Scheme 6.8.

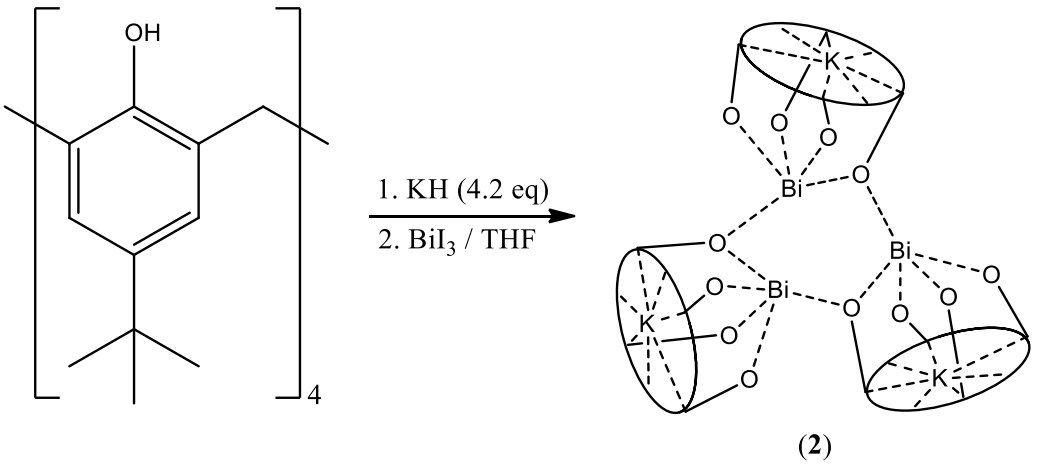

Scheme 6.8. Preparation of compound **2**.

As a result, an attractive trimeric structure was obtained. This new bismuth compound presents two interesting structural characteristics. Firstly, there is coordination of a bismuth atom by an oxygen of another unit to complete its coordination sphere, and which is unusual for a Bi^{3+} aryloxide compound. Secondly, the counter cation (potassium) is located in the cavity of the calixarene ligand (Figure 6.4). These two features advised us to attempt both a direct interaction with carbon dioxide (additional vacancy on bismuth atom) and a substitution reaction where the K^+ could be replaced by a $[VOCl_2]^+$ unit after elimination of KCl.

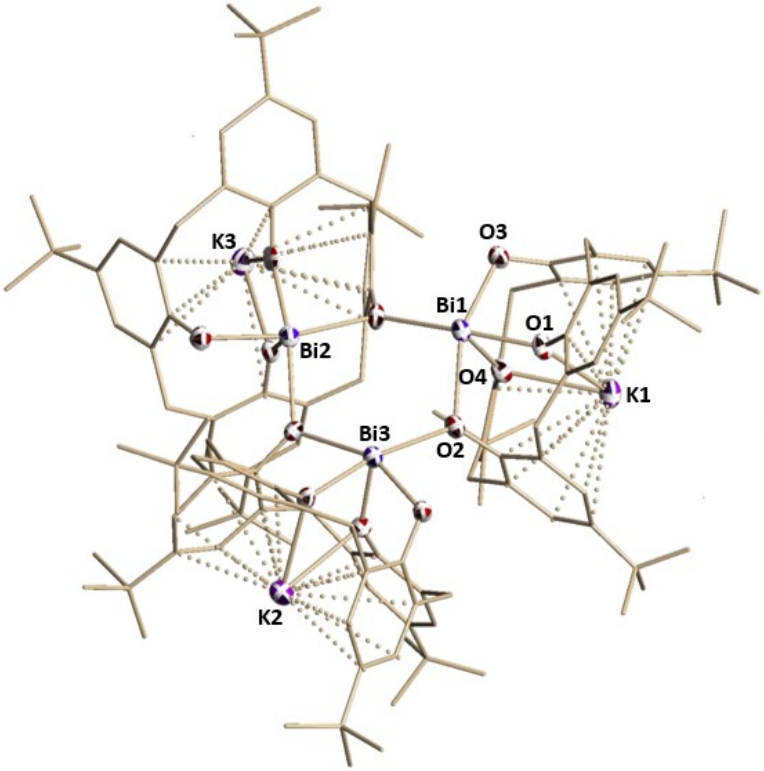

Figure 6.4**.** Thermal ellipsoid plot of **2** with ellipsoids drawn at the 30% probability level. Hydrogen atoms were omitted by clarity.

The reaction of **2** with $VOCl_3$ in the same stoichiometric ratio gave red crystals of a new compound $[(THF)_2KVO(calix[4])]$ (**3**) shown in Figure 6.5. Once again, the reaction did afford trans-metalation with formation of a potassium salt of vanadyl(V) calix[4] and precipitated $BiCl_3$.

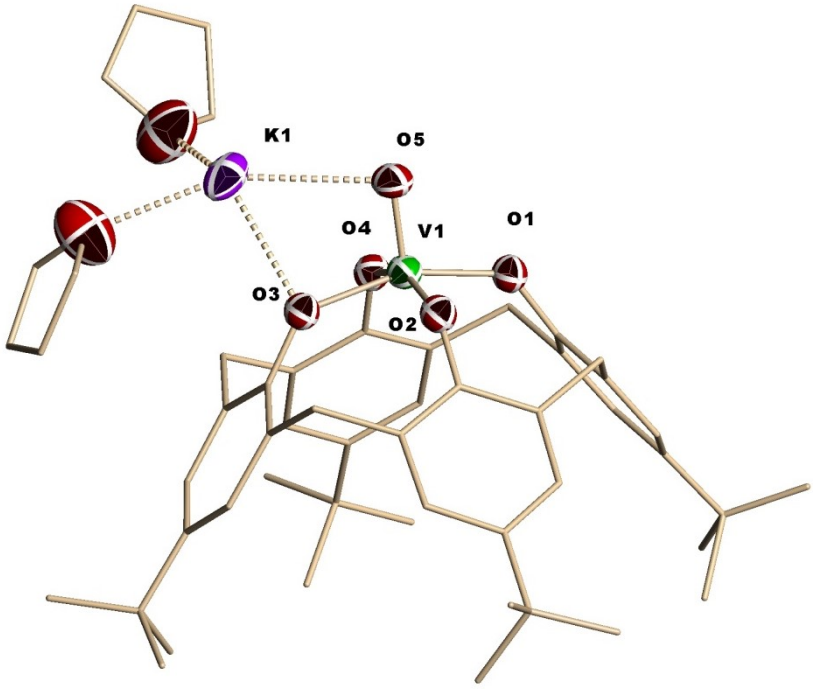

Figure 6.5. Thermal ellipsoid plot of **3** with ellipsoids drawn at the 30% probability level. Hydrogen atoms were omitted by clarity. Selected distances and angles of compound **3** are as follows. V1 – O5 = 1.595 Å, V1 – O1 = 1.844 Å, V1 – O2 = 1.888 Å, V1 – O3 = 1.894 Å, V1 – O4 = 1.850 Å, O5 – K1 = 2.947 Å, K1 – O2 = 2.585 Å, O1-V1-O5 = 102.39^{o} and O2-V1-O5 = 99.33^{o}.

We have finally decided to attempt a one-pot reaction by mixing vanadyl(V) tris-isopropoxide and lithium bis(trimethylsilyl)amide (LiHMDS) as a deprotonating agents for the calix[4] ligand and $BiCl_3$ (Scheme 6.9).

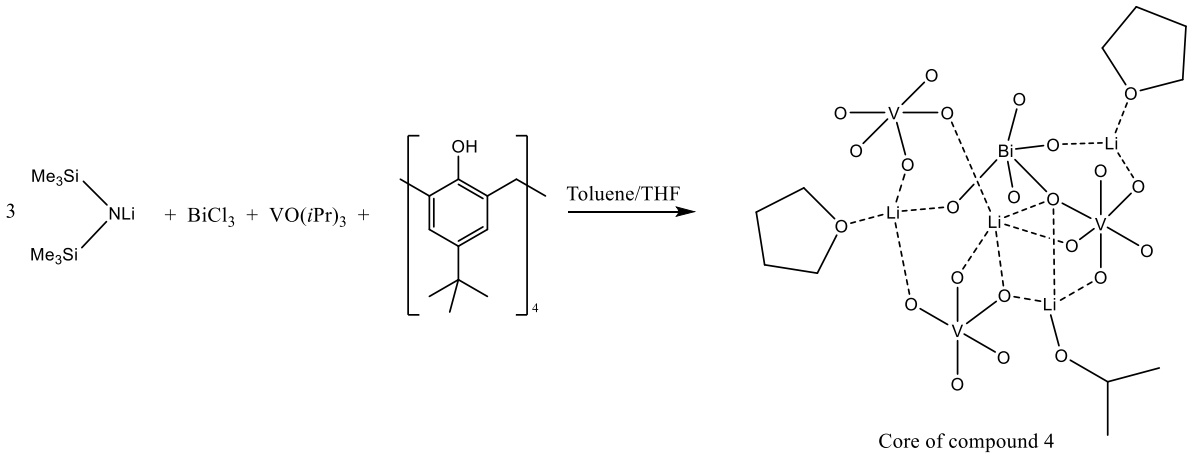

Scheme 6.9. One pot reaction to obtain compound **4**.

The reaction was performed in one-pot but in two separated stages. $BiCl_3$ and LiHMDS were mixed in molar ratio 1:3 respectively in 5 mL of toluene and stirred overnight (mixture A). In a similar way, vanadyl(V) tris-isopropoxide and calix[4]arene-*p*-(tert-butyl)phenol were mixed in equimolar ratio and same conditions as mixture A (mixture B). Each reaction mixture was dried under vacuum and the residues re-dissolved in toluene. The combining of the two resulting solutions gave a mixture of deeper color (deep red). After stirring overnight at room temperature and centrifugation, the dark red solution was left undisturbed while separating red crystals after 1 week at -30^{o}C. The X-ray analysis of the red crystals revealed an extraordinary structure (Figure 6.6) of a hetero-trimetallic compound [Bi(calix[4]){VO (calix[4]}$_3$(OH){μ-Li(iPr)}{μ-Li(THF)}$_2$] (**4**) with the lithium atom having being retained along with both vanadium and bismuth.

Compound **4** is a diamagnetic compound. In the ^{7}Li-NMR spectrum the chemical shift appears as a broad pick at 1.09 ppm. Vanadium is present in the pentavalent state with chemical shifts at 655.14, 679.40 and 709.18 ppm of the ^{51}V-NMR spectrum. Charge-count along with the diamagnetism confirmed the oxidation state +5 for the vanadium atoms, this allowed us to assume a trivalent state for bismuth. This also implies that 3 protons should be present in the structure. A simple test of reacting

4 with water did not afford oxygen gas and indirectly confirmed that the oxidation state of Bi is not higher than +3. The location of the three protons was not possible through difference Fourier maps, most likely because of the large size of the molecule and the large number of oxygen atoms. Instead, FTIR spectra clearly confirmed the presence of hydroxyl groups as a broad band in the region 3511-3450 cm^{-1}.

Several attempts were made to obtain a lithium-free heterobimetallic compound by filtering the mixture A prior to the addition to B. This would allow the formation *in-situ* of the Bi compound $[Bi(N(SiMe_3)_2)_3]$ already published structure by Marko Vehkamäki *et. al*. 2004.[471] We have thus re-prepared this precursor in crystalline form but attempts to obtain heterobimetallic structures were unsuccessful. The presence of lithium in the structure seems indeed necessary to obtain a characterizable material.

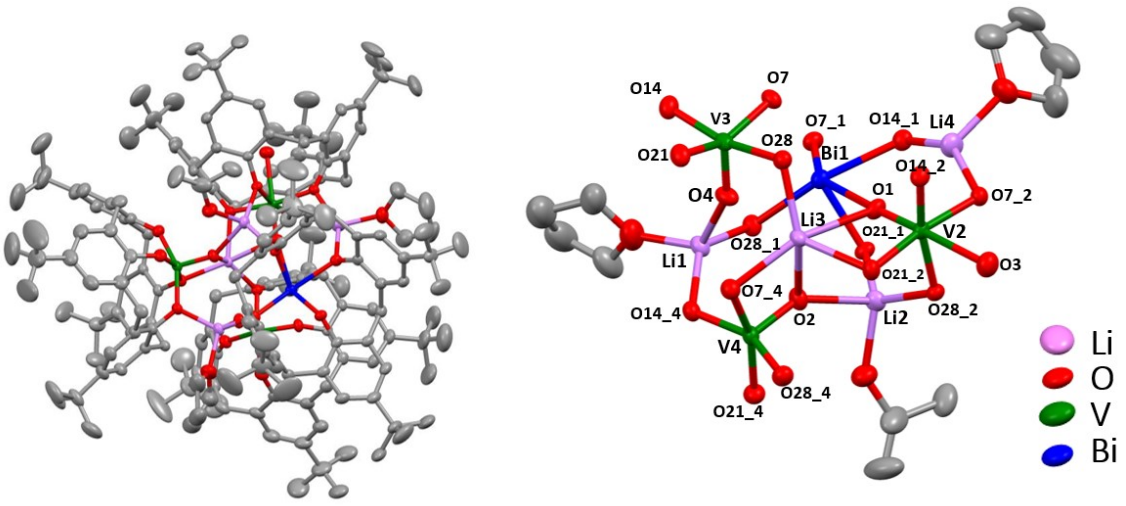

Figure 6.6. a) Thermal ellipsoid plot of **4** with ellipsoids drawn at the 30% probability level. Hydrogen atoms and toluene in the lattice were omitted by clarity. b) core structure of **4** where the carbon atoms in the ligand system calix[4] were omitted by clarity. Selected distances and angles of compound 4 are as follows. Bi_1 – O1 = 2.846 Å, Bi_1 – O7_1 = 2.085 Å, Bi_1 – O28_1 = 2.238 Å, Bi_1 – O14_1 = 2.307 Å, Bi_1 – O21_1 = 2.181 Å, V_2 – O1 = 1.620 Å, V_2 – O7_2 = 1.937 Å, V_2 – O21_2 = 1.928 Å, V_2 – O28_2 = 1.921 Å, V_3 – O4 = 1.617 Å, V_3 – O7_3 = 1.858 Å, V_3 – O14_3 = 1.855 Å, V_3 – O21_3 = 1.809 Å, V_3 – O28_3 = 1.956 Å, V_4 – O2 = 1.625 Å, V_4 – O7_4 = 1.897 Å, V_4 – O14_4 = 1.898 Å, V_4 – O21_4 = 1.884 Å, V_4 – O28_4 = 1.810 Å, Bi_1 – O1 – V_2 = 162.62° , V_3 – O4 – Li1 = 152.57°, Bi_1 – O21_1 – Li2 = 115.81° and V_2-O2-Li2 = 143.81°.

The structure of **4** displays a small cavity between Bi1 and V3 atoms. This structural characteristic might provide space for coordinating CO_2. Unfortunately, compound **4** does not react with CO_2. Using pressures up to 300 PSI and temperatures up to 70°C did not modify the outcome of the reaction.

6.4. Conclusions

Attempts to prepare a heterobimetallic compound that contain bismuth and vanadium were made and compound **4** successfully prepared and characterized. This work was hampered by the presence of a few serious challenges. An unanticipated non-compatibility of trivalent bismuth with vanadium in oxidation state lower than +4 was determined. As a result, metallic bismuth was formed while vanadium was oxidized to a mixed vanadium(IV-V) species. When starting material containing higher oxidation state of vanadium have been used, trasmetallation reaction occurred. A new vanadium(V) complex (**3**) was isolated. In both cases, when both mono- and polydentate ligands were used (MesOH and calix[4]) a trasmetallation was still observed. One-pot reactions allowed the isolation and characterization of a fascinating trimetallic species (**4**). Unfortunately, the target combination of oxidation states could not be obtained given the problems listed above, and, as anticipated, no reactivity was observed with carbon dioxide. Further attempts to obtain an heterobimetallic structure containing the two partner metals in different oxidation state will be necessary by tuning the electron donor ability of the ligand systems.

6.5. Experimental part

Chemical and physical measurements. As before, all manipulations were performed under nitrogen or argon atmosphere with rigorous exclusion of oxygen and water by using standard Schlenk and glovebox techniques. n-Heptane, pentane, ether, toluene and THF were dried over activated Al_2O_3 and deoxygenated prior to use by several vacuum/nitrogen/argon purges. $VO(iPr)_3$, LiHMDS and $BiCl_3$

99.99% in Bi were purchased from Sigma Aldrich and used as initial precursor for preparation of $VCl_3(THF)_3$. Carbon dioxide grade 5.0 was purchased from Linde. The organic ligands used (MesOH and calix[4]) were purchased from Alfa and Aldrich. NMR analysis were performed in an automatic Bruker ADVANCE II 400 MHz. ^{51}V and ^{7}Li NMR were performed in a Bruker ADVANCE II 300 with liquid autotuning broadband probe with Z gradient. Neat $VOCl_3$ was used as standard (-4.12 ppm).

Crystallography and magnetic measurements. The crystals were mounted on thin glass fibers using paraffin oil. Prior to data collection crystals were cooled to 200(2) K. Data were collected on Bruker APEX2 single-crystal diffractometers equipped with sealed Mo tube sources (wavelength 0.71073 Å) and APEX II CCD detectors. Raw data collection and processing were performed with APEX II software package from BRUKER AXS. Semi-empirical absorption corrections based on equivalent reflections were applied. Systematic absences in the diffraction data-set and unit-cell parameters were consistent with the assigned space groups. The structures were solved by direct methods, completed with difference Fourier synthesis, and refined with full-matrix least-squares procedures based on F^2. All non-H atoms were refined anisotropically. All hydrogen atoms positions were calculated based on the geometry of the related non-hydrogen atoms (riding model).

Preparation of compound 1. 2,4,6-$Me_3C_6H_2O$ (3.04 mmol, g) (MesOH) was dissolved in 10 mL of THF and KH (19.9 mmol, 0.799 g) was then added until full deprotonation. After 24 h of stirring the solution, $BiCl_3$ (1.01 mmol, 0.315 g) was added and a resultant yellow color solution was obtained and stirred for another 24 hours to allow the reaction to occur. Centrifugation was done and any side product such as KCl was removed from the solution. The yellow THF solution was dried out and redissolved in toluene. Once more the solution was centrifuged and the yellow product was then put under slow vapor diffusion technique using pentane. After 4 days, pale yellow crystals were obtained and isolated by filtration. The yield of the reaction was 68.1% (0.34 mmol, 0.52 g).

Preparation of compound 2. Calix[4]arene-t-buthylphenol (0.54 mmol, g) was partially dissolved in 10 mL of THF and KH (2.20 mmol, 0.0882 g) was slowly added until full deprotonation. The resultant mixture was stirred for 36 h. After that, $BiCl_3$ (0.56 mmol, 0.177 g) was added. The resultant pale-yellow color solution was stirred for another 24 hours to allow the reaction to occur. Centrifugation was done and any side product such as KCl was removed from the solution. The yellow THF solution was then put under layering diffusion technique using 3 mL of pentane. After 2 days, pale yellow crystals were obtained and isolated by filtration (0.19 mmol, 0.17g). the yield of the reaction was 35.9%.

Preparation of compound 3. Compound 2 (0.259g, 0.25 mmol) was partially dissolved in 5 mL of toluene and the mixture was cooled at -35°C for 2 hours. Cold $VOCl_3$ (0.025 mL, 0.26mmol) was added slowly while the mixture was stirring. The yellow color changed to dark red and some solid precipitated and was removed with centrifugation. The centrifuged solution was vacuum-dried and redissolved in 3 mL of dry THF. Slow vapor diffusion using pentane yielded red crystals that were characterized by single crystal X-ray technique. The yield of the reaction was 42.1% (0.0942 g, 0.11 mmol).

Preparation of compound 4. LiHMDS (2.41 mmol, 0.403 g) was dissolved in 5 mL of dry toluene. $BiCl_3$ (0.79 mmol, 0.249 g) was added and the mixture was stirred for 48 h (Mixture A). In a separate vial, calix[4]arene-t-butylphenol (0.77 mmol, 0.500 g) was partially dissolved in 10 mL of toluene. $VO(iPr)_3$ (0.78 mmol, 0.18 mL) was slowly added until full color change to deep red (Mixture B). Mixture B was stirred for 48h to allow full deprotonation and formation of the respective isopropyl alcohol. After the aforementioned time, mixture B was slowly added into mixture A. The deep red color remains and 24h later, the resultant solution was centrifuged to removed any insoluble product. After 2 weeks, from the red solution, dark red crystals were obtained, isolated and characterized by single crystal X-ray diffraction. The yield of the reaction was 21.2 % (0.61 g, 0.16 mmol).

6.6. Appendix: Support information

Appendix T6.1. ^{51}V and ^{7}Li NMR for compound 4.

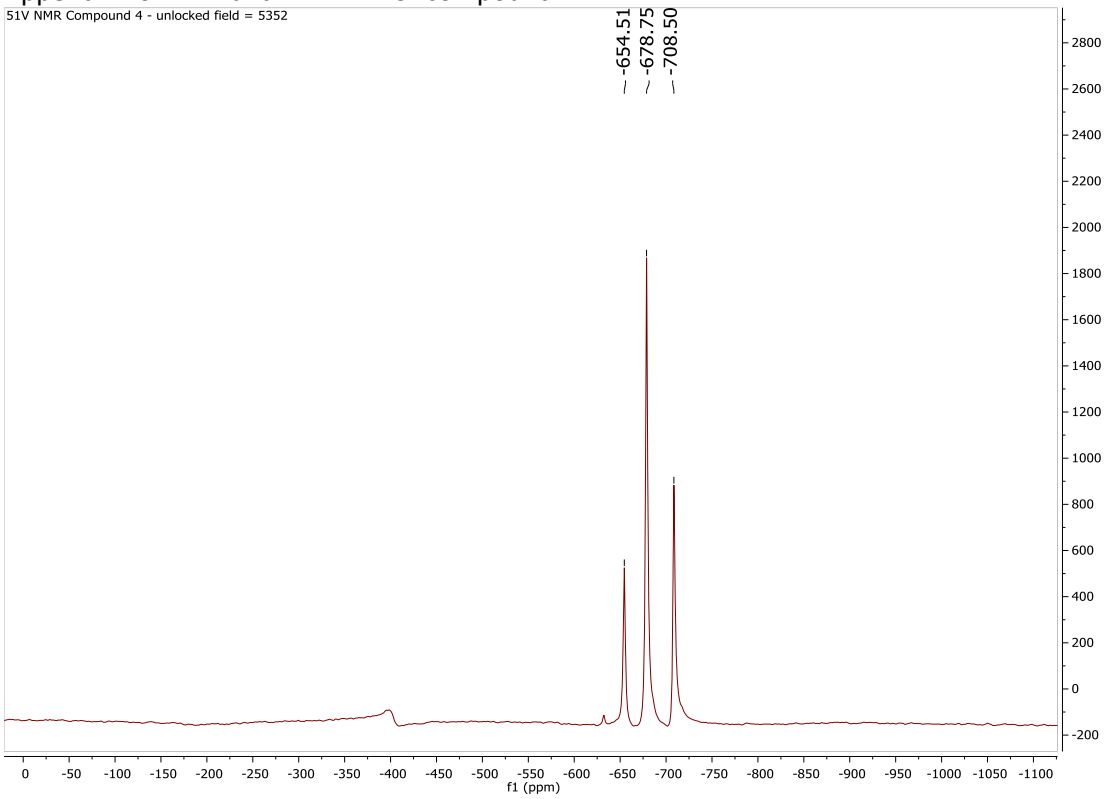

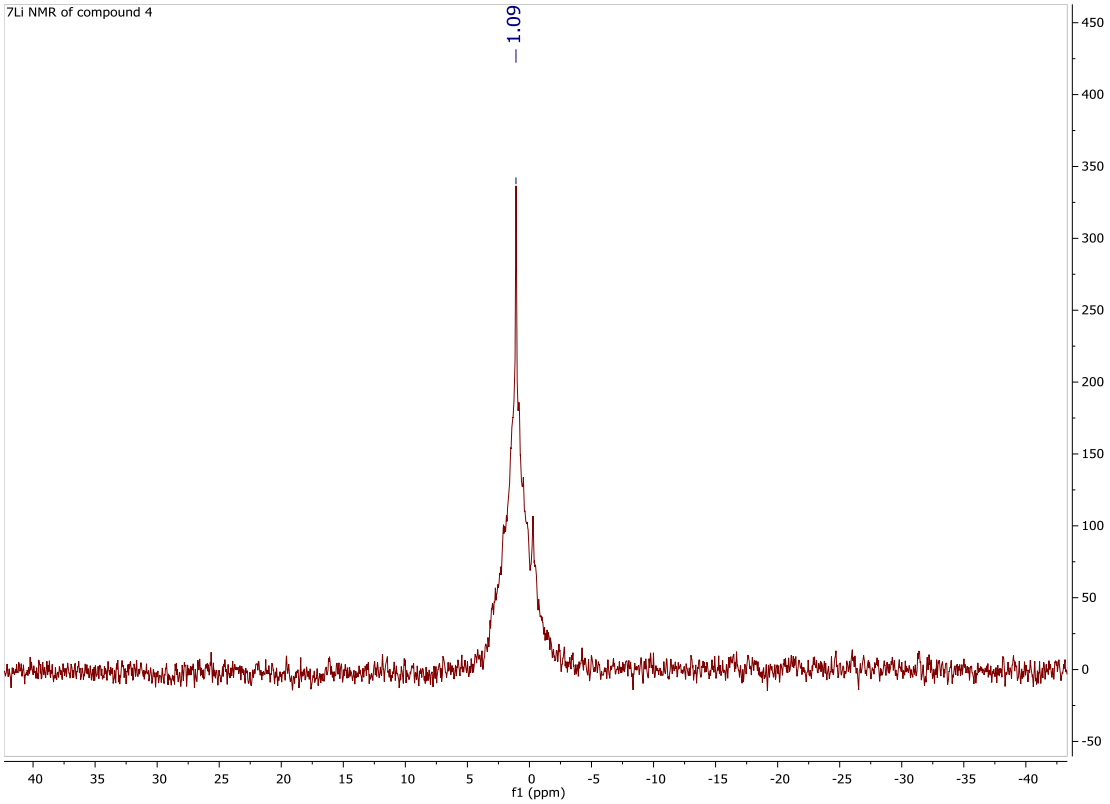

Appendix T6.2. Crystallographic details for compounds 1, 3 and 4.

	1	**3**	**4**
Formula	$C_{65}H_{88}O_{9.75}Bi_2K_2$	$C_{61}H_{80}O_{7.5}V_{0.5}$	$C_{218.50}H_{266}BiLi_4O_{23}V_3$
fw	1521.51	1023.29	3649.86
a (Å)	12.4506(3)	13.0045(3)	18.1879(16)
b (Å)	37.4715(11)	15.6593(4)	20.395(2)
c (Å)	14.8868(4)	15.9104(4)	30.165(3)
α (deg)	90	74.6694(16)	89.818(3)
β (deg)	105.7730(10)	74.0755(15)	82.439(3)
γ (deg)	90	79.2975(15)	84.725(3)
cryst syst	Monoclinic	Triclinic	Triclinic
space group	P2(1)/n	P-1	P-1
V ($Å^3$)	6683.8(3)	2982.35(13)	11044.9(18)
Dc (g cm^{-1})	1.512	1.140	1.097
Z	4	2	2
no. of meas. Reflect.	76158	43265	143846
no. of reflect [$I>2\ \sigma(I)$]	16520	14696	53040
R_{int}	0.0495	0.0593	0.0442
R_1 [$I>2\ \sigma(I)$]	0.0437	0.0827	0.0538
wR_2[$I>2\ \sigma(I)$]	0.0966	0.2239	0.1486
GOF	1.003	1.049	0.658

Chapter 7. General conclusions and aims of future work

7.1. Outlook

The chemistry of vanadium and bismuth poses formidable challenges to researchers aiming at understanding and improving systems for the reduction of carbon dioxide. In this thesis we have tried to contribute to the pressing problem of the recycling of carbon dioxide.

We have confirmed that monoclinic bismuth vanadate could indeed produce methanol by the reverse combustion pathway in a photo-irradiated process. In the contrary, the claims for the formation of ethanol or methane have been disproved by our experiments, and yet, our results provided an improved understanding of how the reverse combustion proceeds. Photoirradiation-EPR experiments on m-$BiVO_4$ were performed and demonstrated that an *in situ*-generated vanadium(IV) species might be the key intermediate. The results reported in chapter 2 generate new insights into the mechanism of the CO_2 photoreduction mediated by *m*-$BiVO_4$ affording formaldehyde, formate and methanol.

Preparation and crystallization of monoclinic and orthorhombic bismuth chromate oxide hydroxides were performed aiming at improving the oxygen-release half-reaction of the reverse combustion process. Unfortunately, no photochemical activity was observed under any testing condition. Nonetheless, *m*-$BiOHCrO_4$ was found to be the most effective catalyst for thermal decomposition of formic acid. Disproportionation of formic acid into formaldehyde, CO_2 and water was performed under mild conditions. Conversion of formic acid into formaldehyde is a step forward towards a neutral formic acid/formaldehyde couple cycle for a Z-scheme hydrogen production. The new species, $BiCrO_4$, was identified as the responsible for the formaldehyde production. $IrCl_3$ was used as the most efficient catalyst among other metal chlorides to dehydrogenate formaldehyde into a highly selective formate production in basic media and to close a catalytic cycle.

Modeling studies have been carried out to understand the role of vanadium in reverse combustion. Lower oxidation states in vanadium aryloxide compounds display a great versatility for reducing CO_2 into CO and formate and radical chemistry including also the involvement of the ligand system (Ch 4 and 5). Some truly unprecedented reactivity with CO_2 has been discovered. DFT calculations on our model compounds have predicted the linear coordination of CO_2. By using a rigid polydentate ligand system (ONNO) it was possible to conclusively prove the coordination mode of CO_2, identify the vanadium oxidation state and fully rationalize the unusual pattern of reactivity.

A vanadium(III)-OH in a rigid $ONNO^{2-}$ ligand environment is the key to coordinate CO_2. The tuning of vanadium reducing power was attempted via ligand modification or addition of a Cl atom in the vanadium coordination sphere a LV-Cl (L = ONNO or ONOO). This has enabled the preparation of a family of complexes. Of a particular interest there is the reaction of a vanadium(III) methoxide with CO_2 to generate formate and formaldehyde.

Finally, we have attempted an assessment of the role of bismuth in reverse combustion through the preparation of Bi-V heterobimetallic model compounds and by using calix[4]arene-*p*-tert-butylphenoxide as ligand. In the compound so far obtained, both bismuth and vanadium retained their initial oxidation states of +3 and +5 respectively. While these oxidation states are inert towards CO_2, we found that lower valent vanadium systematically reduces bismuth to its zero valent state, thus far invalidating aryloxide ligands as models for reverse combustion.

7.2. Future Work

More extensive studies to examine the electron transfer processes of $BiVO_4$ to CO_2 should be carried out. The fact that our EPR work has highlighted that a paramagnetic photoexcited species is a key player of the reverse combustion process, it encourages further work for evaluating the environment of vanadium compounds to improve their electronic characteristics and unveil different reactivity patterns.

Important mechanistic questions still remain about how one-electron transfer could be performed to CO_2 with a multielectron system such as vanadium. The structures of vanadium in different oxidation states and ligand environment provided a very important starting point for studying this challenging redox-chemistry. If an improved and tunable ligand environment could be found and where the electronic density on vanadium may be varied at will, the bonding mode of CO_2 and reactivity patterns may be fully understood.

7.3. References

[1] V. Artero, M. Chavarot-Kerlidou, M. Fontecave, *Angew. Chemie Int. Ed.* **2011**, *50*, 7238–7266.

[2] K. Maeda, *J. Photochem. Photobiol. C Photochem. Rev.* **2011**, *12*, 237–268.

[3] H. Zhang, G. Chen, D. W. Bahnemann, *J. Mater. Chem.* **2009**, *19*, 5089.

[4] A. Kudo, Y. Miseki, *Chem. Soc. Rev.* **2009**, *38*, 253–278.

[5] S. K. Saraswat, D. D. Rodene, R. B. Gupta, *Renew. Sustainable. Energy Rev.* **2018**, *89*, 228–248.

[6] S. Y. Tee, K. Y. Win, W. S. Teo, L. D. Koh, S. Liu, C. P. Teng, M. Y. Han, *Adv. Sci.* **2017**, *4*, DOI 10.1002/advs.201600337.

[7] R. Abe, *J. Photochem. Photobiol. C Photochem. Rev.* **2010**, *11*, 179–209.

[8] D. G. Nocera, *Acc. Chem. Res.* **2012**, *45*, 767–76.

[9] C. Zhu, C. Liu, Y. Zhou, Y. Fu, S. Guo, H. Li, S. Zhao, H. Huang, Y. Liu, Z. Kang, *Appl. Catal. B Environ.* **2017**, *216*, 114–121.

[10] A. Kudo, H. Kato, *Chem. Phys. Lett.* **2000**, *331*, 373–377.

[11] H. Kato, K. Asakura, A. Kudo, *J. Am. Chem. Soc.* **2003**, *125*, 3082–3089.

[12] P. Liao, E. A. Carter, *Chem. Soc. Rev.* **2013**, *42*, 2401–2422.

[13] S. Tabata, H. Nishida, Y. Masaki, K. Tabata, *Catal. Letters* **1995**, *34*, 245–249.

[14] D. J. Martin, P. J. T. Reardon, S. J. a Moniz, J. Tang, *J. Am. Chem. Soc.* **2014**, 2–5.

[15] K. Maeda, *Chem. Commun.* **2013**, *49*, 8404.

[16] C. Pan, T. Takata, M. Nakabayashi, T. Matsumoto, N. Shibata, Y. Ikuhara, K. Domen, *Angew. Chem. Int. Ed.* **2015**, *54*, 2955–2959.

[17] P. Kanhere, Z. Chen, *Molecules* **2014**, *19*, 19995–20022.

[18] T. Takata, C. Pan, K. Domen, *Sci. Technol. Adv. Mater.* **2015**, *16*, 033506.

[19] S. Balaz, S. H. Porter, P. M. Woodward, L. J. Brillson, *Chem. Mater.* **2013**, *25*, 3337–3343.

[20] K. Rakesh, S. Khaire, D. Bhange, P. Dhanasekaran, S. S. Deshpande, S. V. Awate, N. M. Gupta, *J. Mater. Sci.* **2011**, *46*, 5466–5476.

[21] Z. Zou, J. Ye, H. Arakawa, *Chem. Phys. Lett.* **2000**, *332*, 271–277.

[22] L. Zhang, L. O. Herrmann, J. J. Baumberg, *Sci. Rep.* **2015**, *5*, 16660.

[23] Y. H. Ng, A. Iwase, A. Kudo, R. Amal, *J. Phys. Chem. Lett.* **2010**, *1*, 2607–2612.

[24] H. Fujito, H. Kunioku, D. Kato, H. Suzuki, M. Higashi, H. Kageyama, R. Abe, *J. Am. Chem. Soc.* **2016**, jacs.5b11191.

[25] L. An, Y. Park, Y. Sohn, H. Onishi, *J. Phys. Chem. C* **2015**, *119*, 28440–28447.

[26] A. Iwase, H. Kato, A. Kudo, *Catal. Letters* **2006**, *108*, 7–10.

[27] P. Kalisman, Y. Nakibli, L. Amirav, *Nano Lett.* **2016**, *16*, 1776–1781.

[28] A. Galińska, J. Walendziewski, *Energy & Fuels* **2005**, *19*, 1143–1147.

[29] H. J. Kong, D. H. Won, J. Kim, S. I. Woo, *Chem. Mater.* **2016**, acs.chemmater.5b04178.

[30] Z. Jiang, Y. Liu, M. Li, T. Jing, B. Huang, X. Zhang, X. Qin, Y. Dai, *Sci. Rep.* **2016**, *6*, 22727.

[31] E. Nurlaela, T. Shinagawa, M. Qureshi, D. S. Dhawale, K. Takanabe, *ACS Catal.* **2016**, 1713–1722.

[32] T. W. Kim, K.-S. Choi, *Science* **2014**, *343*, 990–4.

[33] T. K. Townsend, E. M. Sabio, N. D. Browning, F. E. Osterloh, *ChemSusChem* **2011**, *4*, 185–190.

[34] Y. Sakata, Y. Matsuda, T. Nakagawa, R. Yasunaga, H. Imamura, K. Teramura, *ChemSusChem* **2011**, *4*, 181–184.

[35] R. Marschall, *Adv. Funct. Mater.* **2014**, *24*, 2421–2440.

[36] T.-F. Yeh, J.-M. Syu, C. Cheng, T.-H. Chang, H. Teng, *Adv. Funct. Mater.* **2010**, *20*, 2255–2262.

[37] N. Gao, X. Fang, *Chem. Rev.* **2015**, *115*, 8294–8343.

[38] J. Guo, Y. Li, S. Zhu, Z. Chen, Q. Liu, D. Zhang, W.-J. Moon, D.-M. Song, *RSC Adv.* **2012**, *2*, 1356–1363.

[39] Y. Liang, Y. Li, H. Wang, J. Zhou, J. Wang, T. Regier, H. Dai, *Nat. Mater.* **2011**, *10*, 780–786.

[40] Y. Li, H. Wang, L. Xie, Y. Liang, G. Hong, H. Dai, *J. Am. Chem. Soc.* **2011**, *133*, 7296–7299.

[41] Q. Li, B. Guo, J. Yu, J. Ran, B. Zhang, H. Yan, J. R. Gong, *J. Am. Chem. Soc.* **2011**, *133*, 10878–10884.

[42] K. Rajeshwar, *J. Appl. Electrochem.* **2007**, *37*, 765–787.

[43] P. Zhang, J. Zhang, J. Gong, *Chem. Soc. Rev.* **2014**, *43*, 4395.

[44] T. M. Suzuki, A. Iwase, H. Tanaka, S. Sato, A. Kudo, T. Morikawa, *J. Mater. Chem. A* **2015**, *3*, 13283–13290.

[45] Q. Wang, Y. Li, T. Hisatomi, M. Nakabayashi, N. Shibata, J. Kubota, K. Domen, *J. Catal.* **2015**, *328*, 308–315.

[46] Y. Yang, M. Forster, Y. Ling, G. Wang, T. Zhai, Y. Tong, A. J. Cowan, Y. Li, *Angew. Chem. Int. Ed.* **2016**, *510275*, 3403–3407.

[47] R. Long, N. J. English, O. V Prezhdo, *J. Phys. Chem. Lett.* **2014**, *5*, 2941–2946.

[48] R. Long, O. V Prezhdo, *ACS Nano* **2015**, *9*, 11143–11155.

[49] W. R. Duncan, W. M. Stier, O. V Prezhdo, *J. Am. Chem. Soc.* **2005**, *127*, 7941–7951.

[50] W. R. Duncan, C. F. Craig, O. V. Prezhdo, *J. Am. Chem. Soc.* **2007**, *129*, 8528–8543.

[51] S. a Fischer, W. R. Duncan, O. V Prezhdo, *J. Am. Chem. Soc.* **2009**, *131*, 15483–15491.

[52] R. Long, O. V Prezhdo, *J. Am. Chem. Soc.* **2011**, *133*, 19240–19249.

[53] R. Long, N. J. English, O. V Prezhdo, *J. Am. Chem. Soc.* **2012**, *134*, 14238–48.

[54] R. Jinnouchi, A. V. Akimov, S. Shirai, R. Asahi, O. V. Prezhdo, *J. Phys. Chem. C* **2015**, *119*, 26925–26936.

[55] R. Long, J. Liu, O. V. Prezhdo, *J. Am. Chem. Soc.* **2016**, *138*, 3884–3890.

[56] A. V Akimov, R. Asahi, R. Jinnouchi, O. V Prezhdo, *J. Am. Chem. Soc.* **2015**, *137*, 11517–11525.

[57] A. V. Akimov, R. Jinnouchi, S. Shirai, R. Asahi, O. V. Prezhdo, *J. Phys. Chem. B* **2015**, *119*, 7186–7197.

[58] K. Ozawa, M. Emori, S. Yamamoto, R. Yukawa, S. Yamamoto, R. Hobara, K. Fujikawa, H. Sakama, I. Matsuda, *J. Phys. Chem. Lett.* **2014**, *5*, 1953–1957.

[59] Y. Park, D. Kang, K.-S. Choi, *Phys. Chem. Chem. Phys.* **2014**, *16*, 1238–1246.

[60] H. Jiang, M. Nagai, K. Kobayashi, *J. Alloys Compd.* **2009**, *479*, 821–827.

[61] S. V. Fedorov, V. V. Belousov, *Russ. J. Electrochem.* **2009**, *45*, 573–575.

[62] Q. Shi, W. Zhao, L. Xie, J. Chen, M. Zhang, Y. Li, *J. Alloys Compd.* **2016**, *662*, 108–117.

[63] L. Chen, Q. Zhang, R. Huang, S.-F. Yin, S.-L. Luo, C.-T. Au, *Dalt. Trans.* **2012**, *41*, 9513.

[64] M. Han, T. Sun, P. Y. Tan, X. Chen, O. K. Tan, M. S. Tse, *RSC Adv.* **2013**, *3*, 24964.

[65] C. Lv, G. Chen, J. Sun, C. Yan, H. Dong, C. Li, *RSC Adv.* **2015**, *5*, 3767–3773.

[66] A. Le Gal, S. Abanades, *J. Phys. Chem. C* **2012**, *116*, 13516–13523.

[67] C. L. Muhich, B. W. Evanko, K. C. Weston, P. Lichty, X. Liang, J. Martinek, C. B. Musgrave, A. W. Weimer, *Science (80-.).* **2013**, *341*, 540–542.

[68] S. Docao, A. R. Koirala, M. G. Kim, I. C. Hwang, M. K. Song, K. B. Yoon, *Energy Environ. Sci.* **2017**, *10*, 628–640.

[69] F. Guo, W. Shi, C. Zhu, H. Li, Z. Kang, *Appl. Catal. B Environ.* **2018**, *226*, 412–420.

[70] S. Wang, P. Chen, Y. Bai, J. H. Yun, G. Liu, L. Wang, *Adv. Mater.* **2018**, *30*, 1–7.

[71] Mike McGee, "CO_2-earth," can be found under https://www.co2.earth/, **n.d.**

[72] Z. Yao, Y. Chen, L. Liu, X. Wu, S. Xiong, Z. Zhang, S. Xiang, *Chempluschem* **2016**, *81*, 850–856.

[73] D. H. Woen, G. P. Chen, J. W. Ziller, T. J. Boyle, F. Furche, W. J. Evans, *Angew. Chem. Int. Ed.* **2017**, *56*, 2050–2053.

[74] A. Paparo, J. Okuda, *Coord. Chem. Rev.* **2017**, *334*, 136–149.

[75] A. R. Sadique, W. W. Brennessel, P. L. Holland, *Inorg. Chem.* **2008**, *47*, 784–6.

[76] N. W. Davies, A. S. P. Frey, M. G. Gardiner, J. Wang, *Chem. Commun.* **2006**, 4853.

[77] G. Ménard, D. W. Stephan, *Angew. Chem. Int. Ed.* **2011**, *50*, 8396–8399.

[78] G. Ménard, D. W. Stephan, *Dalton Trans.* **2013**, *42*, 5447.

[79] G. Ménard, D. W. Stephan, *J. Am. Chem. Soc.* **2010**, *132*, 1796–1797.

[80] M. Pérez-Fortes, J. C. Schöneberger, A. Boulamanti, E. Tzimas, *Appl. Energy* **2016**, *161*, 718–732.

[81] W. Leitner, *Angew. Chem. Int. Ed. Engl.* **1995**, *34*, 2207–2221.

[82] D. W. Stephan, *Acc. Chem. Res.* **2015**, *48*, 306–316.

[83] T. Sakakura, J.-C. Choi, H. Yasuda, *Chem. Rev.* **2007**, *107*, 2365–87.

[84] C. Wu, H. Cheng, R. Liu, Q. Wang, Y. Hao, Y. Yu, F. Zhao, *Green Chem.* **2010**, *12*, 1811–1816.

[85] M. D. Greenhalgh, S. P. Thomas, *J. Am. Chem. Soc.* **2012**, *134*, 11900–11903.

[86] A. Tlili, E. Blondiaux, X. Frogneux, T. Cantat, *Green Chem.* **2015**, *17*, 157–168.

[87] Z. Han, R. Kortlever, H.-Y. Chen, J. C. Peters, T. Agapie, *ACS Cent. Sci.* **2017**, *3*, 853–859.

[88] T. Janes, Y. Yang, D. Song, *Chem. Commun.* **2017**, 11390–11398.

[89] P. B. V. Scholten, J. Demarteau, S. Gennen, J. De Winter, B. Grignard, A. Debuigne, M. A. R. Meier, C. Detrembleur, *Macromolecules* **2018**, *51*, 3379–3393.

[90] A. Bencini, V. Lippolis, *Coord. Chem. Rev.* **2010**, *254*, 2096–2180.

[91] M. Aresta, A. Dibenedetto, *J. Mol. Catal. A Chem.* **2002**, *182–183*, 399–409.

[92] Y. Li, X. Cui, K. Dong, K. Junge, M. Beller, *ACS Catal.* **2017**, *7*, 1077–1086.

[93] A. Darabi, P. G. Jessop, M. F. Cunningham, *Chem. Soc. Rev.* **2016**, *45*, 4391–4436.

[94] X.-T. Gao, C.-C. Gan, S.-Y. Liu, F. Zhou, H.-H. Wu, J. Zhou, *ACS Catal.* **2017**, *7*, 8588–8593.

[95] T. K. Saha, R. Das, *ChemistrySelect* **2018**, *3*, 147–169.

[96] M. Lakshmi Kantam, S. Laha, J. Yadav, S. Bhargava, *Tetrahedron Lett.* **2008**, *49*, 3083–3086.

[97] I. Knopf, M. A. Courtemanche, C. C. Cummins, *Organometallics* **2017**, *36*, 4834–4843.

[98] B. S. Hanna, A. D. Macintosh, S. Ahn, B. T. Tyler, G. T. R. Palmore, P. G. Williard, W. H. Bernskoetter, *Organometallics* **2014**, *33*, 3425–3432.

[99] Y. Zhang, B. S. Hanna, A. Dineen, P. G. Williard, W. H. Bernskoetter, *Organometallics* **2013**, *32*, 3969–3979.

[100] D. C. Graham, C. Mitchell, M. I. Bruce, G. F. Metha, J. H. Bowie, M. A. Buntine, *Organometallics* **2007**, *26*, 6784–6792.

[101] A. Vavasori, L. Calgaro, L. Pietrobon, L. Ronchin, *Pure Appl. Chem.* **2018**, *90*, 315–326.

[102] D. Garbe, *Ullmann's Encycl. Ind. Chem.* **2012**, 467–497.

[103] M. Halmann, *Nature* **1978**, *275*, 115–116.

[104] A. Iwase, S. Yoshino, T. Takayama, Y. H. Ng, R. Amal, A. Kudo, *J. Am. Chem. Soc.* **2016**, jacs.6b05304.

[105] G. Qin, Y. Zhang, X. Ke, X. Tong, Z. Sun, M. Liang, S. Xue, *Appl. Catal. B Environ.* **2013**, *129*, 59–605.

[106] C. Graves, S. D. Ebbesen, M. Mogensen, K. S. Lackner, *Renew. Sustain. Energy Rev.* **2011**, *15*, 1–23.

[107] S. N. Habisreutinger, L. Schmidt-Mende, J. K. Stolarczyk, *Angew. Chem. Int. Ed.* **2013**, *52*, 7372–7408.

[108] J. L. White, J. T. Herb, J. J. Kaczur, P. W. Majsztrik, A. B. Bocarsly, *J. CO_2 Util.* **2014**, *7*, 1–5.

[109] B. J. Trześniewski, W. a. Smith, *J. Mater. Chem. A* **2015**, 2919–2926.

[110] G. Centi, S. Perathoner, *Catal. Today* **2009**, *148*, 191–205.

[111] W. Chanmanee, M. F. Islam, B. H. Dennis, F. M. MacDonnell, *Proc. Natl. Acad. Sci.* **2016**, *113*, 2579–2584.

[112] E. B. Cole, P. S. Lakkaraju, D. M. Rampulla, A. J. Morris, E. Abelev, A. B. Bocarsly, *J. Am. Chem. Soc.* **2010**, *132*, 11539–51.

[113] J. Zhao, X. Wang, Z. Xu, J. S. C. Loo, *J. Mater. Chem. A* **2014**, *2*, 15228.

[114] S. Qin, F. Xin, Y. Liu, X. Yin, W. Ma, *J. Colloid Interface Sci.* **2011**, *356*, 257–261.

[115] W. N. Wang, W. J. An, B. Ramalingam, S. Mukherjee, D. M. Niedzwiedzki, S. Gangopadhyay, P. Biswas, *J Am Chem Soc* **2012**, *134*, 11276–11281.

[116] H. C. Yang, H. Y. Lin, Y. S. Chien, J. C. S. Wu, H. H. Wu, *Catal. Letters* **2009**, *131*, 381–387.

[117] A. Fujishima, K. Honda, *Nature* **1972**, *238*, 37–38.

[118] H. Jung, S. Youn, H. Kim, B. Koun, Y. Jeong, *Catcom* **2016**, *75*, 18–22.

[119] Y. P. Xie, G. Liu, L. Yin, H.-M. Cheng, *J. Mater. Chem.* **2012**, *22*, 6746.

[120] X. Li, J. Chen, H. Li, J. Li, Y. Xu, Y. Liu, J. Zhou, *J. Nat. Gas Chem.* **2011**, *20*, 413–417.

[121] H. Kisch, P. Lutz, *Photochem. Photobiol. Sci.* **2002**, *1*, 240–245.

[122] K. Sekizawa, K. Maeda, K. Domen, K. Koike, O. Ishitani, *J. Am. Chem. Soc.* **2013**, *135*, 4596–4599.

[123] T. M. Suzuki, H. Tanaka, T. Morikawa, M. Iwaki, S. Sato, S. Saeki, M. Inoue, T. Kajino, T. Motohiro, *Chem. Commun.* **2011**, *47*, 8673.

[124] Y. Liu, B. Huang, Y. Dai, X. Zhang, X. Qin, M. Jiang, M.-H. Whangbo, *Catal. Commun.* **2009**, *11*, 210–213.

[125] J. Mao, T. Peng, X. Zhang, K. Li, L. Zan, *Catal. Commun.* **2012**, *28*, 38–41.

[126] S. K. Choi, W. Choi, H. Park, *Phys. Chem. Chem. Phys.* **2013**, *15*, 6499–507.

[127] F. Lin, D. G. Wang, Z. X. Jiang, Y. Ma, J. Li, R. G. Li, C. Li, *Energy Environ. Sci.* **2012**, *5*, 6400–6406.

[128] S. B. Gawande, S. R. Thakare, *Int. Nano Lett.* **2012**, *2*, 11.

[129] G. Xi, J. Ye, *Chem. Commun.* **2010**, *46*, 1893.

[130] T. W. Kim, Y. Ping, G. A. Galli, K.-S. Choi, *Nat. Commun.* **2015**, *6*, 8769.

[131] F. M. Toma, J. K. Cooper, V. Kunzelmann, M. T. McDowell, J. Yu, D. M. Larson, N. J. Borys, C. Abelyan, J. W. Beeman, K. M. Yu, et al., *Nat Commun* **2016**, *7*, 12012.

[132] S. Gao, Y. Lin, X. Jiao, Y. Sun, Q. Luo, W. Zhang, D. Li, J. Yang, Y. Xie, *Nature* **2016**, *529*, 68–71.

[133] Y.-N. Li, R. Ma, L.-N. He, Z.-F. Diao, *Catal. Sci. Technol.* **2014**, *4*, 1498.

[134] S. N. Riduan, Y. Zhang, J. Y. Ying, *Angew. Chem. Int. Ed.* **2009**, *48*, 3322–3325.

[135] S. N. Riduan, J. Y. Ying, Y. Zhang, *ChemCatChem* **2013**, *5*, 1490–1496.

[136] W. Sun, C. Qian, L. He, K. K. Ghuman, A. P. Y. Wong, J. Jia, A. A. Jelle, P. G. O'Brien, L. M. Reyes, T. E. Wood, et al., *Nat. Commun.* **2016**, *7*, 12553.

[137] O. Martin, A. J. Martín, C. Mondelli, S. Mitchell, T. F. Segawa, R. Hauert, C. Drouilly, D. Curulla-Ferré, J. Pérez-Ramírez, *Angew. Chem. Int. Ed.* **2016**, *55*, 6261–6265.

[138] J. Gurnham, S. Gambarotta, I. Korobkov, L. Jasinska-Walc, R. Duchateau, *Organometallics* **2014**, *33*, 4401–4409.

[139] G. A. Luinstra, G. R. Haas, F. Molnar, V. Bernhart, R. Eberhardt, B. Rieger, *Chem. Eur. J.* **2005**, *11*, 6298–6314.

[140] M. Cokoja, C. Bruckmeier, B. Rieger, W. a Herrmann, F. E. Kühn, *Angew. Chem. Int. Ed.* **2011**, *50*, 8510–8537.

[141] S. Kernbichl, M. Reiter, F. Adams, S. Vagin, B. Rieger, *J. Am. Chem. Soc.* **2017**, *139*, 6787–6790.

[142] R. Nakano, S. Ito, K. Nozaki, *Nat. Chem.* **2014**, *6*, 325–331.

[143] S. Labouille, F. Nief, L. Maron, *J. Phys. Chem. A* **2011**, *115*, 8295–8301.

[144] M. Dolg, *Computational Methods in Lanthanide and Actinide Chemistry*, John Wiley & Sons Ltd, Chichester, UK, **2015**.

[145] W. J. Evans, C. a. Seibel, J. W. Ziller, *Inorg. Chem.* **1998**, *37*, 770–776.

[146] M. Rudolph, S. Dautz, E. Jager, *J. Am. Chem. Soc.* **2000**, *122*, 10821–10830.

[147] W. J. Evans, D. B. Rego, J. W. Ziller, A. G. DiPasquale, A. L. Rheingold, *Organometallics* **2007**, *26*, 4737–4745.

[148] R. Angamuthu, P. Byers, M. Lutz, A. L. Spek, E. Bouwman, *Science* **2010**, *327*, 313–315.

[149] L. Castro, S. Labouille, D. R. Kindra, J. W. Ziller, F. Nief, W. J. Evans, L. Maron, *Chem. Eur. J.*

2012, *18*, 7886–7895.

[150] H. Takisawa, Y. Morishima, S. Soma, R. K. Szilagyi, K. Fujisawa, *Inorg. Chem.* **2014**, *53*, 8191–8193.

[151] U. R. Pokharel, F. R. Fronczek, A. W. Maverick, *Nat. Commun.* **2014**, *5*, 5883.

[152] R. K. Yadav, J. Baeg, G. H. Oh, N. Park, K. Kong, J. Kim, D. W. Hwang, S. K. Biswas, *J. Am. Chem. Soc.* **2012**, *134*, 11455–11461.

[153] M. R. Hoffmann, J. A. Moss, M. M. Baum, *Dalton Trans.* **2011**, *40*, 5151.

[154] M. Anpo, *J. CO_2 Util.* **2013**, *1*, 8–17.

[155] G. A. Olah, A. Goeppert, G. K. S. Prakash, *J. Org. Chem.* **2009**, *74*, 487–498.

[156] R. Kortlever, J. Shen, K. J. P. Schouten, F. Calle-Vallejo, M. T. M. Koper, *J. Phys. Chem. Lett.* **2015**, *6*, 4073–4082.

[157] T. Inoue, A. Fujishima, S. Konishi, K. Honda, *Nature* **1979**, *277*, 637–638.

[158] K. S. Joya, Y. F. Joya, K. Ocakoglu, R. van de Krol, *Angew. Chem. Int. Ed.* **2013**, *52*, 10426–10437.

[159] S. Y. Reece, J. a Hamel, K. Sung, T. D. Jarvi, A. J. Esswein, J. J. H. Pijpers, D. G. Nocera, *Science* **2011**, *334*, 645–8.

[160] M. Asadi, K. Kim, C. Liu, A. V. Addepalli, P. Abbasi, P. Yasaei, P. Phillips, A. Behranginia, J. M. Cerrato, R. Haasch, et al., *Science* **2016**, *353*, 467–470.

[161] S. Y. Choi, S. K. Jeong, H. J. Kim, I.-H. Baek, K. T. Park, *ACS Sustain. Chem. Eng.* **2016**, *4*, 1311–1318.

[162] Q. Chen, Y. Qian, *Chem. Commun.* **2001**, *1*, 1402–1403.

[163] D. Marxer, P. Furler, M. Takacs, A. Steinfeld, *Energy Environ. Sci.* **2017**, *10*, 1142–1149.

[164] Q. Lu, J. Rosen, Y. Zhou, G. S. Hutchings, Y. C. Kimmel, J. G. Chen, F. Jiao, *Nat. Commun.* **2014**, *5*, 3242.

[165] Z. Shang, S. Li, L. Li, G. Liu, X. Liang, *Appl. Catal. B Environ.* **2017**, *201*, 302–309.

[166] V. S. Thoi, N. Kornienko, C. G. Margarit, P. Yang, C. J. Chang, *J. Am. Chem. Soc.* **2013**, *135*, 14413–24.

[167] S. Min, X. Yang, A.-Y. Lu, C.-C. Tseng, M. N. Hedhili, L.-J. Li, K.-W. Huang, *Nano Energy* **2016**, *27*, 121–129.

[168] Z. Zou, J. Ye, K. Sayama, H. Arakawa, *Nature* **2001**, *414*, 625–627.

[169] S. Cobo, J. Heidkamp, P.-A. Jacques, J. Fize, V. Fourmond, L. Guetaz, B. Jousselme, V. Ivanova, H. Dau, S. Palacin, et al., *Nat. Mater.* **2012**, *11*, 802–807.

[170] Z. Pu, Y. Luo, A. M. Asiri, X. Sun, *ACS Appl. Mater. Interfaces* **2016**, *8*, 4718–4723.

[171] Z.-K. Tang, W.-J. Yin, Le Zhang, B. Wen, D.-Y. Zhang, L.-M. Liu, W.-M. Lau, *Sci. Rep.* **2016**, *6*,

32764.

[172] Timmaji, Chanmanee, D. Tacconi, Rajeshwar, *J. Adv. Oxid. Technol.* **2011**, *14*, 93–105.

[173] X. J. Lv, S. Zhou, X. Huang, C. Wang, W. F. Fu, *Appl. Catal. B Environ.* **2016**, *182*, 220–228.

[174] E. E. Barton, D. M. Rampulla, A. B. Bocarsly, *J. Am. Chem. Soc.* **2008**, *130*, 6342–4.

[175] G. Seshadri, C. Lin, A. B. Bocarsly, *J. Electroanal. Chem.* **1994**, *372*, 145–150.

[176] W. Yu, J. Zhang, T. Peng, *Appl. Catal. B Environ.* **2016**, *181*, 220–227.

[177] P.-W. Pan, Y.-W. Chen, *Catal. Commun.* **2007**, *8*, 1546–1549.

[178] T. Hisatomi, J. Kubota, K. Domen, *Chem. Soc. Rev.* **2014**, *43*, 7520–7535.

[179] N. M. Dimitrijevic, B. K. Vijayan, O. G. Poluektov, T. Rajh, K. A. Gray, H. He, P. Zapol, *J. Am. Chem. Soc.* **2011**, *133*, 3964–3971.

[180] T. Wang, J. Gong, *Angew. Chem. Int. Ed.* **2015**, *54*, 10718–10732.

[181] N. P. Alderman, J. M. M. Sommers, C. J. Viasus, C. H. T. H. T. Wang, V. Peneau, S. Gambarotta, B. Vidjayacoumar, K. A. A. Al-Bahily, *Dalton Trans.* **2017**, *46*, 49–54.

[182] E. Fabbri, A. Habereder, K. Waltar, R. Kötz, T. J. Schmidt, *Catal. Sci. Technol.* **2014**, *4*, 3800–3821.

[183] D. P. Kumar, N. L. Reddy, M. Karthik, B. Neppolian, J. Madhavan, M. V. Shankar, *Sol. Energy Mater. Sol. Cells* **2016**, *154*, 78–87.

[184] C. Liu, B. C. Colón, M. Ziesack, P. A. Silver, D. G. Nocera, *Science* **2016**, *352*, 1210–1213.

[185] J. Shen, R. Kortlever, R. Kas, Y. Y. Birdja, O. Diaz-Morales, Y. Kwon, I. Ledezma-Yanez, K. J. P. Schouten, G. Mul, M. T. M. Koper, *Nat. Commun.* **2015**, *6*, 8177.

[186] D.-S. Lee, Y.-W. Chen, *J. CO_2 Util.* **2015**, *10*, 1–6.

[187] S. Nahar, M. Zain, A. Kadhum, H. Hasan, M. Hasan, *Materials (Basel).* **2017**, *10*, 629.

[188] R. Li, X. Wang, S. Jin, X. Zhou, Z. Feng, Z. Li, J. Shi, Q. Zhang, C. Li, *Sci. Rep.* **2015**, *5*, 13475.

[189] H. YI, T. Peng, D. Kea, D. Kea, L. Zana, C. Yan, *Int. J. Hydrogen Energy* **2008**, *33*, 672–678.

[190] M. Lei, Y. Pan, X. Ma, *Eur. J. Inorg. Chem.* **2015**, *2015*, 794–803.

[191] A. Walsh, Y. Yan, M. N. Huda, M. M. Al-Jassim, S.-H. H. Wei, *Chem. Mater.* **2009**, *21*, 547–551.

[192] S. Chen, W. Tang, Y. Hu, W. Liu, X. Fu, *Mater. Res. Bull.* **2013**, *48*, 3292–3297.

[193] J. Ye, Z. Zou, M. Oshikiri, A. Matsushita, M. Shimoda, M. Imai, T. Shishido, *Chem. Phys. Lett.* **2002**, *356*, 221–226.

[194] A. Kudo, K. Omori, H. Kato, *J. Am. Chem. Soc.* **1999**, *121*, 11459–11467.

[195] M. V. Malashchonak, E. A. Streltsov, D. A. Kuliomin, A. I. Kulak, A. V. Mazanik, *Mater. Chem. Phys.* **2017**, *201*, 189–193.

[196] X. Zhang, Z. Ai, F. Jia, L. Zhang, X. Fan, Z. Zou, *Mater. Chem. Phys.* **2007**, *103*, 162–167.

[197] S. Kohtani, K. Yoshida, T. Maekawa, A. Iwase, A. Kudo, H. Miyabe, R. Nakagaki, *Phys. Chem. Chem. Phys.* **2008**, *10*, 2986–2992.

[198] R. van de Krol, Y. Liang, J. Schoonman, *J. Mater. Chem.* **2008**, *18*, 2311.

[199] A. B. Murphy, P. R. F. Barnes, L. K. Randeniya, I. C. Plumb, I. E. Grey, M. D. Horne, J. A. Glasscock, *Int. J. Hydrogen Energy* **2006**, *31*, 1999–2017.

[200] H.-H. Huang, *Metals (Basel).* **2016**, *6*, 23.

[201] H. Hirakawa, S. Shiota, Y. Shiraishi, H. Sakamoto, S. Ichikawa, T. Hirai, *ACS Catal.* **2016**, *6*, 4976–4982.

[202] K. Sayama, A. Nomura, T. Arai, T. Sugita, R. Abe, M. Yanagida, T. Oi, Y. Iwasaki, Y. Abe, H. Sugihara, *J. Phys. Chem. B* **2006**, *110*, 11352–11360.

[203] O. Monfort, L. C. Pop, S. Sfaelou, T. Plecenik, T. Roch, V. Dracopoulos, E. Stathatos, G. Plesch, P. Lianos, *Chem. Eng. J.* **2016**, *286*, 91–97.

[204] M. Jitaru, *J. Univ. Chem. Technol. Metall.* **2007**, *42*, 333–344.

[205] G. P. Nagabhushana, A. H. Tavakoli, A. Navrotsky, *J. Solid State Chem.* **2015**, *225*, 187–192.

[206] a W. Sleight, H. Y. Chen, a Ferretti, D. E. Cox, *Mater. Res. Bull.* **1979**, *14*, 1571–1581.

[207] Q. Chen, M. Zhou, D. Ma, D. Jing, *J. Nanomater.* **2012**, *2012*, 1–6.

[208] J. K. Cooper, S. Gul, F. M. Toma, L. Chen, P.-A. Glans, J. Guo, J. W. Ager, J. Yano, I. D. Sharp, *Chem. Mater.* **2014**, *26*, 5365–5373.

[209] D. J. Payne, M. D. M. Robinson, R. G. Egdell, A. Walsh, J. McNulty, K. E. Smith, L. F. J. Piper, *Appl. Phys. Lett.* **2011**, *98*, 1–4.

[210] T. Saison, N. Chemin, C. Chanéac, O. Durupthy, L. Mariey, F. Maugé, V. Brezová, J.-P. Jolivet, *J. Phys. Chem. C* **2015**, *119*, 12967–12977.

[211] K. Ordon, A. Kassiba, M. Makowska-Janusik, *RSC Adv.* **2016**, *6*, 110695–110705.

[212] J. Zhuang, W. Dai, Q. Tian, Z. Li, L. Xie, J. Wang, P. Liu, X. Shi, D. Wang, *Langmuir* **2010**, *26*, 9686–9694.

[213] T. Saison, N. Chemin, C. Chanéac, O. Durupthy, V. Ruaux, L. Mariey, F. Maugé, P. Beaunier, J.-P. Jolivet, *J. Phys. Chem. C* **2011**, *115*, 5657–5666.

[214] Y. Park, K. J. McDonald, K.-S. S. Choi, *Chem. Soc. Rev.* **2013**, *42*, 2321–2337.

[215] Z. F. Huang, L. Pan, J. J. Zou, X. Zhang, L. Wang, *Nanoscale* **2014**, *6*, 14044–14063.

[216] A. Malathi, J. Madhavan, M. Ashokkumar, P. Arunachalam, *Appl. Catal. A Gen.* **2018**, *555*, 47–74.

[217] O. Monfort, G. Plesch, *Environ. Sci. Pollut. Res.* **2018**, *25*, 19362–19379.

[218] H. L. Tan, R. Amal, Y. H. Ng, *J. Mater. Chem. A* **2017**, *5*, 16498–16521.

[219] A. Y. Shvykin, V. V. Platonov, V. P. Proskuryakov, K. B. Chilachava, E. M. Khmarin, I. V. Kovtun, *Russ. J. Appl. Chem.* **2004**, *77*, 1200–1202.

[220] S. Naoki Komatsu; Yoshihiro Matano; Takuji Ogawa; Hitomi, *Organobismuth Chemistry*, **2001**.

[221] T. Kako, Z. Zou, M. Katagiri, J. Ye, *Chem. Mater.* **2007**, 198–202.

[222] T. Arnauld, D. H. R. Barton, E. Doris, *Tetrahedron Lett.* **1997**, *38*, 365–366.

[223] I. Vidyaratne, P. Crewdson, E. Lefebvre, S. Gambarotta, *Inorg. Chem.* **2007**, *46*, 8836–42.

[224] S. Groysman, D. Villagrán, D. E. Freedman, D. G. Nocera, *Chem. Commun.* **2011**, *47*, 10242.

[225] N. Desmangles, H. Jenkins, K. B. Ruppa, S. Gambarotta, *Inorganica Chim. Acta* **1996**, *250*, 1–4.

[226] J. G. Rebelein, Y. Hu, M. W. Ribbe, *ChemBioChem* **2015**, *16*, 1993–1996.

[227] S. Gambarotta, *Coord. Chem. Rev.* **2003**, *237*, 229–243.

[228] J. J. H. Edema, W. Stauthamer, F. Van Bolhuis, S. Gambarotta, W. J. J. Smeets, A. L. Spek, *Inorg. Chem.* **1990**, *29*, 1302–1306.

[229] M. Vivanco, C. Rizzolit, *Organometallics* **1993**, *12*, 1794–1801.

[230] W. Zhao, Y. Liu, Z. Wei, S. Yang, H. He, C. Sun, *Appl. Catal. B Environ.* **2016**, *185*, 242–252.

[231] R. Venkatesan, S. Velumani, M. Tabellout, N. Errien, A. Kassiba, *J. Phys. Chem. Solids* **2013**, *74*, 1695–1702.

[232] I. E. Soshnikov, N. V. Semikolenova, A. a. Shubin, K. P. Bryliakov, V. a. Zakharov, C. Redshaw, E. P. Talsi, *Organometallics* **2009**, *28*, 6714–6720.

[233] K. C. M. Westrup, T. Gregório, D. Stinghen, D. M. Reis, P. B. Hitchcock, R. R. Ribeiro, A. Barison, D. F. Back, E. L. de Sá, G. G. Nunes, et al., *Dalton Trans.* **2011**, *40*, 3198–210.

[234] G. B. Karet, Z. Sun, D. D. Heinrich, J. K. McCusker, K. Folting, W. E. Streib, J. C. Huffman, D. N. Hendrickson, G. Christou, *Inorg. Chem.* **1996**, *35*, 6450–6460.

[235] C. R. Cornman, E. P. Zovinka, Y. D. Boyajian, K. M. Geiser-Bush, P. D. Boyle, P. Singh, *Inorg. Chem.* **1995**, *34*, 4213–4219.

[236] S. Khademinia, M. Behzad, H. S. Jahromi, *RSC Adv.* **2015**, *5*, 24313–24318.

[237] N. C. Castillo, A. Heel, T. Graule, C. Pulgarin, *Appl. Catal. B Environ.* **2010**, *95*, 335–347.

[238] J. H. Thurston, D. Trahan, T. Ould-Ely, K. H. Whitmire, *Inorg. Chem.* **2004**, *43*, 3299–305.

[239] R. Li, X. Wang, S. Jin, X. Zhou, Z. Feng, Z. Li, J. Shi, Q. Zhang, C. Li, *Sci. Rep.* **2015**, *5*, 13475.

[240] J. A. Seabold, K. S. Choi, *J. Am. Chem. Soc.* **2012**, *134*, 2186–2192.

[241] B. Begemann, M. Jansen, *J. Less Common Met.* **1989**, *156*, 123–135.

[242] T. Nash, *Biochem. J.* **1953**, *55*, 416–421.

[243] R. Sleat, R. A. Mah, *Appl. Environ. Microbiol.* **1984**, *47*, 884–5.

[244] K. Sordakis, C. Tang, L. K. Vogt, H. Junge, P. J. Dyson, M. Beller, G. Laurenczy, *Chem. Rev.* **2017**, acs.chemrev.7b00182.

[245] A. J. M. Miller, D. M. Heinekey, J. M. Mayer, K. I. Goldberg, *Angew. Chem. Int. Ed.* **2013**, *52*, 3981–3984.

[246] L. Yang, X. Hua, J. Su, W. Luo, S. Chen, G. Cheng, *Appl. Catal. B Environ.* **2015**, *168–169*, 423–428.

[247] A. Boddien, D. Mellmann, F. Gärtner, R. Jackstell, H. Junge, P. J. Dyson, G. Laurenczy, R. Ludwig, M. Beller, *Science* **2011**, *333*, 1733–1736.

[248] L. E. Heim, N. E. Schlörer, J.-H. Choi, M. H. G. Prechtl, S. Figures, *Nat. Commun.* **2014**, *5*, 3621.

[249] J. G. Burr Jr., W. G. Brown, H. E. Heller, *J. Am. Chem. Soc.* **1950**, *72*, 2560–2562.

[250] A. K. Singh, S. Singh, A. Kumar, *Catal. Sci. Technol.* **2015**, *6*, 12–40.

[251] J. L. L. White, M. F. F. Baruch, J. E. E. Pander, Y. Hu, I. C. C. Fortmeyer, J. E. E. Park, T. Zhang, K. Liao, J. Gu, Y. Yan, et al., *Chem. Rev.* **2015**, *115*, 12888–12935.

[252] J. Li, Q.-L. Zhu, Q. Xu, *Chim. Int. J. Chem.* **2015**, *69*, 348–352.

[253] J. Cheng, X. Gu, P. Liu, T. Wang, H. Su, *J. Mater. Chem. A* **2016**, *4*, 16645–16652.

[254] Y.-Y. Cai, X.-H. Li, Y.-N. Zhang, X. Wei, K.-X. Wang, J.-S. Chen, *Angew. Chem. Int. Ed.* **2013**, *52*, 11822–11825.

[255] H. jin Jeon, Y. M. Chung, *Appl. Catal. B Environ.* **2017**, *210*, 212–222.

[256] C. Hu, J. K. Pulleri, S. W. Ting, K. Y. Chan, *Int. J. Hydrogen Energy* **2014**, *39*, 381–390.

[257] Q.-Y. Bi, J.-D. Lin, Y.-M. Liu, H.-Y. He, F.-Q. Huang, Y. Cao, *Angew. Chem. Int. Ed.* **2016**, *55*, 11849–11853.

[258] J. Li, J. Lu, *Chinese J. Chem. Phys.* **2017**, *30*, 319–324.

[259] J. J. A. Celaje, Z. Lu, E. A. Kedzie, N. J. Terrile, J. N. Lo, T. J. Williams, *Nat. Commun.* **2016**, *7*, 11308.

[260] S. Oldenhof, M. Lutz, B. De Bruin, J. I. Van Der Vlugt, J. N. H. Reek, *Chem. Sci.* **2015**, *6*, 1027–1034.

[261] Y. Manaka, N. Onishi, M. Iguchi, H. Kawanami, Y. Himeda, *J. Japan Pet. Inst.* **2017**, *60*, 53–62.

[262] Y. Du, Y. Bin Shen, Y. L. Zhan, F. Di Ning, L. M. Yan, X. C. Zhou, *Chinese Chem. Lett.* **2017**, *28*, 1746–1750.

[263] C. Tang, A. E. Surkus, F. Chen, M. M. Pohl, G. Agostini, M. Schneider, H. Junge, M. Beller, *Angew. Chem. Int. Ed.* **2017**, *56*, 16616–16620.

[264] V. Henricks, I. Yuranov, N. Autissier, G. Laurenczy, *Catalysts* **2017**, *7*, 348.

[265] Y. Noto, K. Fukuda, T. Onishi, K. Tamaru, *Bull. Chem. Soc. Jpn.* **1967**, *40*, 2722–2722.

[266] C. Chauvier, A. Tlili, C. Das Neves Gomes, P. Thuéry, T. Cantat, *Chem. Sci.* **2015**, *6*, 2938–2942.

[267] Y. Maenaka, T. Suenobu, S. Fukuzumi, *Energy Environ. Sci.* **2012**, *5*, 7360.

[268] Y. H. Lin, N. H. Leung, K. B. Holt, A. L. Thompson, J. D. E. T. Wilton-Ely, *Dalton Trans.* **2009**, 7891.

[269] R. E. DeRight, *J. Am. Chem. Soc.* **1933**, *55*, 4761–4764.

[270] P. Mars, J. J. F. Scholten, P. Zwietering, *Adv. Catal.* **1963**, *14*, 35–113.

[271] S. Savourey, G. Lefèvre, J. Berthet, P. Thuéry, C. Genre, T. Cantat, *Angew. Chem. Int. Ed.* **2014**, *53*, 10466–10470.

[272] I. Mellone, N. Gorgas, F. Bertini, M. Peruzzini, K. Kirchner, L. Gonsalvi, *Organometallics* **2016**, *35*, 3344–3349.

[273] D. Roeda, F. Dollé, *J. Label. Compd. Radiopharm.* **2006**, *49*, 295–304.

[274] K. TAKAI, H. NOZAKI, *Proc. Japan Acad. Ser. B Phys. Biol. Sci.* **2000**, *76*, 123–131.

[275] G. C. Wang, X. Y. Yi, I. D. Williams, W. H. Leung, *Inorg. Chem.* **2011**, *50*, 9141–9146.

[276] R. G. Sarawadekar, S. Jayaraman, *Def. Sci. J.* **1992**, *42*, 177–181.

[277] T. A. and Hewston, B. L. Chamberland, *J. Magn. Magn. Mater.* **1984**, *43*, 89–95.

[278] M. Iglesias, L. A. Oro, *Chem. Soc. Rev.* **2018**, *47*, 2772–2808.

[279] S. Lu, Z. Wang, J. Wang, J. Li, C. Li, *Green Chem.* **2018**, *20*, 1835–1840.

[280] C. Fellay, P. J. Dyson, G. Laurenczy, *Angew. Chem. Int. Ed.* **2008**, *120*, 4030–4032.

[281] P. Losch, A.-S. Felten, P. Pale, *Adv. Synth. Catal.* **2015**, *357*, 2931–2938.

[282] C. Peng, *Chromatographia* **1990**, *29*, 347–350.

[283] B. Aurivillius, A. Lowenhielm, *Acta Chem. Scand.* **1964**, *18*, 1937–1957.

[284] P. S. Lakkaraju, M. Askerka, H. Beyer, C. T. Ryan, T. Dobbins, C. Bennett, J. J. Kaczur, V. S. Batista, *ChemCatChem* **2016**, *8*, 3453–3457.

[285] F. J. Palomares, E. Paz, F. Soria, J. S. Moya, M. Burianek, M. Muehlberg, H. Schneider, *J. Am. Ceram. Soc.* **2009**, *92*, 2993–2998.

[286] H. Idriss, V. S. Lusvardi, M. A. Barteau, *Surf. Sci.* **1996**, *348*, 39–48.

[287] I. Bueno, C. Parada, *Thermochim. Acta* **1994**, *235*, 205–210.

[288] W. E. Morgan, W. J. Stec, J. R. Van Wazer, *Inorg. Chem.* **1972**, *12*, 953–955.

[289] K. A. Grice, *Coord. Chem. Rev.* **2017**, *336*, 78–95.

[290] C. Lorber, F. Wolff, R. Choukroun, L. Vendier, *Eur. J. Inorg. Chem.* **2005**, 2850–2859.

[291] K. Nomura, X. Hou, *Dalton Trans.* **2017**, *46*, 12–24.

[292] H. Yamamoto, W. Z. and, *J. Am. Chem. Soc.* **2007**, 286–287.

[293] C. Miceli, J. Rintjema, E. Martin, E. C. Escudero-Adán, C. Zonta, G. Licini, A. W. Kleij, *ACS Catal.* **2017**, *7*, 2367–2373.

[294] A. Mavrandonakis, K. D. Vogiatzis, A. D. Boese, K. Fink, T. Heine, W. Klopper, *Inorg. Chem.* **2015**, *54*, 8251–8263.

[295] J. Yu, L.-H. Xie, J.-R. Li, Y. Ma, J. M. Seminario, P. B. Balbuena, *Chem. Rev.* **2017**, acs.chemrev.6b00626.

[296] C. W. Machan, S. A. Chabolla, J. Yin, M. K. Gilson, F. A. Tezcan, C. P. Kubiak, *J. Am. Chem. Soc.* **2014**, *136*, 14598–14607.

[297] S. Bontemps, L. Vendier, S. Sabo-Etienne, *J. Am. Chem. Soc.* **2014**, *136*, 4419–4425.

[298] A. J. Morris, G. J. Meyer, E. Fujita, *Acc. Chem. Res.* **2009**, *42*, 1983–1994.

[299] C. Wang, Z. Xie, K. E. DeKrafft, W. Lin, *J. Am. Chem. Soc.* **2011**, *133*, 13445–13454.

[300] J. L. White, M. F. Baruch, J. E. Pander, Y. Hu, I. C. Fortmeyer, J. E. Park, T. Zhang, K. Liao, J. Gu, Y. Yan, et al., *Chem. Rev.* **2015**, *115*, 12888–12935.

[301] J. Klankermayer, S. Wesselbaum, K. Beydoun, W. Leitner, *Angew. Chem. Int. Ed.* **2016**, *55*, 7296–7343.

[302] F.-G. Fontaine, D. W. Stephan, *Curr. Opin. Green Sustain. Chem.* **2017**, *3*, 28–32.

[303] T. Wang, D. W. Stephan, *Chem. Commun.* **2014**, *50*, 7007.

[304] R. Dobrovetsky, D. W. Stephan, *Angew. Chem. Int. Ed.* **2013**, *52*, 2516–2519.

[305] M. J. Sgro, J. Dömer, D. W. Stephan, *Chem. Commun.* **2012**, *48*, 7253.

[306] Z. Jin, X. Zhang, Y. Li, S. Li, G. Lu, *Catal. Commun.* **2007**, *8*, 1267.

[307] D. S. Laitar, P. Müller, J. P. Sadighi, *J. Am. Chem. Soc.* **2005**, *127*, 17196–7.

[308] T. Ishida, R. Kobayashi, T. Yamada, *Org. Lett.* **2014**, *16*, 2430–2433.

[309] T. Ishida, S. Kikuchi, T. Tsubo, T. Yamada, *Org. Lett.* **2013**, *15*, 848–851.

[310] T. Ishida, S. Kikuchi, T. Yamada, *Org. Lett.* **2013**, *15*, 3710–3.

[311] M. Takimoto, Y. Nakamura, K. Kimura, M. Mori, *J. Am. Chem. Soc.* **2004**, *126*, 5956–5957.

[312] D. J. Darensbourg, K. M. Sanchez, A. L. Rheingold, *J. Am. Chem. Soc.* **1987**, *109*, 290–292.

[313] C. M. Mömming, E. Otten, G. Kehr, R. Fröhlich, S. Grimme, D. W. Stephan, G. Erker, *Angew. Chem. Int. Ed.* **2009**, *48*, 6643–6646.

[314] P. Jochmann, D. W. Stephan, *Organometallics* **2013**, *32*, 7503–7508.

[315] A. Berkefeld, W. E. Piers, M. Parvez, *J. Am. Chem. Soc.* **2010**, *132*, 10660–10661.

[316] F. A. LeBlanc, W. E. Piers, M. Parvez, *Angew. Chem. Int. Ed.* **2014**, *53*, 789–792.

[317] S. Gambarotta, F. Arena, C. Floriani, P. F. Zanazzi, *J. Am. Chem. Soc.* **1982**, *104*, 5082–5092.

[318] W. J. Evans, C. A. Seibel, J. W. Ziller, R. J. Doedens, *Organometallics* **1998**, *17*, 2103–2112.

[319] D. R. Kindra, I. J. Casely, M. E. Fieser, J. W. Ziller, F. Furche, W. J. Evans, *J. Am. Chem. Soc.* **2013**, *135*, 7777–7787.

[320] S. M. Mansell, N. Kaltsoyannis, P. L. Arnold, *J. Am. Chem. Soc.* **2011**, *133*, 9036–9051.

[321] S. Moret, P. J. Dyson, G. Laurenczy, *Nat. Commun.* **2014**, *5*, 4017.

[322] M. Aresta, A. Dibenedetto, *Dalton Trans.* **2007**, 2975.

[323] S. Enthaler, *ChemSusChem* **2008**, *1*, 801–804.

[324] T. Panda, P. Pachfule, Y. Chen, J. Jiang, R. Banerjee, *Chem. Commun.* **2011**, *47*, 2011–2013.

[325] P. Sozzani, S. Bracco, A. Comotti, L. Ferretti, R. Simonutti, *Angew. Chem. Int. Ed.* **2005**, *44*, 1816–1820.

[326] H. Furukawa, O. M. Yaghi, *J. Am. Chem. Soc.* **2009**, *131*, 8875–8883.

[327] A. R. Millward, O. M. Yaghi, *J. Am. Chem. Soc.* **2005**, *127*, 17998–17999.

[328] J. J. Chi, T. C. Johnstone, D. Voicu, P. Mehlmann, F. Dielmann, E. Kumacheva, D. W. Stephan, *Chem. Sci.* **2017**, *8*, 3270–3275.

[329] D. Voicu, M. Abolhasani, R. Choueiri, G. Lestari, C. Seiler, G. Menard, J. Greener, A. Guenther, D. W. Stephan, E. Kumacheva, *J. Am. Chem. Soc.* **2014**, *136*, 3875–3880.

[330] D. W. Stephan, *J. Am. Chem. Soc.* **2015**, *137*, 10018–10032.

[331] L. J. Hounjet, C. B. Caputo, D. W. Stephan, *Angew. Chem. Int. Ed.* **2012**, *51*, 4714–4717.

[332] W. Wang, S. Wang, X. Ma, J. Gong, *Chem. Soc. Rev.* **2011**, *40*, 3703–27.

[333] D. J. Darensbourg, *Inorg. Chem.* **2010**, *49*, 10765–10780.

[334] M. Tahir, N. S. Amin, *Renew. Sustain. Energy Rev.* **2013**, *25*, 560–579.

[335] O. Jacquet, C. Das Neves Gomes, M. Ephritikhine, T. Cantat, *J. Am. Chem. Soc.* **2012**, *134*, 2934–2937.

[336] C. Das Neves Gomes, O. Jacquet, C. Villiers, P. Thuéry, M. Ephritikhine, T. Cantat, *Angew. Chem. Int. Ed.* **2012**, *51*, 187–190.

[337] S. Atsumi, W. Higashide, J. C. Liao, *Nat. Biotechnol.* **2009**, *27*, 1177–1180.

[338] R. J. Haines, R. E. Wittrig, C. P. Kubiak, *Inorg. Chem.* **1994**, *33*, 4723–4728.

[339] C. T. Lee, P. A. Psathas, K. P. Johnston, J. DeGrazia, T. W. Randolph, *Langmuir* **1999**, *15*, 6781–6791.

[340] R. F. Tabor, D. Y. C. Chan, F. Grieser, R. R. Dagastine, *Angew. Chem. Int. Ed.* **2011**, *50*, 3454–3456.

[341] M. Pasquali, S. Gambarotta, C. Floriani, A. Chiesi-Villa, C. Guastini, *Inorg. Chem.* **1981**, *20*, 165–171.

[342] G. Fachinetti, C. Floriani, A. Chiesi-Villa, C. Guastini, *J. Am. Chem. Soc.* **1979**, *101*, 1767–1775.

[343] M. Zhang, M. El-Roz, H. Frei, J. L. Mendoza-Cortes, M. Head-Gordon, D. C. Lacy, J. C. Peters, *J. Phys. Chem. C* **2015**, *119*, 4645–4654.

[344] C. T. Saouma, C. C. Lu, M. W. Day, J. C. Peters, *Chem. Sci.* **2013**, *4*, 4042.

[345] F.-G. Fontaine, M.-A. Courtemanche, M.-A. Légaré, É. Rochette, *Coord. Chem. Rev.* **2017**, *334*, 124–135.

[346] H. Schwarz, *Coord. Chem. Rev.* **2017**, *334*, 112–123.

[347] W. J. Evans, J. R. Walensky, J. W. Ziller, *Organometallics* **2010**, *29*, 945–950.

[348] S. Gambarotta, C. Floriani, A. Chiesi-Villa, C. Guastini, *J. Am. Chem. Soc.* **1985**, *107*, 2985–2986.

[349] S. Bellemin-Laponnaz, S. Dagorne, *Chem. Rev.* **2014**, *114*, 8747–8774.

[350] G. Fachinetti, S. Del Nero, C. Floriani, *J. Chem. Soc., Dalt. Trans.* **1976**, *19*, 1046–1049.

[351] M. Pasquali, C. Floriani, A. Chiesi-Villa, C. Guastini, *Inorg. Chem.* **1980**, *19*, 3847–3850.

[352] A. F. R. Kilpatrick, F. G. N. Cloke, *Chem. Commun.* **2014**, *50*, 2769–2771.

[353] T. Tsuda, S. Sanada, T. Saegusa, *J. Organomet. Chem.* **1976**, *116*, C10–C12.

[354] D. Sieh, D. C. Lacy, J. C. Peters, C. P. Kubiak, *Chem. - A Eur. J.* **2015**, *21*, 8497–8503.

[355] C. Schulten, G. von Frantzius, G. Schnakenburg, A. Espinosa, R. Streubel, *Chem. Sci.* **2012**, *3*, 3526.

[356] L. J. Procopio, P. J. Carroll, D. H. Berry, *Organometallics* **1993**, *12*, 3087–3093.

[357] O. T. Summerscales, A. S. P. Frey, F. G. N. Cloke, P. B. Hitchcock, *Chem. Commun.* **2008**, 198–200.

[358] O. R. Allen, S. J. Dalgarno, L. D. Field, *Organometallics* **2008**, *27*, 3328–3330.

[359] C. W. Machan, S. A. Chabolla, C. P. Kubiak, *Organometallics* **2015**, *34*, 4678–4683.

[360] A. Demessence, D. M. D'Alessandro, M. L. Foo, J. R. Long, *J. Am. Chem. Soc.* **2009**, *131*, 8784–6.

[361] P. Braunstein, D. Matt, Y. Dusausoy, J. Fischer, A. Mitschler, L. Ricard, *J. Am. Chem. Soc.* **1981**, *103*, 5115–5125.

[362] J. J. Gassensmith, H. Furukawa, R. A. Smaldone, R. S. Forgan, Y. Y. Botros, O. M. Yaghi, J. F. Stoddart, *J. Am. Chem. Soc.* **2011**, *133*, 15312–15315.

[363] M. Vivanco, J. Ruiz, C. Floriani, A. Chiesi-Villa, C. Rizzoli, *Organometallics* **1993**, *12*, 1794–1801.

[364] A. J. Morris, R. T. McGibbon, A. B. Bocarsly, *ChemSusChem* **2011**, *4*, 191–6.

[365] A. Coletti, C. J. Whiteoak, V. Conte, A. W. Kleij, *ChemCatChem* **2012**, *4*, 1190–1196.

[366] T. Hanna, A. Baranger, R. Bergman, *J. Am. Chem. Soc.* **1995**, *117*, 11363–11364.

[367] P. Frediani, C. Faggi, A. Salvini, M. Bianchi, F. Piacenti, *Inorg. Chim. Acta* **1998**, *272*, 141–149.

[368] K. Huang, C.-L. Sun, Z.-J. Shi, *Chem. Soc. Rev.* **2011**, *40*, 2435.

[369] E. Fujita, D. J. Szalda, C. Creutz, N. Sutin, *J. Am. Chem. Soc.* **1988**, *110*, 4870–4871.

[370] B. Kersting, *Angew. Chem. Int. Ed.* **2001**, *40*, 3987–3990.

[371] F. Calaza, C. Stiehler, Y. Fujimori, M. Sterrer, S. Beeg, M. Ruiz-Oses, N. Nilius, M. Heyde, T. Parviainen, K. Honkala, et al., *Angew. Chem. Int. Ed.* **2015**, *54*, 12484–12487.

[372] S. Meker, O. Braitbard, M. D. Hall, J. Hochman, E. Y. Tshuva, *Chem. Eur. J.* **2016**, *22*, 9986–9995.

[373] R. C. How, R. Hembre, J. A. Ponasik, G. S. Tolleson, M. L. Clarke, *Catal. Sci. Technol.* **2016**, *6*, 118–124.

[374] M. Sutradhar, G. Mukherjee, M. G. B. Drew, S. Ghosh, P. O. Box, R. Rg, *Inorg. Chem.* **2007**, *46*, 5069–5075.

[375] B. Castellano, E. Solari, C. Floriani, R. Scopelliti, N. Re, *Inorg. Chem.* **1999**, *38*, 3406–3413.

[376] I. Vidyaratne, P. Crewdson, E. Lefebvre, S. Gambarotta, *Inorg. Chem.* **2007**, *46*, 8836–8842.

[377] K. Thiele, H. Go, W. I. W. Seidel, È. Disproportionierungs-, *Z. Anorg. Allg. Chem.* **2002**, *628*, 107–108.

[378] I. Castro-Rodríguez, K. Meyer, *Chem. Commun.* **2006**, 1353.

[379] P. D. C. Dietzel, R. E. Johnsen, H. Fjellvåg, S. Bordiga, E. Groppo, S. Chavan, R. Blom, *Chem. Commun.* **2008**, 5125.

[380] E. Manzer, *Inorganic Syntheses*, John Wiley & Sons, Inc., Hoboken, NJ, USA, **1982**.

[381] G. A. Bailey, D. E. Fogg, *ACS Catal.* **2016**, *6*, 4962–4971.

[382] M. D. Eelman, J. M. Blacquiere, M. M. Moriarty, D. E. Fogg, *Angew. Chem. Int. Ed.* **2008**, *47*, 303–306.

[383] J. J. P. Stewart, *J. Mol. Model.* **2013**, *19*, 1–32.

[384] A. Becke, *J. Chem. Phys.* **1993**, *98*, 5648–5652.

[385] C. Lee, W. Yang, R. G. Parr, *Phys. Rev. B* **1988**, *37*, 785–789.

[386] S. H. Vosko, L. Wilk, M. Nusair, *Can. J. Phys.* **1980**, *58*, 1200–1211.

[387] P. J. Stephens, F. J. Devlin, C. F. Chabalowski, M. J. Frisch, *J. Phys. Chem.* **1994**, *98*, 11623–11627.

[388] A. Schäfer, C. Huber, R. Ahlrichs, *J. Chem. Phys.* **1994**, *100*, 5829–5835.

[389] A. Schafer, H. Horn, R. Ahlrichs, *J. Chem. Phys.* **1992**, *97*, 2570–2577.

[390] C. Peng, P. Y. Ayala, H. B. Schlegel, M. J. Frisch, *J. Comput. Chem.* **1996**, *17*, 49–56.

[391] C. Peng, H. B. Schlegel, *Isr. J. Chem.* **1993**, *33*, 449.

[392] K. Fukui, *Acc. Chem. Res.* **1981**, *14*, 363–368.

[393] K. Fukui, *J. Phys. Chem.* **1970**, *74*, 4161–4163.

[394] S. Miertuš, E. Scrocco, J. Tomasi, *Chem. Phys.* **1981**, *55*, 117–129.

[395] R. Cammi, J. Tomasi, *J. Comput. Chem.* **1995**, *16*, 1449–1458.

[396] A.-R. Allouche, *J. Comput. Chem.* **2011**, *32*, 174–82.

[397] M. D. Hanwell, D. E. Curtis, D. C. Lonie, T. Vandermeersch, E. Zurek, G. R. Hutchison, *J. Cheminform.* **2012**, *4*, 17.

[398] G. Fachinetti, C. Floriani, P. F. Zanazzi, *J. Am. Chem. Soc.* **1978**, *100*, 7405–7407.

[399] S. Gambarotta, F. Arena, C. Floriani, A. Gaetani-Manfredotti, *J. Chem. Soc., Chem. Commun.* **1982**, 835–837.

[400] S. Gambarotta, S. Strologo, C. Floriani, A. Chiesi-Villa, C. Guastini, *J. Am. Chem. Soc.* **1985**, *107*, 6278–6282.

[401] G. Fachinetti, C. Floriani, S. Pucci, *J. Chem. Soc., Chem. Commun.* **1978**, 269–270.

[402] D. Gust, T. A. Moore, A. L. Moore, *Acc. Chem. Res.* **2009**, *42*, 1890–1898.

[403] M. E. El-Khouly, E. El-Mohsnawy, S. Fukuzumi, *J. Photochem. Photobiol. C Photochem. Rev.* **2017**, *31*, 36–83.

[404] F. Pan, W. Deng, C. Justiniano, Y. Li, *Appl. Catal. B Environ.* **2018**, *226*, 463–472.

[405] Y. Yamazaki, H. Takeda, O. Ishitani, *J. Photochem. Photobiol. C Photochem. Rev.* **2015**, *25*, 106–137.

[406] R. H. Crabtree, *New J. Chem.* **2011**, *35*, 18–23.

[407] W. Leitner, *Coord. Chem. Rev.* **1996**, *153*, 257–284.

[408] C.-C. Chang, M.-C. Liao, T.-H. Chang, S.-M. Peng, G.-H. Lee, *Angew. Chem. Int. Ed.* **2005**, *44*, 7418–7420.

[409] C. L. Webster, J. W. Ziller, W. J. Evans, *Organometallics* **2012**, *31*, 7191–7197.

[410] E. Steffensmeier, K. M. Nicholas, *Chem. Commun.* **2018**, *54*, 790–793.

[411] S. Sato, T. Arai, T. Morikawa, K. Uemura, T. M. Suzuki, H. Tanaka, T. Kajino, *J. Am. Chem. Soc.* **2011**, *133*, 15240–15243.

[412] S. Zhang, P. Kang, T. J. Meyer, *J. Am. Chem. Soc.* **2014**, *136*, 1734–1737.

[413] W. H. Wang, Y. Himeda, J. T. Muckerman, G. F. Manbeck, E. Fujita, *Chem. Rev.* **2015**, *115*, 12936–12973.

[414] R. G. Pearson, *J. Am. Chem. Soc.* **1963**, *85*, 3533–3539.

[415] R. G. Pearson, *Coord. Chem. Rev.* **1990**, *100*, 403–425.

[416] R. K. Minhas, J. J. H. Edema, S. Gambarotta, A. Meetsma, *J. Am. Chem. Soc.* **1993**, *115*, 6710–6717.

[417] A. Paparo, J. S. Silvia, C. E. Kefalidis, T. P. Spaniol, L. Maron, J. Okuda, C. C. Cummins, *Angew. Chemie Int. Ed.* **2015**, *54*, 9115–9119.

[418] R. Dobrovetsky, D. W. Stephan, *Isr. J. Chem.* **2015**, *55*, 206–209.

[419] E. J. Lawrence, R. J. Blagg, D. L. Hughes, A. E. Ashley, G. G. Wildgoose, *Chem. - A Eur. J.* **2015**, *21*, 900–906.

[420] S. Zhang, A. M. Appel, R. M. Bullock, *J. Am. Chem. Soc.* **2017**, *139*, 7376–7387.

[421] M. Falcone, L. N. Poon, F. Fadaei Tirani, M. Mazzanti, *Angew. Chem. Int. Ed.* **2018**, *57*, 3697–3700.

[422] F.-G. Fontaine, D. W. Stephan, *Philos. Trans. R. Soc. A Math. Phys. Eng. Sci.* **2017**, *375*, 20170004.

[423] D. W. Stephan, *Science* **2016**, *354*, aaf7229-aaf7229.

[424] P. Gao, S. Li, X. Bu, S. Dang, Z. Liu, H. Wang, L. Zhong, M. Qiu, C. Yang, J. Cai, et al., *Nat. Chem.* **2017**, *9*, 1019–1024.

[425] I. Castro-Rodriguez, *Science* **2004**, *305*, 1757–1759.

[426] W. L. F. Amarego, D. D. Perrin, *J. Organomet. Chem.* **1981**, *213*, C62.

[427] T. Yanai, D. P. Tew, N. C. Handy, *Chem. Phys. Lett.* **2004**, *393*, 51–57.

[428] P. J. Hay, W. R. Wadt, *J. Chem. Phys.* **1985**, *82*, 270–283.

[429] P. J. Hay, W. R. Wadt, *J. Chem. Phys.* **1985**, *82*, 299–310.

[430] W. R. Wadt, P. J. Hay, *J. Chem. Phys.* **1985**, *82*, 284–298.

[431] F. Wolff, C. Lorber, R. Choukroun, B. Donnadieu, *Inorg. Chem.* **2003**, *42*, 7839–7845.

[432] F. M. Kerton, S. Holloway, A. Power, R. G. Soper, K. Sheridan, J. M. Lynam, A. C. Whitwood, C. E. Willans, *Can. J. Chem.* **2008**, *86*, 435–443.

[433] A. Veber, M. R. Cicconi, A. Puri, D. de Ligny, *J. Phys. Chem. C* **2018**, acs.jpcc.8b05614.

[434] X. Ding, K. Zhao, L. Zhang, *Environ. Sci. Technol.* **2014**, *48*, 5823–5831.

[435] G. Blasse, O. B. Ho, *J. Lumin.* **1980**, *21*, 165–168.

[436] O. V. Laguta, H. El Hamzaoui, M. Bouazaoui, V. B. Arion, I. M. Razdobreev, *Sci. Rep.* **2017**, *7*, 3178.

[437] S. Lardhi, L. Cavallo, M. Harb, *J. Phys. Chem. C* **2018**, *122*, acs.jpcc.8b03044.

[438] H. Liu, C. Du, M. Li, S. S. Zhang, H. Bai, L. Yang, S. S. Zhang, *ACS Appl. Mater. Interfaces* **2018**, acsami.8b09617.

[439] M. Yoneya, H. Minemawari, T. Yamada, T. Hasegawa, *J. Phys. Chem. C* **2017**, *121*, 8796–8803.

[440] L. G. Hubert-Pfalzgraf, *Inorg. Chem. Commun.* **2003**, *6*, 102–120.

[441] P. C. Andrews, P. C. Junk, I. Nuzhnaya, D. T. Thielemann, *Inorg. Chem.* **2012**, *51*, 751–753.

[442] J. W. Cheng, S. T. Zheng, E. Ma, G. Y. Yang, *Inorg. Chem.* **2007**, *46*, 10534–10538.

[443] J. C. Vites, B. D. Steffey, M. E. Giuseppetti-Dery, A. R. Cutler, *Organometallics* **1991**, *10*, 2827–2834.

[444] J. R. Pinkes, B. D. Steffey, J. C. Vites, A. R. Cutler, *Organometallics* **1994**, *13*, 21–23.

[445] M. L. Man, K. C. Lam, W. N. Sit, S. M. Ng, Z. Zhou, Z. Lin, C. P. Lau, *Chem. Eur. J.* **2006**, *12*, 1004–1015.

[446] J. P. Krogman, M. W. Bezpalko, B. M. Foxman, C. M. Thomas, *Inorg. Chem.* **2013**, *52*, 3022–3031.

[447] J. P. Krogman, B. M. Foxman, C. M. Thomas, *J. Am. Chem. Soc.* **2011**, *133*, 14582–14585.

[448] A. Hicken, A. J. P. White, M. R. Crimmin, *Angew. Chem. Int. Ed.* **2017**, *56*, 15127–15130.

[449] L. Tang, S. Zhang, Q. Wu, X. Wang, H. Wu, Z. Jiang, *J. Mater. Chem. A* **2018**, *6*, 2964–2973.

[450] S. Bagherzadeh, N. P. Mankad, *J. Am. Chem. Soc.* **2015**, *137*, 10898–10901.

[451] K. P. Chiang, S. M. Bellows, W. W. Brennessel, P. L. Holland, *Chem. Sci.* **2014**, *5*, 267–274.

[452] O. Cooper, C. Camp, J. Pécaut, C. E. Kefalidis, L. Maron, S. Gambarelli, M. Mazzanti, *J. Am. Chem. Soc.* **2014**, *136*, 6716–6723.

[453] M. Stolmàr, C. Floriani, A. Chiesi-Villa, C. Rizzoli, *Inorg. Chem.* **1997**, *36*, 1694–1701.

[454] C. C. Lu, C. T. Saouma, M. W. Day, J. C. Peters, *J. Am. Chem. Soc.* **2007**, *129*, 4–5.

[455] I. Bulimestru, S. Shova, N. Popa, P. Roussel, F. Capet, R. Vannier, N. Djelal, L. Burylo, J. Wignacourt, A. Gulea, et al., *Chem. Mater.* **2014**, *26*, 6092–6103.

[456] I. Bratsos, C. Tampaxis, I. Spanopoulos, N. Demitri, G. Charalambopoulou, D. Vourloumis, T. A. Steriotis, P. N. Trikalitis, *Inorg. Chem.* **2018**, *57*, 7244–7251.

[457] L. Bonomo, E. Solari, G. Martin, R. Scopelliti, C. Floriani, *Chem. Commun.* **1999**, *874*, 2319–2320.

[458] W. Kaszuwara, M. Leonowicz, A. Łukasiewicz, *Mater. Lett.* **1992**, *12*, 429–433.

[459] W. Li, A. Zhang, X. Jiang, M. J. Janik, J. Qiu, Z. Liu, X. Guo, C. Song, *J. CO_2 Util.* **2018**, *23*, 219–225.

[460] C. W. Machan, C. P. Kubiak, *Dalton Trans.* **2016**, *45*, 15942–15950.

[461] J. W. Pell, W. C. Davis, H. C. zur Loye, *Inorg. Chem.* **1996**, *35*, 5754–5755.

[462] J. H. Thurston, T. O. Ely, D. Trahan, K. H. Whitmire, *Chem. Mater.* **2003**, *15*, 4407–4416.

[463] T. Ould-Ely, J. H. Thurston, K. H. Whitmire, *Comptes Rendus Chim.* **2005**, *8*, 1906–1921.

[464] V. Stavila, J. H. Thurston, K. H. Whitmire, *Inorg. Chem.* **2009**, *48*, 6945–51.

[465] I. Kumar, P. Bhattacharya, K. H. Whitmire, *J. Organomet. Chem.* **2015**, *794*, 153–167.

[466] I. Kumar, P. Andrews, K. H. Whitmire, *Eur. J. Inorg. Chem.* **2015**, *2015*, 605–608.

[467] I. Kumar, P. Bhattacharya, K. H. Whitmire, *Organometallics* **2014**, *33*, 2906–2909.

[468] C. M. Jones, M. D. Burkart, K. H. Whitmire, *J. Chem. Soc., Chem. Commun.* **1992**, 1638–1639.

[469] K. H. Whitmire, S. Hoppe, O. Sydora, J. L. Jolas, C. M. Jones, *Inorg. Chem.* **2000**, *39*, 85–97.

[470] L. E. Turner, M. G. Davidson, M. D. Jones, H. Ott, V. S. Schulz, P. J. Wilson, *Inorg. Chem.* **2006**, *45*, 6123–6125.

[471] M. Vehkamäki, T. Hatanpää, M. Ritala, M. Leskelä, *J. Mater. Chem.* **2004**, *14*, 3191–3197.

[472] M. Oshikiri, M. Boero, J. Ye, F. Aryasetiawan, G. Kido, *Thin Solid Films* **2003**, *445*, 168–174.

[473] S. C. Roy, O. K. Varghese, M. Paulose, C. a Grimes, *ACS Nano* **2010**, *4*, 1259–1278.

[474] X. Meng, Z. Zhang, *J. Mol. Catal. A Chem.* **2016**, *423*, 533–549.

[475] A. Sisak, E. Sámpár-Szerencsés, V. Galamb, L. Németh, F. Ungváry, G. Pályi, *Organometallics* **1989**, *8*, 1096–1100.

[476] M. C. Boswell, J. V. Dickson, *J. Am. Chem. Soc.* **1918**, *40*, 1779–1786.